



**3D FINITE ELEMENT MODELING OF  
SLIDING WEAR**

Dissertation

Rodolfo G. Buentello Hernandez, Major, USAF

AFIT-ENY-DS-13-D-06

**DEPARTMENT OF THE AIR FORCE  
AIR UNIVERSITY**

**AIR FORCE INSTITUTE OF TECHNOLOGY**

---

---

**Wright-Patterson Air Force Base, Ohio**

**DISTRIBUTION STATEMENT A.**  
APPROVED FOR PUBLIC RELEASE: DISTRIBUTION UNLIMITED

The views expressed in this thesis are those of the author and do not reflect the official policy or position of the United States Air Force, Department of Defense, or the United States Government. This material is declared a work of the U.S. Government and is not subject to copyright protection in the United States.

AFIT-ENY-DS-13-D-06

**3D FINITE ELEMENT MODELING OF SLIDINGWEAR**

DISSERTATION

Presented to the Faculty

Graduate School of Engineering and Management

Air Force Institute of Technology

Air University

Air Education and Training Command

in Partial Fulfillment of the Requirements for the

Degree of Doctor of Philosophy

Rodolfo G. Buentello Hernandez, B. S., M. S., M. A. S.

Major, USAF

December 2013

**DISTRIBUTION STATEMENT A.**

APPROVED FOR PUBLIC RELEASE; DISTRIBUTION UNLIMITED

**3D FINITE ELEMENT MODELING OF SLIDING WEAR**

Rodolfo G. Buentello Hernandez, B. S., M. S., M. A. S.  
Major, USAF

Approved:

\_\_\_\_\_  
Anthony N. Palazotto, PhD (Chairman)

\_\_\_\_\_  
Date

\_\_\_\_\_  
William P. Baker, PhD (Member)

\_\_\_\_\_  
Date

\_\_\_\_\_  
Robert A. Brockman, PhD (Member)

\_\_\_\_\_  
Date

Accepted:

\_\_\_\_\_  
HEIDI R. RIES, PhD

Interim Dean, Graduate School of Engineering  
and Management

\_\_\_\_\_  
Date

## **Abstract**

Wear is defined as “the removal of material volume through some mechanical process between two surfaces”. There are many mechanical situations that can induce wear and each can involve many wear mechanisms. This research focuses on the mechanical wear due to dry sliding between two surfaces.

Currently there is a need to identify and compare materials that would endure sliding wear under severe conditions such as high velocities.

The high costs associated with the field experimentation of systems subject to high-speed sliding, has prevented the collection of the necessary data required to fully characterize this phenomena. Simulating wear through Finite Elements (FE) would enable its prediction under different scenarios and would reduce experimentation costs.

In the aerospace, automotive and weapon industries such a model can aid in material selection, design and/or testing of systems subjected to wear in bearings, gears, brakes, gun barrels, slippers, locomotive wheels, or even rocket test tracks.

The 3D wear model presented in this dissertation allows one to reasonably predict high-speed sliding mechanical wear between two materials. The model predictions are reasonable, when compared against those measured on a sled slipper traveling over the Holloman High Speed Tests Track. This slipper traveled a distance of 5,816 meters in 8.14 seconds and reached a maximum velocity of 1,530 m/s.

## **Acknowledgments**

I will like to express my appreciation to my research advisor, Distinguished Professor Dr. Anthony N. Palazotto, for his continued encouragement, invaluable advice, and ongoing support for this research project. His experience and excitement regarding wear, kept me on track throughout my research. He spent many personal hours helping me on my research. I am grateful for his mentoring and sincerely value his guidance.

I would like to extend my gratitude to Dr. William P. Baker who constantly helped me support the assumptions of this research and to Dr. Robert A. Brockman for his valuable input and constructive feedback throughout my research.

I would like to acknowledge that the influence of my mother was fundamental to achieve this educational milestone; she constantly encouraged me to pursue higher educational goals.

I also extend my deepest thanks to my wife. She managed my home without much help during my many years chasing higher education. I could not have completed my doctorate degree without her support and sacrifice. I love her deeply for these and many other things and cannot foresee myself without her as my lifelong companion.

I want express my apologies to my children for spending long study hours away from them. I decided to do so striving to be their role model and hoping that my quest to live an honorable military life and to continuously pursue higher education will inspire them to strive for similar goals.

Finally, I extend my gratitude to the Air Force Office of Scientific Research for funding this investigation.

Rodolfo G. Buentello Hernandez

## Table of Contents

	Page
Abstract.....	iv
Acknowledgments .....	v
Table of Contents.....	vi
List of Figures.....	xiii
List of Tables .....	xviii
List of Symbols.....	xxi
I. Introduction .....	1
1.1 Problem Statement.....	1
1.2 Research Objectives.....	2
1.3 Research Methodology .....	2
1.4 Research Scope.....	2
1.5 Dissertation Overview .....	3
II. Literature Review.....	5
2.1 Purpose .....	5
2.2 Previous Research.....	5
2.2.1 Wear Classifications .....	5
2.2.2 J. F. Archard and W. Hirst's Model.....	8
2.2.3 M.S. El-Tobgy Model.....	9
2.2.4 A. J. Chmeil's Model .....	10
2.2.5 C. Burton's Model .....	11
2.2.6 C. S. Hale Sub-Model.....	13
2.2.7 J. Dean et al Model .....	15
2.2.8 C.Z. Duan et al Model .....	16
2.2.9 S. P. Meador's Model .....	17
2.2.10 I. Polyzois' Model .....	18

	Page
2.2.11 D. Huber Model .....	21
III. Finite Element Modeling .....	23
3.1 Concept.....	23
3.2 Finite Element Package .....	24
3.3 Geometry and Boundary Conditions .....	25
3.3.1 Encastrated Assembly (Rail) .....	26
3.3.2 Assembly in Motion .....	28
3.3.3 Gap.....	30
3.4 Mesh .....	31
3.5 Material Modeling .....	33
3.5.1 Elastic Response (Part I).....	34
3.5.2 Plastic Response (Part II).....	34
3.5.3 Damage Initiation Criteria (Part III) .....	34
3.5.4 Damage Evolution (Part IV).....	35
3.5.5 Failure Point (Part V).....	36
3.6 Mie-Gruneisen Equation of State (EOS) .....	36
3.7 Contact Interactions .....	37
3.7.1 Element Removal.....	37
3.7.2 Penalty Method .....	37
3.7.3 Friction.....	37
3.8 Dynamic Explicit Step.....	38
3.9 Single Asperity Wear Output.....	39
3.10 Model Extrapolation .....	41
3.10.1 Surface Characterization Tests .....	41
3.10.2 Extrapolating the Normalized Wear .....	45
3.10.3 Normalized Wear Rates.....	47

	Page
3.10.4 Total Wear Rates .....	47
3.11 Model Relation to the Wear Definition .....	48
3.12 Chapter Summary .....	49
IV. Scenario to Simulate .....	50
4.1 HHSTT Background .....	50
4.2 HHSTT January 2008 Mission Overview .....	51
4.3 Original Slipper Dimensions .....	53
4.4 Post-Mission Slipper Measurements .....	53
4.5 DADS Data .....	55
4.6 Wide Velocity Profile .....	56
4.7 Sliding Distance .....	58
4.8 Intermittent Contact .....	59
4.9 Length in Contact .....	60
4.10 Width in Contact .....	66
4.11 Slipper Lateral Motion and Assumed Yaw .....	68
4.12 Skin Temperature .....	69
4.13 Chapter Summary .....	69
V. Results .....	71
5.1 Simulated Wear Patterns .....	71
5.2 Model Results for Each Velocity Interval .....	72
5.3 Strain Rate and Temperature Contributions .....	76
5.3.1 Contributions to the Von Mises Stress .....	76
5.3.2 Contributions to the JC Failure Strain .....	85
5.4 Wear Thermal Influence .....	89
5.4.1 Initial Temperature Influence .....	89
5.4.2 Specific Heat Influence .....	90
5.5 Normalized Wear Rates .....	94
5.6 Normalized Wear Rates Comparison .....	97

	Page
5.7 Total Wear Results .....	98
VI. Summary, Conclusions, Contributions and Recommendations .....	104
6.1 Summary.....	104
6.2 Conclusions of Research .....	106
6.4 Recommendations for Future Research.....	109
Appendix A. Model Results for Each Velocity Interval .....	111
A.1 Results for the 0-50 m/s Interval.....	112
A.2 Results for the 50-150 m/s Interval.....	113
A.3 Results for the 150-250 m/s Interval.....	114
A.4 Results for the 250-350 m/s Interval.....	115
A.5 Results for the 350-450 m/s Interval.....	116
A.6 Results for the 450-550 m/s Interval.....	117
A.7 Results for the 550-650 m/s Interval.....	118
A.8 Results for the 650-750 m/s Interval.....	119
A.9 Results for the 750-850 m/s Interval.....	120
A.10 Results for the 850-950 m/s Interval.....	121
A.11 Results for the 950-1050 m/s Interval.....	122
A.12 Results for the 1050-1150 m/s Interval .....	123
A.13 Results for the 1150-1250 m/s Interval .....	124
A.14 Results for the 1250-1350 m/s Interval .....	125
A.15 Results for the 1350-1450 m/s Interval .....	126
A.16 Results for the 1450-1530 m/s Interval .....	127
A.17 Results for the 1530-1450 m/s Interval .....	128
A.18 Results for the 1450-1350 m/s Interval .....	129
A.19 Results for the 1350-1250 m/s Interval .....	130
A.20 Results for the 1250-1150 m/s Interval .....	131
A.21 Results for the 1150-1050 m/s Interval .....	132
A.22 Results for the 1050-950 m/s Interval .....	133
A.23 Results for the 950-850 m/s Interval.....	134

	Page
A.24 Results for the 850-750 m/s Interval.....	135
A.25 Results for the 750-622 m/s Interval.....	136
A.26 Results for the 650-622 m/s Interval.....	137
Appendix B. Example of the Abaqus Sliding Wear Report.....	138
Appendix C. Theoretical Background .....	143
1.1 Description, Mesh and Formulation .....	144
1.1.1 Types of Descriptions:.....	144
1.1.2 Types of Meshes:.....	144
1.1.3 Types of FE Formulations .....	146
1.2 Deformation, Stress and Strain Measures.....	149
1.2.1 Displacement .....	149
1.2.2 Displacement Vector .....	150
1.2.3 Deformation Gradient Tensor.....	151
1.2.4 The Jacobian Determinant .....	152
1.2.5 Displacement Gradient Tensor .....	152
1.2.6 Velocity Gradient Vectors .....	153
1.2.7 Rate of Deformation .....	155
1.2.8 Strain.....	156
1.2.9 Green's Strain Tensor .....	156
1.2.10 Logarithmic Strain.....	156
1.2.11 Equivalent Plastic Strain and Strain Rate .....	157
1.2.12 Material Derivative.....	158
1.2.13 Internal Traction Vector .....	159
1.2.14 Cauchy or "True" Stress .....	160
1.2.15 Kirchhoff stress.....	161

	Page
1.2.16 First Piola-Kirchhoff Stress Tensor .....	162
1.2.17 Second Piola-Kirchhoff Stress Tensor.....	162
1.2.18 Stress Relations and Representation .....	163
1.2.19 Equivalent Hydrostatic Stress.....	164
1.2.20 Deviatoric Stress .....	164
1.2.21 Von-Von Mises stress.....	164
1.2.22 Jaumann Stress Rate .....	165
1.2.23 Strain Work Conjugates.....	165
1.3 Conservation Laws and Equilibrium .....	167
1.3.1 Conservation Laws .....	167
1.3.2 Conservation of Mass: .....	167
1.3.3 Conservation of Linear Momentum.....	169
1.3.4 Conservation of Angular Momentum .....	172
1.3.5 Conservation of Energy .....	173
1.3.6 Virtual Work .....	174
1.4 Elasto-Viscoplastic Behavior.....	176
1.4.1 Hooke's Law of Elasticity .....	176
1.4.2 Viscoplasticity .....	177
1.4.3 Johnson-Cook Viscoplastic Model .....	178
1.4.4 Johnson-Cook Flow Rule .....	179
1.4.5 Johnson-Cook Dynamic Failure Criterion.....	180
1.4.6 Damage Evolution Criterion.....	181
1.5 Finite Element (FE) Concepts .....	182
1.5.1 FE Analysis (FEA) Package .....	183

	Page
1.5.2 Explicit Dynamic Analysis .....	183
1.5.3 FE Elasto Viscoplastic Straining Algorithm.....	184
1.6 Mie-Gruneisen Equation of State .....	186
1.7 Surface Interactions .....	187
1.7.1 Surface Roughness.....	187
1.7.2 Friction.....	189
1.7.3 Penalty Method .....	191
1.8 Experimentation and Extrapolation Concepts .....	192
1.8.1 Archard’s Wear Rate Model.....	192
1.8.2 Wear Rates and Total Sliding Wear. ....	193
1.8.3 Split Hopkinson Bar (SHB) Tests.....	195
1.8.4 Flyer Impact Plate Tests (FIPT) .....	200
1.9 Appendix Summary .....	201
Appendix D. Input Parameters Determination.....	203
1.1 Johnson-Cook Plasticity Parameters for Low-Strain-Rate Scenarios .....	203
1.2 Johnson-Cook Plasticity Parameters for High-Strain-Rate Scenarios.....	213
1.3 Johnson-Cook Failure Parameters Determination .....	217
1.4 Mie-Gruneisen Equation of State (EOS) .....	225
1.5 Friction Experimentation.....	225
1.6 Initial Temperature Experimentation.....	226
1.7 Appendix Summary .....	228
Bibliography .....	229
Vita .....	239

## List of Figures

	Page
Figure II-1 Abrasive Wear Mechanism [10].....	7
Figure II-2 Abrasive, Ploughing, Cutting, and Fragmentation Wear [106].....	7
Figure II-3 Adhesive Wear Mechanism [10].....	7
Figure II-4 Typical Adhesive Wear Trace [106] .....	8
Figure II-5 Pin on Disk Schematic [4].....	9
Figure II-6 Multiple Particles Damage [34].....	10
Figure II-7 Chmeil’s FE Model [23].....	11
Figure II-8 Burton’s FE Model [20] .....	12
Figure II-9 Hale’s FE Sub-Model [38] .....	13
Figure II-10 Plane Strain Simulation [38] .....	14
Figure II-11 Projectile Penetration Prediction and Observed [32]. .....	16
Figure II-12 Serrate Chip Morphology Comparison [74].....	17
Figure II-13 Model of the Direct Impact Split Hopkinson Apparatus [89] .....	18
Figure II-14 Abaqus Model of the Test Specimen [89].....	19
Figure II-15 Shear Failure Bands of an Impacted Specimen [89] .....	20
Figure II-16 Photomicrograph of an Impacted Specimen [89].....	20
Figure II-17 Pressure Wave Generated by a 1,500 m/s Collision [46].....	22
Figure III-1 Model Concept.....	24
Figure III-2 Two Assemblies (Slipper and Rail) .....	25
Figure III-3 Bottom Assembly.....	26
Figure III-4 Dimensions of the Encastred Assembly (Rail) .....	27
Figure III-5 Width of the Asperity Damage .....	28
Figure III-6 Part in Motion Sketch.....	29
Figure III-7 Dimensions of the Assembly in Motion (Slipper) .....	30
Figure III-8 Model Gap.....	31
Figure III-9 Model Mesh .....	32
Figure III-10 Schematic of the C3D8R Element [86].....	33

	Page
Figure III-11 Typical Uniaxial Stress-Strain Curve.....	33
Figure III-12 Velocity Boundary Condition .....	39
Figure III-13 Single Asperity Wear Over Time.....	40
Figure III-14 Scanning Electron Microscope [106].....	41
Figure III-15 AISI-1080 and VascoMax300 Material Samples [102].....	42
Figure III-16 3D View of AISI 1080 Specimen [102].....	42
Figure III-17 3D View of VascoMax 300 Specimen [102].....	43
Figure III-18 AISI-1080 Steel Distribution of Asperities.....	45
Figure III-19 Micrograph of Worn VascoMax 300 Slipper [38].....	47
Figure IV-1 HHST Aerial View [38].....	51
Figure IV-2 January 2008 Mission Setup [38] .....	52
Figure IV-3 HHSTT Sled System [38].....	52
Figure IV-4 Slipper-Rail Interface [38].....	53
Figure IV-5 Slipper Thickness Measurement Locations [38].....	53
Figure IV-6 Slipper Thickness Measurements Along the Centerline [38] .....	54
Figure IV-7 Slipper Thickness Measurements Along the Side and Lip [38] .....	55
Figure IV-8 Velocity Profile.....	57
Figure IV-9 Mission Velocity Profile.....	57
Figure IV-10 Slipper Vertical Displacement [38] .....	59
Figure IV-11 Running Average of the Percent of Time in Contact.....	60
Figure IV-12 Forward Rotation of Test Slipper [47].....	61
Figure IV-13 Slipper Thickness Along Centerline [38] .....	62
Figure IV-14 Slipper Free Body Diagram .....	62
Figure IV-15 Slipper Variable Area of Contact.....	63
Figure IV-16 HHSTT Assumed Length of Contact Progression.....	63
Figure IV-17 Assumed Max. Lengths in Contact for Each Stage .....	64
Figure IV-18 Estimated Length of Contact vs. Time.....	66
Figure IV-19 Frontal View of the Slipper and Rail Cross Sections .....	67
Figure IV-20 Slipper Roll.....	67

	Page
Figure IV-21 Loads Applied to the Slipper at Points 3 and 4.....	68
Figure IV-22 Slipper Lateral Displacement.....	68
Figure IV-23 Plastic Deformation Patterns Angles .....	69
Figure V-1 Simulated Wear Patterns Resemblance.....	71
Figure V-2 Simulated Wear Patterns with and without Yaw .....	72
Figure V-3 Segments of the Velocity Profile .....	72
Figure V-4 Simulated Wear Pattern Under Different Initial Conditions.....	75
Figure V-5 Location of Element for TDMB Plots.....	76
Figure V-6 Simulated Material Behavior at 700 m/s and 498 °K.....	77
Figure V-7 Simulated Material Behavior at 1500 m/s and 641 °K.....	77
Figure V-8 Simulated Failure Behavior at 700 m/s and 498 °K.....	86
Figure V-9 Simulated Failure Behavior at 1500 m/s and 641 °K.....	87
Figure V-10 Simulated Patterns at Different Temperatures .....	90
Figure V-11 Specific Heat for the AISI-1080 Steel.....	91
Figure V-12 Simulation Patterns Varying the Specific Heat.....	92
Figure V-13 TDMB of Simulations Varying the Specific Heat .....	93
Figure V-14 Extrapolation Concept.....	95
Figure V-15 Methodology to Obtain the HHSTT Slipper Wear .....	101
Figure A-1 Simulated Wear Patterns at 25 m/s and 297 °K .....	112
Figure A-2 Simulated Wear Patterns at 100 m/s and 313 °K .....	113
Figure A-3 Simulated Wear Patterns at 200 m/s and 323 °K .....	114
Figure A-4 Simulated Wear Patterns at 300 m/s and 357 °K .....	115
Figure A-5 Simulated Wear Patterns at 400 m/s and 391 °K .....	116
Figure A-6 Simulated Wear Patterns at 500 m/s and 422 °K .....	117
Figure A-7 Simulated Wear Patterns at 600 m/s and 432 °K .....	118
Figure A-8 Simulated Wear Patterns at 700 m/s and 498 °K .....	119
Figure A-9 Simulated Wear Patterns at 800 m/s and 488 °K .....	120
Figure A-10 Simulated Wear Patterns at 900 m/s and 486 °K .....	121
Figure A-11 Simulated Wear Patterns at 1000 m/s and 472 °K .....	122

	Page
Figure A-12 Simulated Wear Patterns at 1100 m/s and 525 °K .....	123
Figure A-13 Simulated Wear Patterns at 1200 m/s and 608 °K .....	124
Figure A-14 Simulated Wear Patterns at 1300 m/s and 609 °K .....	125
Figure A-15 Simulated Wear Patterns at 1400 m/s and 660 °K .....	126
Figure A-16 Simulated Wear Patterns at 1500 m/s and 641 °K .....	127
Figure A-17 Simulated Wear Patterns at 1500 m/s and 641 °K .....	128
Figure A-18 Simulated Wear Patterns at 1400 m/s and 660 °K .....	129
Figure A-19 Simulated Wear Patterns at 1300 m/s and 609 °K .....	130
Figure A-20 Simulated Wear Patterns at 1200 m/s and 608 °K .....	131
Figure A-21 Simulated Wear Patterns at 1100 m/s and 525 °K .....	132
Figure A-22 Simulated Wear Patterns at 1000 m/s and 472 °K .....	133
Figure A-23 Simulated Wear Patterns at 900 m/s and 486 °K .....	134
Figure A-24 Simulated Wear Patterns at 800 m/s and 488 °K .....	135
Figure A-25 Simulated Wear Patterns at 700 m/s and 498 °K .....	136
Figure A-26 Simulated Wear Patterns at 635 m/s and 432 °K .....	137
Figure C-1 Lagrangian Mesh [106]. .....	145
Figure C-2 Eulerian Mesh [106]. .....	146
Figure C-3 Body Displacement Representation [106]. .....	150
Figure C-4 Components of Stress [31] .....	159
Figure C-5 Cauchy's Stress Tensor [99]. .....	160
Figure C-6 Stress Tensors Representation [99] .....	163
Figure C-7 Algorithm Elasto Viscoplastic Straining During a Time Step .....	185
Figure C-8 Schematic of Surfaces in Contact and their Contact Points [12]. .....	188
Figure C-9 Qualitative Dependence of Friction Coefficient on Length Scale... ..	191
Figure C-10 Schematic of the Penalty Method Equivalent Stiffness .....	192
Figure C-11 UDRI Split Hopkinson Bar Test Apparatus [24]. .....	196
Figure C-12 Split Hopkinson Bar Test Apparatus for Direct Impact Tests [57]	197
Figure C-13 Schematic of SHB Test Specimen [24]. .....	197
Figure C-14 SHB Test Apparatus Heating Element [24]. .....	198

	Page
Figure C-15 Flyer Plate Test Apparatus and Schematic [24].	201
Figure D-1 SHB Specimen Dimensions [57].	203
Figure D-2 Stress-Strain Curves for AISI-1080 Steel [57].	204
Figure D-3 Strain Hardening Factor “B” and Index “n” for Test 474-2 [57].	206
Figure D-4 Strain Hardening Factor “B” and Index “n” for Test 474-3 [57].	206
Figure D-5 Strain Rate Sensitivity, “C”, of AISI-1080 Steel [57].	208
Figure D-6 Thermal Softening Coefficient “m” for the AISI-1080 Steel [57].	209
Figure D-7 Stress-Strain Rate Curves for AISI-1080 Steel [26].	210
Figure D-8 Stress-Strain Curves for VascoMax 300 [26].	212
Figure D-9 Stress-Strain Rate Curves for VascoMax 300 [26].	212
Figure D-10 Flyer Test Results vs. Model of VascoMax300 [26].	214
Figure D-11 Flyer Test Comparison vs. Original Model of AISI-1080 [26].	214
Figure D-12 Flyer Test Results vs. “Best Fit” Model of VascoMax300 [26].	215
Figure D-13 Flyer Test Results vs. “Best Fit” Model of AISI-1080 [26].	216
Figure D-14 Fracture Point of Interest [40].	217
Figure D-15 Johnson-Cook Predictions vs. Experimental Data [40].	220
Figure D-16 Strain Rate Dependent Data [41].	221
Figure D-17 Strain Rate Sensitivity for Ti-6Al-4V [40].	222
Figure D-18 Temperature Dependent Data [40].	223
Figure D-19 Strain Rate Sensitivity for Ti-6Al-4V [40].	224
Figure D-20 Montgomery’s Coefficient of Friction [81].	226

## List of Tables

	Page
Table III-1 Young’s Modulus .....	34
Table III-2 Johnson-Cook Plasticity Model Parameters .....	34
Table III-3 Johnson-Coom Dynamic Failure Parameters .....	35
Table III-4 Mie-Gruneisen EOS Parameters.....	36
Table III-5 Roughness Measurements of VascoMax300 [102].....	44
Table III-6 Roughness Measurements of AISI-1080 Steel [102].....	44
Table IV-1 Mission Summary [38].....	58
Table IV-2 Intervals Sliding Distance .....	58
Table IV-3 Mission Summary .....	65
Table IV-4 Estimated Length of Contact .....	65
Table V-1 Velocity Intervals Data.....	73
Table V-2 Simulated and Calculated Values at 700 m/s and 498 °K .....	80
Table V-3 Simulated and Calculated Values at 700 m/s and 498 °K (cont.).....	81
Table V-4 Simulated and Calculated Values at 1500 m/s and 641 °K .....	82
Table V-5 Simulated and Calculated Values at 1500 m/s and 641 °K (cont.).....	83
Table V-6 Normalized Wear Rates Results Varying the Specific Heat .....	98
Table V-7 Estimated Wear of the 750 -850 m/s Velocity Interval .....	100
Table V-8 Total Estimated Wear for the HHSTT Mission of January 2008.....	102
Table A-1 Normalized Wear at 25 m/s .....	112
Table A-2 Estimated Wear of the 0-50 m/s Velocity Interval .....	112
Table A-3 Normalized Wear at 100 m/s .....	113
Table A-4 Estimated Wear of the 50-150 m/s Velocity Interval .....	113
Table A-5 Normalized Wear at 200 m/s .....	114
Table A-6 Estimated Wear of the 150-250 m/s Velocity Interval .....	114
Table A-7 Normalized Wear at 300 m/s .....	115
Table A-8 Estimated Wear of the 250 -350 m/s Velocity Interval .....	115
Table A-9 Normalized Wear at 400 m/s .....	116

	Page
Table A-10 Estimated Wear of the 350 -450 m/s Velocity Interval .....	116
Table A-11 Normalized Wear at 500 m/s .....	117
Table A-12 Estimated Wear of the 450 -550 m/s Velocity Interval .....	117
Table A-13 Normalized Wear at 600 m/s .....	118
Table A-14 Estimated Wear of the 550 -650 m/s Velocity Interval .....	118
Table A-15 Normalized Wear at 700 m/s .....	119
Table A-16 Estimated Wear of the 650 -750 m/s Velocity Interval .....	119
Table A-17 Normalized Wear at 800 m/s .....	120
Table A-18 Estimated Wear of the 750 -850 m/s Velocity Interval .....	120
Table A-19 Normalized Wear at 900 m/s .....	121
Table A-20 Estimated Wear of the 850 -950 m/s Velocity Interval .....	121
Table A-21 Normalized Wear at 1000 m/s .....	122
Table A-22 Estimated Wear of the 950 -1050 m/s Velocity Interval .....	122
Table A-23 Normalized Wear at 1100 m/s .....	123
Table A-24 Estimated Wear of the 1050 -1150 m/s Velocity Interval .....	123
Table A-25 Normalized Wear at 1200 m/s .....	124
Table A-26 Estimated Wear of the 1150 -1250 m/s Velocity Interval .....	124
Table A-27 Normalized Wear at 1300 m/s .....	125
Table A-28 Estimated Wear of the 1250 -1350 m/s Velocity Interval .....	125
Table A-29 Normalized Wear at 1400 m/s .....	126
Table A-30 Estimated Wear of the 1350 -1450 m/s Velocity Interval .....	126
Table A-31 Normalized Wear at 1500 m/s .....	127
Table A-32 Estimated Wear of the 1450 -1530 m/s Velocity Interval .....	127
Table A-33 Normalized Wear at 1500 m/s .....	128
Table A-34 Estimated Wear of the 1530 -1450 m/s Velocity Interval .....	128
Table A-35 Normalized Wear at 1400 m/s .....	129
Table A-36 Estimated Wear of the 1350 -1450 m/s Velocity Interval .....	129
Table A-37 Normalized Wear at 1300 m/s .....	130
Table A-38 Estimated Wear of the 1350 -1250 m/s Velocity Interval .....	130

	Page
Table A-39 Normalized Wear at 1200 m/s .....	131
Table A-40 Estimated Wear of the 1250 -1150 m/s Velocity Interval .....	131
Table A-41 Normalized Wear at 1100 m/s .....	132
Table A-42 Estimated Wear of the 1150 -1050 m/s Velocity Interval .....	132
Table A-43 Normalized Wear at 1000 m/s .....	133
Table A-44 Estimated Wear of the 1050 -950 m/s Velocity Interval .....	133
Table A-45 Normalized Wear at 900 m/s .....	134
Table A-46 Estimated Wear of the 950 -850 m/s Velocity Interval .....	134
Table A-47 Normalized Wear at 800 m/s .....	135
Table A-48 Estimated Wear of the 850 -750 m/s Velocity Interval .....	135
Table A-49 Normalized Wear at 700 m/s .....	136
Table A-50 Estimated Wear of the 650 -750 m/s Velocity Interval .....	136
Table A-51 Normalized Wear at 600 m/s .....	137
Table A-52 Estimated Wear of the 650 -622 m/s Velocity Interval .....	137
Table C-1 Relations Between Stresses .....	163
Table C-2 Stress and Strain Conjugates.....	166
Table D-1 SHB Test Results for AISI-1080 Steel [57] .....	204
Table D-2 Strain Rate Data [57] .....	208
Table D-3 Temperature Dependent Data [57] .....	209
Table D-4 SHB Test Results for Vascomax300 Steel [57].....	211
Table D-5 JC Plasticity Parameters Obtained from SHB Tests.....	213
Table D-6 Summary of UDRI Flyer Plate Tests [57] .....	213
Table D-7 JC Plasticity Parameters Refined with Flyer Tests.....	216
Table D-8 Ductile Fracture Simulations Results of the Ti-6Al-4V [41] .....	219
Table D-9 JC Dynamic Failure Parameters .....	224
Table D-10 Mie-Gruneisen EOS Parameters.....	225
Table D-11 Thermal Analysis Results [66] .....	227
Table D-12 3D FE Wear Model Input Parameters .....	228

## List of Symbols

$A$	Johnson-Cook viscoplasticity model material constant
$A_c$	area of contact
$B$	Johnson-Cook viscoplasticity model material constant
$c_0$	reference speed of sound
$C$	Johnson-Cook viscoplasticity model material constant
$d_1 - d_5$	Johnson-Cook dynamic failure model material constants
$D_s$	sliding distance
$E$	Young's modulus
$E_H$	Hugoniot specific energy
$F$	deformation gradient matrix
$J$	Jacobian determinant
$k_A$	Archard's coefficient
$k_s$	Shear failure model material parameter
$l_a$	average length
$l_f$	final length
$l_0$	initial length
m	meter
$m$	Johnson-Cook viscoplasticity model material constant
$n$	Johnson-Cook viscoplasticity model material constant
$N$	Newton
$P$	pressure
$q$	Von Mises stress
$Q$	heat
$R_a$	average asperity size

$R_q$	effective asperity size
$s$	second
$S$	entropy
$\mathbf{S}$	1 <sup>st</sup> Piola-Kirchoff stress tensor
$T$	temperature
$T_0$	Ambient temperature
$T_m$	Melt temperature
$T^*$	Homologus temperature
$\mathbf{T}^{(n)}$	internal traction vector
$U$	internal energy
$U_p$	particle velocity
$U_s$	linear shock velocity
$\bar{\mathbf{u}}$	displacement vector
$\nabla \mathbf{u}$	displacement gradient vector
$\mathbf{v}$	velocity
$\nabla \mathbf{v}$	velocity gradient vector
$v_a$	average velocity
$v_f$	final velocity
$v_0$	initial velocity
$V$	volume
$V_{SA}$	single asperity volumetric damage
$V_{uA}$	volumetric damage per unit of area
$w$	Johnson-Cook dynamic failure model damage parameter
$W$	work
$W$	wear rate
$W_m$	mechanical wear

$W_{SA}$	single asperity wear rate
$W_{uA}$	wear rate per unit of area
$\Sigma$	2 <sup>nd</sup> Piola-Kirchoff stress tensor
$\beta$	inelastic heat fraction
$\varepsilon$	Green's strain
$\dot{\varepsilon}$	rate of deformation
$\bar{\varepsilon}_p$	equivalent plastic strain
$\dot{\bar{\varepsilon}}_p$	equivalent plastic strain rate
$\dot{\bar{\varepsilon}}_0$	reference strain rate
$\bar{\varepsilon}_f$	equivalent plastic strain rate at failure
$\mu$	friction coefficient
$\mu s$	micro-second
$\zeta_i$	Eulerian Cartesian coordinates
$\rho$	material density
$\sigma_h$	hydrostatic stress
$\sigma_n$	normal stress
$\sigma_{VM}$	Von Mises stress
$\sigma_\cdot$	deviatoric stress
$\sigma^\nabla$	Jaumann stress rate
$\sigma_y$	yield stress
$\tau$	Kirchoff's stress
$\tau_n$	shear stress
$\%Cont$	percent of distance in contact

# 3D FINITE ELEMENT MODELING OF SLIDING WEAR

## I. Introduction

### 1.1 Problem Statement

Currently there is a need to identify and compare materials that will endure sliding wear under severe conditions such as high velocities.

The high costs associated with the field experimentation of systems subject to high-speed sliding, has prevented the collection of the necessary data required to fully characterize this phenomenon. Simulating wear through a Finite Elements (FE) model will enable its prediction under different scenarios and will reduce the experimentation required.

During the last few years, the Air Force Institute of Technology (AFIT) has studied the high-speed sliding wear phenomenon. AFIT students have developed several two-dimensional (2D) FE models that have aided to better understand the factors influencing sliding wear and have been able to simulate wear, with a certain degree of accuracy. These AFIT studies suggested that the wear environment is truly three-dimensional (3D) and concluded that sliding wear can be simulated by modeling micro asperity collisions.

The 3D wear model presented in this dissertation was developed in an effort to build upon the lessons learned from these former AFIT studies. The model simulates in a 3D manner the asperity collisions occurring at the contact points, between the two apparently flat sliding surfaces. This model incorporates algorithms to account for the effects of pressure, velocity, temperature, viscoplasticity, fracture, friction, shock waves, etc. The simulated wear due to single asperity collisions is then extrapolated to predict the total wear, based on the statistical distribution of the asperities on the materials.

In the aerospace, automotive and weapon industries such a model can aid in material selection, design and/or testing of systems subjected to wear in bearings, gears, brakes, gun barrels, slippers, locomotive wheels and rails, or even rocket test tracks.

## **1.2 Research Objectives**

The primary objective of this research is to develop a 3D FE model to reasonably simulate high-speed mechanical sliding wear.

The secondary objective of this research is to compare the model results against the wear measured on a slipper recovered from a rocket test mission executed at the Holloman High Speed Test Track (HHSTT) on January 2008.

## **1.3 Research Methodology**

Although to the naked eye many machined surfaces appear smooth, when one zooms into the contact edges between these apparently smooth surfaces, one can see their micro-level characteristics. These surfaces are in fact rough; they are formed by many peaks and valleys. At the micro-level one can also observe that these surfaces contact each other only at specific peak points, generally called asperities. Thereafter, if these surfaces slide over each other, they will collide at many of these asperity contact points.

This model was developed assuming sliding wear can be represented by modeling these asperity collisions. The simulated collisions attempt to replicate the physical interactions occurring at the contact points between the two sliding surfaces. This 3D wear model incorporates the appropriate algorithms to account for the effects of pressure, velocity, temperature, viscoplasticity, fracture, shock waves, friction, etc.

The model was developed with Abaqus [31], a commercially available FE software package. It incorporates the Johnson-Cook's viscoplastic and dynamic failure algorithms, Coulomb's friction equation, and the Mie-Gruneisen Equation of State. It simulates the high-speed wear phenomenon assuming an adiabatic process were the temperature rises due to plastic deformation.

## **1.4 Research Scope**

Wear is a complex phenomenon that under any given situation may involve many mechanisms; therefore, to understand it and be able to model it appropriately, it is necessary to isolate the situation to be modeled. In order to understand the effects of

each mechanism and its interdependencies, one must limit the mechanisms involved in each model, before coupling together.

This research was limited to study only the mechanical wear due to high speed sliding. Since the model focuses on the micro-level wear, situations involving lubrications or coatings were not considered because they significantly alter the micro level surface interactions. AFIT is currently pursuing in parallel to this study investigations to assess the thermal wear and the wear due to the ploughing mechanism.

## **1.5 Dissertation Overview**

This dissertation is divided into nine chapters:

- Chapter I: States this research problem, objective and methodology
- Chapter II: Provides the literature review, presenting summaries of the most relevant writings related to this research, organized in chronological order and highlighting their key concepts.
- Chapter III: Presents an overview of the finite element model.
- Chapter IV: Provides an overview of the Holloman High Speed Tests Track and of the wear analysis conducted on a slipper recovered from a mission executed at it on January 2008.
- Chapter V: Provides the model results under different initial conditions and compares these results against those measured on the recovered HHSTT slipper.
- Chapter VI: Summarizes this research and provides its conclusions, significant contributions and recommendations.
- Appendix A: Presents pictures of the Abaqus simulated wear patterns, carried out with different initial conditions. It includes the calculations to obtain the normalized wear rates
- Appendix B: Provides an example of the Abaqus report used to estimate the single asperity sliding wear

- Appendix C: Explains the theoretical background necessary to understand the concepts and algorithms employed in the model.
- Appendix D: Presents the experimentation required to obtain the parameters and/or tables required for each of the model algorithms.

## II. Literature Review

### 2.1 Purpose

Many models to predict wear, viscoplastic material behavior, and/or failure mechanisms have been developed on the last few decades. The main purpose of this literature review was to search for studies related to high-speed sliding wear. Moreover, to examine the compilation of journal articles, thesis, dissertations and reports available in the AFIT's Hypervelocity Center database. The objective was to build the model based on the lessons learned from previous AFIT studies. This dissertation highlights the key concepts of the studies considered most relevant to this research.

### 2.2 Previous Research

#### 2.2.1 Wear Classifications

There are many different definitions of wear. The American Society for Testing and Materials (ASTM) defines wear as “damage to a solid surface, generally involving progressive loss of material, due to relative motion between that surface and a contacting substance or substances” [6].

Bayer mentions on reference [8] that “Wear is a system property, not a material property. Materials can wear by a variety of mechanisms and combinations of mechanisms, depending on the tribo-system in which it is used. Wear behavior is frequently nonlinear. Transitions can occur in wear behavior as a function of a wide variety of parameters.” Bayer [10] also defines three ways to classify wear:

***By the appearance of wear.*** The surface may be described as scratched, polished, pitted, etc.

***By the physical mechanism leading to surface damage.*** Some of these mechanisms include adhesion, abrasion, melting, fatigue and oxidation.

***By the situation of the event.*** Some of these situations include dry sliding wear, lubricated wear, rolling wear, and impact wear.

Kato [55] classifies the wear mechanisms as mechanical, chemical, and thermal. Each of them defined by the ASTM as follow:

***Mechanical wear:*** removal of material due to mechanical processes under conditions of sliding, rolling, or repeated impacts; includes adhesive wear, abrasive wear, and fatigue wear; but not corrosive wear and thermal wear.

***Chemical wear:*** A wear process in which chemical or electrochemical reaction with the environment predominates. Corrosive and oxidative wear are chemical mechanisms.

***Thermal wear:*** Removal of material due to softening, melting, or evaporation during sliding, rolling, or impact.

This research investigates only the mechanical sliding wear situation. Moreover, since the situations of interest for this research will unlikely involve much fatigue wear, the research focuses only on the abrasive mechanism. In addition, it only focuses on the dry sliding wear. Coatings significantly change the micro-level interactions between two surfaces, therefore, scenarios involving coatings may require, in addition to the characterization of the surface, the empirical data to characterize the coating behavior throughout the sliding scenario.

The two types of mechanical sliding wear to be considered in this research, adhesive and abrasive, are defined by the ASTM [6] as:

***Abrasive Wear.*** Abrasive wear occurs when asperities along the interface of the sliding bodies collide. The tangential force causes plastic deformation and eventually removes the asperity [6]. It can involve ploughing, cutting or fragmenting. Figure II-1 depicts this mechanism and the metallographic pictures presented in Figure II-2 show typical examples of how this abrasive wear looks at the micro-level.



**Figure II-1 Abrasive Wear Mechanism [10]**

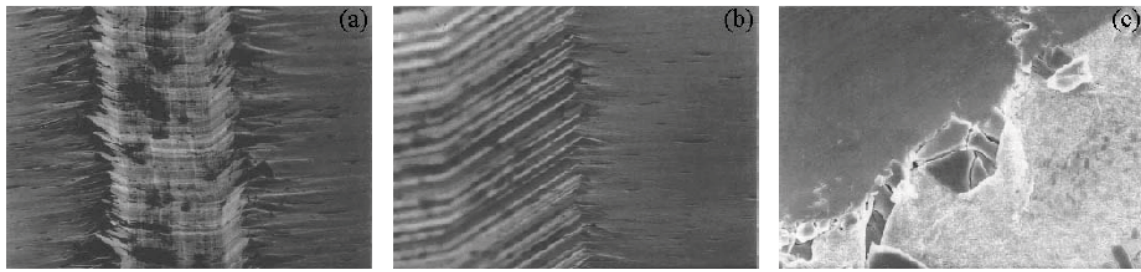


**Figure II-2 Abrasive, Ploughing, Cutting, and Fragmentation Wear [106]**

**Adhesive Wear.** Adhesive wear occurs when two surfaces contact at an asperity contact point and bond together. As the sliding motion continues, asperities from the softer material will shear off and adhere to the harder material. The adhered fragments later break free forming worn material. Figure II-3 depicts this mechanism. A typical adhesive wear case is presented in Figure II-4 and on it one can easily see the trace characteristic of this wear mechanism. Sometimes in the literature adhesive wear is used as a synonym for dry un-lubricated sliding wear.



**Figure II-3 Adhesive Wear Mechanism [10]**

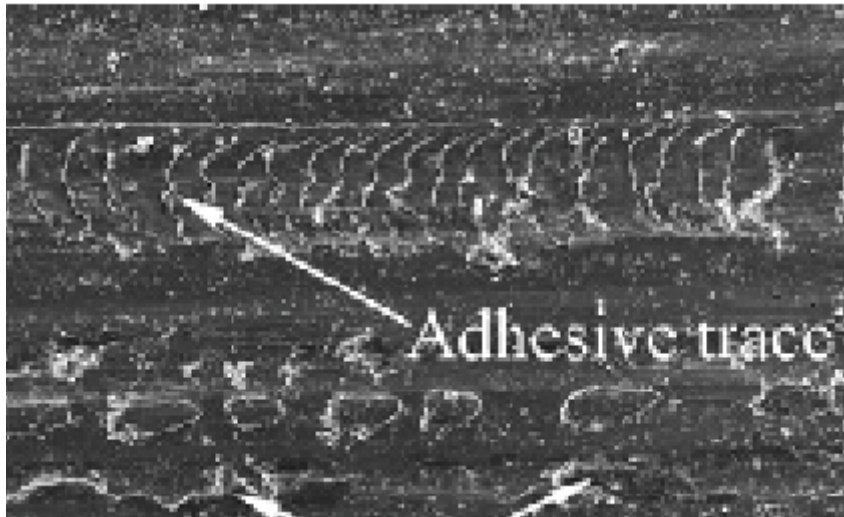


**Figure II-4 Typical Adhesive Wear Trace [106]**

The following models presented in chronological order, help one understand the key features to consider and the appropriate algorithms to incorporate into the 3D FE model.

### **2.2.2 J. F. Archard and W. Hirst's Model**

In 1956, Archard and Hirst [4] experimented with a pin on disk system to study the wear of metals under dry conditions. They employed a low speed rotating disk with a pin over its surface; the setup is depicted in Figure II-5. They researched the wear effects due to a load applied to the pin at low velocities. These researchers were able to relate wear rates to normal loads and material hardness.

Archard and Hirst observed that the wear rates depended initially on time, but after an initial “running in” period they became practically constant. The constant wear rates begin when the sliding surfaces reach interface equilibrium, in other words when the surface layers become stable. They also observed that the wear rates are independent of the apparent area of contact.

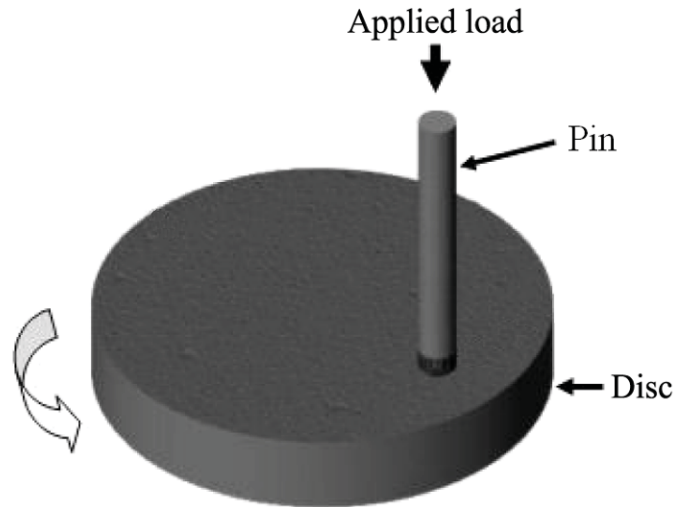


**Figure II-5 Pin on Disk Schematic [4]**

Archard and Hirst's model results are reasonable for low velocity experiments and many other researchers followed these pin and disk type of experiments.

The theoretical background regarding this model is presented in Appendix C of this dissertation.

### **2.2.3 M.S. El-Tobgy Model**

In 2005, M. S. El-Tobgy [34] presented an Abaqus 3D FE model to simulate the erosion process for a Ti-6Al-4V alloy. The model used the Johnson-Cook viscoplastic criterion to simulate the non-linear effects of strain hardening, strain rate and temperature. It also incorporated the Johnson-Cook dynamic failure criterion.

This model considered the impact of multiple particles. El-Tobgy et al concluded that the erosion rate stabilized only after the effect of three or more particles. Figure II-6 shows the simulated effect of erosion by multiple particles [34].

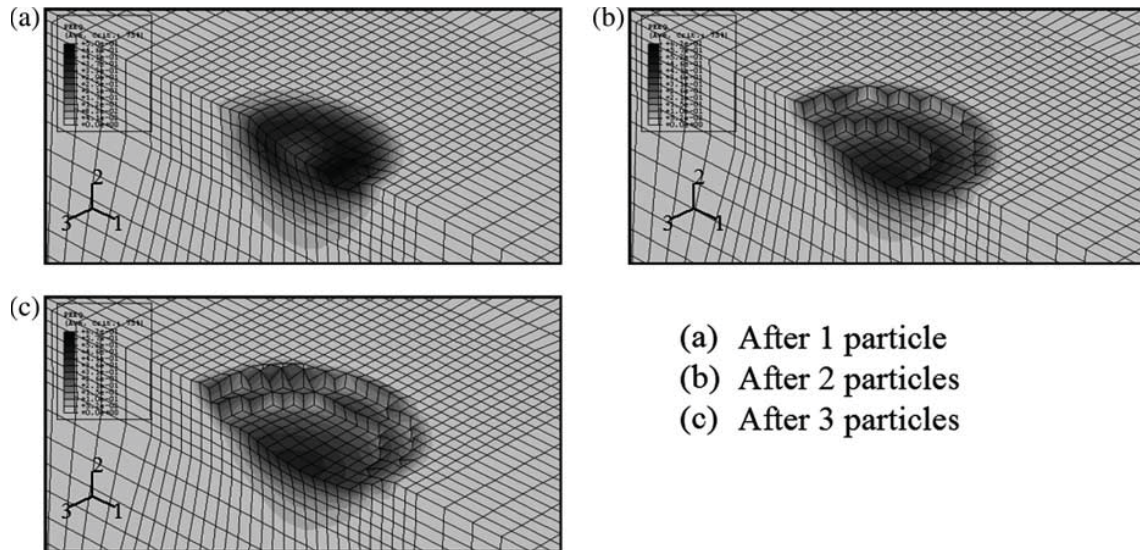


**Figure II-6 Multiple Particles Damage [34]**

Figure II-6 (a) shows the model erosion prediction due the impact of one particle, (b) shows the predicted erosion due to the sequential impact of two particles, and (c) shows the simulated erosion after the collision of three particles. This FE model offered the advantage of modeling the residual stresses generated during the erosion process, which were found to follow a profile similar to that observed in a shot peening process. The model allowed one to study the effects of the particles size, velocity and impact angle. The predicted results are in agreement with the results obtained experimentally and are documented in reference [34]

It is important to note that in an erosion scenario, the colliding particles have a very small mass and their momentum decreases rapidly before causing too much damage, therefore the cumulative damage from sequential collisions is relevant. In contrast, on a high-speed sliding wear scenario, the asperities are attached to the surfaces, and therefore they don't lose their momentum as easily causing a greater damage than that of a particle traveling on a fluid of similar characteristics.

#### **2.2.4 A. J. Chmeil's Model**

In 2008, Chmeil [23] investigated the feasibility to predict slipper wear using finite element analysis. He investigated two methods: a macro-scale incremental method that used Archard's wear equations, and a micro-scale material property method that used

a failure criterion to determine wear. The study focused on lower velocities in order to compare the results with those found in the literature available at that time. Chmeil had many numerical problems with the macro level method and concluded that the micro-level material property method was the most feasible solution. Chmeil's FE micro model is presented in Figure II-7 [23].

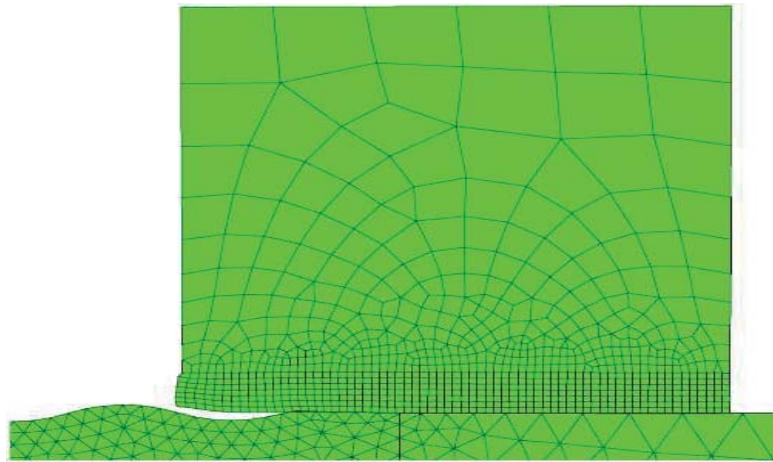


**Figure II-7 Chmeil's FE Model [23]**

### **2.2.5 C. Burton's Model**

In 2009, C. Burton [20] investigated the surface roughness of both the VascoMax 300 and the AISI-1080 steel material samples. He measured their surface roughness with an optical profilometer. After determining the surface height profile, he filtered it to remove sharp edges and sudden changes in profile, which can lead to singularities in a FE model.

He used this model to study the effect of mesh refinement on the coefficient of friction,  $\mu$ , between the two sliding bodies. His model is presented in the Figure II-8.

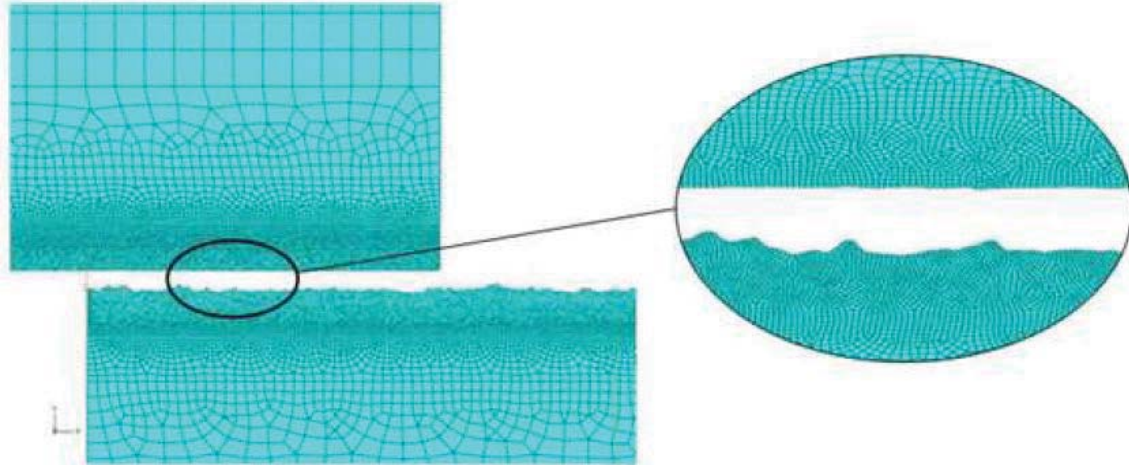


**Figure II-8 Burton's FE Model [20]**

In Chad A. Burton and Robert A. Brockman article “Frictional Interactions in High-speed Sliding Contact” they state that: “friction coefficient is an empirical parameter that accounts for sources of resistance to relative motion on a scale smaller than that represented explicitly in one’s model ...”. They suggested that all the frictional resistance arising from surface waviness, asperities, and smaller micro-structural features must be bundled into a specified value of  $\mu$ . If the model has details about surface waviness or asperities, then the appropriate value of the friction coefficient must change: the features represented explicitly in the model, produce additional frictional resistance that was previously accounted by the value of  $\mu$  at the higher level. They conclude that the value of  $\mu$  does not disappear, since smaller-scale features will still contribute to sliding friction but will not be manifested in the model physics automatically [20].

Burton and Brockman concluded that if one doesn’t incorporate the key features of the surfaces irregularities into the model, then both, the model’s coefficient of friction and the effective coefficient of friction for the macroscopic forces could be considered as the same [20].

Burton’s observations aided to understand that the appropriate friction coefficient for a micro-level model should be based on the smaller micro-structural features, not on experiments that provide the frictional coefficient of a macro system due to the surfaces waviness [20].

### 2.2.6 C. S. Hale Sub-Model

In 2009, C. Hale [38] developed a micro-scale 2D FE Abaqus model to evaluate mechanical wear rates. This model is depicted in Figure II-9. Hale's model attempted to replicate a HHSTT test mission executed in January 2008. He used a plane strain approach to simulate a VascoMax 300 test slipper sliding over an AISI-1080 steel rail with a semicircular asperity with a radius of 6  $\mu\text{m}$ . The damage criterion used by Hale was based on the maximum Von Mises stress. He employed two different techniques to determine this stress: 1) Using the Johnson-Cook plasticity equation for given strain rates, and 2) Using a tensile analysis in ABAQUS. Once the maximum Von Mises stresses were calculated in the slipper, the results were transferred to a Matlab code to determine the damage area.

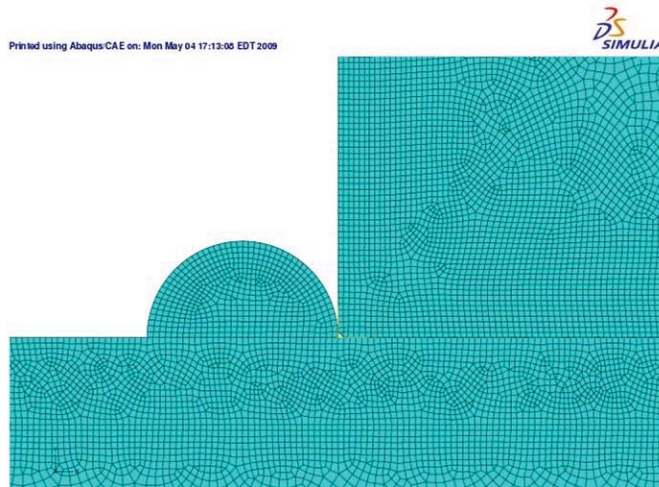


**Figure II-9 Hale's FE Sub-Model [38]**

Since his model was two dimensional, Hale ran the plane strain simulation against 6  $\mu\text{m}$ , 4  $\mu\text{m}$  and 2  $\mu\text{m}$  semi-circular asperities, and then integrated the results to approximate them to those of a 3D semi-spherical surface asperity. By observing the integration results, he found that the variation of the value obtained from these integrations was negligible; the average integration value was practically 8.3. Hale called this value the spherical coefficient factor and used it to convert the rest of the plane strain wear rates to 3D. Figure II-10 illustrates how the plane strain results were related to the

3-dimensional analysis by integrating the results of plane strain simulation against 6  $\mu\text{m}$ , 4  $\mu\text{m}$  and 2  $\mu\text{m}$  semi-circular asperities.

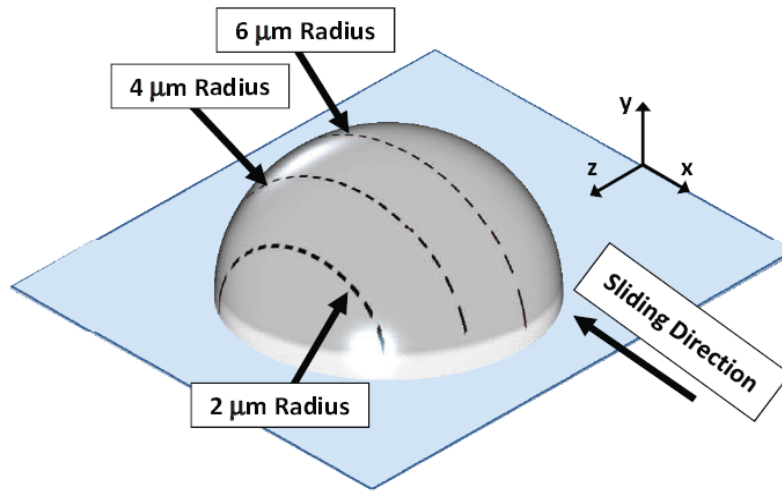


**Figure II-10 Plane Strain Simulation [38]**

In order to obtain his single asperity wear rates, he thereafter divided the simulated 3D single asperity damage by the distance assumed to impose this damage. The distance was assumed to be 110% the asperity radius, or 6.6 micro meters.

Since, in a typical sliding wear scenario the slipper slides across numerous asperities, in order to account for multiple asperity collisions, Hale developed a scaling factor to extrapolate the results of a single asperity damage to approximate the damage of many. This scaling factor was determined by calibrating the predicted single asperity wear rate at 10m/s with the wear rate calculated with Archard's model [38]. The value of this dimensionless N factor was 11.77.

To calculate the cumulative total wear, Hale then multiplied the wear rates obtained using the above mentioned methodology by the distance slid at each velocity range and then these results were added.

In order to take into consideration the actual bouncing of the slipper, the total wear was multiplied by the cumulative percentage of distance in contact between the slipper and rail during the entire test run. The cumulative percent of distance in contact employed was obtained from the DADS data (defined in section 4.5) of a similar mission. This value was 30.63 percent.

The wear measured from the slipper, recovered from the January 2008 HHST mission, was 10516 mm<sup>3</sup>. Combining the mechanical wear approximated using Hale's model with the melting wear considered also in his research. Hale's total predicted wear was 3760 mm<sup>3</sup>, approximately 35.7% of the measured wear [38].

Some of Hale's [38] important contributions to this study include his observation that wear can be reasonably modeled at the micro-mechanical level, and that the wear rate from a mechanical point of view is not history oriented. In other words, the mechanical wear at any given time is independent of the material already worn.

### **2.2.7 J. Dean et al Model**

In 2009, Dean [32] presented a research concerned with energy absorption in thin steel plates during perforations by spherical projectiles of hardened steel. The impact velocities of these projectiles varied between 200 and 600 m/s. Dean measured the absorbed energy and projectile velocities. Their simulations accurately predicted their experiments. The model well captured the failure transitions well, as the projectile velocity increased, as shown in Figure II-11. This model was considered important for this study because it successfully simulates a high strain-rate scenario using a Lagrangian FE package with many of the same algorithms chosen for the 3D wear model. Both models are built with the Abaqus/Explicit package using the Johnson and Cook plasticity and failure criterions.

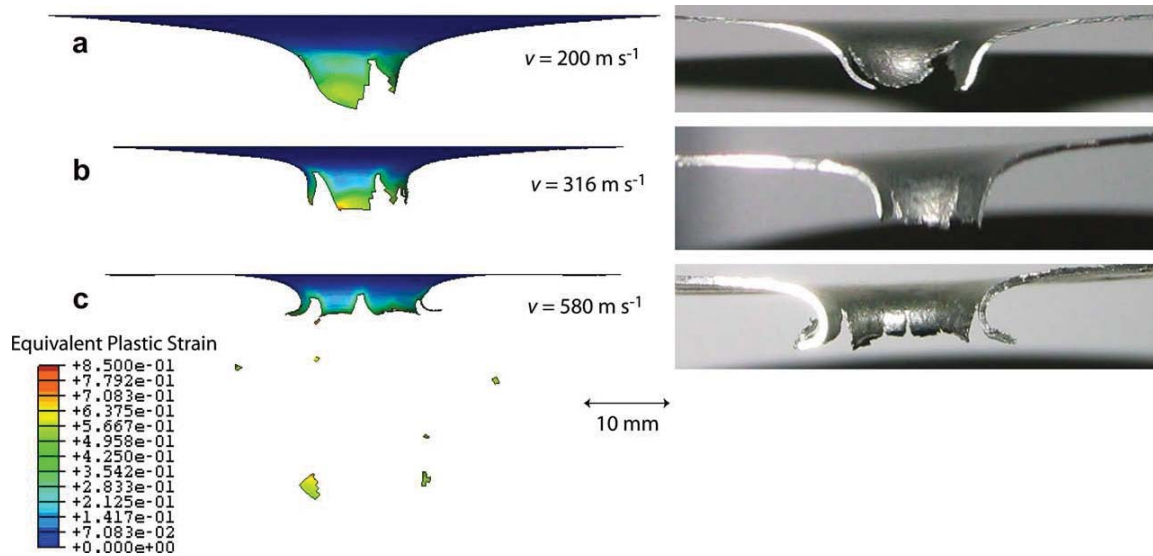


**Figure II-11 Projectile Penetration Prediction (left) and Observed (right) [32].**

### 2.2.8 C.Z. Duan et al Model

In 2009, C.Z. Duan and others [33] developed a model to simulate the high speed machining of steel. They observed and measured the serrated chip morphology and the cutting force in their experiments. Figure II-12 shows a schematic of the comparison between experimental and simulated serrate chip morphology. During the experiments, the Adiabatic Shear Bands (ASB) were clearly observed inside the serrated chips, as seen on the picture bellow. An adiabatic shear band is one of the many mechanisms of failure that occur in metals deformed at a high strain rate in processes, this band appear because the heat produced due to the plastic deformation is retained in the zone where it is created. Duan mentions that this indicates that the main reason to generate serrated chip is the occurrence of an adiabatic shear instability.

The investigation concluded that the simulations were consistent with the experiments and also that the Abaqus model could accurately predict the chip morphology and the cutting force during the high speed machining of AISI 1045 hardened steel. This successful 2D model was built with the Abaqus/Explicit package using the Johnson and Cook plasticity and failure criterions.

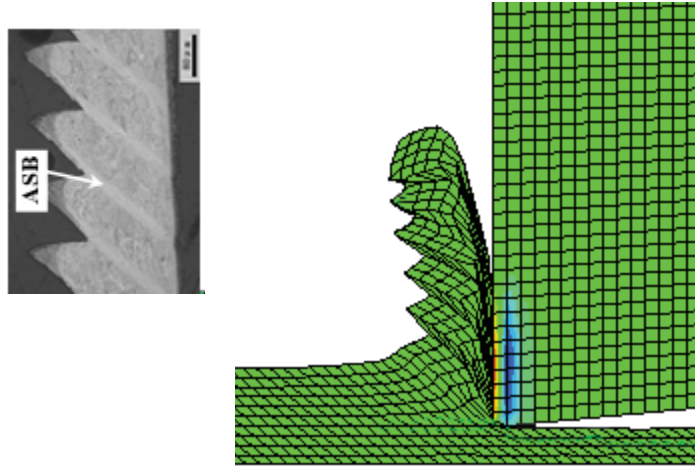


**Figure II-12 Serrate Chip Morphology Comparison [74]**

### **2.2.9 S. P. Meador's Model**

In 2010, S. P. Meador investigated the wear phenomenon using a hydrocode [74]. Meador developed a model focused on estimating the wear of a slipper recovered from a Holloman High Speed Test Track (HHSTT) mission executed in January 2008. This investigation was done as part of his master's degree investigation at AFIT. Meador used as his failure criterion the maximum Von Mises stress calculated via the Johnson Cook plasticity equation. Meador predicted the wear of a slipper traveling up to a maximum velocity of 3,000 m/s. He used a two dimensional plane strain model to evaluate the materials failure due to the collision with a single asperity.

Meador teaming up with Palazotto [74] used an Eulerian-Lagrangian hydrocode called CTH, developed by Sandia National Laboratory. This hydrocode was previously used by Cameron, Cinnamon, Laird and Szmerekovsky for similar HHSTT hypervelocity studies [21, 26, 65, 100] at AFIT.

Meador simulated the wear rates at various stages of the HHSTT mission to predict the total wear of the slipper. The predicted total wear accounted for approximately 46% of the total measured wear measured on the recovered slipper. Meador and Palazotto documented these results on their article "considerations of Wear at High Velocities Using a Hydrocode" [74].

### 2.2.10 I. Polyzois' Model

In 2010 Polyzois [89] built an Abaqus 3D FE model to simulate the tests of a modified direct impact Split Hopkinson Pressure Bar apparatus. He simulated the high strain rate compression of three armor materials: Maraging steel 300, high hardness armor (HHA), and aluminum alloy 5083. The University of Manitoba and others tested these armor materials provided by the Canadian Department of National Defense. For his 3D model Polyzois employed both the Johnson-Cook viscoplastic and failure models. Figures II-13 and II-14 depict Polyzois model.

He produced a series of stress-time plots at various projectile impact moments and then compared the results against experimental data. He investigated the formation of adiabatic shear bands caused by deformation at high strains and strain rates through simulations.



**Figure II-13 Model of the Direct Impact Split Hopkinson Apparatus [89]**

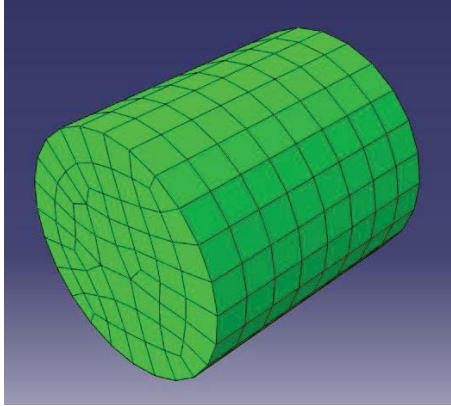


**Figure II-14 Abaqus Model of the Test Specimen [89]**

Polyzois concluded that the Johnson-Cook model incorporated into Abaqus could accurately simulate the plastic behavior of metals, up to the point of thermal instability. He also stated that the model can represent large fluctuations in the dynamic stress response caused by possible nucleation of transformed shear bands that lead to complete shear failure in the specimen. His model incorporated the Johnson Cook dynamic failure criterion and showed that shear failure started in the center of the specimen and propagated outwards diagonally forming an hourglass pattern. This pattern matched the behavior of the experimentally tested specimens [89].

Polyzois concluded that the Abaqus Johnson-Cook model was not capable of showing the effects of thermal softening because the model is purely phenomenological. The strain, strain rate, and temperature dependencies of the flow stress are only used to scale the overall behavior of the metal. The models deformation, failure and fracture depend only on the mechanical instabilities [89].

He stated that the simulations of the impact momentums, that display shear failure, closely agree with the momentums contributing to the shear band formation observed in experimental work, for both Maraging Steel 300 and High Hardness Armor (HHA). Figure II-15 displays the model results and Figure II-16 shows a micrograph of an impacted AISI 4340 Steel specimen [89].

His model predicted nucleation of shear failure in the center of a specimen that causes a drop in the maximum compressive stress. The time to reach this stress closely matches the experimental results for both of the metals tested.

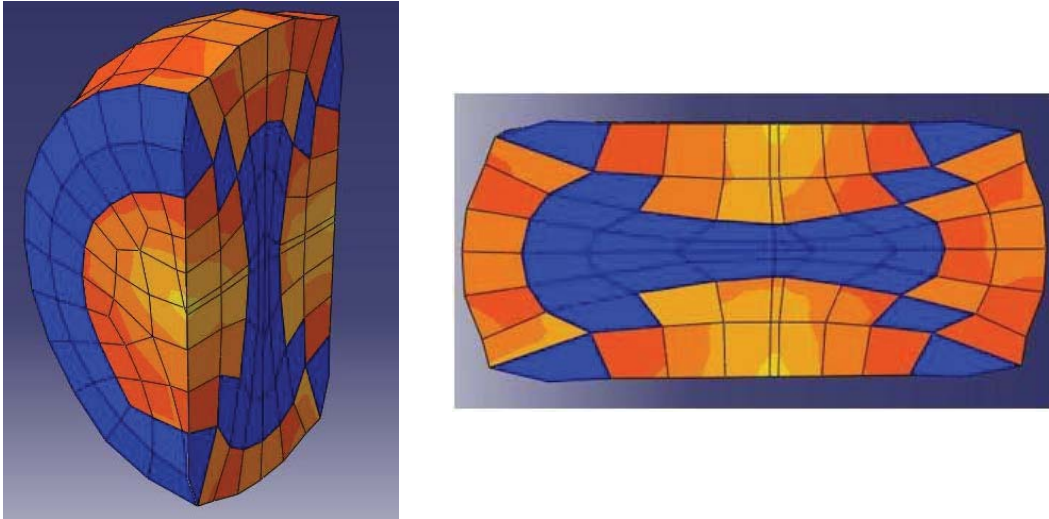


**Figure II-15 Shear Failure Bands of an Impacted Specimen [89]**

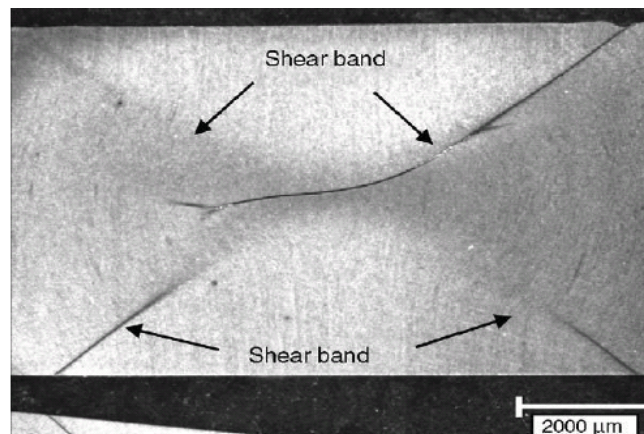


**Figure II-16 Photomicrograph of an Impacted Specimen [89]**

In Figures II-15 and II-16, one can see how the model failure pattern matched the one on the test specimen; both show the formation of adiabatic shear bands known to lead to complete shear failure. In this model, the mechanical maximum shear stress failure, nucleating from the center of the specimen, was used to indicate the time when these shear bands begin to form. The simulated time and compressive stress necessary to form adiabatic shear bands, matched closely to the experimental ones.

Polyzois successfully modeled, with Abaqus, the tests of a modified direct impact Split Hopkinson Pressure Bar apparatus. This model is important to this investigation

because it allows to derive the J-C Plasticity and failure criteria parameters used for our simulations. This Abaqus model can be used instead of the EPIC-2 model used by Johnson and Holmquist [89].

This model is relevant to this research since this, or a similar model, can be used to obtain the Johnson-Cook's Dynamic Failure parameters. These parameters were obtained by Johnson and Holmquist [89] using an EPIC-2 hydrocode to simulate the dimensionless pressure stress ratio as a function of the equivalent strain, in the center of a Split Hopkinson bar test specimen. A summary of their experiments is presented in Appendix D, section 1.3. Polyzois model can be used to obtain these parameters instead of using EPIC-2 hydrocode.

#### **2.2.11 D. Huber Model**

In 2011, Huber [46] researched methods to predict mechanical sliding wear at high velocities. Focusing on the wear of test sled slippers at the HHSTT, he developed a 2D finite element model to simulate the high-speed sliding phenomenon. He used the same CTH Eulerian-Lagrangian hydrocode used by Laird [64], Szmerekovsky [100], Cinnamon [25], Meador [74], and Cameron [21] for their HHSTT hypervelocity studies [46] at AFIT. CTH allowed him to simulate wear at velocities between 200 and 1,500 meters per second.

To consider the pressure waves in the slipper due to the collision, Huber employed equations to represent the onset of plasticity and elastic wave speed through a material under plane strain conditions. Figure II-17 shows a pressure wave generated by the collision of the VascoMax 300 slipper with an asperity at 1,500 m/s. One can observe that the pressure wave extends into both the VascoMax 300 slipper and the AISI-1080 steel rail [46].

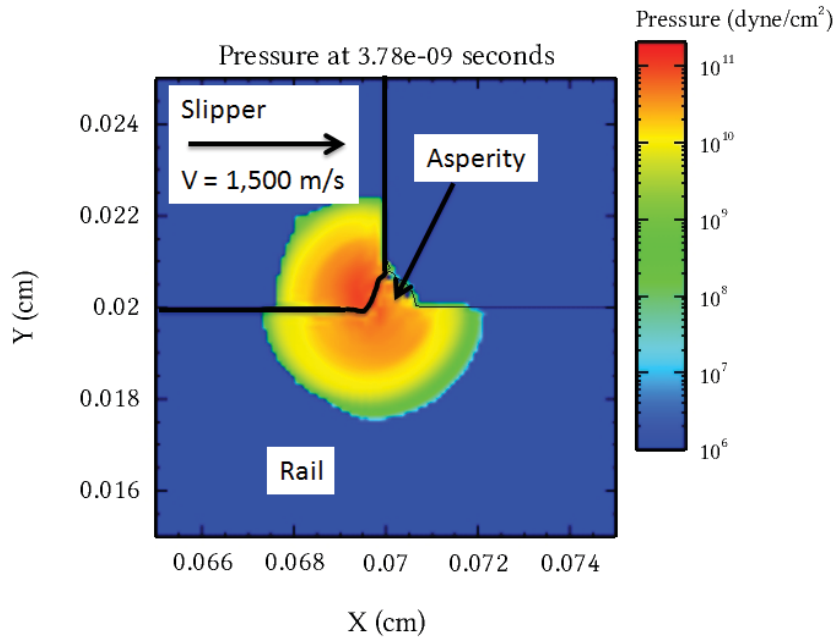


**Figure II-17 Pressure Wave Generated by a 1,500 m/s Collision [46]**

His CTH model, similar to Hale [39] model, used a plane strain analysis of a slipper colliding with a 6  $\mu\text{m}$  radius semi-circular surface asperity. He used Hale's spherical coefficient to convert the results into 3D and Hale's N factor to extrapolate the results and obtain the effect of multiple asperities.

Huber evaluated several failure criterions to estimate damaged material from the sliding body. He also used the Johnson and Cook viscoplastic model due its ability to handle high strains, strain rates, and temperatures. Huber's model used various fracture criterion. He predicted the slipper wear to be between 49.31% and 80.87% of the experimental estimated wear measured. The estimated wear measured from the slipper used on the HHSTT January 2008 test mission [46], was 10,500  $\text{mm}^3$ .

### **III. Finite Element Modeling**

This chapter will summarize how the finite element model was developed. It explains the model concept and presents an overview of each one of its main features. The theory behind these features is presented in Appendix C and the experiments required to obtain the input parameters is described in Appendix D.

#### **3.1 Concept**

Although to the naked eye, many machined surfaces appear smooth, when one zooms into the contact edges between these apparently smooth surfaces, one can see their micro-level characteristics. These surfaces are in fact rough; they are formed by many peaks (also called asperities) and valleys. At the micro-level, one can also observe that these surfaces make contact with each other only at specific contact points, generally involving asperities. Thereafter, if these surface slide over each other, then their asperities will collide at many of these contact points. This 3D wear model attempts to simulate the plastic deformation evidence observed on SEM samples, assumed to be due to asperities collisions, by simulating these collisions at the micron level. It employs algorithms to account for the effects of viscoplasticity, fracture, friction, and surface roughness parameters. The asperities average sizes and distribution used to build the model are based on surface roughness characterization analysis of the sliding materials. Figure III-1 depicts this wear model concept.

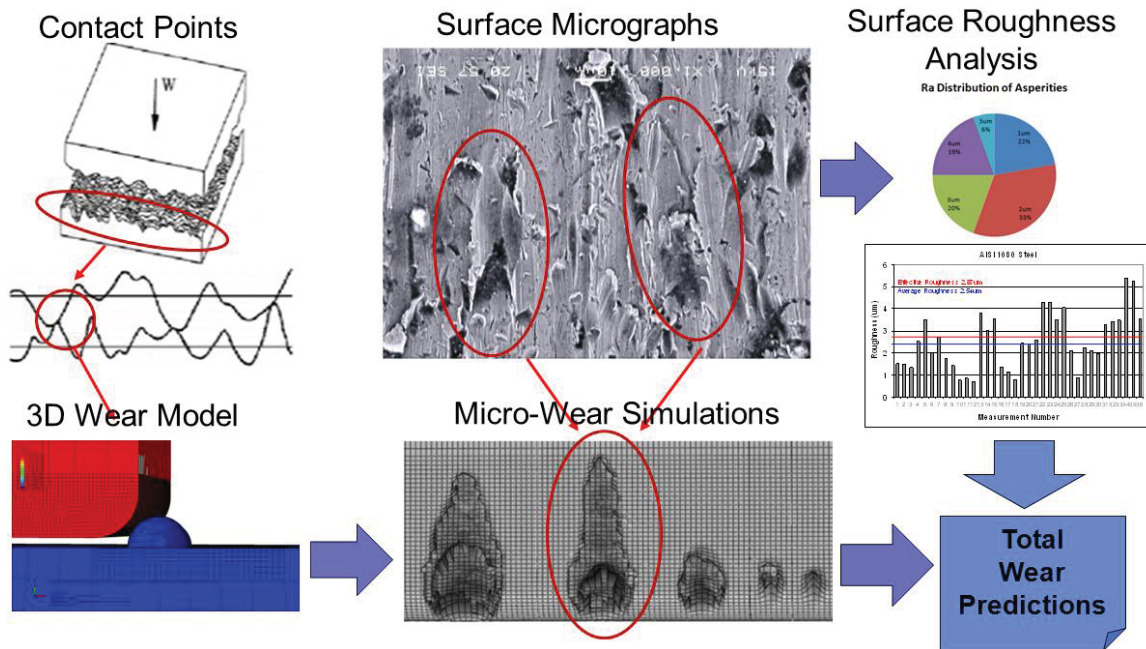


**Figure III-1 Model Concept**

### **3.2 Finite Element Package**

The Finite Element (FE) Package selected for the simulations of this research is Abaqus, a general purpose package generally used to model the behavior of materials and/or structures.. This FE package is commercially available and counts with two solvers for time-dependent dynamic systems: Abaqus Standard and Explicit [31]. The Abaqus explicit solver is extensively used because it is very good simulating dynamic time-dependant problems, such as blasts, impact, erosion, and other fracture related mechanisms. Some of the previous models built using this package to solve similar high-strain rate problems include those presented in references [24, 32, 33, 34, 39, 40, 56, and 89]. This explicit solver is useful for our model since it deals with a time dependent material behavior problem and the strain rate effects at high velocities need to be accounted for. An overview of the explicit time integration algorithms used for this model is presented in Appendix C, section 1.5.3

### **3.3 Geometry and Boundary Conditions**

The model is composed of two main assemblies, one sliding atop of the other one. In the next figure, the assembly atop, depicted in gray, is in constant motion and is called the sliding part (also called slipper). The assembly at the bottom, depicted on a green color, contains the hemispherical asperities and is encastrated at the bottom.

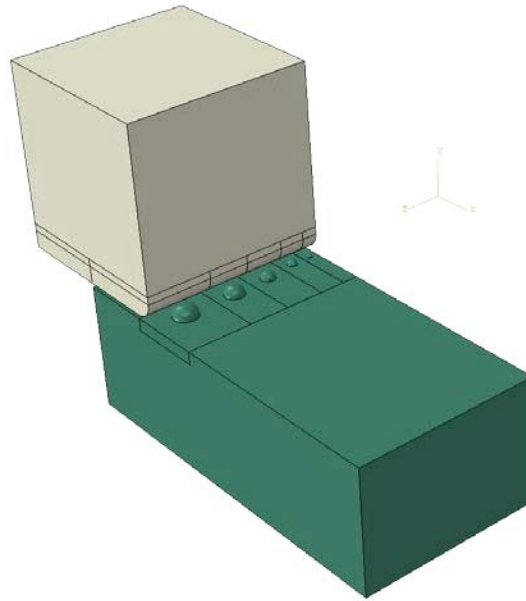


**Figure III-2 Two Assemblies (Slipper and Rail)**

These two assemblies are composed of various parts mainly for the following reasons: 1) To reduce the number of mesh elements and therefore the computational load, 2) to allow a more refined mesh near the asperity collision points, 3) to be able to easily change the size and number of the asperities (depending in the surface characteristics), and 4) to report the wear due to each individual asperity separately.

These parts of these assemblies are assembled using a rough contact interaction between their contact surfaces. This rough contact interaction prevents any sliding motion between the two surfaces in contact but allows the elastic slip associated with penalty method presented in Appendix C, section 1.7.3. These assemblies are assembled as follow;

### 3.3.1 Encastrated Assembly (Rail)

The encastrated assembly, presented in Figure II-1, is composed of six parts as shown in the next figure. The largest one (bisque) is encastrated in the bottom, meaning that all the displacements ( $u_1, u_2, u_3$ ) and rotations ( $ur_1, ur_2,$  and  $ur_3$ ) along the three axes are set equal to zero. The other five parts represent the five hemispherical asperities and their vicinities. The asperity sizes are 1  $\mu\text{m}$  (green), 2  $\mu\text{m}$  (yellow), 3  $\mu\text{m}$  (red), 4  $\mu\text{m}$  (blue) and 5  $\mu\text{m}$  (magenta) all selected according to Dr. Voyiadjis surface roughness characterization of the AISI-1080 steel presented in section 3.10.1. The encastrated assembly is symmetric in the X and Z axis.

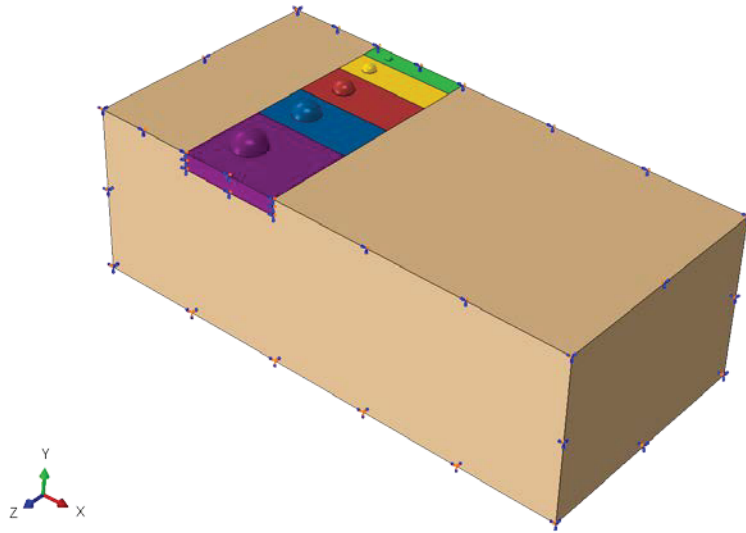


**Figure III-3 Bottom Assembly**

The original dimensions of the model were based on the 2D dimensions of Hale's [38] model and only extruded trough the Z axis to create a 3D model. The length of the base part is 150  $\mu\text{m}$ , the height is 50  $\mu\text{m}$  and the width 75  $\mu\text{m}$ . Figure III-4 depicts these parts dimensions in the XY plane.

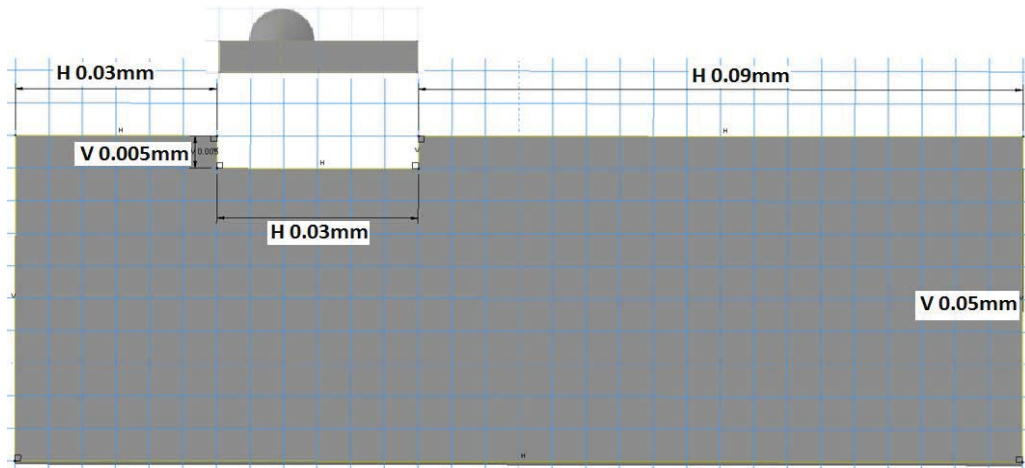


**Figure III-4 Dimensions of the Encastrated Assembly (Rail)**

Figure III-5 shows the frontal damage due to an asperity colliding at 1500m/s. The picture above shows the frontal view of the area of the slipper damaged by the rail asperity. The bottom picture shows the original asperity shape in gray, and its shape after the collision in yellow. On this picture one can observe that the width of the damage due to an asperity collision (about 14  $\mu\text{m}$ ) is greater than the undeformed asperity diameter (10  $\mu\text{m}$ ). The damage extends beyond the original asperity diameter edges for both, the rail and the slipper.

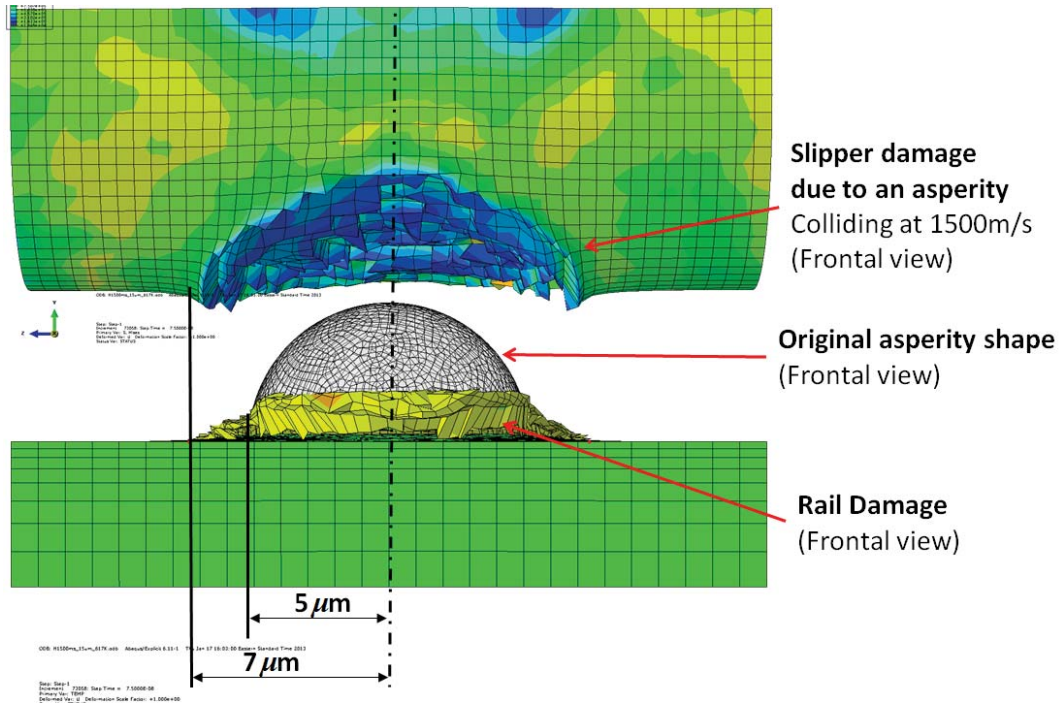


**Figure III-5 Width of the Asperity Damage**

The sizes of the hemispherical asperities were selected according to Dr. Voyiadjis surface characterization of the AISI-1080 steel, presented in section 3.10.1. The asperity parts were built with hemispherical asperities of radius of 1  $\mu\text{m}$ , 2  $\mu\text{m}$ , 3  $\mu\text{m}$ , 4  $\mu\text{m}$  and 5  $\mu\text{m}$ . Due to the observation mentioned in the previous paragraph and attempting to prevent the asperity collisions from influencing the results of each other, the width of the parts with the asperities is about five times the radius of their respective asperity. The widths of the parts with the asperities atop are 5  $\mu\text{m}$ , 10  $\mu\text{m}$ , 15  $\mu\text{m}$ , 20  $\mu\text{m}$ , and 25  $\mu\text{m}$ .

### 3.3.2 Assembly in Motion

The assembly in motion, sliding atop the encastated one, is programmed to begin the simulation with a horizontal sliding velocity and its corresponding skin-temperature applied to the entire assembly. It includes a downward vertical velocity component of 1 m/s. This vertical velocity was incorporated based on the average downward velocity of the bouncing slipper, as reported by DADS. This assembly in motion is symmetric along the Z-axis and is composed of six parts, as shown in Figure III-6.

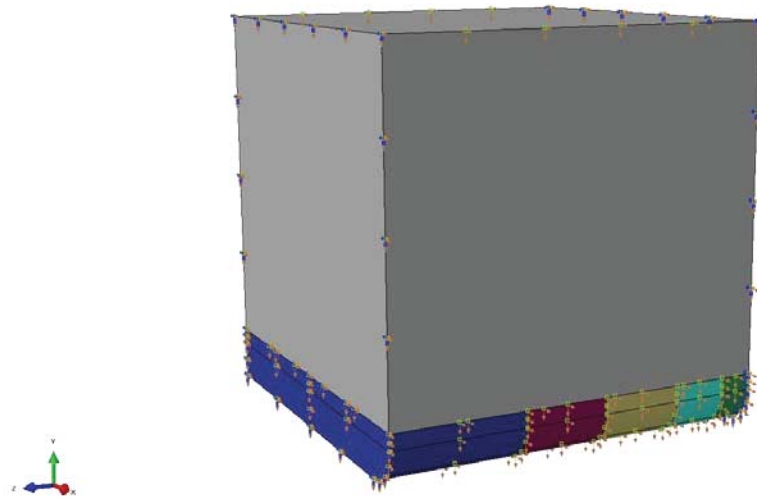


**Figure III-6 Part In Motion Sketch**

The dimensions of the top part (gray) are: Length  $75\ \mu\text{m}$ , height  $65\ \mu\text{m}$  and width  $75\ \mu\text{m}$ . All five bottom parts have a length of  $75\ \mu\text{m}$  and a height of  $10\ \mu\text{m}$ . The widths of these parts are:  $5\ \mu\text{m}$  (green),  $10\ \mu\text{m}$  (turquoise),  $15\ \mu\text{m}$  (yellow),  $20\ \mu\text{m}$  (red), and  $25\ \mu\text{m}$  (blue). These five parts are set to collide with the rail asperities; therefore their widths were selected with the intention to wrap the potential damage of their colliding asperity. A lateral view of this assembly, showing the dimensions of its parts, is shown in Figure III-7.

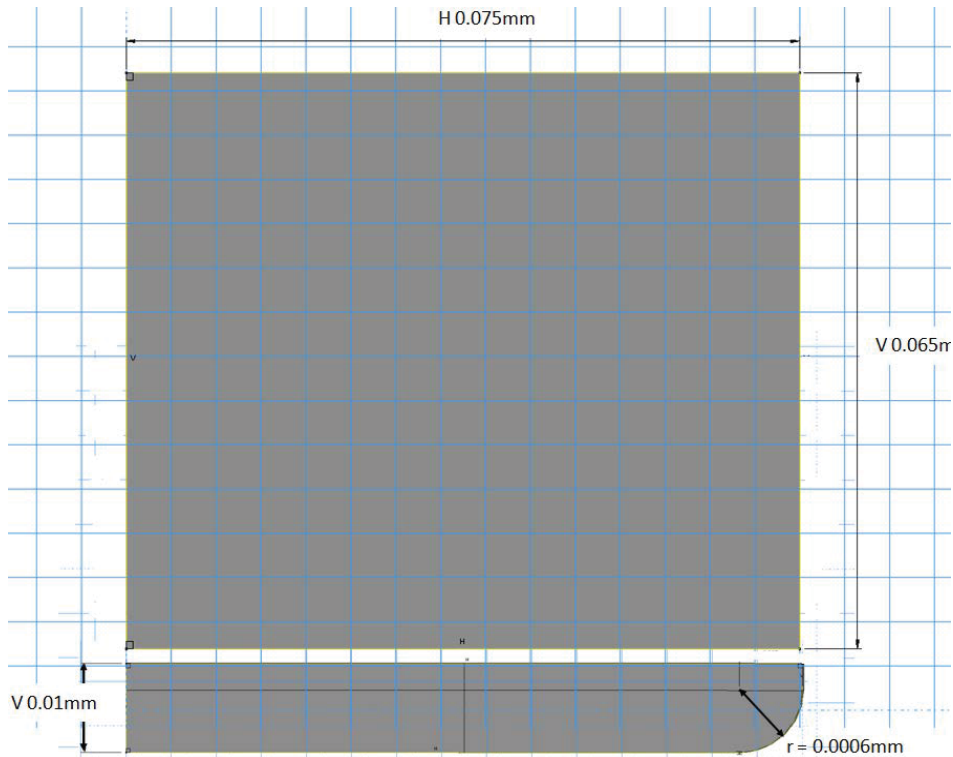


**Figure III-7 Dimensions of the Assembly in Motion (Slipper)**

The bottom parts have a  $6\ \mu\text{m}$  radius fillet placed at the leading edge. The fillet size was selected based on the average asperity size of the VascoMax300 steel. Deciding the frontal plane of collision was not an easy task since the slipper is bouncing, pitching, rolling, and wearing as it slides. Moreover, the collisions occur not only in the front of the slipper, but all over its bottom surface, full of micro peaks and valleys. The fillet was selected larger than any of the rail asperities to prevent the asperities from colliding against a vertical flat surface.

### 3.3.3 Gap

The assembly in motion, also called slipper, travels atop of the rail. Initially separated by a  $1.5\ \mu\text{m}$  gap, as shown in Figure III-8. The model incorporates a gap between the two surfaces in relative motion due to the following reasons: 1) because, as explained in section 3.3.3, the contact between two apparently flat surfaces only occurs at discrete contact points, everywhere else these surfaces are separated by a gap, 2) to provide a physical place where the material failed elements can be assumed to go after

they fracture or melt; 3) to provide a model calibration device, and 4) to avoid excessive shear due to the proximity of the sliding assembly, e.g. without a gap, the sliding assembly acts like a “paper cutter” mainly cutting the asperities at low velocities

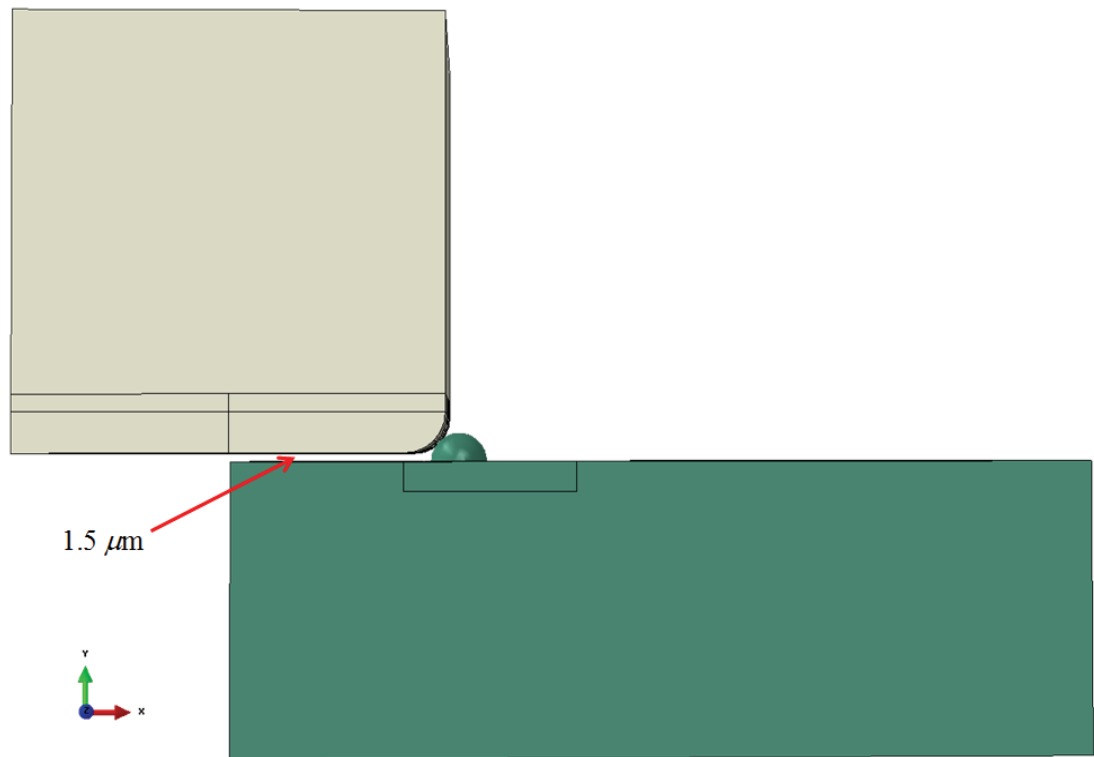


**Figure III-8 Model Gap**

### **3.4 Mesh**

In order to reduce the computations, the model was divided in multiple parts. The parts subject to the asperity collision were simulated with a much finer mesh. Several different mesh configurations were evaluated. Initially the model had only two parts (the rail and the slipper) and their meshes biased the size of the elements in a way to place the smaller ones near the collision. Due to the complexity of these two parts, meshing them was not an easy task. Since the model configuration will change depending on the surface roughness characteristics, an alternative approach to allow the user to easily mesh this adaptive model was desired. The alternative approach used to facilitate the meshing was to build the model using two assemblies with multiple parts. For the parts subject to

the asperities collisions, the approximate length of the elements is about 600 nanometers. The approximate length of the elements on the top of the slipper and the base of the rail parts is 5  $\mu\text{m}$ . The slipper assembly is composed of 269722 elements and the rail assembly of 89421. Figure III-9 shows the model mesh.

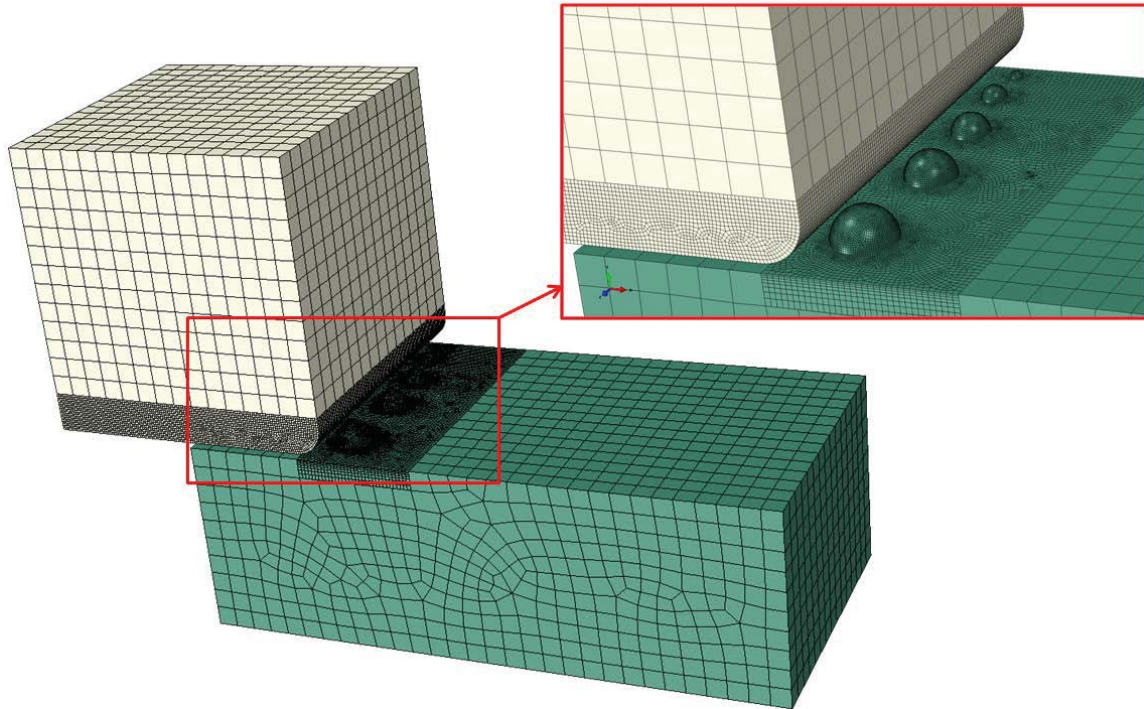


**Figure III-9 Model Mesh**

The type of elements used for this model is the C3D8R. This type is a **C**ontinuum **3-Dimensional 8-node** linear hexahedral element that uses a **R**educed integration. This type of element was developed for 3D simulations of continuous solids. Eight-node linear hexahedral element means that each element consists of 8 nodes arranged as shown in Figure III-10 Schematic of the C3D8R Element [86]. Reduced integration was selected for the model instead of full one because it may increase the accuracy of the FE solution, since it tends to soften the stiffness of the model. Hourglass control was selected to control the zero-energy modes. Zero-energy modes are those that regardless of the deformation of the element, their integration points do not experience any strain. Earlier successful FE models [32, 33, 34, 40, 56, and 89] demonstrate that this is an appropriate type of element to be used for high-strain rate simulations.

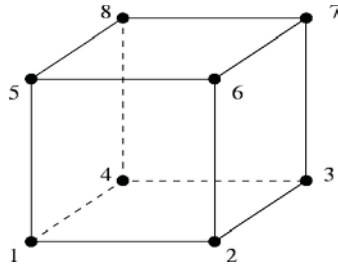


Figure III-10 Schematic of the C3D8R Element [86]

### 3.5 Material Modeling

Abaqus can simulate a ductile material's stress-strain response as the one illustrated in Figure III-11 Typical Uniaxial Stress-Strain. This plot shows that the material response is initially linear elastic (section a-b), followed by plastic yielding with strain hardening and/or a thermal softening (section b-c). The material damage initiates at point c and beyond it, there is a reduction of load-carrying ability until reaching rupture at point d. The material fails at point d.

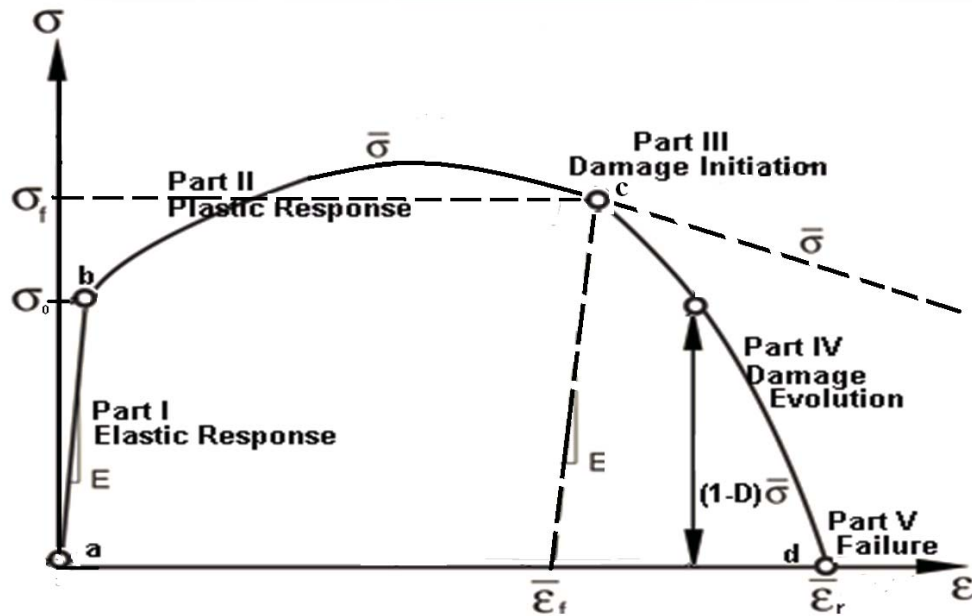


Figure III-11 Typical Uniaxial Stress-Strain Curve

For this model the material behavior was programmed in Abaqus in five parts, as follows:

### 3.5.1 Elastic Response (Part I)

Hooke's law of elasticity, presented in Appendix C, section 1.4.1, is used to model the materials elastic behavior. The Young's Modulus of elasticity,  $E$ , used to simulate the materials elastic response is presented in the next table.

<b>Materials</b>	<b><math>E</math> (GPa)</b>
<b>VascoMax 300</b>	180.7
<b>AISI-1080 Steel</b>	202.8

**Table III-1 Young's Modulus**

### 3.5.2 Plastic Response (Part II)

The Johnson-Cook plastic criterion presented in Appendix C, section 1.4.3 is used to simulate the undamaged plastic material behavior. The parameters used in Abaqus to simulate the VascoMax 300 and AISI-1080 Steel are presented on Table III.1 and are taken from Cinnamon's Flyer Test experiments, presented in Appendix D and documented in References [26, 27].

<b>Materials</b>	<b><math>A</math> (GPa)</b>	<b><math>B</math> (GPa)</b>	<b><math>C</math></b>	<b><math>m</math></b>	<b><math>n</math></b>	<b><math>T_m</math> (°K)</b>	<b><math>T_0</math> (°K)</b>	<b><math>\dot{\epsilon}_0</math> (s<sup>-1</sup>)</b>
<b>VascoMax 300</b>	2.1	.124	0.03	0.8	0.3737	1685	293	1
<b>AISI-1080 Steel</b>	0.7	3.6	0.17	0.25	0.6	1670	293	1

**Table III-2 Johnson-Cook Plasticity Model Parameters**

### 3.5.3 Damage Initiation Criteria (Part III)

The Johnson-Cook dynamic failure criterion is used to estimate the damage initiation criterion. This criterion is commonly used for problems involving high-strain-rate deformation of metals and it is generally appropriate for truly dynamic situations

[30]. The criterion is presented in reference [51] and summarized in Appendix C, section 1.4.5.

Due to the limited Johnson-Cook dynamic failure data available for the specific materials of this research, the parameters used were based on metals whose physical properties are similar to them. For the simulation of the VascoMax 300 the parameters used were those of the Ti-6Al-4V alloy [31]. To simulate the AISI-1080 Steel the parameters of the AIS- 1045 Steel were used. Appendix D, section 1.3 summarizes how these parameters can be derived.

Materials	Parameters of materials with similar properties:	$d_1$	$d_2$	$d_3$	$d_4$	$d_5$
VascoMax 300	Ti-6Al-4V <sup>[31]</sup>	-0.09	0.27	0.48	0.014	3.87
AISI-1080 Steel	AISI Steel 1045 <sup>[31]</sup>	0.7	3.6	0.17	0.25	0.6

**Table III-3 Johnson-Coom Dynamic Failure Parameters**

### 3.5.4 Damage Evolution (Part IV)

The Abaqus damage evolution criterion assumes that damage progressively degrades the material stiffness, leading to failure. For this model, the equivalent plastic displacement necessary to fail,  $\bar{u}_{pf}$ , was introduced as an input. The damage evolution was assumed to follow a linear relation between the equivalent plastic displacement,  $\bar{u}_p$ , and the damage variable,  $d$ . Before the onset of damage,  $\bar{u}_p = 0$ , there is no stiffness degradation ( $d=0$ ). After the damage initiation point, the rate of change of the equivalent plastic displacement is calculated as the product of characteristic length of the element by the equivalent plastic strain,  $\dot{\bar{u}}_p = L\dot{\bar{\epsilon}}_p$ . At failure  $\bar{u}_p = \bar{u}_{pf}$  and the stiffness is fully degraded ( $d=1$ ). The damage variable varies according to:

$$\dot{d} = \frac{\dot{\bar{u}}_p}{\bar{u}_{pf}} = \frac{L\dot{\bar{\epsilon}}_p}{\bar{u}_{pf}} \quad (\text{III-1})$$

where  $\dot{d}$  is the rate of change of the damage variable,  $\dot{\bar{\epsilon}}_p$  is the equivalent plastic strain rate,  $L$  is the element characteristic length, and  $\bar{u}_{pf}$  is the plastic displacement at the failure point.

For this model the projected plastic displacement at the failure point was selected to be 100 nanometers. This displacement is 1/6 of the characteristic length of the elements near the collision. Their length is about 600 nanometers.

After reaching the damage initiation point the stress decreases according to:

$$\sigma = (1 - d)\bar{\sigma}_y$$

where  $\sigma$  is the flow stress,  $\bar{\sigma}_y$  is the JC stress due to an undamaged response, and  $d$  is the damage variable representing the material stiffness degradation.

### 3.5.5 Failure Point (Part V)

For this Abaqus model, the elements are removed at the failure point  $c$ . Once this point is reached, the material stiffness is fully degraded and the element has no load carrying capacity. Beyond this failure point both the deviatoric stress and the pressure stress of the element are set to zero for the remaining calculations.

### 3.6 Mie-Gruneisen Equation of State (EOS)

The concepts related to the Mie-Gruneisen Equation of State are presented in Appendix C, section 1.6. This EOS is generally used for problems involving impact at high velocities [31]. It is therefore used for this model dealing with velocities between the 0-1500 m/s range

The necessary material properties to implement this relationship in Abaqus were obtained from materials with similar properties, as explained in Appendix C, section 1.4. The properties of these materials were obtained from AFIT's CTH database and summarized in Table III-4.

Materials	Parameters of materials with similar properties:	$c_0$ (km/s)	$s$	$\Gamma_0$
VascoMax 300	VascoMax250 <sup>[CTH]</sup>	4.605	1.456	1.65
AISI-1080 Steel	CTH Iron-Alpha <sup>[CTH]</sup>	3.980	1.580	1.6

**Table III-4 Mie-Gruneisen EOS Parameters**

### **3.7 Contact Interactions**

The Abaqus general contact algorithm is used in this model because it searches for any possible contact between faces and/or between edges, even among themselves or even when the original surface has evolved. This algorithm is the most robust one for explicit simulations and the only one that can maintain the contact interaction when the surfaces are wearing out.

#### **3.7.1 Element Removal**

The general contact algorithm allowed one to select the element removal feature for this model. This feature removes the elements from the mesh once the material stiffness is fully degraded, and the element has lost all its load carrying capacity [31], as explained in Appendix C, section 1.4.6. One cannot specify surface-to-surface interactions for this model because the surface topology evolves as it wears out.

#### **3.7.2 Penalty Method**

The penalty method, presented in Appendix C, section 1.7.3, is employed to permit an elastic slip. This method has received a wider acceptance than its alternative, the Lagrange Multiplier method. The Abaqus defaults for this algorithm are used, therefore the penalty stiffness is chosen automatically and the magnitude of the penalty constraint is continually adjusted to enforce this condition [31].

#### **3.7.3 Friction**

For this research, the Coulomb's friction model, presented in Appendix C, section 1.7.2, is used. The friction coefficient was based on Montgomery's muzzle wear of canon research [75]. Montgomery's coefficient of friction was incorporated into Abaqus in a tabular form. The experimentation involved obtain this COF was presented in Appendix D, section 1.5.

### **3.8 Dynamic Explicit Step**

This model uses an explicit time integration step (Appendix C, section 1.5.2). This dynamic explicit step is applied with an adiabatic thermal-stress condition (Appendix C, section 1.3.5) which is typically used to simulate high-speed processes involving large amounts of inelastic strain, where the heating of the material caused due its deformation is an important effect.

During this step, a velocity equal to the initial pre-defined velocity is applied to the assembly in motion, but now only to its top and aft surfaces. This velocity has two components: a horizontal component based on the sliding velocity and a vertical one of 1 m/s based on the DADS data. Limiting this condition only to these surfaces maintains the forward and downward velocity of the entire assembly while allowing it to deform properly on the vicinity of the asperity collisions. An overview of the explicit direct integration theory is presented in Appendix C, section 1.5.2. The next figure shows the location of the velocity boundary condition applied during the time step.

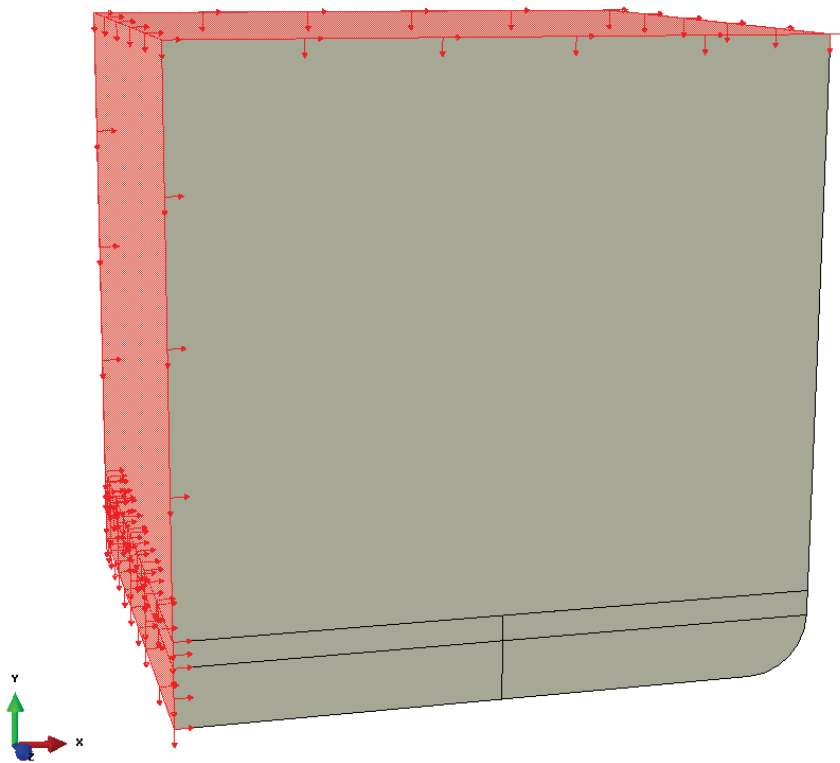


**Figure III-12 Velocity Boundary Condition**

### **3.9 Single Asperity Wear Output**

This 3D FE wear model simulates the mechanical sliding wear due to a single asperity. One of the investigation challenges was to decide when, during the simulation, to evaluate this wear. Previous AFIT studies evaluated the wear once the slipper penetrated half the length of the asperity; however, these models did so mainly because they were built without an element removal feature (presented in section 3.5.5) and had to stop the simulation at a pre-decided material penetration point. This 3D model was built using the Abaqus element removal feature and therefore the simulations can be ran long after reaching this point. In Figure III-13 one can observe how the slipper continues to fracture well after reaching half the length of the asperity (left picture) or even the full length of the asperity (middle picture). One can observe that the curve of the single asperity wear against time becomes asymptotic once the asperity wears to a certain point;

afterwards any further damage to the slipper is negligible (right picture). Based on these observations, it was decided to measure the damage at this point.

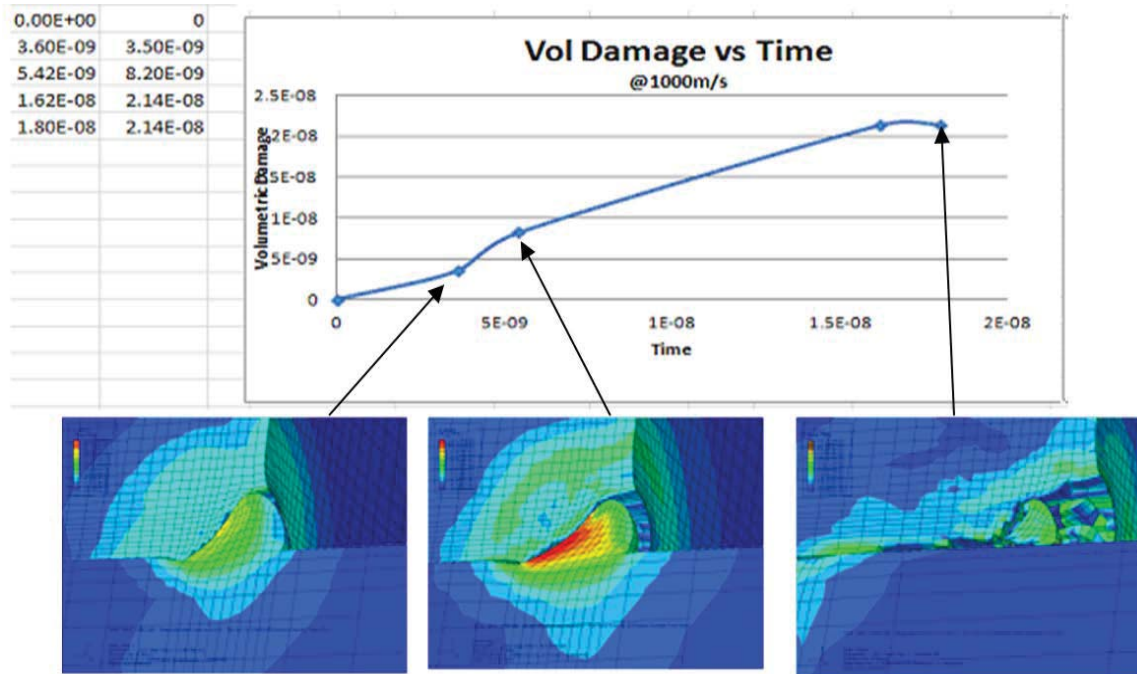


**Figure III-13 Single Asperity Wear Over Time**

The single asperity wear at this point is approximated by adding the original volume of all the elements that have failed up to this time. In Abaqus, variable STATUS, which is only available when using the Johnson-Cook failure criterion, provides the status of an element: One if the element is active or zero if is not. This STATUS variable can be used in conjunction with the element volume variable, EVOL, to calculate the wear or in other words the volume of the damaged material. Using only these two variables one can request Abaqus to directly report the cumulative volume of all the failed elements (wear).

### **3.10 Model Extrapolation**

#### **3.10.1 Surface Characterization Tests**

In 2005, Voyiadjis and others measured with a Scanning Electron Microscope (SEM) samples of the VascoMax 300 and AISI-1080 steel surfaces. The SEM sends a stream of light to the surface to be measured and from its reflection they create 3D surface profile of the material sample. Figure III-14 shows a picture of a SEM. Figure III-15 shows the AISI-1080 and VascoMax300 steel samples used for the SEM analysis. Figure III-16 and Figure III-17 show the 3D pictures of these samples [102].



**Figure III-14 Scanning Electron Microscope [106]**

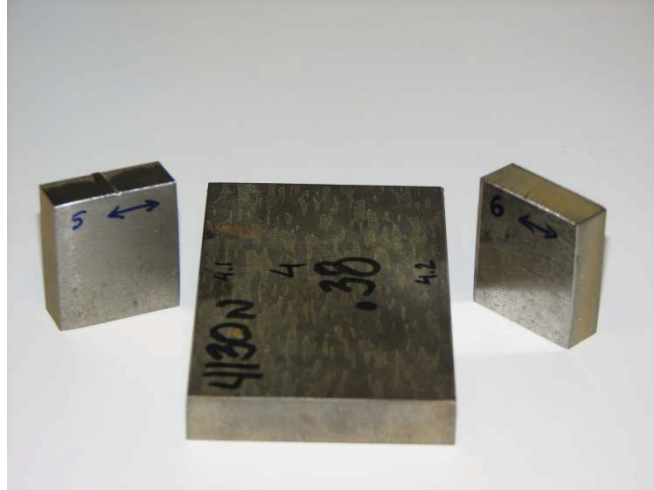


**Figure III-15 AISI-1080 and VascoMax300 Material Samples [102]**

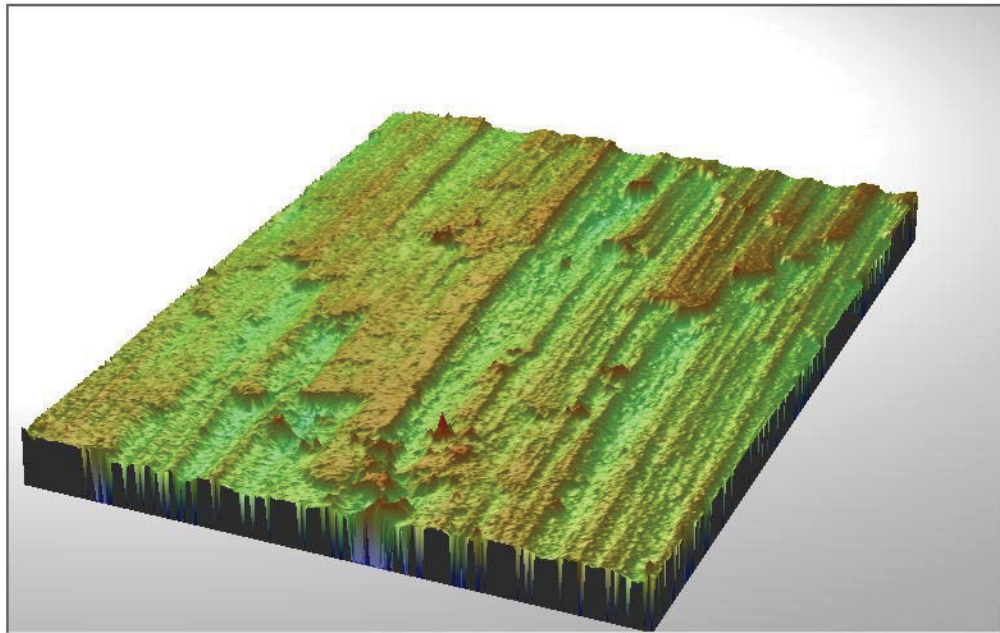


**Figure III-16 3D View of AISI 1080 Specimen [102]**

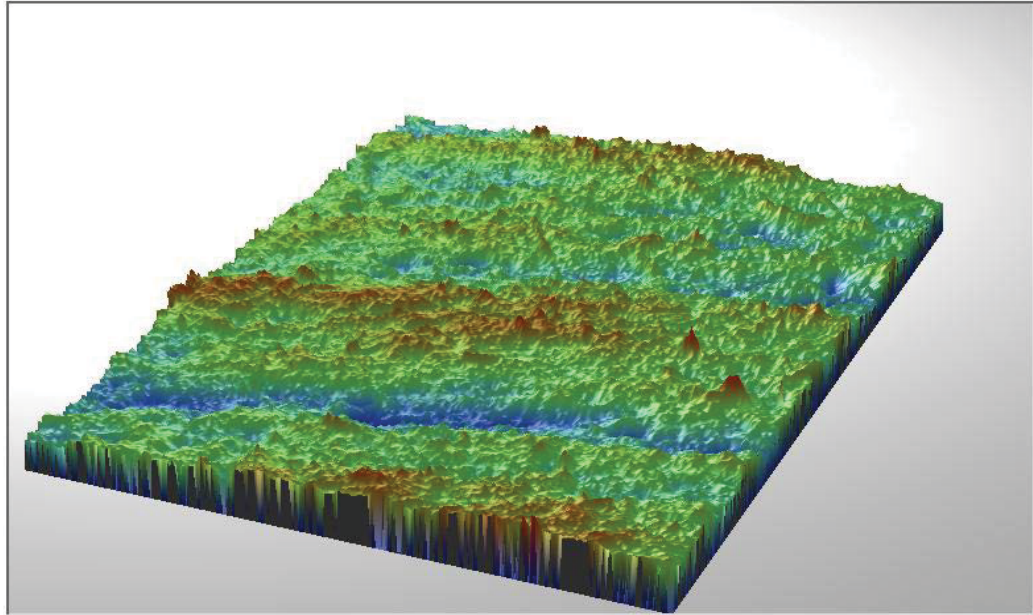


**Figure III-17 3D View of VascoMax 300 Specimen [102]**

The SEM measurements are sent directly to a computer. This computer, loaded with advanced software, allows the interpretation and visualization of the results. The software provides 2D and 3D pictures of the measured surfaces that show graphical representation of their profile along any line within the scanned area [102]. On these 3D pictures one can appreciate how different the two steels are at the micro level, in terms of their amplitude parameters which can provide us statistical information about the shape of the height distribution histogram. The high points on the histogram are called asperities or peaks, and the low points are called valleys [102].

These SEM measurements also helped to gather the statistical data to characterize the surface roughness for both materials of interest. The average roughness difference between specimens of the same material was relatively small. The next two tables show the roughness measurements of the two steels [102].

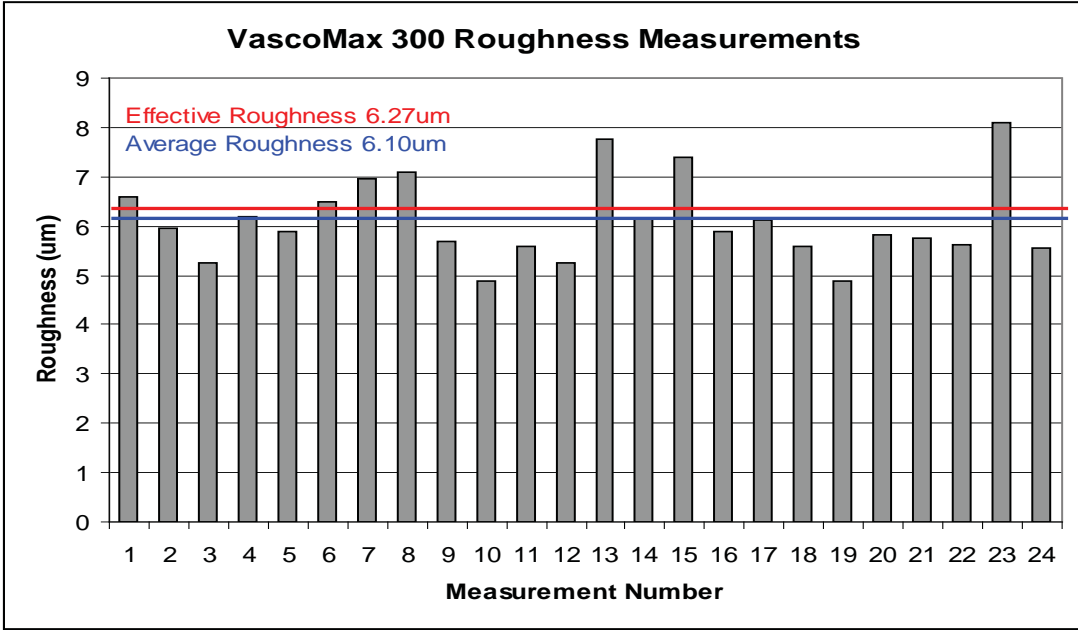


**Table III-5 Roughness Measurements of VascoMax300 [102]**

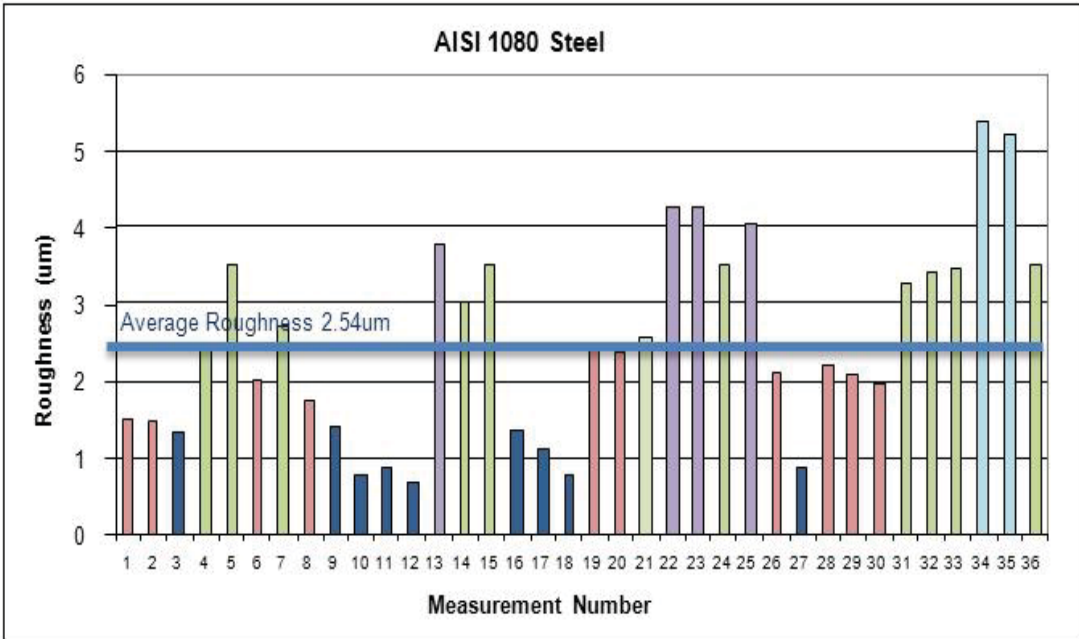


**Table III-6 Roughness Measurements of AISI-1080 Steel [102]**

On tables Table III-5 and Table III-6, one can see that for the VascoMax300 the average asperity sizes is  $R_a = 6.1 \mu\text{m}$ . For the AISI-1080  $R_a = 2.54 \mu\text{m}$ . In addition, from the data presented on these tables one can derive the range of asperity sizes and the

percentage of asperities of each size for each material. For example for the AISI-1080 steel the average asperity sizes varied from approximately 1  $\mu\text{m}$  to approximately 5  $\mu\text{m}$ . The percentage of the asperities at each average size between this range of 1-5  $\mu\text{m}$  is presented in the next pie chart.

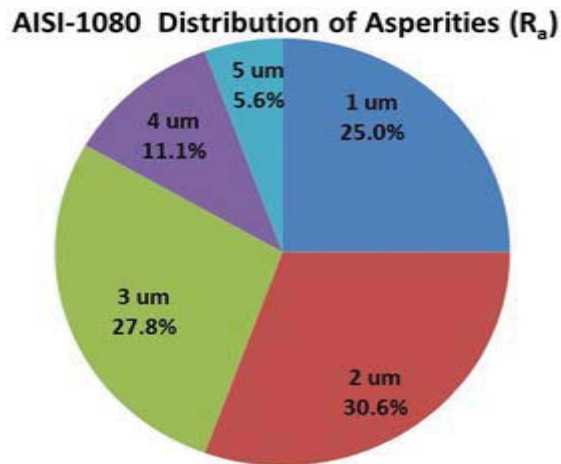


**Figure III-18 AISI-1080 Steel Distribution of Asperities**

The parameters obtained from these experiments were used in this 3D wear, first to create a model with hemispherical asperities of different sizes based on the surface characterizations average size and range. The geometry of this model is presented on section 3.3. Second, the total wear of a scenario is extrapolated based on the results of the single asperity collisions and the distribution of asperities in the material surface.

### 3.10.2 Extrapolating the Normalized Wear

To estimate the normalized wear, one can extrapolate the model's simulated single asperity damage based on the surface roughness characterization analysis. The bar chart presented in the Table III-6 shows the average asperity size measurements from these studies, these results were used to select the sizes of the model's hemispherical asperities. Figure III-18 shows the statistical distribution of asperities, the percentage of asperities of each relevant size, ranging from 1-5  $\mu\text{m}$ .

With the surface characterization analysis data one can estimate the volumetric wear per unit of area at any given velocity  $v$ ,  $V_{uA-v}$ , as follow:

$$V_{uA-v} = \# Asp_{uA} \sum_{n=1}^{n=5} \% Asp_n V_{SA-n-v} \quad (III-2)$$

where  $\# Asp_{uA}$  is the number of asperities per unit of area,  $n$  is the size of the asperities,  $\% Asp_n$  is the percentage of asperities of size  $n$ , and  $V_{SA-n-v}$  is the simulated volumetric wear due to an asperity of size  $n$  at a velocity  $v$ .

The number of asperities per unit of area,  $Asp_{uA}$ , was not reported by Voyiadjis [102]. To overcome this issue, this value was estimated based on the number of plastic deformations patterns observed in a micrograph of the recovered slipper. This methodology assumes that one can correlate the number of asperities per unit of area on the rail to the plastic deformation patterns observed on the worn slipper. These patterns are assumed to be inflicted by the collision of the rail asperities.

For this investigation the  $\# Asp_{uA}$  was estimated based on the plastic deformation patterns observed in the micrograph presented in Figure III-19. In this figure, one can observe three clear plastic deformation patterns (disregarding the ambiguous small patterns). These patterns are assumed to be created by the collisions of the larger rail asperities. According to the measurements presented in Table III-6 the large asperities are those between 3-5  $\mu\text{m}$ . Figure III-18 shows that the asperities around 3-5  $\mu\text{m}$  account for 44.4% of the total number of asperities. Based on this value, one can estimate the total number of asperities by dividing the number of clear deformation patterns by 44.4%.

Using the formulation presented in Appendix C, section 1.7.1, one can calculate the total number of asperities per unit of area as follow:

$$\# Asp_{uA} = \frac{\text{Number of asperities}}{M \times N} = \frac{(3 / 0.444)}{0.125 \times 0.09} = 601 \text{ asperities/mm}^2$$

where  $M$  and  $N$  are the width and length of the rectangular micrograph presented in Figure III-19.  $M= 0.125 \text{ mm}$  and  $N= 0.09 \text{ mm}$ .

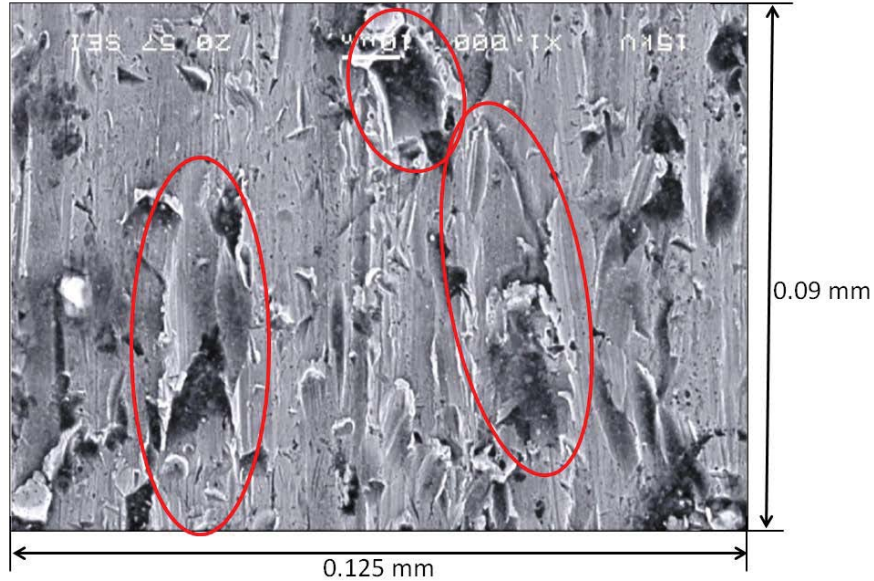


**Figure III-19 Micrograph of Worn VascoMax 300 Slipper [38]**

### 3.10.3 Normalized Wear Rates

In Appendix C, section, 1.8.2, the wear rates are defined as the volume of material removed per unit of sliding distance [12]. To obtain the normalized wear rates,  $W_{uA}$ , one can divide the wear per unit of area,  $V_{uA}$ , by the unit of sliding distance,  $D_s$ . These dimensionless wear rates are given by:

$$W_{uA} = \frac{V_{uA}}{D_s} \quad \text{(III-3)}$$

The normalized wear rates can be directly applied to estimate the wear of systems with an area of contact,  $A_c$ , that varies. The area can vary due to the wear of an irregular sliding part and/or the rotation of it. An example of such case is the HHSTT scenario, where a slipper sliding over a rail rotates as a function of its acceleration, continually varying its area of contact. This HHSTT scenario is summarized in Chapter IV.

### 3.10.4 Total Wear Rates

The normalized wear rates are generally a function of the sliding velocity. If the velocity is not constant, one can estimate the total mechanical sliding wear by:

- 1) Dividing the velocity profile into a number,  $n$ , of discrete velocity intervals;

2) Evaluating the sliding wear at each velocity interval with equation III-4 (presented in Appendix C, section 1.8.2):

$$V_{d-n} = W_{uA} \times l_c \times w_c \times D_s \times \%Cont \quad (\text{III-4})$$

3) Estimating the total mechanical sliding wear with equation III-5 (presented in Appendix C, section 1.8.2):

$$V_d = \sum_1^n W_{uA_n} \times l_{c_n} \times w_{c_n} \times D_{s_n} \times \%Cont_n \quad (\text{III-5})$$

where  $l_c$  and  $w_c$  are the slipper length and width in contact with the rail,  $D_s$  is the sliding distance,  $\%Cont$  is the percent of time in contact, and  $n$  is velocity interval..

### **3.11 Model Relation to the Wear Definition**

The American Society for Testing and Materials (ASTM) defines wear as the “damage to a solid surface, generally involving progressive loss of material, due to relative motion between that surface and a contacting substance or substances” [6]. This 3D FE model attempts to incorporate each of the key words (the ones underlined) on this definition as follow:

- Damage: Employing the Johnson-Cook plasticity and dynamic failure criterions.
- Solid surface: Developing the FE model using 3D solid continuum elements.
- Progressive: Analyzing the time dependent material behavior simulated through a dynamic explicit time step.
- Loss of material: Coupling the Johnson-Cook failure criterion with the Abaqus element deletion feature. Then, estimating the wear based on the volume of the failed elements.
- Relative motion: Displacing one of the assemblies while keeping the other one encastrated during the dynamic step.
- Contacting: Incorporating the surface roughness characteristics (e.g. asperity sizes and gap) via the model geometry and applying the FE package general contact algorithm during the dynamic explicit time step.

### **3.12 Chapter Summary**

Chapter III presented the 3D FE sliding wear model. This chapter presented the model concept and an overview of each one of its features (such as geometry, boundary conditions, material modeling, contact interactions, etc). The theory behind the model features is presented in Appendix C and the experiments required to obtain the model's input parameters is described in Appendix D.

This third chapter explained the methodology to extrapolate the model's single asperity damage to obtain the normalized wear rates. This proposed methodology is based on the roughness characteristics of the surfaces in contact.

Chapter III also presented the approach used to estimate the total mechanical sliding wear based on the normalized wear rates and the sliding system characteristics.

Finally, this chapter explained the relation between the ASTM definition of wear and the model approach to simulate it.

## IV. Scenario to Simulate

This chapter will provide an overview of the Holloman High Speed Test Track (HHSTT) and a summary of the mission executed on this track on January 2008.

Appendix C, section 1.8.2, develops the formulation to calculate the total wear from scenarios with a wide velocity range, a variable length in contact, a variable width in contact, variable sliding distances, and an intermittent contact. The HHSTT mission of interest meets all the characteristics of such scenario. The total wear for these types of scenarios can be estimated by dividing the velocity profile into a number,  $n$ , of discrete velocity ranges, evaluating then the wear rates at each discrete range, and then adding the results from all the discrete ranges. The formula developed in Appendix C, section 1.8.2, to carry out these calculations is:

$$V_d = \sum_1^n W_{uA_n} \times l_{c_n} \times w_{c_n} \times D_{s_n} \times \%Cont_n \quad (\text{IV-1})$$

where  $V_d$  is the total wear,  $W_{uA_n}$  are the normalized wear rates,  $l_{c_n}$  is the length in contact,  $w_{c_n}$  is the width in contact,  $D_{s_n}$  is the sliding distance in contact,  $\%Cont_n$  is the percent of distance in contact and the suffix  $n$  denotes the discrete velocity range number.

Chapter four will explain how the test data, from the HHSTT mission, was used to estimate each one of the factors in this equation. This chapter presents only the necessary information to estimate the factors required to predict the total wear of the HHSTT mission of interest. It doesn't attempt to provide a comprehensive description of the mission events or a detailed account of the metallographic analysis. Hale [38] documents in detail the mission events and Voyiadjis [103] documents the metallographic analysis.

### 4.1 HHSTT Background

The Holloman High Speed Test Track is located at Holloman AFB, New Mexico. This test facility belongs to the Air Force Research Laboratory (AFRL) and its division is in charge of a variety of investigations, such as testing aircraft munitions, egress systems or hypersonic aerodynamic effects. The test track provides a cheaper and more efficient

alternative to flight-testing. This test facility has recorded events with speeds up to 2885 m/s (6,453 miles per hour), and the AFRL is interested in performing tests at speeds surpassing 3000 m/s [38].

On this facility, sled rocket systems travel over two parallel rails made of AISI-1080 steel, set to cover a length of about 16 kilometers (10 miles), as shown in Figure IV-1 [38].



**Figure IV-1 HHST Aerial View [38]**

#### **4.2 HHSTT January 2008 Mission Overview**

A typical sled setup to test munitions resembles a train. The setup for the mission executed on January 2008 consisted of four rocket-powered sleds that ignited sequentially as shown in Figure IV-2. The first two sleds, called “Pupfish pushers”, provided the initial thrust to the system. Both of these sleds were propelled by six Multiple Launch Rocket System (MLRS) rocket motors. The two forward sleds were propelled by Single Super Roadrunner (SRR) rocket motors. The SSR forebody sled carried the payload and the test instrumentation [38].

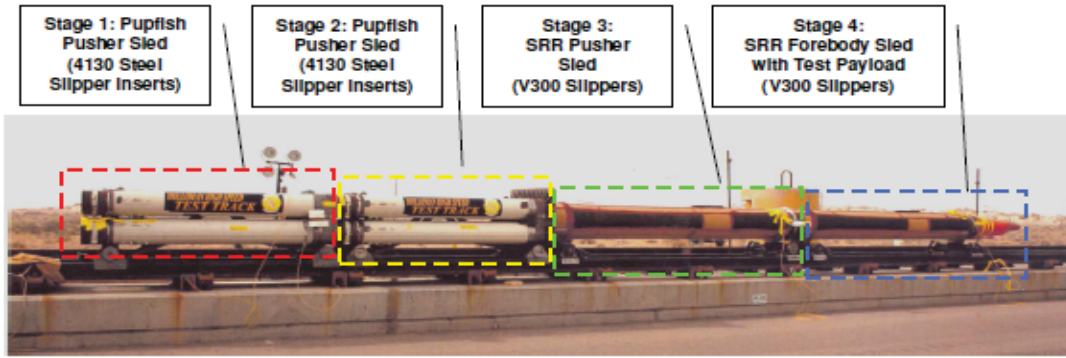


**Figure IV-2 January 2008 Mission Setup [38]**

The rocket sleds travel along the test track attached to it by slippers that slide over the steel rails. Figure IV-3 shows a picture of this HHSTT sled system [38].



**Figure IV-3 HHSTT Sled System [38]**

Figure IV-4 shows a close look of the slipper-rail interface [38]. In this figure one can observe a gap between the rail and the slipper.

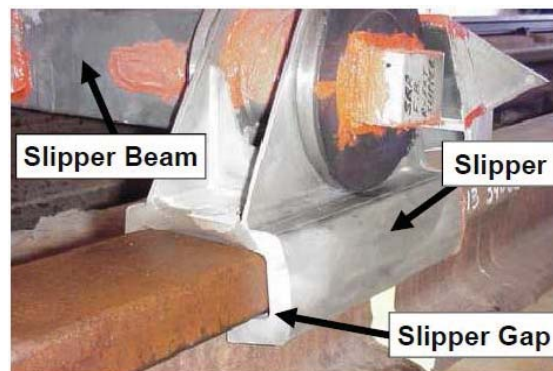


#### Figure IV-4 Slipper-Rail Interface [38]

Generally, the slippers are useless after each test due to their wear. After executing the January 2008 mission, one of the slippers from third stage pusher was recovered, dissected, and submitted to several investigations. The investigations of the recovered slipper included: wear volume measurements, surface characterization analysis, hardness testing, optical microscopy, and energy dispersive x-ray spectroscopy (EDS) [38].

#### 4.3 Original Slipper Dimensions

The original slipper dimensions were not measured prior to the mission. The original top slipper thickness was approximated based on the technical drawings and on the measurements of a new slipper manufactured for Hale [38] investigations. The assumed top slipper thickness was estimated to be 14.7 mm. Based on this thickness, the top slipper volume was estimated to be 300,900 mm<sup>3</sup> [38].

#### 4.4 Post-Mission Slipper Measurements

The thickness of the recovered slipper was measured at three locations, as shown in Figure IV-5.

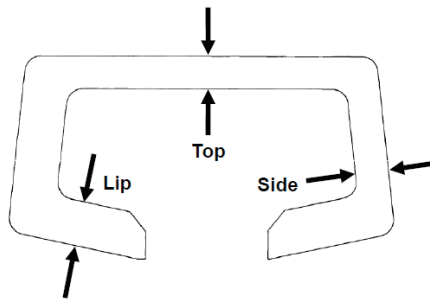
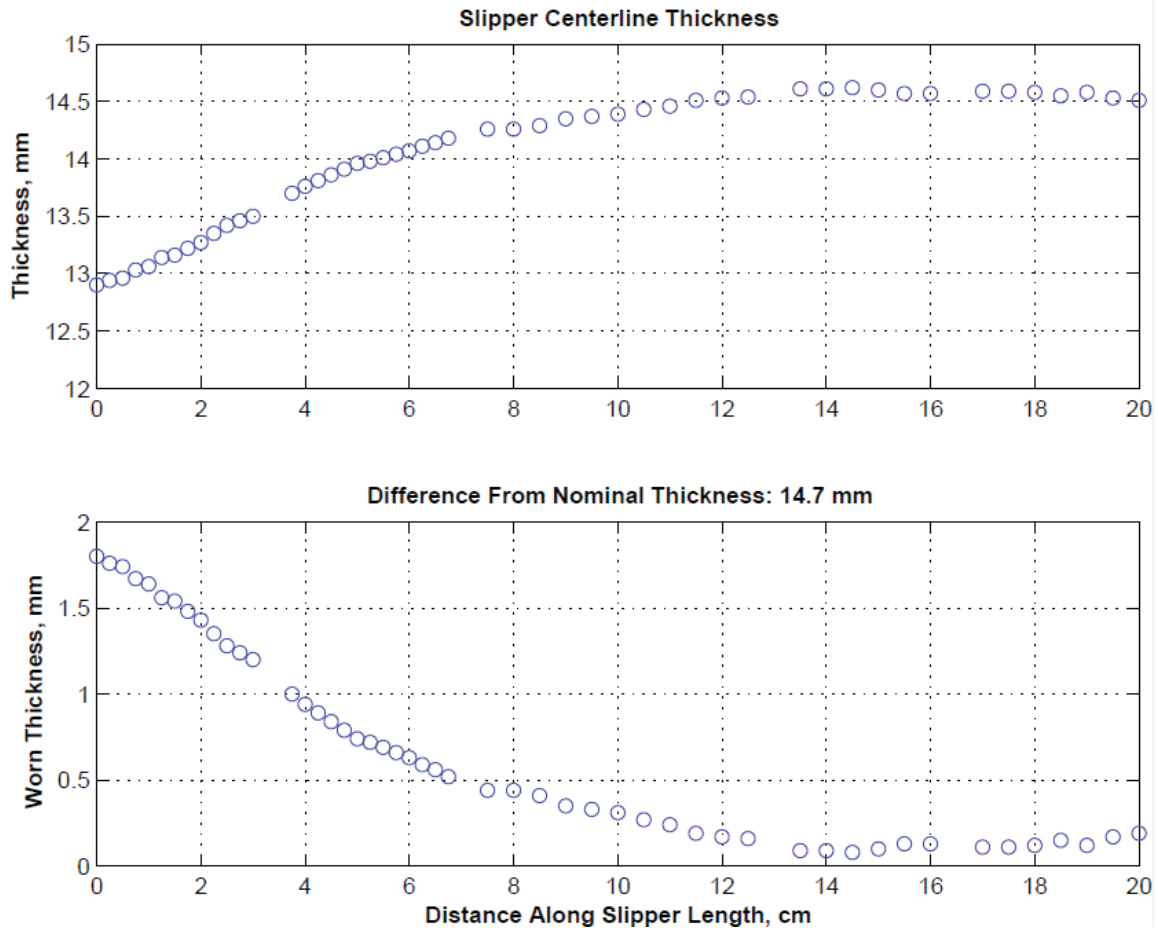


Figure IV-5 Slipper Thickness Measurement Locations [38]

Figure IV-6 shows two plots of the slipper thickness measurements taken on the top of the slipper. These measurements were taken along the length of the slipper. In the two plots the front of the slipper is represented with a length equal to zero and the back of the slipper with a length equal to twenty. In both plots one can see that the slipper top

exhibited more wear in the front than in the back. The bottom plot shows the difference between the nominal thickness, 14.7 mm, and the thickness measured along the slipper centerline. The worn area for the centerline cross-section was determined to be 103.5 mm<sup>2</sup>. This value was obtained by integrating the worn centerline thickness along the length of the slipper.



**Figure IV-6 Slipper Thickness Measurements Along the Centerline [38]**

Figure IV-7 shows the slipper thickness measurements taken on the sides and lips of the slipper. These measurements were taken along the length of the slipper. In the two plots the front of the slipper is represented with a length equal to zero and the back of the slipper with a length equal to twenty. In the top plot one can see that the side measurements are almost constant. In the bottom plot one can observe that the left side

lip exhibited more wear than the right side one. Moreover, one can observe that the slipper lips showed more wear in the back than in the front.

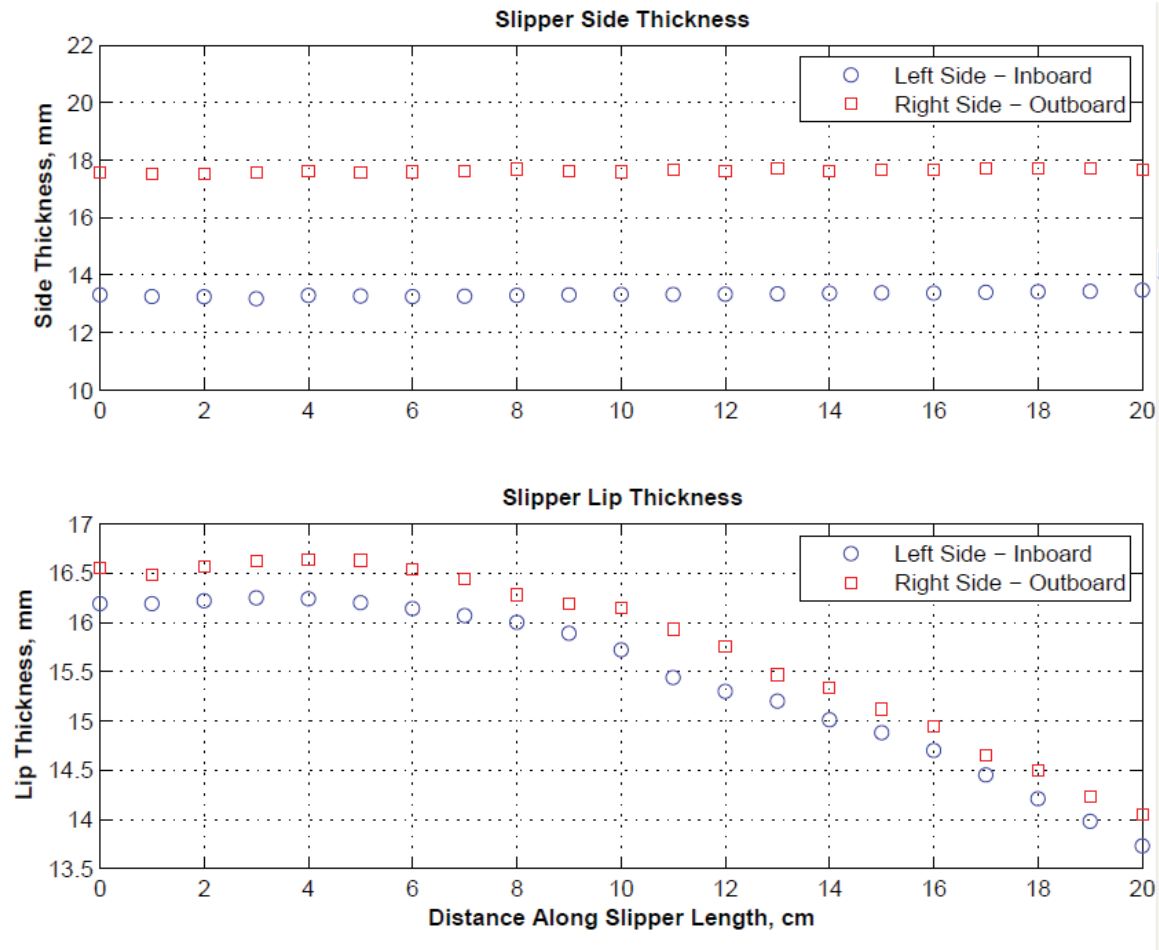


**Figure IV-7 Slipper Thickness Measurements Along the Side and Lip [38]**

The total volumetric damage or wear of the slipper was determined to be 10, 520 mm<sup>3</sup>. It was calculated by the product of the worn thickness along the centerline cross section (103.5 mm<sup>2</sup>) by an assumed constant width (101.0 mm). This total wear value accounted for 3.49% of the assumed original volume of 300.9 cm<sup>3</sup> [41].

#### **4.5 DADS Data**

Due to the inability to gather high-speed sliding wear data in a controlled environment, such a laboratory. This 3D wear model was compared against the data gathered from a munitions test mission, executed at the HHSTT back on January 2008.

The data gathered from the HHSTT mission was analyzed with a package called the Design Analysis of Dynamic Systems (DADS). DADS compiled and filtered the mission raw data and provided reports that included: test time, contact forces, contact time, displacement, velocity, and acceleration data [38]. Due to the DADS package maturity and proven performance, the data reported by it was considered “truth” data for this investigation.

Even with the data gathered by DADS, estimating the necessary parameters to predict the slipper wear after traveling over the HHSTT was not an easy task. Cinnamon [24] states on his AFIT dissertation that *“The shoes are machined to allow a slight gap between their structure and the rail head. This allows the vehicle to maintain a limited “free-flight” condition as the vehicle accelerates down the track. The consequence of this free flight condition is that the shoe can roll, pitch, or yaw with relation to the rail during the test and these results in intermittent contact between the shoe and the rail.”* The rapid acceleration of the slipper, coupled with this “free-flight” condition, introduced the following challenges to the wear estimations:

#### **4.6 Wide Velocity Profile**

The wide velocity profile of the sled system, traveling along the HHSTT during the 2008 mission, is presented in Figure IV-8. This plot is based on the DADS data.

The slipper recovered and analyzed for this research traveled according to the velocity profile depicted with the blue line. The slipper accelerated from 0- 1,530 m/s in about 5 seconds. Upon reaching the third rocket stage, the forebody of the sled system continued according to the velocity profile plotted in red; meanwhile the pusher that was attached to the rail with the recovered slipper was released and began to decelerate. It decelerated for 3.14 s and exited the test track at 622 m/s [38].

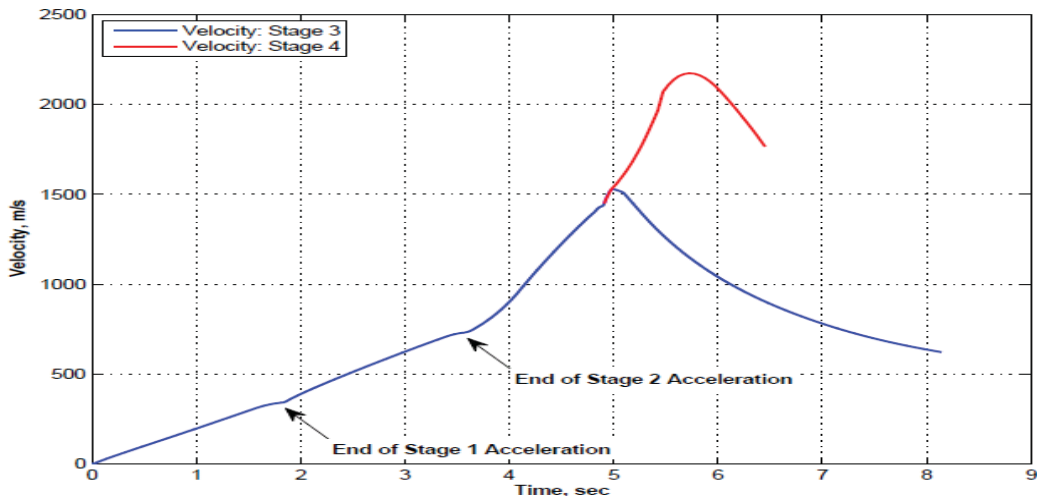


**Figure IV-8 Velocity Profile**

Since Hale [38] studies concluded that the wear rates are independent of the worn history, then, the mission velocity profile was divided into discrete velocity segments. Most segments covering a range of 100 m/s, as shown in Figure IV-9. Table IV-2 lists all the velocity intervals.

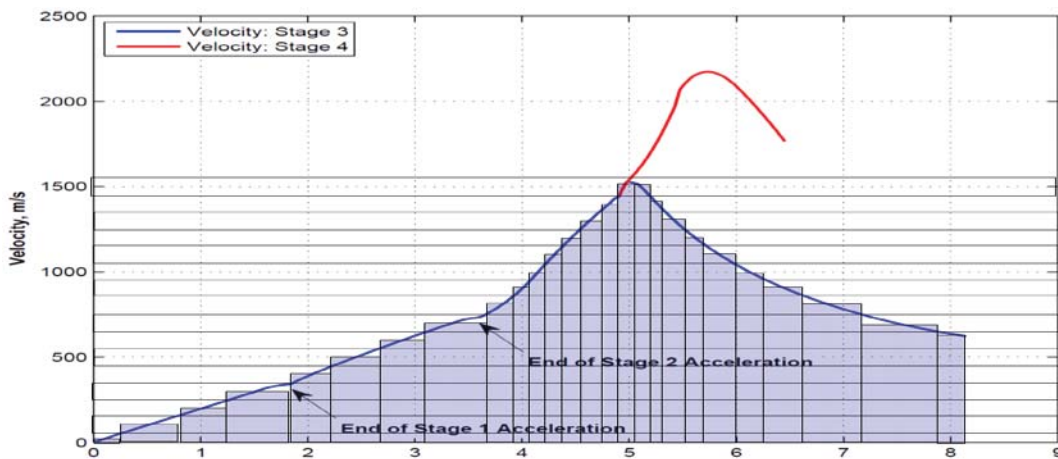


**Figure IV-9 Mission Velocity Profile**

Table IV-1 presents the DADS test and evaluation summary values for the January 2008 HHSTT mission

Stage	Sled Type	Slipper Material	Distance (m)	Time (s)	Max Velocity (m/s)
1	Pupfish pusher	AISI 4130 Steel	2,940	1.9	342
2	Pupfish pusher	AISI 4130 Steel	4,761	3.8	731
3	SRR Pusher	VascoMax 300	5,816	5.0	1530
4	SRR Forebody	VascoMax 300	5,816	8.14	2256

**Table IV-1 Mission Summary [38]**

#### **4.7 Sliding Distance**

The sliding distance traveled at each velocity interval was estimated using the DADS data. This distance was calculated as the product of the average velocity by the time of the interval. The values used for these calculations are presented in Table IV-2.

Velocity Interval	Interval Time (s)	Average Velocity (m/s)	Interval Sliding Distance (m)
0-50	0.3	25	7.5
50-150	0.5	100	50
150-250	0.5	200	100
250-350	0.6	300	180
350-450	0.4	400	160
450-550	0.5	500	250
550-650	0.5	600	300
650-750	0.6	700	420
750-850	0.2	800	160
850-950	0.12	900	108
950-1050	0.12	1000	120
1050-1150	0.12	1100	132
1150-1250-	0.12	1200	144
1250-1350	0.12	1300	156
1350-1450	0.12	1400	168
1450-1530	0.18	1500	270
1450-1530	0.2	1500	300
1350-1450	0.2	1400	280
1250-1350	0.2	1300	260
1150-1250	0.2	1200	240
1050-1150	0.2	1100	220
950-1050	0.3	1000	300
850-950	0.3	900	270
750-850	0.5	800	400
650-750	0.8	700	560
550-650	0.2	650	130

**Table IV-2 Intervals Sliding Distance**

The model was ran at each discrete velocity. The total wear was extrapolated from these simulations using among other factors these estimated sliding distances.

#### 4.8 Intermittent Contact

The rocket sleds were designed to be aerodynamic to minimize the loads and consequently reduce wear. In addition, the slipper was designed to allow a gap between it and the rail of about 3.175 mm. These two system design factors allowed the slipper to bounce as it travels.

The slipper bouncing fact can be observed in Figure IV-10, which plots the vertical displacement of the slipper with respect to its center of gravity, as reported by DADS.

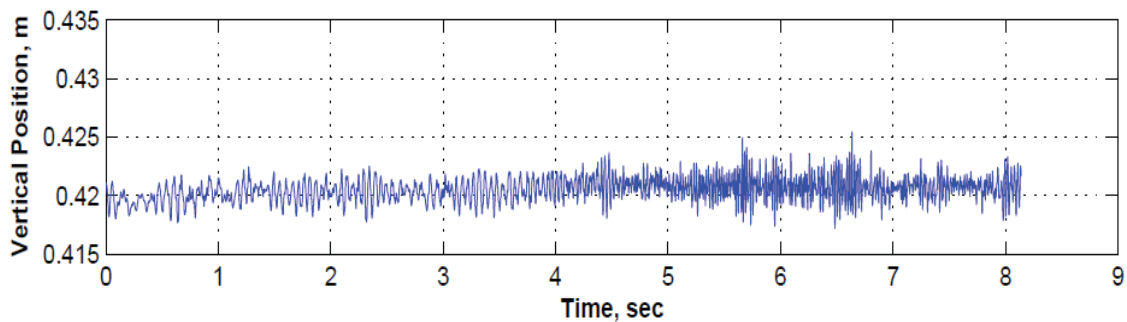


**Figure IV-10 Slipper Vertical Displacement [38]**

The percent of time in contact can have a significant impact on the wear predictions, since this factor can be quite low for scenarios with intermittent contact. For the wear estimates of the HHSTT mission of interest (presented in Chapter 4), this factor is very important because the slipper traveled bouncing due to the aerodynamic design of the sled system. This factor was formerly assumed to be 30%. For this investigation this factor was evaluated at each velocity interval, to have a more refined approximation.

DADS reported the loads on the top inner surface of the slipper (points 4 and 3 in Figure IV-11) and at its bottom lips (points 1 and 6 in Figure IV-11). The percent of time in contact was estimated, for each velocity interval, based on the percentage of time the loads were applied to each of these surfaces. In Figure IV-11 one can observe how the slipper time in contact continuously varies. It is higher at low velocities and lower at high velocities. In addition, it transitions from mainly contact at the top during the acceleration to mainly contact at the bottom during the deceleration phase.

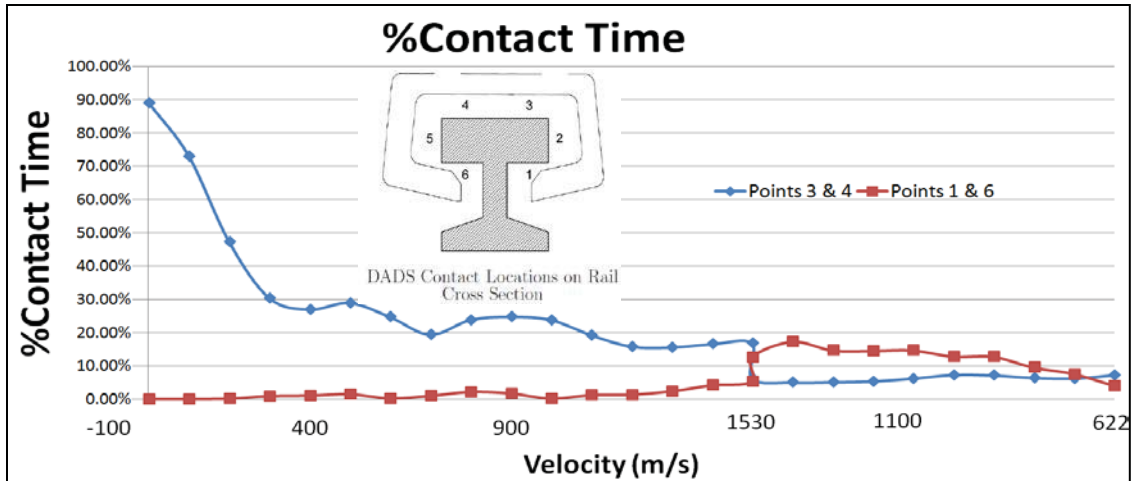


**Figure IV-11 Running Average of the Percent of Time in Contact**

#### **4.9 Length in Contact**

For this investigation the slipper is assumed to rotate along the z-axis (pitch). Cinnamon mentions this slipper rotation in his AFIT dissertation [27]. It is probable that the gap that allows the slipper vertical motion, reported by DADS, also allows it to slightly rotate as it travels.

The assumption of the slipper pitch is supported by photographic evidence of the rotation of a similar slipper during a similar mission. The photographic evidence was captured on several high speed image motion compensation (IMC) photographs taken during a mission executed on April 2003. Figure IV-12 shows two of these pictures.



(a) 80X-G1 Test Mission, April 2003,  $V = 2,853$  m/s.



(b) 80X-G1 Test Mission, April 2003,  $V = 2,861$  m/s.

#### **Figure IV-12 Forward Rotation of Test Slipper [47]**

In both of these pictures, the forebody sled was traveling from left to right. In these pictures one can clearly see the slipper rotation. In the second picture, one can also see what is called the “slipper fire” due to the departing wear debris. Krupovage [57] mentioned this phenomenon. There are no pictures from the January 2008 test mission however; it is assumed that a similar rotation occurred because both missions were similar on their setup and execution.

The slipper’s worn thickness measurements are believed to support this rotation assumption. Figure IV-13 presents the slipper top thickness measurements along the length centerline of the slipper. Note that to better appreciate the slipper rotation effects the units of the axis are different; the abscissa units are centimeters while the ordinate units are micrometers.

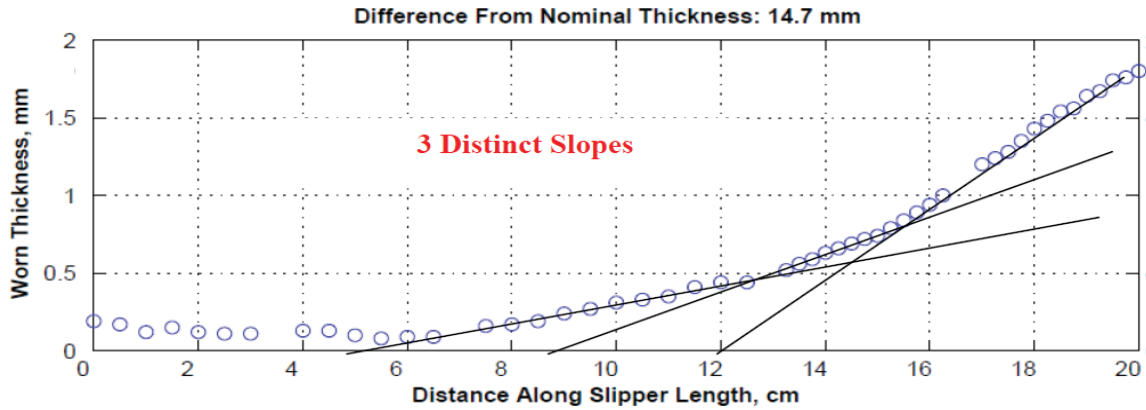


**Figure IV-13 Slipper Thickness Along Centerline [38]**

In Figure IV-13 one can see three distinct worn slopes on the front of the slipper (right side on the figure). These three slopes can be associated with the three rocket acceleration stages. The assumption is that the pitch angle of the slipper varies as a function of the sled acceleration; consequently the slipper will wear at an angle, as observed on the worn slipper measurements along the centerline.

Figure IV-14 shows a notional free body diagram of the slipper, depicting some of the forces acting upon it. In this diagram, one can see how the force,  $F$ , (determined by the mass,  $m$ , and acceleration,  $a$ , of the system) and the frictional forces,  $f_1$  and  $f_2$ , contribute to the slipper clockwise rotation. Meanwhile, the rail reaction forces  $R_1$  and  $R_2$  restrain this rotation.

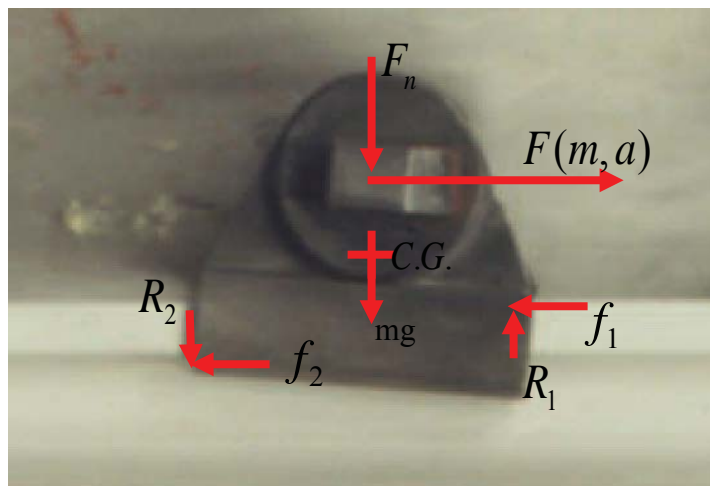


**Figure IV-14 Slipper Free Body Diagram**

During the deceleration phase of the mission, the force,  $F$ , inverts its direction. This change in direction is assumed to reverse the rotation of the slipper to a counterclockwise direction.

The slipper rotation introduces a challenge on the estimation of the system wear. If the slipper rotates then it doesn't wear evenly because its length in contact varies as it slides along the rail. Moreover, every time the slipper rotates its length in contact becomes practically a corner and as it travels the length in contact increases as the slipper wears out. Figure IV-15 depicts this concept.

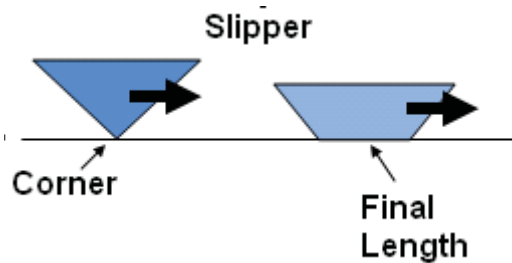


**Figure IV-15 Slipper Variable Area of Contact**

Figure IV-16 graphically depicts how the length in contact of the slipper is assumed to vary as a function of the rotation of the slipper and the distance traveled during the HHSTT mission of interest.

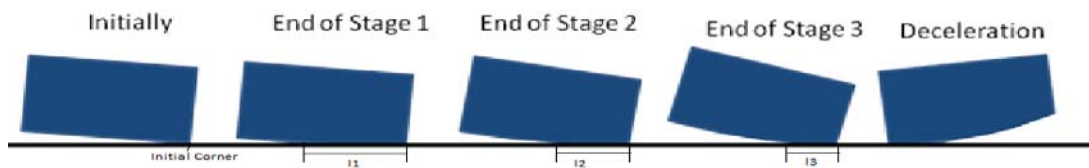


**Figure IV-16 HHSTT Assumed Length in Contact Progression**

For this mission the actual length in contact is an unknown variable that had to be estimated. To estimate the lengths in contact at the end of each acceleration stage it was assumed that the three slopes observed in the plot of the slipper worn thickness along its length (Figure IV-17) correlate to the three sled system acceleration stages. The higher the slipper acceleration the greater the pitch and the steeper the worn thickness slope.

The worn length at the end of the first stage is assumed to be about 14 cm (the red line). The worn length at the end of the second stage is assumed to be 7 cm (the blue line). The third stage maximum worn length is assumed to be 4.5 cm (the purple line). The maximum deceleration worn length is assumed to be 7 cm (the yellow line).

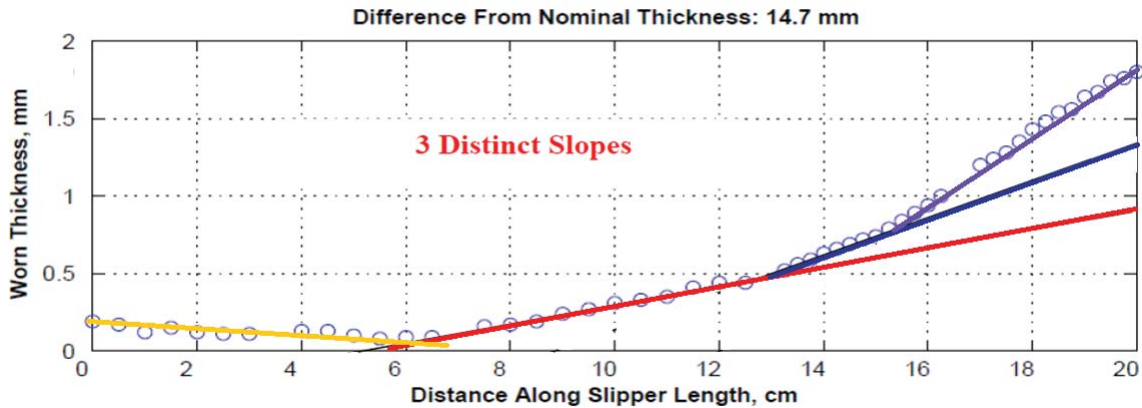


**Figure IV-17 Assumed Max. Lengths in Contact for Each Stage**

To estimate the length in contact at any given time, this length was assumed to wear linearly. The length in contact was approximated with the following equation:

$$l_n = \frac{t_n - t_0}{t_f - t_0} l_f \quad (\text{IV-2})$$

were  $l_n$  and  $l_f$  are the lengths at the target velocity and at the final velocity of that rocket stage respectively, and  $t_n$ ,  $t_0$  and  $t_f$  are the times at the target velocity, the beginning and end of the rocket stage respectively.

The length in contact of the slipper really decreases non-linearly as a function of many factors such as the wear rates at the given velocity, the skin temperature, the percent of time in contact, etc. For this investigation it was assumed to decrease linearly only to obtain a rough estimate of it. This simplistic approach was employed to avoid digressing from the main investigation objectives.

From the DADS data, one can obtain the start and end time,  $t_0$  and  $t_f$  of each rocket stage. Table IV-3 tabulates these values and the assumed worn lengths at the end of each stage.

Mission Phase	Start Time $t_0$ (s)	End Time $t_f$ (s)	Worn Length $l_f$ (mm)
Stage 1	0	1.9	140
Stage 2	1.9	3.8	70
Stage 3	3.8	5	45
Decel.	5	8.14	70

**Table IV-3 Mission Summary**

With the values presented in Table IV-3 and the time to reach the average velocity of the interval,  $t_n$  (also obtained from DADS), one can estimate the average length in contact of each velocity interval using equation IV-2. These results are tabulated on the following table and plotted in Figure IV-18.

Phase	Velocity Interval (m/s)	Avg. Velocity (m/s)	Time to Reach Avg. Velocity (m/s)	Worn Length (mm)
Stage 1	0-50	25	0.15	11.1
Stage 1	50-150	100	0.55	40.5
Stage 1	150-250	200	1.05	77.4
Stage 1	250-350	300	1.6	117.9
Stage 2	350-450	400	2.2	11.1
Stage 2	450-550	500	2.55	23.9
Stage 2	550-650	600	3.05	42.4
Stage 2	650-750	700	3.6	62.6
Stage 3	750-850	800	4	7.5
Stage 3	850-950	900	4.1	11.3
Stage 3	950-1050	1000	4.2	15.0
Stage 3	1050-1150	1100	4.4	22.5
Stage 3	1150-1250-	1200	4.5	26.3
Stage 3	1250-1350	1300	4.6	30.0
Stage 3	1350-1450	1400	4.8	37.5
Stage 3	1450-1530	1500	4.9	41.3
Decelaration	1450-1530	1500	5.1	2.2
Decelaration	1350-1450	1400	5.3	6.7
Decelaration	1250-1350	1300	5.5	11.1
Decelaration	1150-1250	1200	5.7	15.6
Decelaration	1050-1150	1100	5.9	20.1
Decelaration	950-1050	1000	6.15	25.6
Decelaration	850-950	900	6.45	32.3
Decelaration	750-850	800	6.85	41.2
Decelaration	650-750	700	7.65	59.1
Decelaration	550-650	650	8	66.9

**Table IV-4 Estimated Length of Contact**

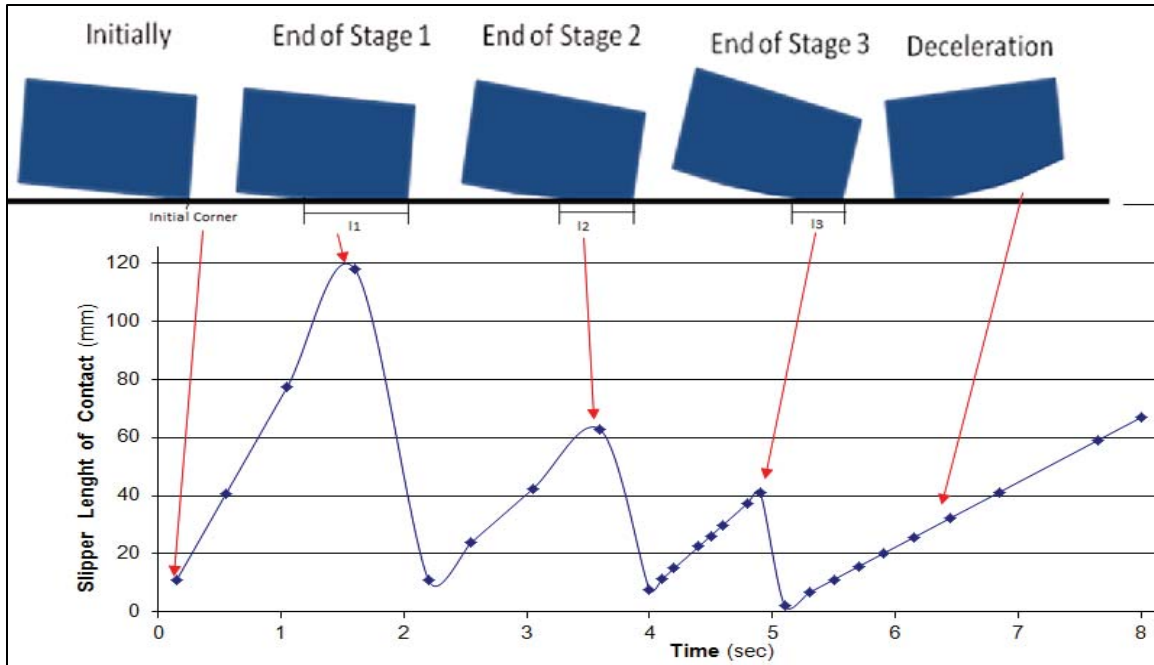
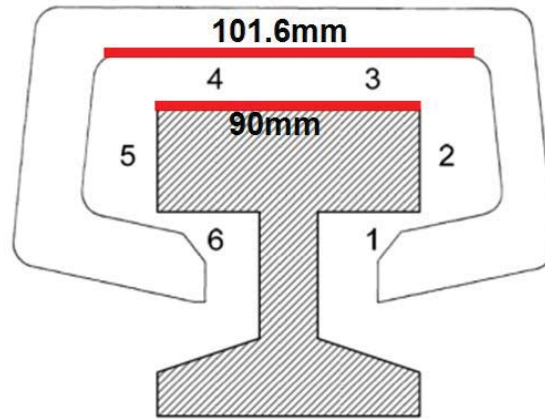


**Figure IV-18 Estimated Length of Contact vs. Time**

In Figure IV-18, one can see how the length of contact oscillates based on the pitch of the slipper. The sequence of events, as the slipper travels through the rail, are assumed to be as follow: Initially the slipper rotates to an angle proportional to the acceleration of stage 1, at this point the area of contact is a corner as depicted on the figure above. This length of contact starts increasing as the corner wears out reaching a length,  $l_1$ , at the end of stage one. Then the slipper rotates to an angle proportional to the acceleration of stage 2 and its length of contact becomes a corner again. This new corner wears out reaching a reaching a length,  $l_2$ , at the end of the stage two. This sequence of events repeats for stage 3. Once stage 3 ends, the slipper begins to decelerate and instead of pitching downward, now it starts pitching upward, therefore. During the deceleration the slipper wear its back instead of its front.

#### **4.10 Width in Contact**

Figure IV-19 shows the dimensions of the slipper and rail cross sections. In this figure one can see that, in theory, the maximum width, of contact between these two surfaces, is 90 mm.



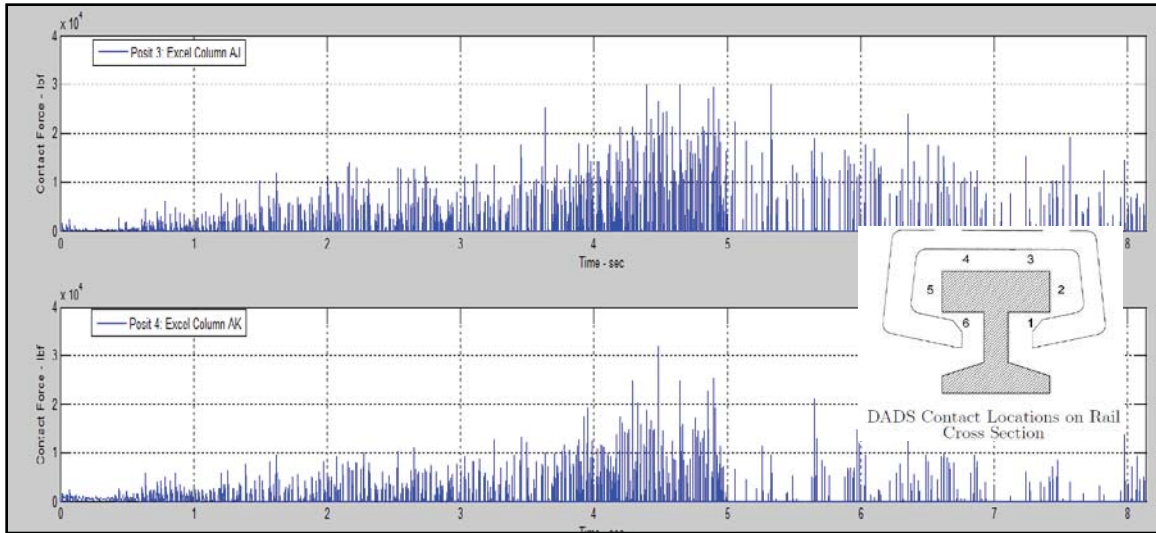
**Figure IV-19 Frontal View of the Slipper and Rail Cross Sections**

Figure IV-20 shows a picture of a cross-section of the rail inserted on a slipper. This picture illustrates how due to the gap between the rail and the slipper, it is physically possible for the slipper to roll as it travels along the rail.



**Figure IV-20 Slipper Roll**

This roll assumption is supported by the asynchronous loads reported by DADS for the pair of points 3 and 4, both located on the top surface of the slipper. Without any roll the loads on these points should be the same, however, these loads are typically different. The asynchronous loads are presented in Figure IV-21.



**Figure IV-21 Loads Applied to the Slipper at Points 3 and 4**

Figure IV-7 also supports this slipper roll hypothesis. In this figure one can observe that the left lip of the slipper ended wearing more than the right lip. Due to this roll motion the width of the slipper in contact with the rail varies. Although, at any given time, the slipper width in contact with the rail is unknown, is always a fraction of the theoretical maximum width, 90 mm. For this investigation the width of the worst case scenario, 90 mm, was used.

#### **4.11 Slipper Lateral Motion and Assumed Yaw**

Figure IV-22 plots the lateral displacement of the slipper with respect to its center of gravity as reported by DADS.

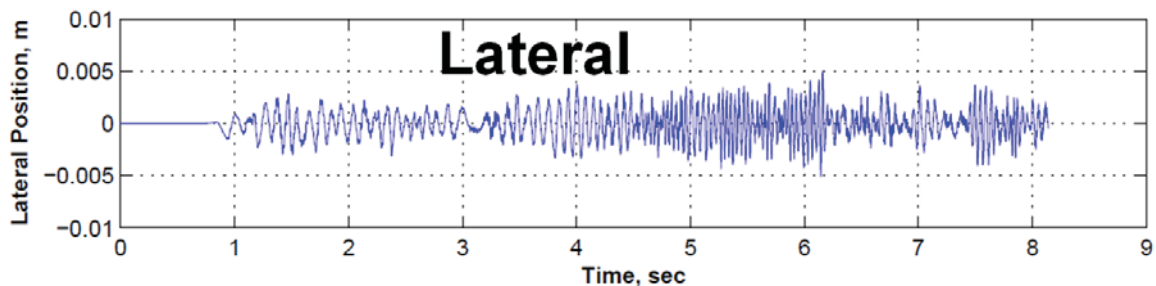


**Figure IV-22 Slipper Lateral Displacement**

The slippers' lateral displacement fact triggered the idea of the possibility that the same gap that allows this lateral motion can also allow it to slightly yaw as it travels.

This supposition is assumed to explain why the wear patterns observed in the SEM micrographs have different angles.

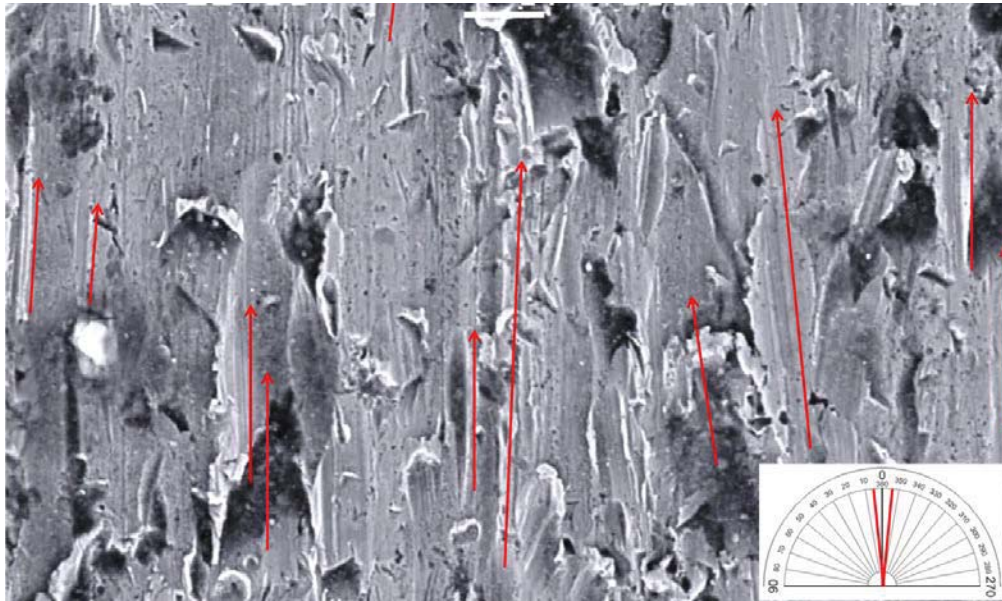


**Figure IV-23 Plastic Deformation Patterns Angles**

#### **4.12 Skin Temperature**

The instrumentation used to collect the data from the HHSTT mission didn't include any devices to measure the skin temperature of the slipper. To overcome this challenge and estimate the skin temperature, Le [65] carried out a thermal analysis to characterize the amount of heat flow going into the slipper as it slid and to predict the total melt wear of the slipper. Appendix D, section 1.6, summarizes Le [65] studies and presents the preliminary skin temperature profile as a function of the DADS percent of contact.

#### **4.13 Chapter Summary**

Chapter four explained why the HHSTT mission executed on January 2008 is a good example of a wear scenario carried out over a wide velocity profile on a system that is subject to intermittent contact and that varies its length and width in contact as it slides.

Appendix C, section 1.8.2 develops the formulation to calculate the total wear of scenarios with these characteristics. The formula to carry out these calculations is:

$$V_d = \sum_1^n W_{uA_n} \times l_{c_n} \times w_{c_n} \times D_{s_n} \times \%Cont_n \quad (IV-3)$$

where  $V_d$  is the total wear,  $W_{uA_n}$  is the normalized wear rate,  $l_{c_n}$  is the length in contact,  $w_{c_n}$  is the width in contact,  $D_{s_n}$  is the sliding distance in contact,  $\%Cont_n$  is the percent of distance in contact and the suffix  $n$  denotes the discrete velocity range number.

This chapter presented the methodology to estimate all the factors required to evaluate this equation. Explained why estimating each one of these factors was a challenge and highlighted some of the simulation limitations, such as:

- The dimensions of the recovered slipper were not measured prior to the mission.
- The inability to gather high-speed sliding wear data in a controlled environment, such a laboratory.
- The data available to compare the model results was gathered during a mission executed in the HHSTT to test a weapon system. This mission was conducted several years prior and the complexity of the system introduced many challenges.
- The test instrumentation was not tailored to gather some of the most relevant data. Including the actual area of contact and the thermal data from the slipper skin.

## V. Results

### 5.1 Simulated Wear Patterns

In the micrographs of the recovered slipper, as the one shown in Figure V-1, one can see plastic deformation patterns. These patterns are assumed, on this investigation, to be created due to the collision of asperities. Figure V-1 shows how the simulated asperity wear patterns resemble the morphology of the plastic deformations observed in the slipper micrographs. The simulated pattern presented in Figure V-1 was obtained from a simulation executed with the following initial conditions: 622 m/s and 866 °K.

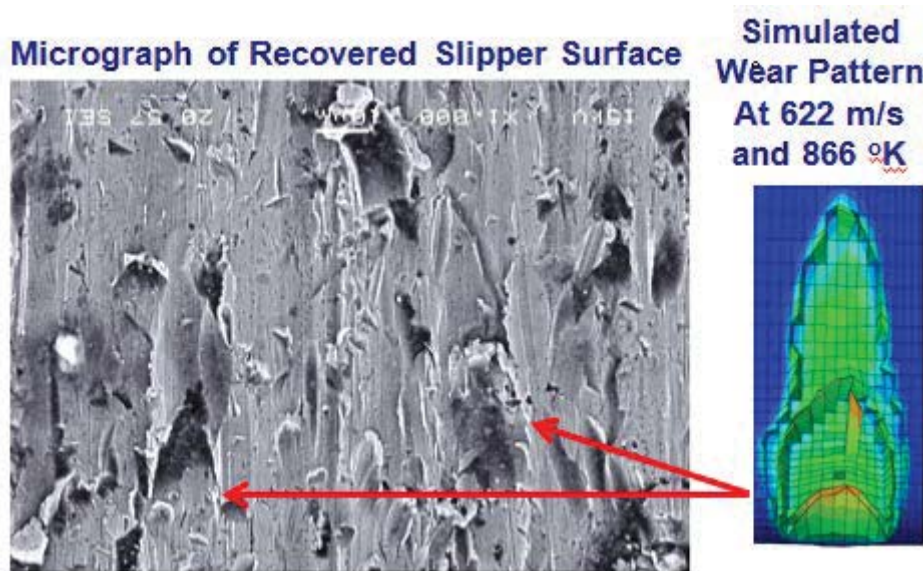


**Figure V-1 Simulated Wear Patterns Resemblance**

These observed collision patterns could be created at different times under different sliding conditions. Conditions such as different velocities, pitch, roll, and yaw. Considering this observation, one can hypothesize that the inclined plastic deformation patterns can be due to the slipper yaw motion. Figure V-2 shows two patterns of simulations carried out with the same initial conditions. On the simulation presented in the left side of Figure V-2 the slipper traveled straight forward. On the simulation presented on the right side of the Figure V-2 the slipper traveled with a yaw angle of

seven degrees. This yaw angle was exaggerated (is greater than the possible slipper yaw) to better depict the effects of yaw in the picture.



Figure V-2 Simulated Wear Patterns with and without Yaw

## 5.2 Model Results for Each Velocity Interval

Hale [38] studies concluded that the wear rates are independent of the worn history. Considering this investigation conclusion, the HHSTT velocity profile for the mission executed on January 2008 was partitioned into discrete velocity segments and the wear simulations were executed at the average velocity of each of these velocity segments. Figure V-3 depicts this partitioned velocity profile.

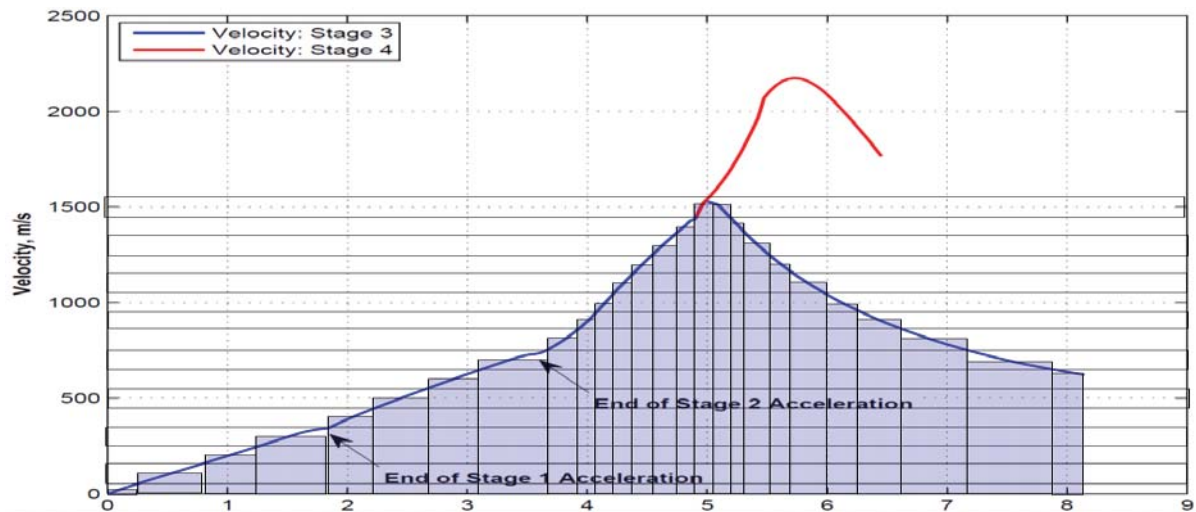


Figure V-3 Segments of the Velocity Profile

Table V-1 shows the velocity intervals and the average velocities employed for the wear simulations. This table also includes the duration of the velocity intervals, the end times, and the sliding distances. All these values are based on the DADS data.

<i>v</i> (m/s)	<i>Velocity Interval</i>	<i>Interval Time</i> (s)	<i>Interval End Time</i> (s)	<i>D<sub>s</sub></i> (mm)
25	0-50	0.25	0.25	6.E+03
100	50-150	0.5	0.75	5.E+04
200	150-250	0.5	1.3	1.E+05
300	250-350	0.6	1.9	2.E+05
400	350-450	0.4	2.3	2.E+05
500	450-550	0.5	2.8	3.E+05
600	550-650	0.5	3.3	3.E+05
700	650-750	0.6	3.9	4.E+05
800	750-850	0.2	4.1	2.E+05
900	850-950	0.12	4.22	1.E+05
1000	950-1050	0.12	4.34	1.E+05
1100	1050-1150	0.12	4.46	1.E+05
1200	1150-1250-	0.12	4.58	1.E+05
1300	1250-1350	0.12	4.7	2.E+05
1400	1350-1450	0.12	4.82	2.E+05
1500	1450-1530	0.18	5	3.E+05
1500	1450-1530	0.2	5.2	3.E+05
1400	1350-1450	0.2	5.4	3.E+05
1300	1250-1350	0.2	5.6	3.E+05
1200	1150-1250	0.2	5.8	2.E+05
1100	1050-1150	0.2	6	2.E+05
1000	950-1050	0.3	6.3	3.E+05
900	850-950	0.3	6.6	3.E+05
800	750-850	0.5	7.1	4.E+05
700	650-750	0.8	7.9	6.E+05
650	550-622	0.2	8.1	1.E+05

**Table V-1 Velocity Intervals Data**

The initial temperatures introduced for these simulations were obtained from Le [65] preliminary thermal analysis. This analysis is summarized in Appendix D, section 1.6.

Appendix A presents the simulation results for all these velocity segments. This appendix includes larger pictures of the simulated wear patterns, the values required to estimate the normalized wear rates, and the values to estimate the wear of each velocity segment

Figure V-4 presents a compilation of the pictures obtained from these simulations; it shows the simulated asperity wear patterns for each velocity interval. Note that the model includes five asperities ranging from 1-5  $\mu\text{m}$ . In Figure V-4, the patterns on the top of each picture are those due to the collision of the 5  $\mu\text{m}$  asperities. The ones next to them are those due to the collisions of the 4  $\mu\text{m}$  asperities, followed by the patterns of the 3  $\mu\text{m}$  asperities on some of the pictures. The asperities of sizes 2  $\mu\text{m}$  and 1  $\mu\text{m}$  didn't cause any observable damage. Recalling that the model includes a 1.5  $\mu\text{m}$  gap between the two assemblies in motion, this is reasonable, since the 1  $\mu\text{m}$  asperity doesn't even collide against the slipper due to this gap and the 2  $\mu\text{m}$  asperity barely does.

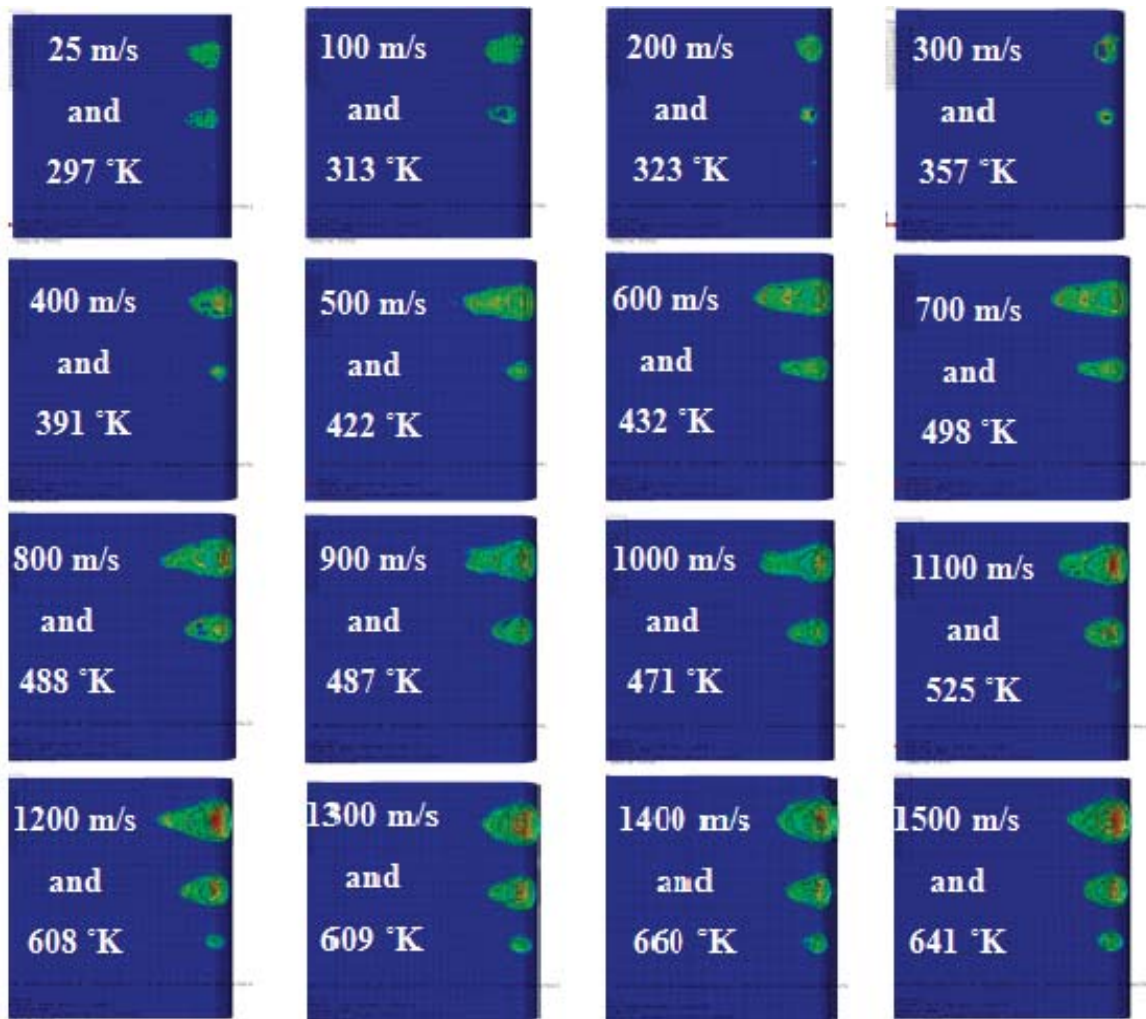


**Figure V-4 Simulated Wear Pattern Under Different Initial Conditions**

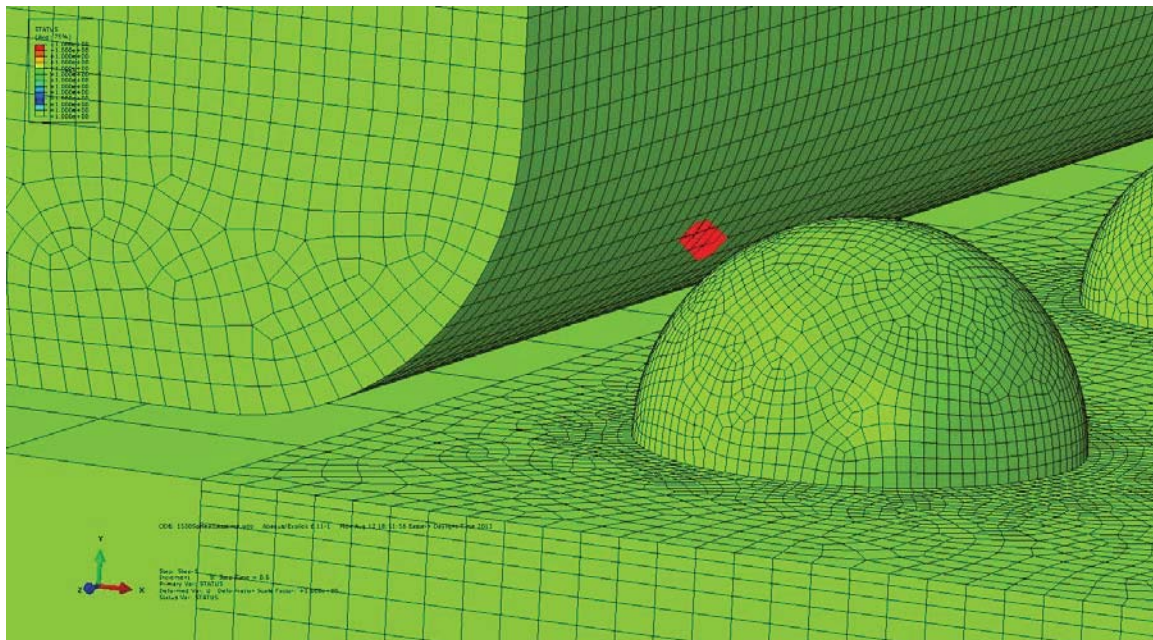
One can observe in Figure V-4 that the simulated wear patterns vary according to the initial velocity and skin temperature. Typically, the greater the initial velocity and/or the skin temperature the greater the simulated damage. Appendix A provides the normalized wear rates of each of these simulations. These observations make sense considering that the process was assumed to be adiabatic (defined in Appendix C, section 1.3.5.1) and that the materials are modeled using the JC plasticity and the JC fracture criteria. Both of these JC criteria (defined in Appendix C, sections 1.4.3 and 1.4.5) predict the materials to behave as a function of the strain rate, which is a function of the velocity, and the homologous temperature (defined in Appendix C, section 1.4.3).

The JC plasticity criterion predicts the flow stress to increase with higher strain rates and decrease with higher temperatures. In the wear simulations, as one increases the initial sliding velocity, the elements collide at higher strain rates and this tends to increase the Von Mises stress. On the other hand, under an adiabatic assumption the heat generated in the element by the plastic work results in a rise in temperature that decreases the Von Mises stress, or softens the material. Section 5.3 will discuss the strain rate and thermal contributions.

### 5.3 Strain Rate and Temperature Contributions

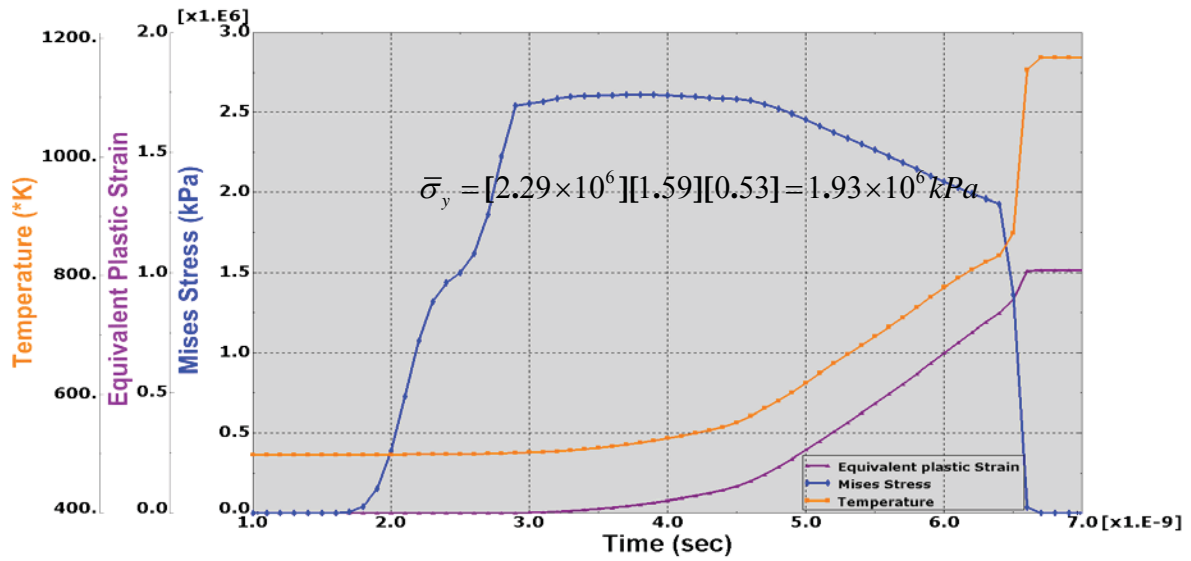
#### 5.3.1 Contributions to the Von Mises Stress

Figures V-6 and V-7 show the simulated Time Dependent Material Behavior (TDMB) of one of the slipper elements closest to the collision of a 5  $\mu\text{m}$  asperity. This element was chosen because is one of the first elements to fail during the simulations. Figure V-5 shows the location of this element, numbered by Abaqus as element 75845.



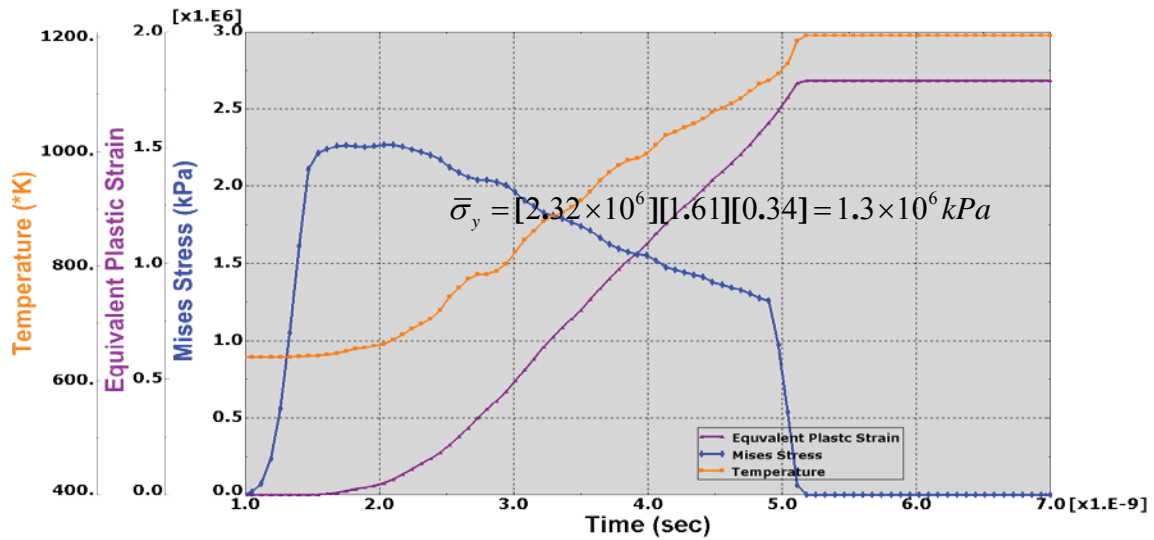
**Figure V-5 Location of Element for TDMB Plots**

Figure V-6 plots the time dependent material behavior of element number 75845. The initial conditions introduced for this simulation were 700 m/s and 498 °K



**Figure V-6 Simulated Material Behavior at 700 m/s and 498 °K**

Figure V-7 also plots the material behavior of element number 75845. However, the initial conditions introduced for this simulation are 1500 m/s and 641 °K.



**Figure V-7 Simulated Material Behavior at 1500 m/s and 641 °K**

Comparing these two plots, of the time dependent material behavior, one can see that the material behaves according to how it was programmed in Abaqus. In this model's case, the material was programmed to behave in accordance to the Johnson-Cook plasticity equation (presented in Appendix C, section 1.4.3) and therefore it varies

as a function of the equivalent plastic strain, equivalent plastic strain rate, and the temperature. Figure V-6 and Figure V-7 plot the Von Mises stress (in blue) and the three factors that influence it. The equivalent plastic strain is represented on these figures with the magenta curves. The equivalent plastic strain rate is the slope of these magenta curves. The orange curves represent the temperatures. The individual contributions of these factors would be discussed next.

Tables V-2 through V-4 report the Abaqus values for the points used to plot the previous two figures. These tables include the simulated values of the Von Mises stress, equivalent plastic strain, temperature, triaxiality, damage initiation criterion, and stiffness degradation. With these values, one can analytically calculate each of the brackets of the JC plasticity equation V-1 and the overall Von Mises stress. The results from these calculations are also included in these two tables.

$$\bar{\sigma}_y = [A + B(\bar{\epsilon}_p)^n][1 + CLn(\frac{\dot{\bar{\epsilon}}_p}{\dot{\bar{\epsilon}}_0})][1 - (\frac{T - T_0}{T_m - T_0})^m] \quad (V-1)$$

Note that the equivalent plastic strain rate, which represents the slope of the equivalent plastic strain versus time curve, was calculated by subtracting the equivalent plastic strain from the one of the previous time and dividing this difference by the time interval. The formula used was:

$$\dot{\bar{\epsilon}}_{p_i} = \frac{\bar{\epsilon}_{p_i} - \bar{\epsilon}_{p_{i-1}}}{t_i - t_{i-1}} \quad (V-2)$$

This approximation facilitated the calculations, but introduced a minor error. The calculated results therefore are slightly different from the ones reported by Abaqus. The Abaqus simulations use the values of the strain rates obtained at the mid-point between the two time intervals (explained in Appendix C, section 1.5.2).

The purpose of providing the calculations for each bracket of the JC plasticity equation is to demonstrate the stress contributions due to the strain rate and due to the temperature. The second bracket of the equation represents the strain rate contributions to the Von Mises stress. The third bracket represents the thermal contributions to it. The final column provides the product of these three brackets, in other words it provides the Von Mises stress according to the JC plasticity equation. Note that after the damage

imitation criterion is reached this column follows the damage evolution criterion presented in Appendix C, section 1.4.6. Under this criterion the Von Mises stress calculated with the JC equation has to be multiplied by one minus damage evolution criterion. Mathematically expressed as:

$$\sigma = \bar{\sigma}(1 - d_{EC}) \quad (V-3)$$

where  $\sigma$  is the flow stress,  $\bar{\sigma}$  is the JC flow stress due to an undamaged response, and  $d_{EC}$  is the damage evolution criterion variable. This variable represents the material's stiffness degradation. When  $d_{EC}=0$  the material has no stiffness degradation.

When  $d_{EC}=1$  the material stiffness is completely degraded and fracture is assumed to occur [31].

Simulation Values							Calculated Values										
at 700 m/s and 498 °K							JC Plasticity Equation					JC Dyn. Failure Equation					
Time (s)	Equiv. Plastic Strain	Temp (°K)	Stiffness Degrad.	Triax.	JC Mises Stress (kPa)	JC Damg Init. Crit.	Eq. Plastic Strain Rate (s <sup>-1</sup> )	1 <sup>st</sup> Bracket	2 <sup>nd</sup> Bracket	3 <sup>rd</sup> Bracket	Equation Results (kPa)	Eq. Plastic Strain Incrmt	1 <sup>st</sup> Bracket	2 <sup>nd</sup> Bracket	3 <sup>rd</sup> Bracket	Strain at failure	JC Damg Init. Crit.
0	0.000	498.0	0.00	0.00	0.00E+00	0.00											
1.00E-10	0.000	498.0	0.00	0.00	5.55E-01	0.00											
2.01E-10	0.000	498.0	0.00	0.00	9.60E-01	0.00											
3.02E-10	0.000	498.0	0.00	0.00	1.33E+00	0.00											
4.01E-10	0.000	498.0	0.00	0.00	1.89E+00	0.00											
5.01E-10	0.000	498.0	0.00	0.00	2.51E+00	0.00											
6.01E-10	0.000	498.0	0.00	0.00	3.09E+00	0.00											
7.01E-10	0.000	498.0	0.00	0.00	3.68E+00	0.00											
8.00E-10	0.000	498.0	0.00	0.00	4.15E+00	0.00											
9.01E-10	0.000	498.0	0.00	0.00	4.43E+00	0.00											
1.00E-09	0.000	498.0	0.00	0.00	4.73E+00	0.00											
1.10E-09	0.000	498.0	0.00	0.00	5.19E+00	0.00											
1.20E-09	0.000	498.0	0.00	0.00	5.79E+00	0.00											
1.30E-09	0.000	498.0	0.00	0.00	6.39E+00	0.00											
1.40E-09	0.000	498.0	0.00	0.00	6.87E+00	0.00											
1.50E-09	0.000	498.0	0.00	0.00	2.46E+01	0.00											
1.60E-09	0.000	498.0	0.00	-0.83	9.15E+02	0.00											
1.70E-09	0.000	498.0	0.00	-0.69	7.97E+03	0.00											
1.80E-09	0.000	498.0	0.00	-0.65	4.34E+04	0.00											
1.90E-09	0.000	498.0	0.00	-0.60	1.53E+05	0.00											
2.00E-09	0.000	498.1	0.00	-0.54	3.87E+05	0.00											
2.10E-09	0.000	498.3	0.00	-0.44	7.26E+05	0.00											
2.20E-09	0.000	498.6	0.00	-0.33	1.08E+06	0.00											
2.30E-09	0.000	498.8	0.00	-0.24	1.32E+06	0.00											
2.40E-09	0.000	498.9	0.00	-0.21	1.44E+06	0.00											
2.50E-09	0.000	499.0	0.00	-0.24	1.50E+06	0.00											
2.60E-09	0.000	499.2	0.00	-0.26	1.62E+06	0.00											
2.70E-09	0.000	499.5	0.00	-0.23	1.86E+06	0.00											
Plasticity Onset																	
2.80E-09	0.000	500.1	0.00	-0.21	2.12E+06	0.00	4.23E+03	2.17E+06	1.25	0.78	2.12E+06	0.000	0.21	1.12	1.58	0.37	0.00
2.90E-09	0.000	501.0	0.00	-0.23	2.54E+06	0.00	4.00E+06	2.18E+06	1.46	0.78	2.48E+06	0.000	0.21	1.21	1.58	0.41	0.00
3.00E-09	0.002	501.8	0.00	-0.27	2.55E+06	0.00	1.62E+07	2.18E+06	1.50	0.78	2.55E+06	0.002	0.22	1.23	1.58	0.42	0.00
3.10E-09	0.004	502.7	0.00	-0.25	2.57E+06	0.01	1.83E+07	2.19E+06	1.50	0.78	2.56E+06	0.002	0.22	1.23	1.58	0.42	0.01
3.20E-09	0.006	503.8	0.00	-0.23	2.59E+06	0.02	2.51E+07	2.19E+06	1.51	0.78	2.58E+06	0.003	0.21	1.24	1.59	0.42	0.02
3.30E-09	0.010	505.4	0.00	-0.24	2.60E+06	0.02	3.43E+07	2.19E+06	1.52	0.78	2.59E+06	0.003	0.21	1.24	1.59	0.42	0.02
3.40E-09	0.014	507.4	0.00	-0.28	2.60E+06	0.03	4.14E+07	2.20E+06	1.53	0.78	2.60E+06	0.004	0.22	1.25	1.60	0.44	0.03
3.50E-09	0.018	509.7	0.00	-0.35	2.60E+06	0.04	4.59E+07	2.20E+06	1.53	0.77	2.60E+06	0.005	0.23	1.25	1.60	0.46	0.04

Elastic Region

**Table V-2 Simulated and Calculated Values at 700 m/s and 498 °K**

Simulation Values							Calculated Values										
at 700 m/s and 498 °K							JC Plasticity Equation					JC Dyn. Failure Equation					
Time (s)	Equiv. Plastic Strain	Temp (°K)	Stffness Degrad.	Triax.	JC Mises Stress (kPa)	JC Damg Init. Crit.	Eq. Plastic Strain Rate (s <sup>-1</sup> )	1 <sup>st</sup> Bracket	2 <sup>nd</sup> Bracket	3 <sup>rd</sup> Bracket	Equation Results (kPa)	Eq. Plastic Strain Incrmnt	1 <sup>st</sup> Bracket	2 <sup>nd</sup> Bracket	3 <sup>rd</sup> Bracket	Strain at failure	JC Damg Init. Crit.
3.70E-09	0.029	515.1	0.00	-0.45	2.61E+06	0.07	5.85E+07	2.20E+06	1.54	0.77	2.61E+06	0.006	0.24	1.25	1.62	0.50	0.07
3.80E-09	0.036	518.3	0.00	-0.47	2.61E+06	0.08	6.84E+07	2.21E+06	1.54	0.77	2.61E+06	0.007	0.25	1.25	1.63	0.51	0.08
3.90E-09	0.044	521.8	0.00	-0.49	2.61E+06	0.09	7.67E+07	2.21E+06	1.54	0.76	2.61E+06	0.008	0.25	1.25	1.64	0.52	0.09
4.00E-09	0.052	525.7	0.00	-0.51	2.61E+06	0.11	8.39E+07	2.21E+06	1.55	0.76	2.60E+06	0.008	0.25	1.26	1.65	0.53	0.11
4.10E-09	0.062	530.1	0.00	-0.53	2.60E+06	0.13	9.24E+07	2.21E+06	1.55	0.76	2.60E+06	0.009	0.26	1.26	1.66	0.54	0.13
4.20E-09	0.072	534.7	0.00	-0.55	2.60E+06	0.15	1.02E+08	2.22E+06	1.55	0.75	2.59E+06	0.010	0.26	1.26	1.67	0.55	0.15
4.30E-09	0.083	539.7	0.00	-0.54	2.59E+06	0.17	1.11E+08	2.22E+06	1.56	0.75	2.59E+06	0.011	0.26	1.26	1.69	0.55	0.17
4.40E-09	0.095	545.2	0.00	-0.54	2.59E+06	0.19	1.24E+08	2.22E+06	1.56	0.75	2.58E+06	0.012	0.26	1.26	1.70	0.56	0.19
4.50E-09	0.111	552.8	0.00	-0.61	2.58E+06	0.22	1.59E+08	2.23E+06	1.57	0.74	2.58E+06	0.016	0.27	1.26	1.72	0.59	0.21
4.60E-09	0.133	563.3	0.00	-0.76	2.57E+06	0.25	2.20E+08	2.23E+06	1.58	0.73	2.57E+06	0.022	0.30	1.27	1.75	0.66	0.25
4.70E-09	0.161	576.2	0.00	-0.84	2.55E+06	0.29	2.78E+08	2.23E+06	1.58	0.72	2.55E+06	0.028	0.31	1.27	1.79	0.71	0.29
4.80E-09	0.192	589.2	0.00	-0.78	2.52E+06	0.34	3.14E+08	2.24E+06	1.59	0.71	2.52E+06	0.031	0.30	1.27	1.82	0.70	0.33
4.90E-09	0.226	603.5	0.00	-0.72	2.49E+06	0.38	3.38E+08	2.24E+06	1.59	0.70	2.49E+06	0.034	0.29	1.27	1.86	0.69	0.38
5.00E-09	0.262	619.5	0.00	-0.80	2.45E+06	0.44	3.61E+08	2.25E+06	1.59	0.69	2.45E+06	0.036	0.31	1.28	1.91	0.74	0.43
5.10E-09	0.300	635.8	0.00	-0.93	2.42E+06	0.48	3.76E+08	2.25E+06	1.59	0.67	2.41E+06	0.037	0.33	1.28	1.95	0.83	0.47
5.20E-09	0.338	651.8	0.00	-0.98	2.38E+06	0.53	3.83E+08	2.25E+06	1.59	0.66	2.38E+06	0.038	0.34	1.28	2.00	0.87	0.52
5.30E-09	0.377	667.1	0.00	-0.93	2.34E+06	0.57	3.89E+08	2.26E+06	1.59	0.65	2.34E+06	0.039	0.33	1.28	2.04	0.86	0.56
5.40E-09	0.416	682.5	0.00	-0.86	2.30E+06	0.62	3.93E+08	2.26E+06	1.59	0.64	2.30E+06	0.040	0.32	1.28	2.08	0.84	0.61
5.50E-09	0.456	697.8	0.00	-0.83	2.26E+06	0.67	3.98E+08	2.26E+06	1.59	0.63	2.26E+06	0.039	0.31	1.28	2.13	0.85	0.66
5.60E-09	0.496	713.4	0.00	-0.82	2.23E+06	0.71	4.00E+08	2.27E+06	1.59	0.62	2.23E+06	0.040	0.31	1.28	2.17	0.86	0.70
5.70E-09	0.536	729.2	0.00	-0.88	2.19E+06	0.76	4.06E+08	2.27E+06	1.59	0.60	2.19E+06	0.040	0.32	1.28	2.21	0.91	0.75
5.80E-09	0.579	746.3	0.00	-1.10	2.15E+06	0.80	4.21E+08	2.27E+06	1.60	0.59	2.15E+06	0.042	0.37	1.28	2.26	1.06	0.79
5.90E-09	0.622	764.1	0.00	-1.38	2.11E+06	0.84	4.35E+08	2.27E+06	1.60	0.58	2.10E+06	0.044	0.43	1.28	2.31	1.28	0.82
6.00E-09	0.665	780.2	0.00	-1.49	2.07E+06	0.87	4.32E+08	2.28E+06	1.60	0.57	2.07E+06	0.043	0.46	1.28	2.35	1.39	0.85
6.10E-09	0.709	795.7	0.00	-1.55	2.03E+06	0.90	4.37E+08	2.28E+06	1.60	0.56	2.03E+06	0.044	0.48	1.28	2.40	1.46	0.88
6.20E-09	0.752	810.2	0.00	-1.53	1.99E+06	0.93	4.32E+08	2.28E+06	1.60	0.55	1.99E+06	0.043	0.47	1.28	2.44	1.48	0.91
6.30E-09	0.794	823.0	0.00	-1.39	1.96E+06	0.96	4.15E+08	2.28E+06	1.60	0.54	1.96E+06	0.042	0.44	1.28	2.47	1.38	0.94
6.40E-09	0.833	834.3	0.00	-1.14	1.93E+06	0.99	3.90E+08	2.29E+06	1.59	0.53	1.93E+06	0.039	0.38	1.28	2.50	1.21	0.97
Damage Evolution																	
6.50E-09	0.889	872.0	0.27	-2.90	1.36E+06	1.00	5.66E+08	2.29E+06	1.60	0.50	1.3E+06						
6.60E-09	1.007	1146.2	0.97	-18.58	3.76E+04	1.00	1.17E+09	2.29E+06	1.63	0.32	3.7E+04						
6.70E-09	1.011	1167.3	1.00	0.00	0.00E+00	1.00	3.83E+07	2.29E+06	1.52	0.31	0.0E+00						

**Table V-3 Simulated and Calculated Values at 700 m/s and 498 °K (cont.)**

Simulation Values							Calculated Values										
at 1500 m/s and 498 °K							JC Plasticity Equation					JC Dyn. Failure Equation					
Time (s)	Equiv. Plastic Strain	Temp (°K)	Stiff. Degrad.	Triax.	JC Mises Stress (kPa)	JC Damg Init. Crit.	Eq. Plastic Strain Rate (s <sup>-1</sup> )	1 <sup>st</sup> Bracket	2 <sup>nd</sup> Bracket	3 <sup>rd</sup> Bracket	Equation Results (kPa)	Eq. Plastic Strain Incrmnt	1 <sup>st</sup> Bracket	2 <sup>nd</sup> Bracket	3 <sup>rd</sup> Bracket	Strain at failure	JC Damg Init. Crit.
<b>Elasticity Onset</b>																	
0	0.000	641.0	0.00	0.00	0.0E+00	0.00											
7.12E-11	0.000	641.0	0.00	0.00	8.1E-01	0.00											
1.41E-10	0.000	641.0	0.00	0.00	1.5E+00	0.00											
2.11E-10	0.000	641.0	0.00	0.00	2.1E+00	0.00											
2.80E-10	0.000	641.0	0.00	0.00	2.7E+00	0.00											
3.50E-10	0.000	641.0	0.00	0.00	3.2E+00	0.00											
4.20E-10	0.000	641.0	0.00	0.00	3.9E+00	0.00											
4.91E-10	0.000	641.0	0.00	0.00	4.6E+00	0.00											
5.61E-10	0.000	641.0	0.00	0.00	5.5E+00	0.00											
6.31E-10	0.000	641.0	0.00	0.00	6.3E+00	0.00											
7.01E-10	0.000	641.0	0.00	0.00	7.1E+00	0.00											
7.71E-10	0.000	641.0	0.00	0.00	7.8E+00	0.00											
8.41E-10	0.000	641.0	0.00	0.00	1.9E+01	0.00											
9.10E-10	0.000	641.0	0.00	-0.74	4.3E+02	0.00											
9.80E-10	0.000	641.0	0.00	-0.72	3.6E+03	0.00											
1.05E-09	0.000	641.0	0.00	-0.62	2.0E+04	0.00											
1.12E-09	0.000	641.0	0.00	-0.58	7.9E+04	0.00											
1.19E-09	0.000	641.0	0.00	-0.56	2.4E+05	0.00											
1.26E-09	0.000	641.0	0.00	-0.54	5.6E+05	0.00											
1.33E-09	0.000	641.0	0.00	-0.51	1.1E+06	0.00											
1.40E-09	0.000	641.6	0.00	-0.47	1.6E+06	0.00											
<b>Plasticity Onset</b>																	
1.47E-09	0.000	643.3	0.00	-0.40	2.1E+06	0.00	4.18E+05	2.17E+06	1.39	0.67	2.0E+06	0.000	0.24	1.18	1.97	0.55	0.00
1.54E-09	0.002	644.1	0.00	-0.37	2.2E+06	0.00	2.39E+07	2.18E+06	1.51	0.67	2.2E+06	0.002	0.23	1.24	1.98	0.57	0.00
1.61E-09	0.005	645.3	0.00	-0.39	2.2E+06	0.01	4.32E+07	2.19E+06	1.53	0.67	2.2E+06	0.003	0.24	1.25	1.98	0.58	0.01
1.68E-09	0.010	647.9	0.00	-0.52	2.3E+06	0.02	7.50E+07	2.19E+06	1.54	0.66	2.3E+06	0.005	0.26	1.25	1.99	0.64	0.02
1.75E-09	0.017	651.6	0.00	-0.71	2.3E+06	0.03	1.06E+08	2.20E+06	1.55	0.66	2.3E+06	0.007	0.29	1.26	2.00	0.73	0.03
1.82E-09	0.026	655.4	0.00	-0.83	2.3E+06	0.04	1.17E+08	2.20E+06	1.56	0.66	2.3E+06	0.008	0.31	1.26	2.01	0.79	0.04
1.89E-09	0.033	658.1	0.00	-0.77	2.3E+06	0.05	1.10E+08	2.21E+06	1.56	0.66	2.3E+06	0.008	0.30	1.26	2.02	0.77	0.05
1.96E-09	0.042	660.6	0.00	-0.61	2.3E+06	0.06	1.19E+08	2.21E+06	1.56	0.66	2.3E+06	0.008	0.27	1.26	2.02	0.69	0.06
2.03E-09	0.053	664.8	0.00	-0.52	2.3E+06	0.08	1.64E+08	2.21E+06	1.57	0.65	2.3E+06	0.012	0.26	1.26	2.03	0.66	0.08
2.10E-09	0.070	671.7	0.00	-0.62	2.3E+06	0.10	2.34E+08	2.22E+06	1.58	0.65	2.3E+06	0.016	0.27	1.27	2.05	0.71	0.10
2.17E-09	0.090	681.0	0.00	-0.86	2.3E+06	0.13	2.94E+08	2.22E+06	1.58	0.64	2.3E+06	0.021	0.32	1.27	2.08	0.84	0.12
2.24E-09	0.112	690.5	0.00	-1.05	2.2E+06	0.15	3.19E+08	2.23E+06	1.59	0.63	2.2E+06	0.022	0.36	1.27	2.11	0.96	0.15
2.31E-09	0.135	699.0	0.00	-1.04	2.2E+06	0.18	3.22E+08	2.23E+06	1.59	0.63	2.2E+06	0.023	0.35	1.27	2.13	0.96	0.17
2.38E-09	0.158	707.9	0.00	-1.05	2.2E+06	0.20	3.35E+08	2.23E+06	1.59	0.62	2.2E+06	0.024	0.36	1.27	2.15	0.98	0.19

Elastic Region

**Table V-4 Simulated and Calculated Values at 1500 m/s and 641 °K**

Simulation Values							Calculated Values										
at 1500 m/s and 498 °K							JC Plasticity Equation					JC Dyn. Failure Equation					
Time (s)	Equiv. Plastic Strain	Temp (°K)	Stiff. Degrad.	Triax.	JC Mises Stress (kPa)	JC Damg Init. Crit.	Eq. Plastic Strain Rate (s <sup>-1</sup> )	1 <sup>st</sup> Bracket	2 <sup>nd</sup> Bracket	3 <sup>rd</sup> Bracket	Equation Results (kPa)	Eq. Plastic Strain Incrmt	1 <sup>st</sup> Bracket	2 <sup>nd</sup> Bracket	3 <sup>rd</sup> Bracket	Strain at failure	JC Damg Init. Crit.
2.52E-09	0.216	746.2	0.00	-2.76	2.1E+06	0.24	4.49E+08	2.24E+06	1.60	0.59	2.1E+06	0.031	0.92	1.28	2.26	2.67	0.22
2.59E-09	0.252	762.6	0.00	-3.12	2.1E+06	0.25	5.00E+08	2.24E+06	1.60	0.58	2.1E+06	0.035	1.12	1.28	2.31	3.30	0.23
2.66E-09	0.291	778.2	0.00	-3.33	2.1E+06	0.26	5.70E+08	2.25E+06	1.60	0.57	2.1E+06	0.040	1.24	1.28	2.35	3.75	0.25
2.73E-09	0.333	785.5	0.00	-2.92	2.0E+06	0.27	5.83E+08	2.25E+06	1.61	0.56	2.0E+06	0.041	1.01	1.28	2.37	3.07	0.26
2.80E-09	0.371	786.5	0.00	-1.93	2.0E+06	0.29	5.48E+08	2.26E+06	1.60	0.56	2.0E+06	0.038	0.59	1.28	2.37	1.80	0.28
2.87E-09	0.407	792.0	0.00	-1.00	2.0E+06	0.32	5.30E+08	2.26E+06	1.60	0.56	2.0E+06	0.037	0.35	1.28	2.39	1.06	0.31
2.94E-09	0.446	803.8	0.00	-0.59	2.0E+06	0.36	5.45E+08	2.26E+06	1.60	0.55	2.0E+06	0.039	0.27	1.28	2.42	0.83	0.36
3.01E-09	0.493	825.0	0.00	-1.49	2.0E+06	0.41	6.75E+08	2.27E+06	1.61	0.54	2.0E+06	0.047	0.46	1.28	2.48	1.47	0.39
3.08E-09	0.541	846.2	0.00	-2.19	1.9E+06	0.43	6.82E+08	2.27E+06	1.61	0.52	1.9E+06	0.048	0.68	1.28	2.54	2.23	0.41
3.15E-09	0.588	861.9	0.00	-2.33	1.9E+06	0.45	6.76E+08	2.27E+06	1.61	0.51	1.9E+06	0.047	0.73	1.28	2.58	2.44	0.43
3.22E-09	0.640	879.3	0.00	-2.55	1.8E+06	0.47	7.32E+08	2.28E+06	1.61	0.50	1.8E+06	0.051	0.83	1.29	2.63	2.80	0.45
3.29E-09	0.682	886.8	0.00	-1.99	1.8E+06	0.49	6.08E+08	2.28E+06	1.61	0.49	1.8E+06	0.043	0.61	1.28	2.65	2.08	0.47
3.36E-09	0.724	893.7	0.00	-1.13	1.8E+06	0.51	5.91E+08	2.28E+06	1.61	0.49	1.8E+06	0.041	0.37	1.28	2.67	1.28	0.51
3.43E-09	0.761	902.8	0.00	-0.41	1.8E+06	0.55	5.36E+08	2.28E+06	1.60	0.48	1.8E+06	0.037	0.24	1.28	2.70	0.83	0.55
3.50E-09	0.800	914.8	0.00	-0.19	1.7E+06	0.60	5.54E+08	2.28E+06	1.60	0.48	1.7E+06	0.039	0.21	1.28	2.73	0.72	0.60
3.57E-09	0.845	930.7	0.00	-0.92	1.7E+06	0.66	6.55E+08	2.29E+06	1.61	0.46	1.7E+06	0.046	0.33	1.28	2.77	1.17	0.64
3.64E-09	0.891	948.9	0.00	-1.84	1.7E+06	0.68	6.48E+08	2.29E+06	1.61	0.45	1.7E+06	0.046	0.56	1.28	2.82	2.04	0.67
3.71E-09	0.934	965.2	0.00	-2.47	1.6E+06	0.70	6.16E+08	2.29E+06	1.61	0.44	1.6E+06	0.043	0.79	1.28	2.87	2.92	0.68
3.78E-09	0.974	976.9	0.00	-2.60	1.6E+06	0.72	5.75E+08	2.29E+06	1.61	0.43	1.6E+06	0.040	0.85	1.28	2.90	3.16	0.69
3.85E-09	1.012	985.0	0.00	-2.39	1.6E+06	0.73	5.45E+08	2.29E+06	1.60	0.43	1.6E+06	0.038	0.76	1.28	2.92	2.85	0.71
3.92E-09	1.046	988.6	0.00	-1.56	1.6E+06	0.74	4.83E+08	2.30E+06	1.60	0.43	1.6E+06	0.034	0.48	1.28	2.93	1.80	0.73
3.99E-09	1.083	996.6	0.00	-1.11	1.6E+06	0.77	5.25E+08	2.30E+06	1.60	0.42	1.5E+06	0.037	0.37	1.28	2.96	1.40	0.75
4.06E-09	1.128	1012.7	0.00	-1.95	1.5E+06	0.79	6.45E+08	2.30E+06	1.61	0.41	1.5E+06	0.045	0.60	1.28	3.00	2.30	0.77
4.13E-09	1.172	1029.0	0.00	-2.74	1.5E+06	0.81	6.24E+08	2.30E+06	1.61	0.40	1.5E+06	0.044	0.92	1.28	3.05	3.59	0.78
4.20E-09	1.208	1034.7	0.00	-2.33	1.5E+06	0.82	5.17E+08	2.30E+06	1.60	0.40	1.5E+06	0.036	0.74	1.28	3.06	2.88	0.80
4.27E-09	1.247	1042.8	0.00	-2.11	1.4E+06	0.83	5.52E+08	2.30E+06	1.60	0.39	1.4E+06	0.038	0.65	1.28	3.08	2.59	0.81
4.34E-09	1.281	1048.7	0.00	-1.63	1.4E+06	0.85	5.02E+08	2.31E+06	1.60	0.39	1.4E+06	0.035	0.50	1.28	3.10	1.98	0.83
4.41E-09	1.319	1057.3	0.00	-1.45	1.4E+06	0.87	5.31E+08	2.31E+06	1.60	0.38	1.4E+06	0.038	0.45	1.28	3.12	1.81	0.85
4.48E-09	1.360	1069.7	0.00	-2.01	1.4E+06	0.89	5.88E+08	2.31E+06	1.61	0.37	1.4E+06	0.041	0.62	1.28	3.16	2.50	0.87
4.55E-09	1.396	1076.7	0.00	-1.71	1.4E+06	0.90	5.10E+08	2.31E+06	1.60	0.37	1.4E+06	0.036	0.52	1.28	3.18	2.13	0.88
4.62E-09	1.432	1084.6	0.00	-1.54	1.3E+06	0.92	5.24E+08	2.31E+06	1.60	0.36	1.3E+06	0.037	0.47	1.28	3.20	1.95	0.90
4.69E-09	1.470	1093.3	0.00	-1.50	1.3E+06	0.94	5.47E+08	2.31E+06	1.60	0.36	1.3E+06	0.038	0.46	1.28	3.23	1.92	0.92
4.76E-09	1.514	1105.5	0.00	-2.02	1.3E+06	0.96	6.19E+08	2.31E+06	1.61	0.35	1.3E+06	0.043	0.62	1.28	3.26	2.61	0.94
4.83E-09	1.561	1118.9	0.00	-2.61	1.3E+06	0.98	6.76E+08	2.32E+06	1.61	0.34	1.3E+06	0.047	0.85	1.28	3.30	3.61	0.95
4.90E-09	1.606	1124.9	0.00	-1.88	1.3E+06	0.99	6.37E+08	2.32E+06	1.61	0.34	1.3E+06	0.045	0.57	1.28	3.31	2.45	0.97
Damage Evolution																	
4.97E-09	1.659	1136.9	0.21	-2.01	9.8E+05	1.00	7.63E+08	2.32E+06	1.61	0.33	9.8E+05						
5.04E-09	1.715	1154.3	0.55	-3.05	5.4E+05	1.00	7.96E+08	2.32E+06	1.61	0.32	5.3E+05						
5.11E-09	1.779	1193.6	0.94	-6.55	6.8E+04	1.00	9.08E+08	2.32E+06	1.62	0.29	6.7E+04						
5.18E-09	1.789	1203.4	1.00	0.00	0.0E+00	1.00	1.43E+08	2.32E+06	1.56	0.29	0.0E+00						

**Table V-5 Simulated and Calculated Values at 1500 m/s and 641 °K (cont.)**

Table V-2 and Table V-3 present the results of the simulation carried at 700 m/s and 498 °K. In Table V-2 one can observe that at the onset of plasticity (at t=2.8 nano-seconds) the material reaches the material's yield stress, 2.1 GPa. Afterwards, the material behaves plastically and the Von Mises stress decreases according to the JC plasticity equation until reaching the damage initiation criterion, at t=6.4 nano-seconds. Note on Table V-3 that at the damage initiation point, the maximum contributions of the strain rate and temperature occur. The calculations for the damage initiation point, using the values from the row of Table V-3, colored green, are presented next as an example:

$$\begin{aligned}\bar{\sigma}_y &= [A + B(\bar{\epsilon}_p)^n][1 + CLn(\frac{\dot{\bar{\epsilon}}_p}{\dot{\bar{\epsilon}}_0})][1 - (\frac{T - T_0}{T_m - T_0})^m] \\ \bar{\sigma}_y &= [2.17 \times 10^6 + 0.12 \times 10^6 (0.833)^{0.37}][1 + 0.03Ln(\frac{3.9 \times 10^8}{1})] \\ &\quad [1 - (\frac{834.3 - 293}{1685 - 293})^{0.8}] \\ \bar{\sigma}_y &= [2.29 \times 10^6][1.59][0.53] = 1.93 \times 10^6 \text{ kPa}\end{aligned}\tag{V-4}$$

where  $A$ ,  $B$ ,  $C$ ,  $m$ , and  $n$  are the JC material parameters obtained from the experiments presented in Appendix D, section Appendix B for the VascoMax 300 steel.  $T_0$  and  $T_m$  are the reference and melting temperature of the material.

From these calculations, one can conclude that at the damage initiation point the strain rate contribution, obtained from the second bracket calculations, is a Von Mises stress increase of 59%. The maximum thermal contribution, obtained from the third bracket calculations, is a Von Mises stress decrease of 53%. Multiplying the values of these two brackets one gets:  $1.59 \times 0.53 = 0.8427$ . This means that these two factors combined reduced the stress 84.3%, so the thermal contributions outweighed the strain rate one.

Table V-4 and Table V-5 show the values for the simulation carried at 1500 m/s and 641 °K. Repeating the above calculations, for the stress at the damage initiation point, with the values from the row of Table V-5, colored green, one gets:

$$\begin{aligned}
\bar{\sigma}_y &= [A + B(\bar{\epsilon}_p)^n][1 + CLn(\frac{\dot{\bar{\epsilon}}_p}{\dot{\bar{\epsilon}}_0})][1 - (\frac{T - T_0}{T_m - T_0})^m] \\
\bar{\sigma}_y &= [2.17 \times 10^6 + 0.12 \times 10^6 (1.606)^{0.37}][1 + 0.03Ln(\frac{6.37 \times 10^8}{1})] \\
&\quad [1 - (\frac{1124.9 - 293}{1685 - 293})^{0.8}] \\
\bar{\sigma}_y &= [2.32 \times 10^6][1.61][0.34] = 1.3 \times 10^6 \text{ kPa}
\end{aligned} \tag{V-5}$$

Hence, for the simulations at 1500 m/s and 641 °K, the maximum strain rate contribution is a Von Mises stress increase of 61%, while the maximum thermal contribution is a Von Mises stress decrease of 34%. Multiplying the values of these two brackets, as before, one gets: 1.61x0.34=0.5474. This means that these two factors combined reduced the Von Mises stress 54.7%, so the thermal contributions again outweighed the strain rate one.

If one compares the results at the damage initiation point for these simulations, one can conclude that the greater the speed the greater the strain rate contribution. However, higher speeds typically correlate with higher skin temperatures, mainly responsible for softening the material. One can also conclude that the thermal contributions typically outweigh the strain rate ones at the damage initiation point.

### 5.3.2 Contributions to the JC Failure Strain

Tables V-2 through V-4 include the simulated values of temperature, triaxiality, damage initiation criterion, and stiffness degradation. With these values, one can analytically calculate each of the brackets of the JC Dynamic failure equation, the strain at failure, and the evolution of the damage initiation criterion. The results from these calculations are also included in these tables. The equation used to compute the strain at failure (presented in Appendix C, section 1.4.5) is:

$$\bar{\epsilon}_f = [d_1 + d_2 \exp(d_3 \frac{p}{q})][1 + d_4 Ln(\frac{\dot{\bar{\epsilon}}_p}{\dot{\bar{\epsilon}}_0})][1 + d_5 (\frac{T - T_0}{T_m - T_0})] \tag{V-6}$$

where  $\dot{\epsilon}_p$  is the plastic strain rate,  $\dot{\epsilon}_0$  is the reference strain rate,  $T$  is the current temperature,  $T_m$  is the melting temperature,  $T_0$  is the transition temperature,  $p$  is the pressure stress,  $q$  is the Von Mises stress, and  $d_1$  through  $d_5$  are the models' fracture constants [31].

Figure V-8 and Figure V-9 show the simulation plots of the Von Mises stress (colored blue), the triaxiality (colored green), and the damage initiation criterion (colored in red) for both of the simulations. Figure V-8 shows the results of the simulations carried at 700 m/s and 498 °K. Figure V-9 shows the results for the simulations carried at 1500 m/s and 641 °K.

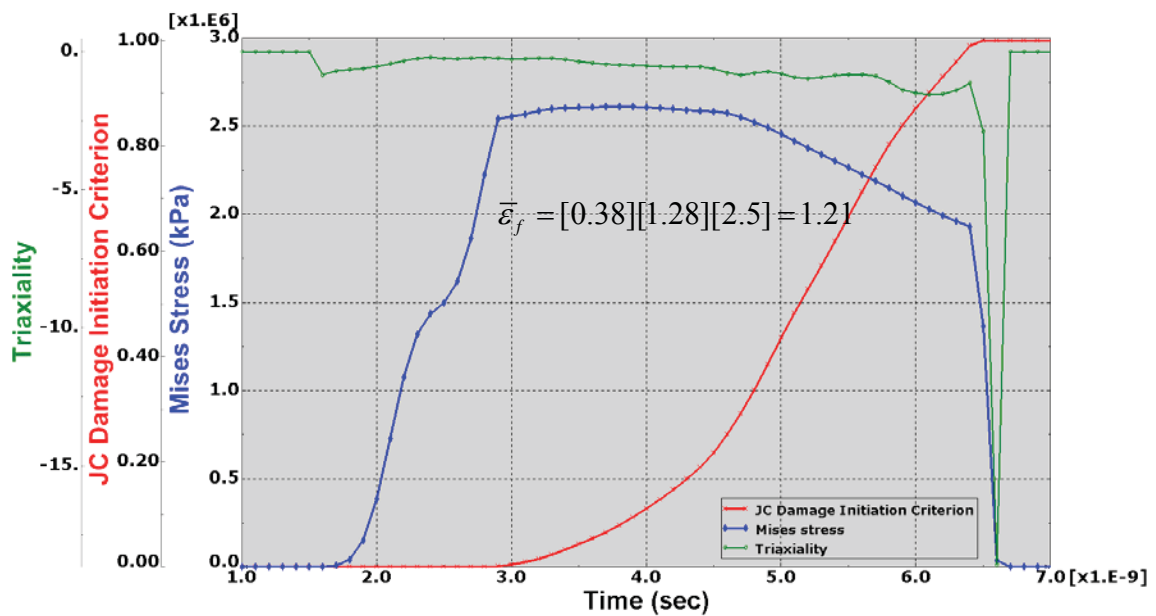


**Figure V-8 Simulated Failure Behavior at 700 m/s and 498 °K**

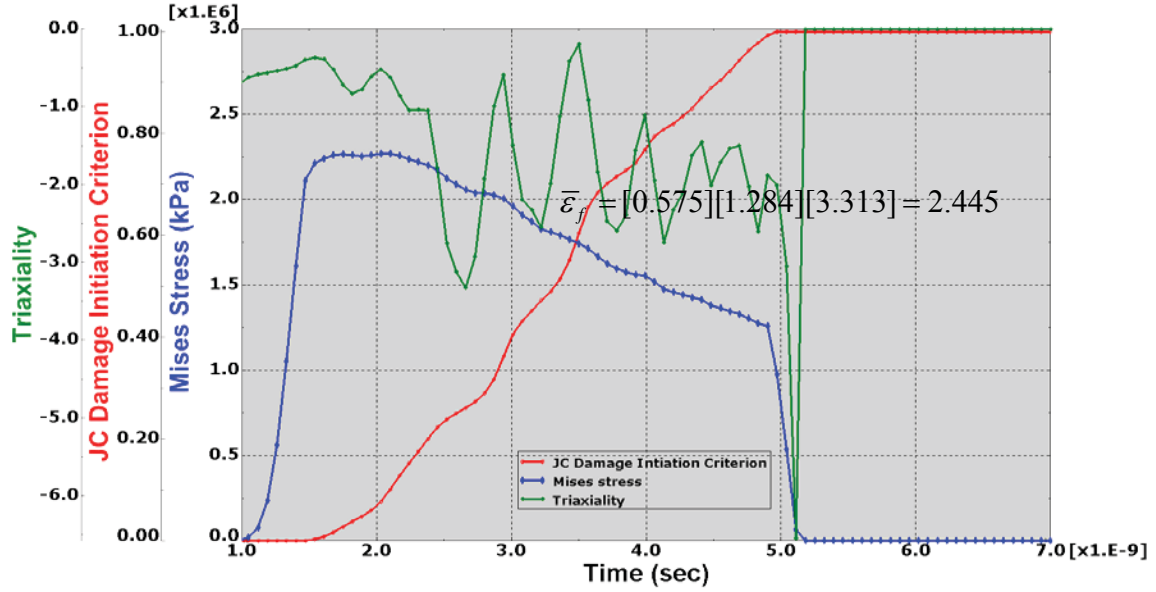


**Figure V-9 Simulated Failure Behavior at 1500 m/s and 641 °K**

Note in Table V-3 the contributions to the failure strain, due to the strain rate and temperature, at the damage initiation point (row colored in green). The calculations at the damage initiation point, using the values from this row in Table V-3, colored green, are presented next, as an example:

$$\bar{\epsilon}_f = [d_1 + d_2 \exp(d_3 \frac{p}{q})][1 + d_4 \ln(\frac{\dot{\epsilon}_p}{\dot{\epsilon}_0})][1 + d_5 (\frac{T - T_0}{T_m - T_0})]$$

$$\bar{\epsilon}_f = [-0.09 + 0.27 \exp(0.48 \times 1.14)][1 + 0.014 \ln(\frac{3.9 \times 10^8}{1})]$$

$$[1 + 3.87(\frac{838.4 - 293}{1685 - 293})]$$

$$\bar{\epsilon}_f = [0.38][1.28][2.5] = 1.21 \quad (V-7)$$

From these calculations, one can conclude that, at the damage initiation point, the strain rate contribution, obtained from the second bracket calculations, is an increase of the predicted failure strain of 28%. The maximum thermal contribution, obtained from the third bracket calculations, is an increase of the predicted failure strain of 250%. These two factors combined increased the predictions of the strain rate  $1.28 \times 2.5 = 320\%$ .

Similarly, using the values from the row in Table V-5, colored green, one can obtain the contributions to the failure strain for the simulation carried out at 1500 m/s and 641 °K.

$$\begin{aligned}
\bar{\varepsilon}_f &= [d_1 + d_2 \exp(d_3 \frac{P}{q})][1 + d_4 \text{Ln}(\frac{\dot{\varepsilon}_p}{\dot{\varepsilon}_0})][1 + d_5 (\frac{T - T_0}{T_m - T_0})] \\
\bar{\varepsilon}_f &= [-0.09 + 0.27 \exp(0.48 \times 1.88)][1 + 0.014 \text{Ln}(\frac{6.37 \times 10^8}{1})] \\
&\quad [1 + 3.87(\frac{1124.9 - 293}{1685 - 293})] \\
\bar{\varepsilon}_f &= [0.575][1.28][3.31] = 2.45
\end{aligned} \tag{V-8}$$

From these calculations, one can confirm that at the damage initiation point the strain rate contribution is an increase of the predicted failure strain of 28%. Note that this 1.28 contribution didn't vary significantly from the one obtained from the simulations at 700 m/s.

The maximum thermal contribution is an increase of the predicted failure strain. The value of the thermal factor for this simulation is 3.31. These two factors, strain rate and thermal, combined increased the predictions of the strain rate  $1.28 \times 3.31 = 424\%$ .

Using the data from these tables, one can also analytically calculate the damage initiation criterion applying the following formula:

$$\omega_{JC} = \frac{\sum \Delta \bar{\varepsilon}_p}{\bar{\varepsilon}_f} \tag{V-9}$$

For example, for the simulation carried out at 700 m/s and 498 °K, this values are obtained by adding all the quotients of the equivalent plastic strain rate (column eight) over their respective strains at failure (column seventeen), obtained from tables V-2 and V-3:

$$\omega_{JC} = \sum \left( \frac{4.2 \times 10^3}{0.37} + \frac{4.0 \times 10^6}{0.41} \dots + \frac{1.96 \times 10^6}{1.38} + \frac{1.93 \times 10^6}{1.21} \right) = 0.97 \tag{V-10}$$

One can observe on Table V-3 that at high-speeds the thermal contributions to the failure strain are typically greater than those of the strain rate for the VascoMax 300 steel.

## 5.4 Wear Thermal Influence

### 5.4.1 Initial Temperature Influence

The material behavior was simulated using the empirical JC plasticity and dynamic failure criterions. Both of these criterions are a function of the homologous temperature:

$$T^* = \frac{T - T_0}{T_m - T_0} \quad (\text{V-11})$$

where  $T_o$ ,  $T_m$  and  $T$  are the initial, melting and current temperatures.

Considering that the higher the initial temperature the softer the initial state of the material, one needs to introduce into the model an appropriate temperature. The initial temperature introduced into this wear model was determined via a one-dimensional heat conduction analysis reported by Le [65]. The analysis considered the material's conductivity and the system contact interactions as summarized in Appendix C, section 1.4.5.

Figure V-10 shows the wear patterns obtained from simulations carried with various initial temperatures. In order to compare the effects of the initial temperature for these simulations the only condition varied was the initial temperature. These simulations were executed with an initial velocity of 1200 m/s and with the following initial temperatures: 293 °K (typical room temperature), 608 °K (the temperature provided by Le [65] preliminary thermal analysis), and 900 °K (a high temperature chosen arbitrarily). In Figure V-10, one can see the initial temperature impact. In these simulation pictures, the wear patterns on the top represent the damage due to the 5-micrometer asperities, followed by the wear patterns of the 4 μm asperities. The wear patterns on the bottom of these figures are those created by the 3 μm asperities.

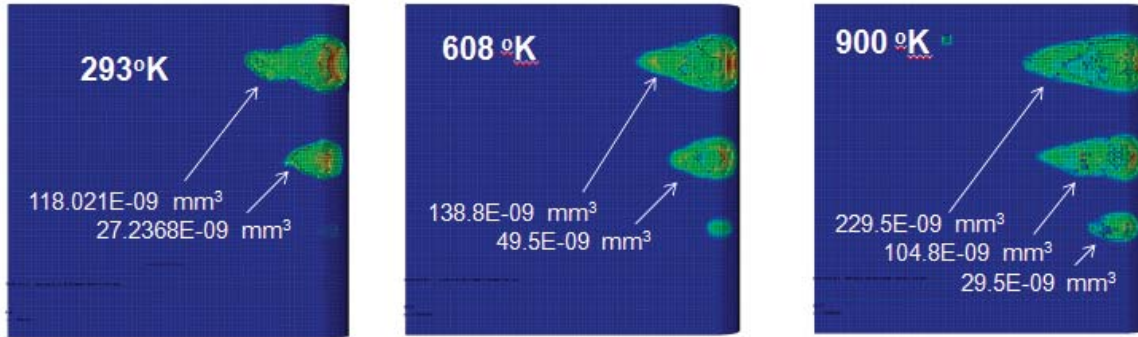


**Figure V-10 Simulated Patterns at Different Temperatures**

Dividing the damage due to the 5  $\mu\text{m}$  asperity, simulated at room temperature against the damage obtained from the simulation using the temperature provided by Le [65], 293  $^{\circ}\text{K}$ , one gets:  $118.02/138.8 \times 100 = 85\%$ . On this case, one can conclude that using the room temperature for the simulations resulted in a 15% reduction of the simulated wear. One can also conclude that using an overestimated value of the skin temperature, for example 900  $^{\circ}\text{K}$ , can result on a 65% ( $229.5/138.8 = 1.65$ ) increase of the simulated wear for this asperity size.

#### 5.4.2 Specific Heat Influence

The specific heat is defined as “the amount of heat required to increase the temperature of a unit mass by one degree” [104]. The specific heat for a process where the heat is supplied keeping the pressure constant is:

$$c_p = \left. \frac{\partial U_m}{\partial T} \right|_p \quad (\text{V-12})$$

During an asperity collision, the heat generated due to the plastic work causes a rise of the local temperature. This temperature rise is a function of the specific heat and generally softens the material, nevertheless, the specific heat depends on the temperature. For example, Figure V-11 shows a plot of the specific heat values obtained from MatWeb [73] for the AISI-1080 steel, normalized at 900  $^{\circ}\text{C}$ .

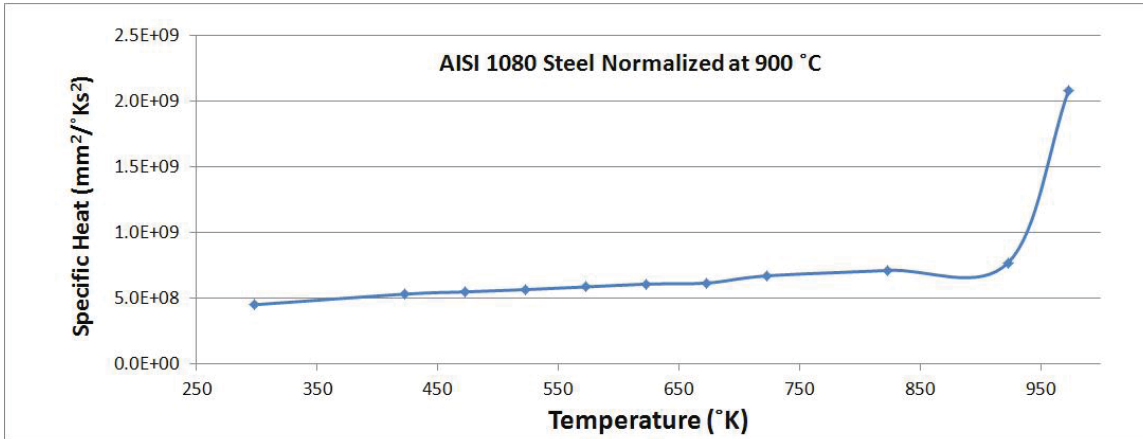


**Figure V-11 Specific Heat for the AISI-1080 Steel**

Observing the plot in Figure V-11, one can see that at higher temperatures the specific heat is greater. Consequently, one can conclude that at higher temperatures it takes more heat to increase the temperature of a unit mass by one degree. Recognizing this physical phenomenon, the model was executed varying the specific heat while keeping constant all the other initial conditions. The results of these simulations are presented in Figure V-12.

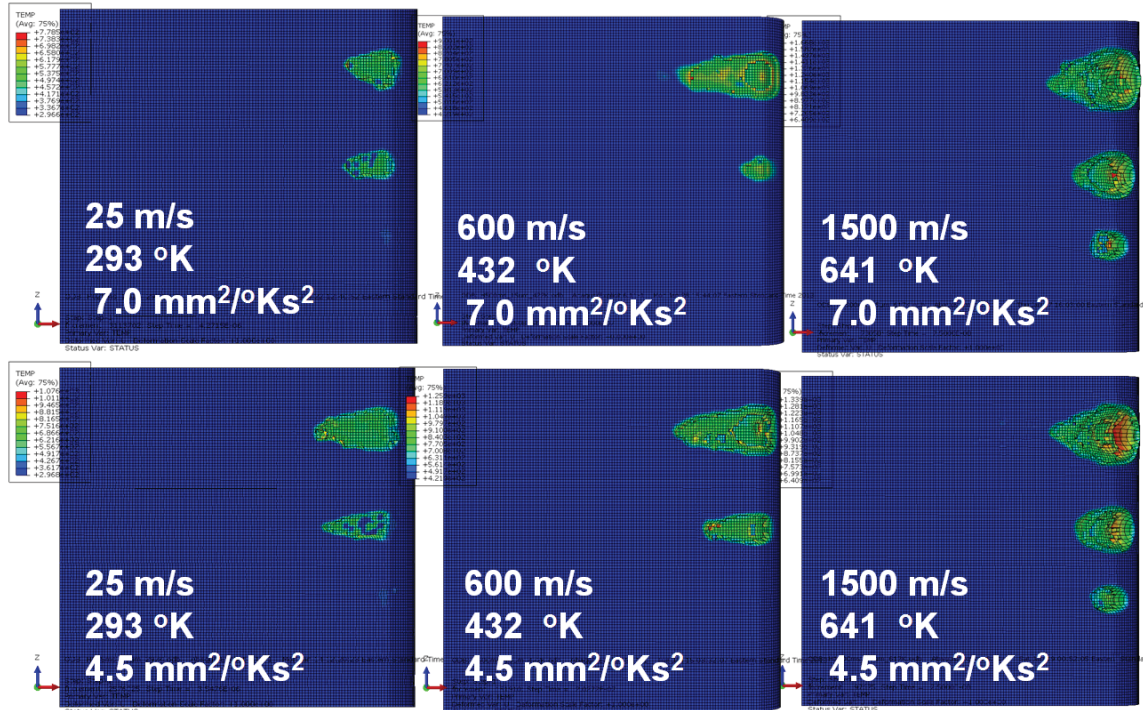


**Figure V-12 Simulation Patterns Varying the Specific Heat**

The pictures in Figure V-12 show the results for three simulations with a specific heat of  $4.5 \text{ mm}^2/\text{°K s}^2$  and three other simulations under the same conditions with a specific heat of  $7.0 \text{ mm}^2/\text{°K s}^2$ .

The specific heat at high temperatures was not available for the VascoMax 300, therefore it was assumed to be similar to the one of the AISI-1080 steel. The  $7.0 \text{ mm}^2/\text{°K s}^2$  value was selected because is the approximate specific heat for the AISI-1080 steel at a temperature of  $488 \text{ °K}$ , according to MatWeb [73]. In the pictures of the simulations, one can see the effects of the specific heat on the simulated wear. One can confirm that introducing a smaller specific heat resulted on more wear.

One of the reasons for this results is that on the runs carried at  $7.0 \text{ mm}^2/\text{°K s}^2$ , it takes longer for the material to soften because it requires more heat to increase the temperature of a unit mass by one degree. One can observe this behavior in Figure V-13. The plots in this figure follow the time dependent material behavior of one of the elements that fail in the simulation. The location of the element is presented in Figure V-5. This element was chosen because is one of the first elements to fail during the simulations.

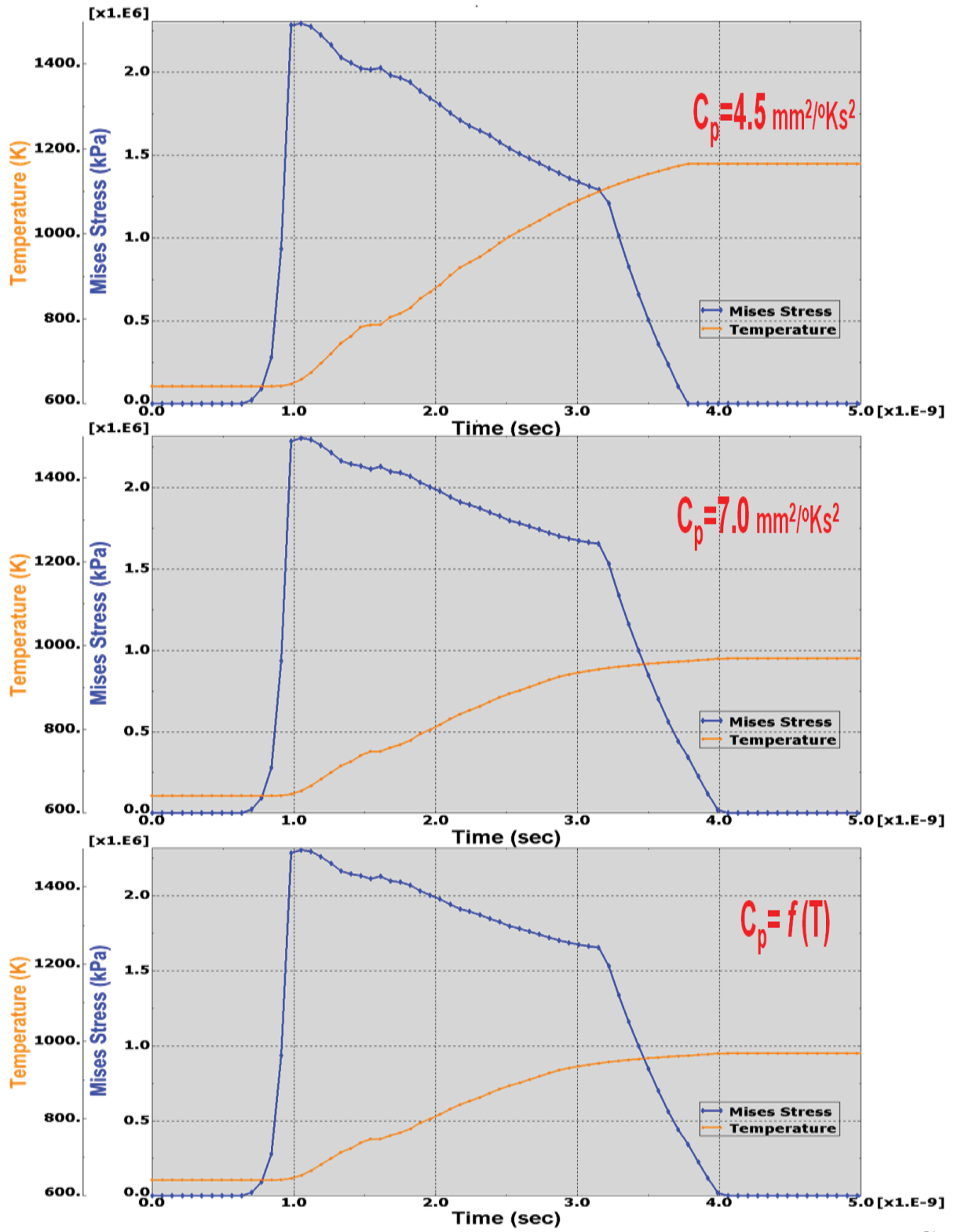


Figure V-13 TDMB of Simulations Varying the Specific Heat

The three plots in Figure V-13 show the time dependent material behavior of runs carried out with a specific heat of  $4.5 \text{ mm}^2/\text{K s}^2$ , a specific heat of  $7.0 \text{ mm}^2/\text{K s}^2$ , and a specific heat as a function of temperature, tabulated based on the AISI-1080 steel values obtained from MatWeb [73]. The blue plots represent the Von Mises stress and the orange ones the temperature. The slope of the orange curve represents the rate of change of the temperature with time.

This rate of temperature change is a function of the specific heat. From the definition of the specific heat, one can observe that for a process with a constant pressure the rise in temperature can be calculated with equation V-122. From this equation one can infer that the rise in temperature is directly proportional to the internal energy per unit of mass and inversely proportional to the specific heat. In other words, the smaller the specific heat the greater the temperature increments and consequently the steeper the temperature slope. In the plots of Figure V-13, one can observe this behavior: the slope of the temperature curve for the simulation with a specific heat of  $4.5 \text{ mm}^2/\text{K s}^2$  is steeper than the other two. One can also observe that in the bottom plot, since the specific heat is increasing as the temperature rises according to the tabulated values, then the slope of the temperature curve tends to decrease also as the temperature increases. By looking at these plots one can conclude that if the temperature rate of change is large then the material will soften faster and failure will typically occur earlier.

### **5.5 Normalized Wear Rates**

To estimate the normalized wear, one can extrapolate the simulated single asperity damage based on the surface roughness analysis (presented in section 3.10.1). For this model, the necessary inputs from the surface roughness analysis include: the average roughness measurements, the number of asperities per unit of area, and the percentage of asperities per asperity size. With the values of this measurements, one can estimate the normalized wear according to the following formula developed in section 3.10.3:

$$V_{uA-v} = \# Asp_{uA} \sum_{n=1}^{n=5} \% Asp_n V_{SA-n-v} \quad (\text{V-13})$$

where  $\#Asp_{uA}$  is the number of asperities per unit of area,  $n$  is the size of the asperities,  $\%Asp_n$  is the percentage of asperities of size  $n$ , and  $V_{SA-n-v}$  is the simulated damage due to an asperity of size  $n$  at a velocity  $v$ .

Figure V-14 shows the concept of how the simulation results, the surface characterization data, and this formula can be used to estimate the wear rates for the simulation at 800 m/s and 488 °K. The graphics of this figure are small because the intention of the figure is only to show the concept. Larger images of these charts were presented in section 3.10.1, which explains this concept in more detail.

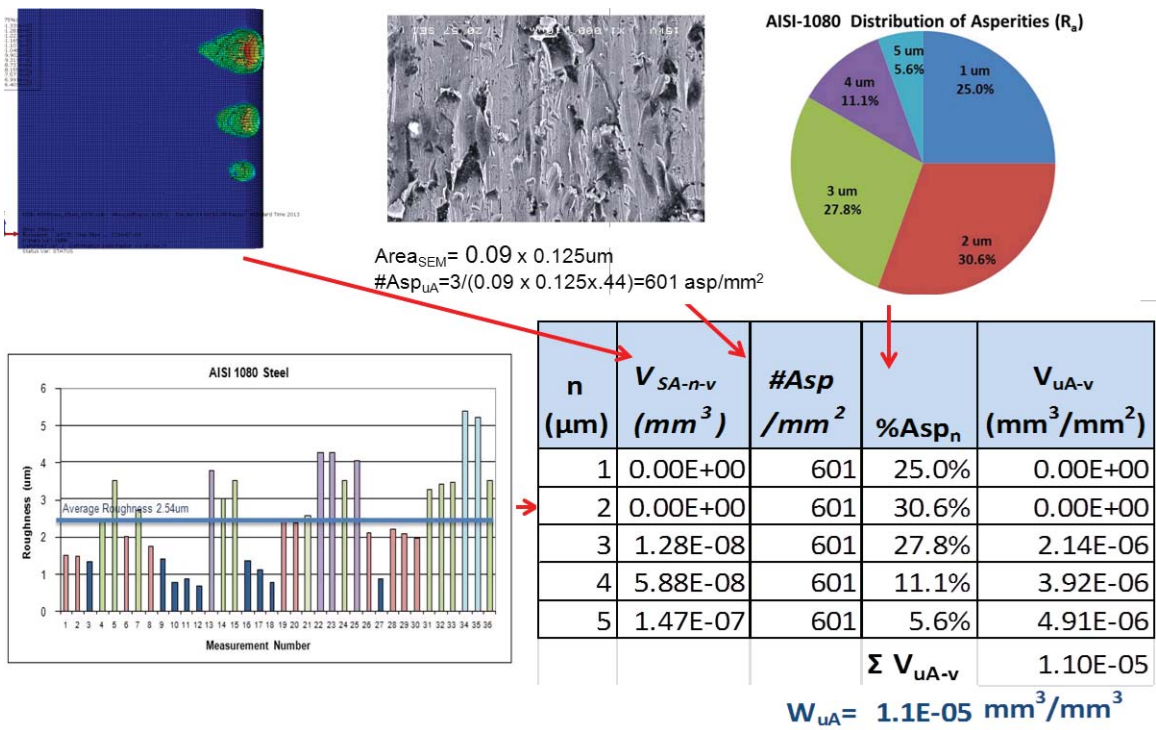


**Figure V-14 Extrapolation Concept**

In Figure V-14, the first column of the embedded table lists the average roughness measurements for the AISI-1080 steel, based on the results from Voyiadjis analysis [101]. According to these studies, the average roughness between measurements ranged from 1  $\mu\text{m}$  to 5  $\mu\text{m}$  (as presented in section 3.10.1 and in the small bar chart above).

The second column reports the simulated damage at 800 m/s and 488 °K reported by Abaqus (these reports are included in Appendix B) due to the collision of the five asperities of sizes 1 μm , 2 μm ,3 μm ,4 μm and 5 μm.

The third column reports the estimated total number of asperities per square millimeter. This parameter was not provided by the surface characterization analysis therefore, for this investigation, it was estimated based on the plastic deformations observed in the micrographs of the surface of the recovered slipper. It is important to note that this is not the preferred approach to obtain this parameter. For this investigation this approach was used because this parameter was not recorded during the surface characterization analysis. The value of this parameter was estimated to be 601 asperities per square millimeter. This value was obtained from the following calculation explained in section 3.10.1.

$$\# Asp_{uA} = \frac{(3 / 0.444)}{0.125 \times 0.09} = 601 \text{ asperities/mm}^2 \quad (V-14)$$

The fourth column presents the percentage of asperities of each size. This value was obtained from the bar chart presented in Table III-6. For example, according to this bar chart, two (the two bars colored in blue) of 36 measurements reported an average roughness,  $R_a$ , close to 5 μm, therefore the percentage of asperities of size 5 μm can be estimated as  $2/36=5.6\%$ . Using the same calculation approach, one can obtain the percentage for each of the other asperity sizes: 25%, for  $R_a=1 \mu\text{m}$ , 30.6% for  $R_a=2 \mu\text{m}$ , 27.8% for  $R_a=3 \mu\text{m}$ , and 11.1% for  $R_a=4 \mu\text{m}$  (This calculations were presented in Section 5.10).

The fifth column represents the damage per unit of area due to all the asperities of that row size, and is calculated as the product of the values of the three preceding columns. In a mathematical form the values in this column represents the product.

$V_{uA-v} = V_{SA-n-v} \# Asp_{uA} \% Asp_n$ . For  $R_a=5 \mu\text{m}$  for example this product is  $4.9 \times 10^{-6} \text{ mm}^3$  and represents the damage due to all the asperities of a size close to  $R_a=5 \mu\text{m}$  on a square millimeter.

The sum of the values of the fifth column represents the equation to calculate the wear per unit of area at a given velocity presented in section 3.10.1:

$$V_{uA-v} = \# Asp_{uA} \sum_{n=1}^{n=5} \% Asp_n V_{SA-n-v} \quad (V-15)$$

The fifth column sum resulted in a value of  $1.1 \times 10^{-5} \text{ mm}^3/\text{mm}^2$ , this value represents the wear per unit of area. Or the volumetric damage due to all the asperities of sizes between 1-5  $\mu\text{m}$  in a square millimeter. Note that this damage was calculated for simulations carried at a velocity,  $V_{uA-v}$ , of 800 m/s and an initial temperature 488 °K.

Finally, to normalize (make dimensionless) the wear rates,  $W_{uA-v}$  one can divide the wear per unit of area,  $V_{uA-v}$ , by the unit of sliding distance (as explained in section 3.10.2). In this case the unit area is  $1 \text{ mm}^2$  and the unit distance is 1 mm, therefore dividing the wear results by 1 mm provides the normalized, or dimensionless, wear rates. The normalized wear rates for this simulation carried out at 800 m/s and 488 °K was estimated to be  $1.1 \times 10^{-5} \text{ mm}^3/\text{mm}^3$ . The calculations for all the other velocities are included in Appendix A. The next section will show a comparison between the results, presented in appendix A, using a specific heat of  $7.0 \text{ mm}^2/\text{°Ks}^2$  and those carried out with a specific heat of  $4.5 \text{ mm}^2/\text{°Ks}^2$  (room temperature).

## **5.6 Normalized Wear Rates Comparison**

To quantify the model results in terms of the normalized wear rates the model was ran at each velocity interval of the HHSTT mission with the corresponding skin temperature provided by Le [65]. All these runs were executed with a specific heat of  $4.9 \text{ mm}^2/\text{°Ks}^2$  for the AISI-1080 at room temperature and a specific heat of  $4.5 \text{ mm}^2/\text{°Ks}^2$  for the VascoMax 300 steel. Then repeated with a VascoMax300 specific heat of  $7.0 \text{ mm}^2/\text{°Ks}^2$ . This value was selected because according to Table V-5 the approximate specific heat for the AISI-1080 steel with a temperature of 488 °K is about  $7.0 \text{ mm}^2/\text{°Ks}^2$ . For the VascoMax300 the specific heat at high temperatures was not found therefore it was assumed to be similar to the one of the AISI-1080 steel, since both have similar specific heats at room temperature. All the calculations to obtain the normalized wear rates for these runs are presented in appendix A. The next table summarizes these results.

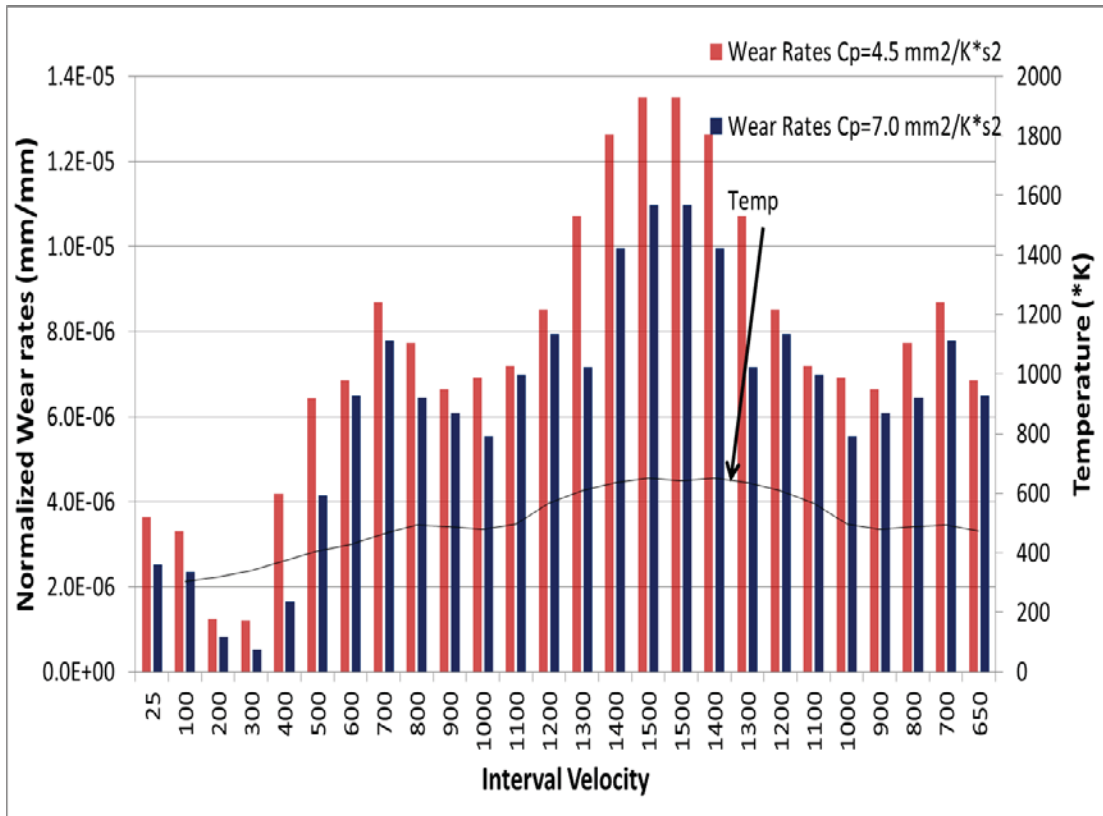


**Table V-6 Normalized Wear Rates Results Varying the Specific Heat**

Table V-6 quantitatively compares the normalized wear rates of the simulations with a specific heat of  $4.5 \text{ mm}^2 / \text{°Ks}^2$  with those carried out with a specific heat of  $7.0 \text{ mm}^2 / \text{°Ks}^2$ . One can see, in this table, that when comparing the simulations carried at the same velocity and temperature, the normalized wear rates were always greater with a specific heat of  $4.5 \text{ mm}^2 / \text{°Ks}^2$ . One of the reasons of this difference is that, for the simulations carried out at  $7.0 \text{ mm}^2 / \text{°Ks}^2$  it takes longer for the material to soften, because it requires more heat to increase the temperature of a unit mass by one degree.

### **5.7 Total Wear Results**

To obtain the wear at each velocity interval the normalized wear rates had to be multiplied by the factors affecting the sliding contact and by the sliding distance. Section 3.10.4 explains the factors that affect the rail-slipper contact and how to incorporate them into the formula to estimate the total wear. The formula used is:

$$V_d = \sum_1^v W_{uA_v} \times l_{c_v} \times w_{c_v} \times D_{s_v} \times \%Cont_v \quad (V-16)$$

where  $l_c$  and  $w_c$  are the current slipper length and width that is in contact with the rail,  $D_s$  is the sliding distance and  $\%Cont$  is the percent of distance or time in contact, all of these terms estimated for each velocity interval,  $n$ .

The normalized wear rates used in this equation were obtained based on the calculations presented in the section 5.6.

Since Hale [38] studies concluded that the wear rates are independent from the worn history then the velocity profile for the HHSTT mission was partitioned in discrete velocity segments. These velocity intervals are presented in Table IV-4.

The calculations to obtain the values of the length in contact were presented on section 4.7. The values employed for this length are those presented in Table IV-4.

The width in contact used for these calculations is a constant value of 90 mm, based on the width of the top of the rail.

The sliding distance at each interval was obtained from the DADS data. These values are presented in Table IV-2.

The percent of contact was derived from the DADS data. DADS reported the loads on the slipper at the top and at its bottom lips as explained in section 4.8. These values were used to estimate a the percent of time in contact of the slipper on each of the velocity intervals as explained in section 4.6 and presented in Table V-8.

With all these values (the current slipper length and width in contact, the sliding distance and the percent time in contact, for each velocity interval) one can calculate the wear for each velocity interval. For example, for the velocity interval of 650-750 m/s. The model was ran with an initial velocity of 700 m/s and an initial skin temperature of 498 °K. The temperature value was provided by Le [65] thermal analysis. The normalized wear rate for this simulation was estimated to be  $1.1 \times 10^{-5} \text{ mm}^3/\text{mm}^3$ , as explained in section 3.10.3. The length in contact was obtained from Table IV-4. This value is 7.0 mm. The width in contact was determined to be a constant value of 90 mm (neglecting the slipper roll). The sliding distance obtained from the DADS data and used for the calculations is 160 m. This values was obtained from Table IV-2. The percent in

contact according to DADS is 23.78. This value was obtained from Table V-8. All these values are summarized in Table V-7.

$v$ (m/s)	$T$ (°K)	$l_c$ (mm)	$w_c$ (mm)	$D_s$ (mm)	$W_{uA}$	%Cont	Interval Wear (mm <sup>3</sup> )
800	488	7.0	90	2.E+05	6.45E-06	23.78%	154.6

**Table V-7 Estimated Wear of the 750 -850 m/s Velocity Interval**

The wear of the 750-850 m/s velocity interval can be calculated as the product of the normalized wear rates by the average length in contact, width in contact, sliding distance, and percent in contact of that interval. For example:

$$\begin{aligned}
 V_d &= W_{uA_n} \times l_{c_n} \times w_{c_n} \times D_{s_n} \times \%Cont_n \\
 V_d &= (6.45 \times 10^6)(7.0)(90)(2 \times 10^5)(0.2378) \\
 V_d &= 156.6 \text{ mm}^3
 \end{aligned}
 \tag{V-17}$$

Appendix A includes tables similar to Table V-7 for each of the mission velocity intervals.

To calculate the total wear, one adds the wear results of all the velocity intervals. Mathematically expressed, with the formulation developed in Appendix C, section 1.8.2, as:

$$V_d = \sum_1^n W_{uA_n} \times l_{c_n} \times w_{c_n} \times D_{s_n} \times \%Cont_n
 \tag{V-18}$$

The following flow chart presents the methodology followed to obtain the total wear rates of the HHSTT mission executed in January 2008.

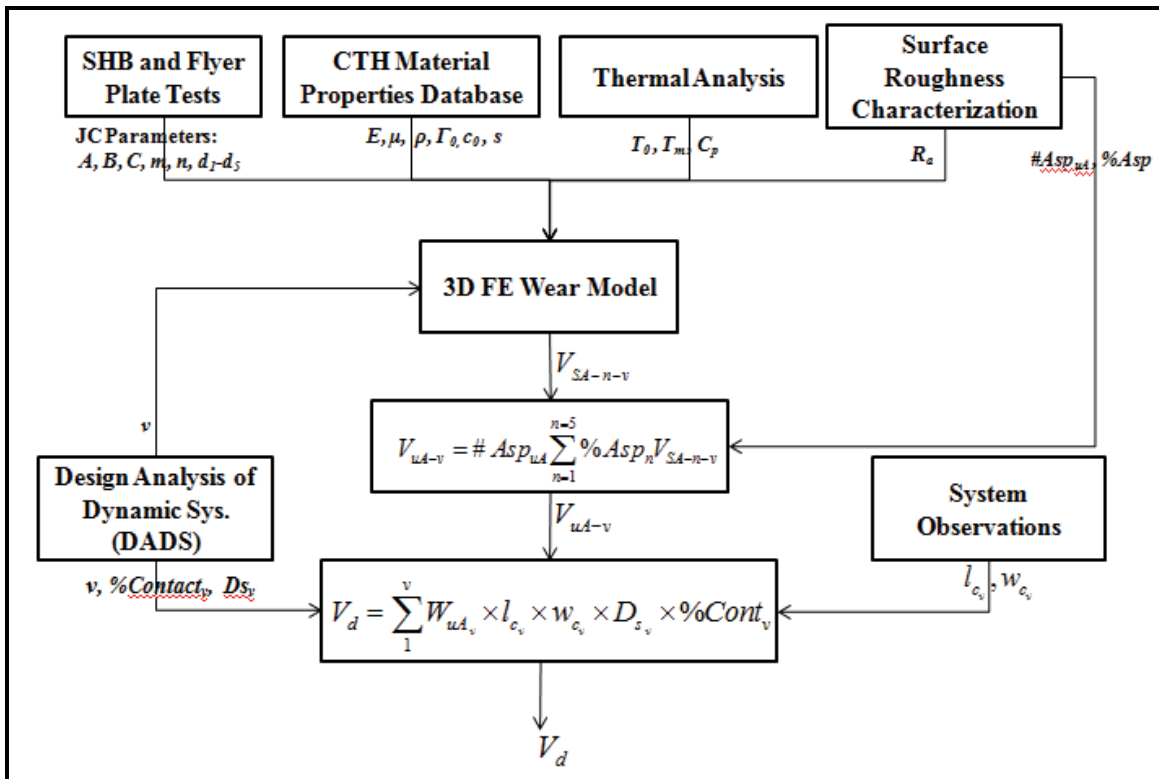


**Figure V-15 Methodology to Obtain the HHSTT Slipper Wear**

In this flow chart one can see the methodology followed on this investigation to obtain the total wear of the HHSTT scenario based in the 3D FE wear model results. In this chart one can see that the model requires inputs from several sources: From the SHB and flyer plate experiments, it requires the JC plasticity and fracture parameters. This parameters should be calibrated at different regions of the velocity and temperature spectrum. From the thermal analysis requires the estimated skin temperature, the material melting temperature and the appropriate specific heats. The surface roughness characterization provides the average asperity sizes used in the model geometry. The remaining material parameters were obtained from AFIT’s CTH material database.

Fed with the appropriate parameters the Abaqus wear model can report the single asperity wear. The output then can be extrapolated to obtain the total wear, based on the observations of the system interactions and the information provided by DADS. DADS provides the velocity profile, sliding distance and the percent of contact at each velocity interval. One then can estimate the effective area of contact based on the DADS data and the system interaction observations.

Table V-8 presents a summary of the wear values for each velocity interval obtained following the methodology presented in the previous flow chart. This table includes the total wear estimated using a specific heat of  $4.5 \text{ mm}^2/\text{K s}^2$  and the results using a specific heat of  $7.0 \text{ mm}^2/\text{K s}^2$ .

$v$ (m/s)	$T$ ( $^{\circ}\text{K}$ )	$l_c$ (mm)	$w_c$ (mm)	$D_s$ (mm)	Normalized Wear Rate (Cp=4.5 mm <sup>2</sup> /K*s <sup>2</sup> )	Normalized Wear Rate (Cp=7 mm <sup>2</sup> /K*s <sup>2</sup> )	%Cont	Interval Wear (mm <sup>3</sup> )	Interval Wear (mm <sup>3</sup> )	
25	297	11.1	90	6.E+03	3.64E-06	2.52E-06	89.02%	20.1	13.9	
100	313	40.5	90	5.E+04	3.30E-06	2.34E-06	72.98%	439.3	311.5	
200	323	77.4	90	1.E+05	1.25E-06	8.17E-07	47.28%	412.0	269.1	
300	357	117.9	90	2.E+05	1.21E-06	5.24E-07	30.37%	701.3	304.0	
400	391	11.1	90	2.E+05	4.18E-06	1.64E-06	26.93%	179.3	70.3	
500	422	23.9	90	3.E+05	6.43E-06	4.15E-06	28.90%	1001.8	645.4	
600	432	42.4	90	3.E+05	6.85E-06	6.49E-06	24.70%	1936.0	1833.0	
700	498	62.6	90	4.E+05	8.70E-06	7.78E-06	19.36%	3985.4	3567.9	
800	488	7.0	90	2.E+05	7.73E-06	6.45E-06	23.78%	185.4	154.6	
900	487	10.5	90	1.E+05	6.63E-06	6.09E-06	24.72%	167.3	153.7	
1000	471	14.0	90	1.E+05	6.90E-06	5.53E-06	23.77%	248.0	198.9	
1100	525	21.0	90	1.E+05	7.19E-06	6.98E-06	19.27%	345.8	335.4	
1200	608	24.5	90	1.E+05	8.53E-06	7.94E-06	15.82%	428.3	398.9	
1300	609	28.0	90	2.E+05	1.07E-05	7.16E-06	15.57%	656.1	438.2	
1400	660	35.0	90	2.E+05	1.26E-05	9.94E-06	16.54%	1106.6	870.6	
1500	641	38.5	90	3.E+05	1.35E-05	1.10E-05	16.86%	2129.9	1730.7	
1500	641	2.0	90	3.E+05	1.35E-05	1.10E-05	6.11%	44.6	36.2	
1400	660	6.0	90	3.E+05	1.26E-05	9.94E-06	5.03%	96.0	75.6	
1300	609	10.0	90	3.E+05	1.07E-05	7.16E-06	5.10%	128.0	85.5	
1200	608	14.0	90	2.E+05	8.53E-06	7.94E-06	5.36%	138.1	128.6	
1100	525	18.0	90	2.E+05	7.19E-06	6.98E-06	6.22%	159.3	154.6	
1000	471	23.0	90	3.E+05	6.90E-06	5.53E-06	7.30%	312.8	250.9	
900	487	10.5	90	3.E+05	6.63E-06	6.09E-06	7.17%	121.4	111.5	
800	488	19.9	90	4.E+05	7.73E-06	6.45E-06	6.42%	355.1	296.0	
700	498	38.6	90	6.E+05	8.70E-06	7.78E-06	6.23%	1053.1	942.7	
650	450	46.7	90	1.E+05	6.85E-06	6.49E-06	7.26%	271.9	257.5	
<b>Total Simulated Wear using a Cp=4.5 mm<sup>2</sup>/K*s<sup>2</sup></b>								<b>16623.0</b>		mm <sup>3</sup>
<b>Total Simulated Wear using a Cp=7.0 mm<sup>2</sup>/K*s<sup>2</sup></b>									<b>13635.1</b>	mm <sup>3</sup>
<b>Total Measured Wear (Based on the technical drawings dimensions)</b>									<b>10519.0</b>	mm <sup>3</sup>

**Table V-8 Total Estimated Wear for the HHSTT Mission of January 2008**

Section 4.3, explains how the actual slipper dimensions were not measured prior to the mission. The original top slipper thickness was assumed based on the technical drawings and on the measurements of a new slipper manufactured for Hale [38] investigations. The assumed top slipper thickness was projected to be 14.7 mm. Based

on the assumed thickness, and the thickness measurements of on the top of the recovered slipper the total wear of the slipper is estimated to be 10, 520 mm<sup>3</sup>.

The simulated wear with a specific heat 4.5 mm<sup>2</sup>/°K s<sup>2</sup> was estimated to be 16,623 mm<sup>3</sup>, this value is 58.0% more than the measured wear. The simulated wear with a specific heat 7.0 mm<sup>2</sup>/°K s<sup>2</sup> was estimated to be 13,635 mm<sup>3</sup>; this value is only 29.6% greater than the measured value.

The wear estimate using a specific heat of heat 7.0 mm<sup>2</sup>/°K s<sup>2</sup> is reasonable considering all the required approximations specific to the complex HHSTT scenario. These approximations include: the estimated original volume of the slipper, the length in contact (varying due to the pitch), the percent of time in contact (varying due to the bouncing), the lack of the experiments required to obtain some of the material parameters (such as the JC dynamic failure ones), the estimated skin temperature based on the thermal analysis.

Two factors that can help to refine these total wear estimations include: First, the fact that the slipper experienced some roll during the sliding and due to it, the width in contact of the slipper used for the calculations should be reduced. The width used for these estimates was 90 mm, but considering the roll the width in contact should be less than this value. The second factor is the reduction in wear due to the coatings applied to the rail. The slipper traveled the first 4,000 m over a bare rail. Afterwards it traveled 760 m over a rail coated with a red oxide and the last 1,059 m over a rail coated with a white epoxy. The impact to wear due to coatings was not in the scope of this investigation.

These two factors, the effective width in contact and the coatings can easily reduce the estimated wear to values less than the measured wear.

## **VI. Summary, Conclusions, Contributions and Recommendations**

### **6.1 Summary**

The main objective of this investigation was to develop a FE model able to reasonable simulate high-speed sliding wear. The results presented in this dissertation demonstrate that this objective was achieved.

The 3D wear model presented in this dissertation was developed building upon the lessons learned from former AFIT studies, two of these lessons come from Hale[38] studies. Hale[38] concluded that wear can be reasonable predicted simulating the collision of a micro-asperity and that the wear rates are independent of the worn history. Based on the first lesson the model simulates in a 3D manner the micro-asperity collisions occurring at the contact points, between the two apparently flat sliding surfaces. Based on the second lesson the velocity profile of the HHSTT scenario was partitioned on discrete velocity intervals and the model was ran at each velocity interval to calculate its wear rates.

The 3D model was developed using Abaqus, a commercially available FE software package. It incorporates the Johnson-Cook's plasticity and dynamic failure algorithms, Coulomb's friction equation, and the Mie-Gruneisen Equation of State. It simulates the high-speed wear phenomenon assuming an adiabatic process, where the temperature rises due to plastic deformation.

For this model, as for any other, to obtain the proper results one needs to carry the appropriate experiments to obtain the parameters required for each of the algorithms used on it. Inappropriate model inputs generally result in inappropriate model outputs. This is an area that can be improved since, due the lack of experimental resources, some of the material parameters were based on the values reported for similar materials.

This model reports the wear due to each single asperity collision; therefore, it requires a methodology to extrapolate these results to obtain the normalized wear rates. The extrapolation approach, proposed for this investigation, is based on the surface roughness characterization of the materials involved. It requires the average surface

roughness, the number of asperities per unit of area, and the statistical distribution of the asperities on the materials. An average surface roughness serves for the extrapolation approach but it is required to create the model geometry, the rail assembly was based in the average asperity sizes measured during the surface roughness analysis.

With the normalized wear rates estimated, then one can apply these values to the macro system of interest to calculate the total wear. However, wear is a complex process that involves many variables both at the micro-asperity collision level and at the macro-system level. Recognizing the factors involved in both of these levels is essential to produce reasonable predictions. For the micro-simulations the model requires the proper model inputs. Similarly, for the total wear estimations, one needs to look all the macro-level system interactions and attempt to determine factors that can influence the total wear estimates.

To avoid difficulties estimating these macro-system interactions the best scenario to gather the appropriate wear data is a laboratory, equipped with a test fixture that can control the factors contributing to wear. No such facility is currently available and therefore for this investigation, the scenario used for comparison was the HHSTT mission executed on January 2008.

This HHSTT mission is a very complex scenario to simulate. This scenario introduces many variables to the wear process, specific to it, such as a wide velocity range, intermittent contact, pitch, roll, yaw, coatings, etc. To carry out the comparison against this scenario, the HHSTT velocity profile was partitioned on several intervals and all these factors had to be estimated for each velocity interval.

The model simulations were carried with the estimated velocity and skin temperature for each interval. The model results showed that higher speeds typically correlate with higher skin temperatures. The results also showed that the sliding wear simulations are highly dependent on the initial temperatures obtained from the AFIT's thermal studies and on the specific heat introduced into the model. The thermal contributions typically outweighed the strain rate ones at the damage initiation point.

It was important for this investigation to recognize that the specific heat is a function of temperature and therefore it should be introduced as such into the model. The

specific heat regulates the temperature increase rate; and therefore is used to calculate the temperature at each explicit time increment. The approximated temperature is then used to calculate the homologous temperature employed in both the JC plasticity criterion, to evaluate the Von Mises stress and on the JC Dynamic failure criterion to calculate the damage initiation criterion

It is important to note that the wear patterns obtained from the simulations resemble the morphology of the plastic deformations observed in the slipper micrographs.

Finally, the simulated results for the HHSTT mission are reasonable considering all the approximations specific to the complex HHSTT scenario such as the estimated original volume of the slipper, the wide velocity range, the intermittent contact, pitch, roll, yaw, coatings, etc.

## **6.2 Conclusions of Research**

- The main objective of this investigation was successfully achieved. The results presented in this dissertation demonstrate that this is a reasonable model to simulate high-speed sliding wear.
- The 3D model was developed using Abaqus. It incorporates the Johnson-Cook's plasticity and dynamic failure criteria, Coulomb's friction equation, and the Mie-Gruneisen equation of state. These tools have been used by many recent models to successfully simulate high-strain-rate problems. These models include El-Tobgy [34], Duan [33], Polyzois [89], Kay [56], and Dean [32].
- There is no plasticity or fracture criterion that can predict the material behavior over a wide range of temperatures or strain-rates. Most criteria require these wide ranges to be partitioned in smaller ranges and to have the parameters re-calibrated for each smaller range.
- Under the JC plasticity criterion the material behavior varies as a function of the equivalent plastic strain, equivalent plastic strain rate and the temperature.
  - This criterion predicts the Von Mises stress to increase with higher strain rates and decrease with higher temperatures.

- Under an adiabatic process the heat generated in the element by the plastic work results in a rise in temperature that decreases the Von Mises stress, or softens the material.
- For the high-speed sliding wear simulations the material behavior greatly depends on the initial conditions.
  - Inappropriate model inputs generally result in inappropriate model outputs.
  - As one increases the initial sliding velocity the elements collide at higher strain rates and these higher strain rates tend to increase the Von Mises stress.
  - An incorrect initial skin temperature can lead to significant errors on the wear estimates. Typically the greater this temperature, the softer the initial state of the material, which leads to a greater simulated damage.
  - An incorrect specific heat value can lead to erroneous wear rates, since it controls the rate of change of the temperature. The smaller the specific heat the greater the temperature increments and consequently the steeper the temperature slope. A steeper slope causes the material to thermally soften faster.
  - The specific heat depends on the material's temperature and it is important to introduce it as function of temperature into the model. Mistakenly using the specific heat reported at room temperature can lead to over estimates of wear.
- The maximum contributions to Von Mises stress due to the strain rates and temperatures occur at the damage initiation point.
  - The greater the initial speed the greater the strain rate contribution.
  - Greater initial speeds generally correlated with higher skin temperatures.
  - The thermal contributions typically outweigh the strain rate ones near the damage initiation point.
- The maximum contributions to the failure strain, due to the strain rates and temperatures, also occur at the damage initiation point.

- The strain rate contributions don't vary too much for the high-speeds.
- The thermal contributions are typically greater than the strain rate ones.
- Wear is a complex process that involves many variables both at the micro-asperity collision level and at the macro-system level. Recognizing the factors involved in both of these levels is essential to produce reasonable predictions.
  - For the total wear estimations, one needs to scrutinize all the macro-level system interactions and attempt to determine factors that can influence the total wear estimates such as a wide velocity range, intermittent contact, pitch, roll, yaw, coatings, etc.
- It is possible to decrease the total wear calculations by including the roll effects and also by including the effects of coating (which needs to be studied).
- Creating a model with a gap between the two sliding surfaces simulates better the real contact at the micro-level, since the contact between flat surfaces only occurs at distinct contact points. In addition, this gap provides a place where the failed elements can be assumed to go after fracture and helps avoid excessive shear.
- The general contact algorithm used for this model allows the surfaces to evolve by removing the elements from the mesh, once the material stiffness is fully degraded.
  - The simulated wear patterns obtained using this element removal feature resemble the morphology of the plastic deformations observed in the micrographs of the worn slipper.

### **6.3 Significant Contributions**

- Provided an extrapolation method based on the surface characterization analysis.
  - The method is based on the average roughness and the distribution of the asperities. It replaced the requirement for a spherical factor to convert the 2D simulations and the requirement to calibrate against a factor obtained from Archard's low strain rate experiments.

- Provided a better understanding of the physical factors influencing the wear of the HHSTT mission and a simple methodology to estimate some of them.
  - Shifted the focus away from the micro-level simulation to observe the “big test picture”. Scrutinized all the macro-level system interactions and approximated the factors that can influence the total wear estimates such as a wide velocity range, intermittent contact, pitch, roll, coatings, etc.
  - Improved the wear results with simplistic estimates to account for the slipper’s intermittent contact and six degrees of freedom.

Other original contributions, from this investigation, include:

- Shifted AFIT’s wear prediction approach from simulating it with 2D FE plane-strain models to simulating it with a 3D FE model.
- Recognized the influence of the specific heat in the wear process. Highlighted that the specific heat controls the temperature that determines the thermal contributions to both the JC plasticity and failure criterions.

#### **6.4 Recommendations for Future Research**

- For this investigations the JC parameters obtained from the Split-Hopkinson bar tests were adjusted with the results from the flyer plate tests, but this research simulations are carried even at greater temperatures and-strain-rates than those experienced during the flyer plate tests
  - One should consider calibrating the JC parameters at various temperatures and velocity ranges to avoid employing the same parameters for a wide range of strain rates or temperatures.
  - One may consider even investigating alternative criterions, since this JC failure criterion is limited in covering anisotropic material properties.
- The effective width in contact for the slipper recovered from the HHSTT can also be further investigated. The slipper experienced some roll during the sliding and

due to it; the width in contact of the slipper varies. The width used for these estimates was 90 mm, but considering the roll the effective width in contact should be less than this value. One should consider using a more appropriate width more likely can reduce these total wear estimations.

- One should consider refining the thermal analysis, since; the wear results are heavily dependent on the estimated skin temperatures.
- One should consider obtaining the appropriate specific heat as function of temperature for the VascoMax 300 steel.
- One should consider also obtaining the appropriate JC dynamic failure parameters,  $d_l$  trough  $d_s$ , for the VascoMax 300 steel. For these model simulations these parameters were substituted with those of the Ti6Al4V alloy, which has similar mechanical properties than the VascoMax 300 steel.

## Appendix A. Model Results for Each Velocity Interval

This appendix presents pictures of the Abaqus simulated wear patterns, carried out with different initial velocities and temperatures.

It includes the tabulated calculations to obtain the normalized wear rates according to the following equations:

$$V_{uA-v} = \# Asp_{uA} \sum_{n=1}^{n=5} \% Asp_n V_{SA-n-v} \quad (A-1)$$

$$W_{uA} = \frac{V_{uA}}{D_s} \quad (A-2)$$

where  $n$  is the index denoting the asperity size in micrometers ,  $V_{SA-n-v}$  is the simulated wear due to an asperity of size  $n$  colliding at a velocity  $v$  (from the Abaqus simulation reports such as the one included in Appendix B),  $\# Asp_{uA}$  is the number of asperities per unit of area,  $\% Asp_n$  is the percentage of asperities of size  $n$  (based in the AISI-1080 asperity distribution)

This appendix also contains the tabulated calculations to obtain the estimated sliding wear from each velocity interval. These calculations are based in the following equation, developed in Appendix C, section 1.8.2.

$$V_d = \sum_1^v W_{uA_v} \times l_{c_v} \times w_{c_v} \times D_{s_v} \times \%Cont_v \quad (A-3)$$

where  $l_c$  is the estimated length in contact (from Table IV-4).  $w_c$  is the estimated width in contact (from Table V-1) ,  $D_s$  is the sliding distance at the velocity interval  $v$  (from Table IV-2) and  $\%Cont$  is the percent of time in contact for that velocity interval (from Table V-8) .

## A.1 Results for the 0-50 m/s Interval

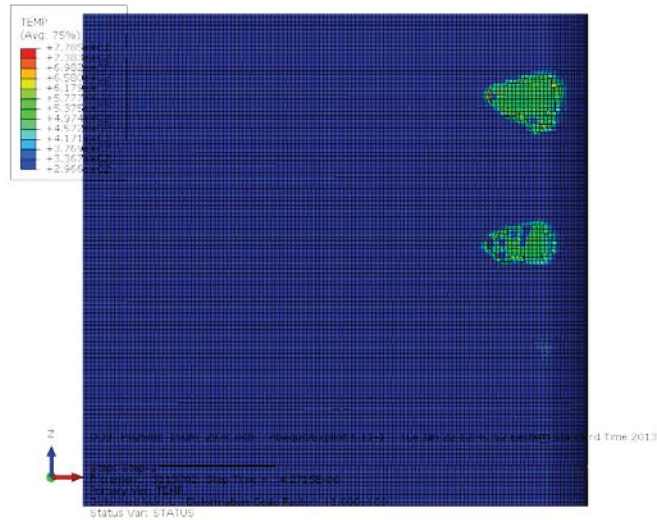


Figure A-1 Simulated Wear Patterns at 25 m/s and 297 °K

$$V_{uA-v} = \# Asp_{uA} \sum_{n=1}^{n=5} \% Asp_n V_{SA-n-v}$$

n	$V_{SA-n-v}$ ( $mm^3$ )	#Asp / $mm^2$	%Asp <sub>n</sub>	$V_{uA-v}$ ( $mm^3/mm^2$ )
1	0.00E+00	601	25.0%	0.00E+00
2	0.00E+00	601	30.6%	0.00E+00
3	0.00E+00	601	27.8%	0.00E+00
4	2.25E-08	601	11.1%	1.50E-06
5	3.04E-08	601	5.6%	1.02E-06
$\Sigma V_{uA-v}$				2.52E-06

$$W_{uA} = 2.5E-06 \text{ mm}^3/mm^3$$

Table A-1 Normalized Wear at 25 m/s

$$V_d = \sum_{v=1}^v W_{uA_v} \times l_{c_v} \times w_{c_v} \times D_{s_v} \times \%Cont_v$$

v	T	$l_c$	$w_c$	$D_s$	$W_{uA}$	%Cont	Interval Wear ( $mm^3$ )
(m/s)	(°K)	(mm)	(mm)	(mm)			
25	297	11.1	90	6.E+03	2.52E-06	89.02%	13.9

Table A-2 Estimated Wear of the 0-50 m/s Velocity Interval

## A.2 Results for the 50-150 m/s Interval

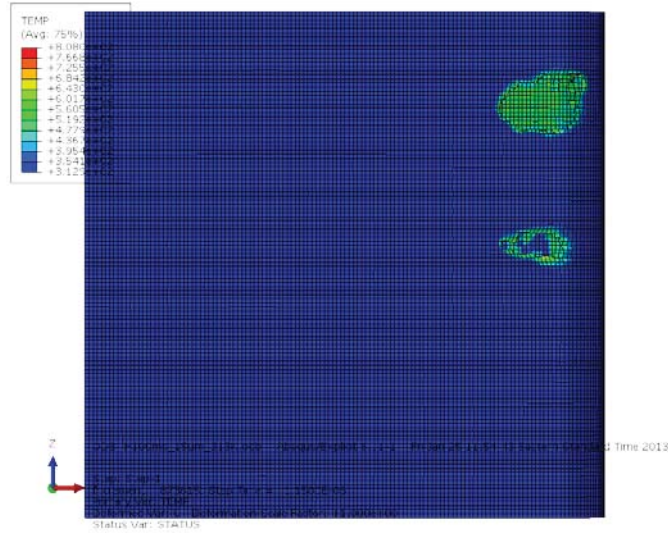


Figure A-2 Simulated Wear Patterns at 100 m/s and 313 °K

$$V_{uA-v} = \# Asp_{uA} \sum_{n=1}^{n=5} \% Asp_n V_{SA-n-v}$$

n ( $\mu\text{m}$ )	$V_{SA-n-v}$ ( $\text{mm}^3$ )	#Asp / $\text{mm}^2$	$\% Asp_n$	$V_{uA-v}$ ( $\text{mm}^3/\text{mm}^2$ )
1	0.00E+00	601	25.0%	0.00E+00
2	0.00E+00	601	30.6%	0.00E+00
3	0.00E+00	601	27.8%	0.00E+00
4	1.34E-08	601	11.1%	8.93E-07
5	4.34E-08	601	5.6%	1.45E-06
$\Sigma V_{uA-v}$				2.34E-06

$$W_{uA} = 2.3E-06 \text{ mm}^3/\text{mm}^3$$

Table A-3 Normalized Wear at 100 m/s

$$V_d = \sum_v W_{uA_v} \times l_{c_v} \times w_{c_v} \times D_{s_v} \times \%Cont_v$$

v (m/s)	T (°K)	$l_c$ (mm)	$w_c$ (mm)	$D_s$ (mm)	$W_{uA}$	$\%Cont$	Interval Wear ( $\text{mm}^3$ )
100	313	40.5	90	5.E+04	2.34E-06	72.98%	311.5

Table A-4 Estimated Wear of the 50-150 m/s Velocity Interval

### A.3 Results for the 150-250 m/s Interval

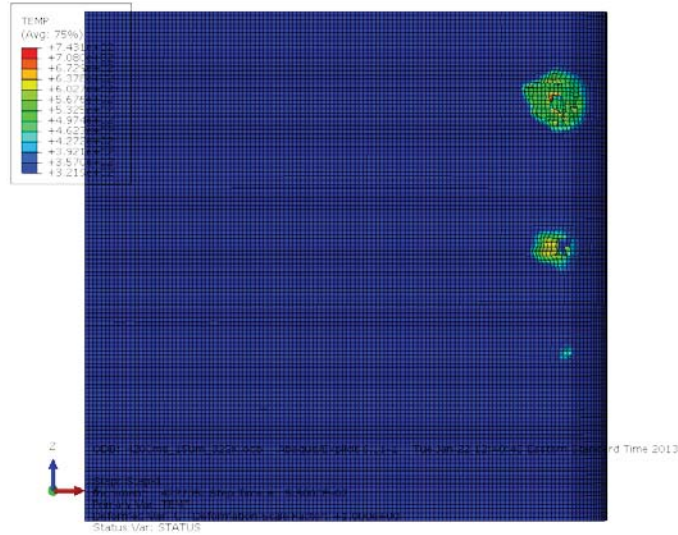


Figure A-3 Simulated Wear Patterns at 200 m/s and 323 °K

$$V_{uA-v} = \# Asp_{uA} \sum_{n=1}^{n=5} \% Asp_n V_{SA-n-v}$$

n	$V_{SA-n-v}$ ( $mm^3$ )	#Asp / $mm^2$	$\% Asp_n$	$V_{uA-v}$ ( $mm^3/mm^2$ )
1	0.00E+00	601	25.0%	0.00E+00
2	0.00E+00	601	30.6%	0.00E+00
3	0.00E+00	601	27.8%	0.00E+00
4	1.94E-09	601	11.1%	1.30E-07
5	2.06E-08	601	5.6%	6.87E-07
$\Sigma V_{uA-v}$				8.17E-07

$$W_{uA} = 8.2E-07 \text{ mm}^3/mm^3$$

Table A-5 Normalized Wear at 200 m/s

$$V_d = \sum_v W_{uA_v} \times l_{c_v} \times w_{c_v} \times D_{s_v} \times \% Cont_v$$

v	T	$l_c$	$w_c$	$D_s$	$W_{uA}$	$\% Cont$	Interval Wear ( $mm^3$ )
(m/s)	(°K)	(mm)	(mm)	(mm)			
200	323	77.4	90	1.E+05	8.17E-07	47.28%	269.1

Table A-6 Estimated Wear of the 150-250 m/s Velocity Interval

#### A.4 Results for the 250-350 m/s Interval

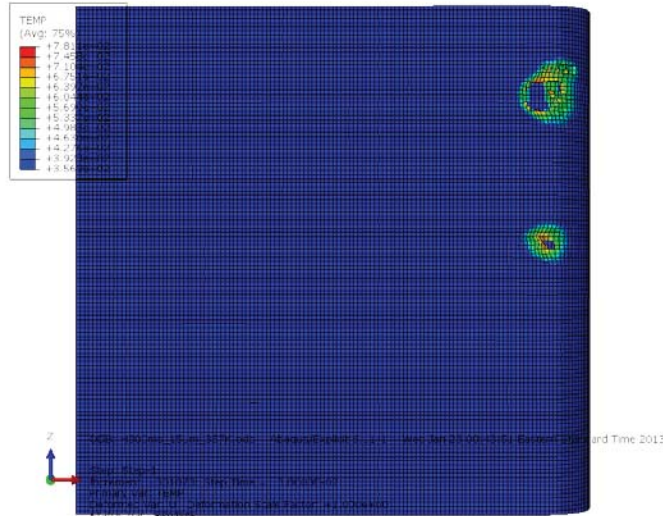


Figure A-4 Simulated Wear Patterns at 300 m/s and 357 °K

$$V_{uA-v} = \# Asp_{uA} \sum_{n=1}^{n=5} \% Asp_n V_{SA-n-v}$$

n ( $\mu\text{m}$ )	$V_{SA-n-v}$ ( $\text{mm}^3$ )	#Asp / $\text{mm}^2$	$\% Asp_n$	$V_{uA-v}$ ( $\text{mm}^3/\text{mm}^2$ )
1	0.00E+00	601	25.0%	0.00E+00
2	0.00E+00	601	30.6%	0.00E+00
3	0.00E+00	601	27.8%	0.00E+00
4	9.86E-10	601	11.1%	6.59E-08
5	1.37E-08	601	5.6%	4.58E-07
$\Sigma V_{uA-v}$				5.24E-07
$W_{uA} =$				$5.2E-07 \text{ mm}^3/\text{mm}^3$

Table A-7 Normalized Wear at 300 m/s

$$V_d = \sum_v W_{uA_v} \times l_{c_v} \times w_{c_v} \times D_{s_v} \times \%Cont_v$$

v (m/s)	T (°K)	$l_c$ (mm)	$w_c$ (mm)	$D_s$ (mm)	$W_{uA}$	$\%Cont$	Interval Wear ( $\text{mm}^3$ )
300	357	117.9	90	2.E+05	5.24E-07	30.37%	304.0

Table A-8 Estimated Wear of the 250 -350 m/s Velocity Interval

## A.5 Results for the 350-450 m/s Interval

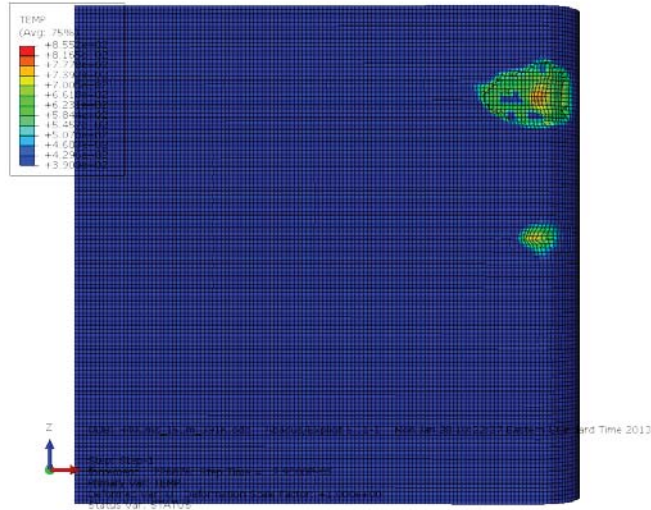


Figure A-5 Simulated Wear Patterns at 400 m/s and 391 °K

$$V_{uA-v} = \# Asp_{uA} \sum_{n=1}^{n=5} \% Asp_n V_{SA-n-v}$$

n ( $\mu\text{m}$ )	$V_{SA-n-v}$ ( $\text{mm}^3$ )	#Asp / $\text{mm}^2$	%Asp <sub>n</sub>	$V_{uA-v}$ ( $\text{mm}^3/\text{mm}^2$ )
1	0.00E+00	601	25.0%	0.00E+00
2	0.00E+00	601	30.6%	0.00E+00
3	0.00E+00	601	27.8%	0.00E+00
4	0.00E+00	601	11.1%	0.00E+00
5	4.91E-08	601	5.6%	1.64E-06
			$\Sigma V_{uA-v}$	1.64E-06
				$W_{uA} = 1.6\text{E-}06 \text{ mm}^3/\text{mm}^3$

Table A-9 Normalized Wear at 400 m/s

$$V_d = \sum_{v=1}^v W_{uA_v} \times l_{c_v} \times w_{c_v} \times D_{s_v} \times \%Cont_v$$

v (m/s)	T (°K)	$l_c$ (mm)	$w_c$ (mm)	$D_s$ (mm)	$W_{uA}$	%Cont	Interval Wear ( $\text{mm}^3$ )
400	391	11.1	90	2.E+05	1.64E-06	26.93%	70.3

Table A-10 Estimated Wear of the 350 -450 m/s Velocity Interval

## A.6 Results for the 450-550 m/s Interval

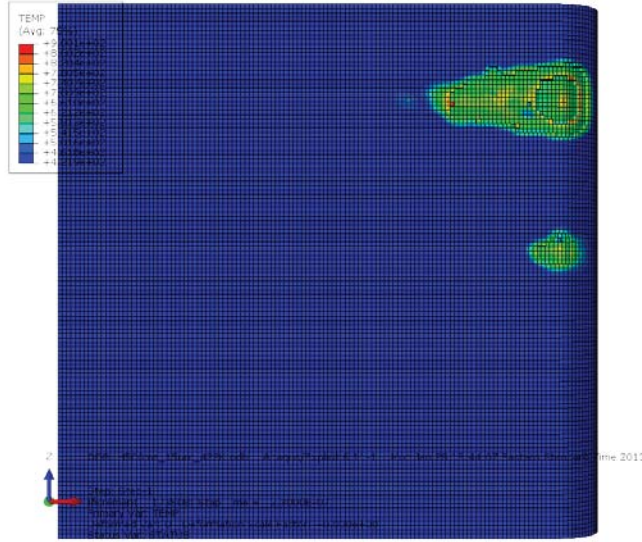


Figure A-6 Simulated Wear Patterns at 500 m/s and 422 °K

$$V_{uA-v} = \# Asp_{uA} \sum_{n=1}^{n=5} \% Asp_n V_{SA-n-v}$$

n	$V_{SA-n-v}$ ( $mm^3$ )	#Asp / $mm^2$	%Asp <sub>n</sub>	$V_{uA-v}$ ( $mm^3/mm^2$ )
1	0.00E+00	601	25.0%	0.00E+00
2	0.00E+00	601	30.6%	0.00E+00
3	0.00E+00	601	27.8%	0.00E+00
4	9.02E-09	601	11.1%	6.02E-07
5	1.06E-07	601	5.6%	3.54E-06
$\Sigma V_{uA-v}$				4.15E-06

$$W_{uA} = 4.1E-06 \text{ mm}^3/mm^3$$

Table A-11 Normalized Wear at 500 m/s

$$V_d = \sum_1^v W_{uA_v} \times l_{c_v} \times w_{c_v} \times D_{s_v} \times \%Cont_v$$

v	T	$l_c$	$w_c$	$D_s$	$W_{uA}$	%Cont	Interval Wear ( $mm^3$ )
(m/s)	(°K)	(mm)	(mm)	(mm)			
500	422	23.9	90	3.E+05	4.15E-06	28.90%	645.4

Table A-12 Estimated Wear of the 450 -550 m/s Velocity Interval

## A.7 Results for the 550-650 m/s Interval

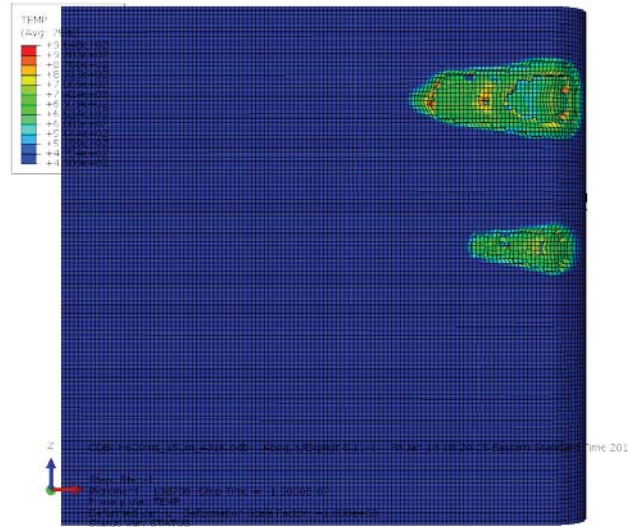


Figure A-7 Simulated Wear Patterns at 600 m/s and 432 °K

$$V_{uA-v} = \# Asp_{uA} \sum_{n=1}^{n=5} \% Asp_n V_{SA-n-v}$$

n	$V_{SA-n-v}$ ( $mm^3$ )	#Asp / $mm^2$	%Asp <sub>n</sub>	$V_{uA-v}$ ( $mm^3/mm^2$ )
1	0.00E+00	601	25.0%	0.00E+00
2	0.00E+00	601	30.6%	0.00E+00
3	0.00E+00	601	27.8%	0.00E+00
4	3.38E-08	601	11.1%	2.26E-06
5	1.27E-07	601	5.6%	4.23E-06
			$\Sigma V_{uA-v}$	6.49E-06

$$W_{uA} = 6.5E-06 \text{ mm}^3/mm^3$$

Table A-13 Normalized Wear at 600 m/s

$$V_d = \sum_1^v W_{uA_v} \times l_{c_v} \times w_{c_v} \times D_{s_v} \times \%Cont_v$$

v	T	$l_c$	$w_c$	$D_s$	$W_{uA}$	%Cont	Interval Wear ( $mm^3$ )
(m/s)	(°K)	(mm)	(mm)	(mm)			
600	432	42.4	90	3.E+05	6.49E-06	24.70%	1833.0

Table A-14 Estimated Wear of the 550 -650 m/s Velocity Interval

## A.8 Results for the 650-750 m/s Interval

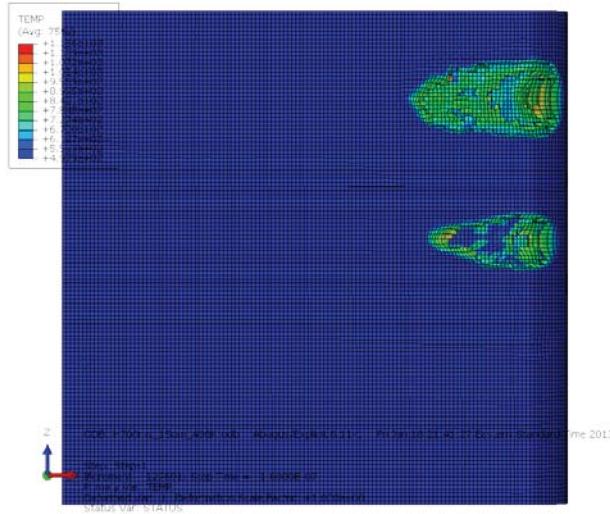


Figure A-8 Simulated Wear Patterns at 700 m/s and 498 °K

$$V_{uA-v} = \# Asp_{uA} \sum_{n=1}^{n=5} \% Asp_n V_{SA-n-v}$$

n	$V_{SA-n-v}$ ( $mm^3$ )	#Asp / $mm^2$	$\% Asp_n$	$V_{uA-v}$ ( $mm^3/mm^2$ )
1	0.00E+00	601	25.0%	0.00E+00
2	0.00E+00	601	30.6%	0.00E+00
3	0.00E+00	601	27.8%	0.00E+00
4	4.93E-08	601	11.1%	3.29E-06
5	1.34E-07	601	5.6%	4.49E-06
$\Sigma V_{uA-v}$				7.78E-06

$$W_{uA} = 7.8E-06 \text{ mm}^3/\text{mm}^3$$

Table A-15 Normalized Wear at 700 m/s

$$V_d = \sum_1^v W_{uA_v} \times l_{c_v} \times w_{c_v} \times D_{s_v} \times \%Cont_v$$

v	T	$l_c$	$w_c$	$D_s$	$W_{uA}$	$\%Cont$	Interval Wear ( $mm^3$ )
(m/s)	(°K)	(mm)	(mm)	(mm)			
700	498	62.6	90	4.E+05	7.78E-06	19.36%	3567.9

Table A-16 Estimated Wear of the 650 -750 m/s Velocity Interval

## A.9 Results for the 750-850 m/s Interval

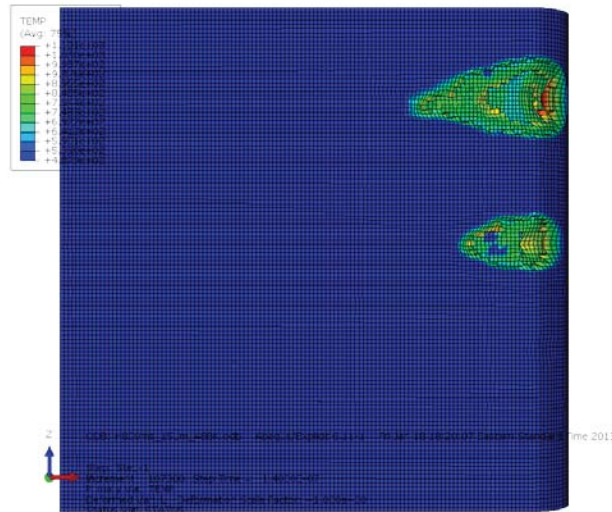


Figure A-9 Simulated Wear Patterns at 800 m/s and 488 °K

$$V_{uA-v} = \# Asp_{uA} \sum_{n=1}^{n=5} \% Asp_n V_{SA-n-v}$$

n ( $\mu\text{m}$ )	$V_{SA-n-v}$ ( $\text{mm}^3$ )	#Asp / $\text{mm}^2$	%Asp <sub>n</sub>	$V_{uA-v}$ ( $\text{mm}^3/\text{mm}^2$ )
1	0.00E+00	601	25.0%	0.00E+00
2	0.00E+00	601	30.6%	0.00E+00
3	0.00E+00	601	27.8%	0.00E+00
4	3.73E-08	601	11.1%	2.49E-06
5	1.18E-07	601	5.6%	3.95E-06
$\Sigma V_{uA-v}$				6.45E-06

$$W_{uA} = 6.4E-06 \text{ mm}^3/\text{mm}^3$$

Table A-17 Normalized Wear at 800 m/s

$$V_d = \sum_v W_{uA_v} \times l_{c_v} \times w_{c_v} \times D_{s_v} \times \%Cont_v$$

v (m/s)	T (°K)	$l_c$ (mm)	$w_c$ (mm)	$D_s$ (mm)	$W_{uA}$	%Cont	Interval Wear ( $\text{mm}^3$ )
800	488	7.0	90	2.E+05	6.45E-06	23.78%	154.6

Table A-18 Estimated Wear of the 750 -850 m/s Velocity Interval

## A.10 Results for the 850-950 m/s Interval

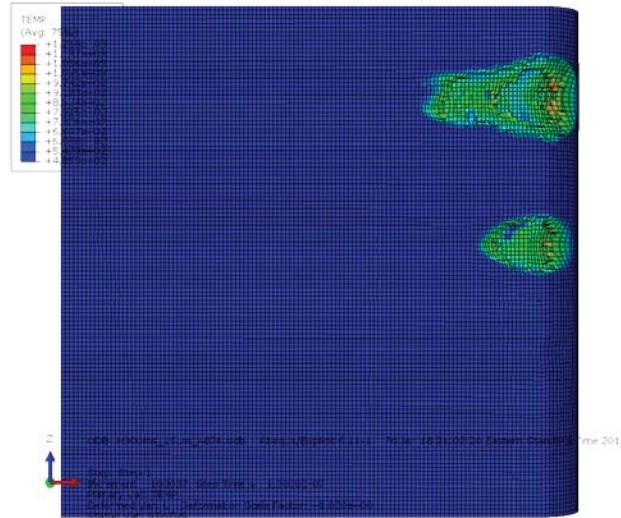


Figure A-10 Simulated Wear Patterns at 900 m/s and 486 °K

$$V_{uA-v} = \# Asp_{uA} \sum_{n=1}^{n=5} \% Asp_n V_{SA-n-v}$$

n	$V_{SA-n-v}$ ( $mm^3$ )	#Asp / $mm^2$	$\% Asp_n$	$V_{uA-v}$ ( $mm^3/mm^2$ )
1	0.00E+00	601	25.0%	0.00E+00
2	0.00E+00	601	30.6%	0.00E+00
3	0.00E+00	601	27.8%	0.00E+00
4	3.00E-08	601	11.1%	2.00E-06
5	1.22E-07	601	5.6%	4.09E-06
			$\Sigma V_{uA-v}$	6.09E-06
				$W_{uA} = 6.1E-06 \text{ mm}^3/mm^3$

Table A-19 Normalized Wear at 900 m/s

$$V_d = \sum_v W_{uA_v} \times l_{c_v} \times w_{c_v} \times D_{s_v} \times \% Cont_v$$

v	T	$l_c$	$w_c$	$D_s$	$W_{uA}$	$\% Cont$	Interval Wear ( $mm^3$ )
(m/s)	(°K)	(mm)	(mm)	(mm)			
900	487	10.5	90	1.E+05	6.09E-06	24.72%	153.7

Table A-20 Estimated Wear of the 850 -950 m/s Velocity Interval



## A.12 Results for the 1050-1150 m/s Interval

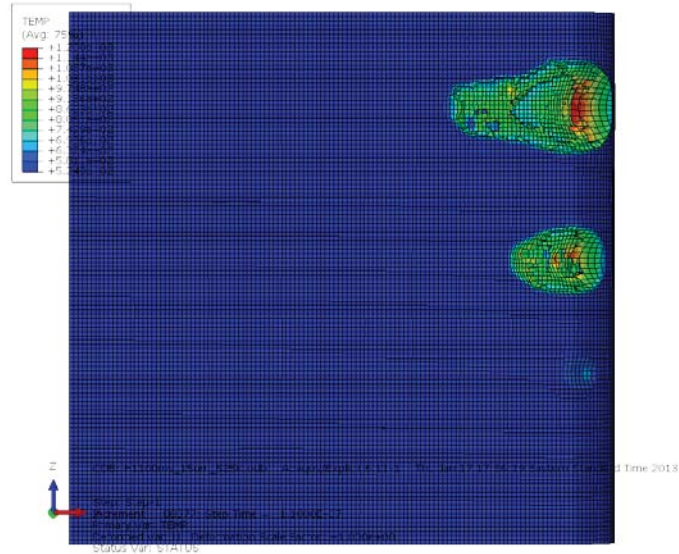


Figure A-12 Simulated Wear Patterns at 1100 m/s and 525 °K

$$V_{uA-v} = \# Asp_{uA} \sum_{n=1}^{n=5} \% Asp_n V_{SA-n-v}$$

n ( $\mu\text{m}$ )	$V_{SA-n-v}$ ( $\text{mm}^3$ )	#Asp / $\text{mm}^2$	%Asp <sub>n</sub>	$V_{uA-v}$ ( $\text{mm}^3/\text{mm}^2$ )
1	0.00E+00	601	25.0%	0.00E+00
2	0.00E+00	601	30.6%	0.00E+00
3	0.00E+00	601	27.8%	0.00E+00
4	3.65E-08	601	11.1%	2.43E-06
5	1.36E-07	601	5.6%	4.54E-06
$\Sigma V_{uA-v}$				6.98E-06

$$W_{uA} = 7.0E-06 \text{ mm}^3/\text{mm}^3$$

Table A-23 Normalized Wear at 1100 m/s

$$V_d = \sum_v W_{uA_v} \times l_{c_v} \times w_{c_v} \times D_{s_v} \times \%Cont_v$$

v (m/s)	T (°K)	$l_c$ (mm)	$w_c$ (mm)	$D_s$ (mm)	$W_{uA}$	%Cont	Interval Wear ( $\text{mm}^3$ )
1100	525	21.0	90	1.E+05	6.98E-06	19.27%	335.4

Table A-24 Estimated Wear of the 1050 -1150 m/s Velocity Interval

### A.13 Results for the 1150-1250 m/s Interval

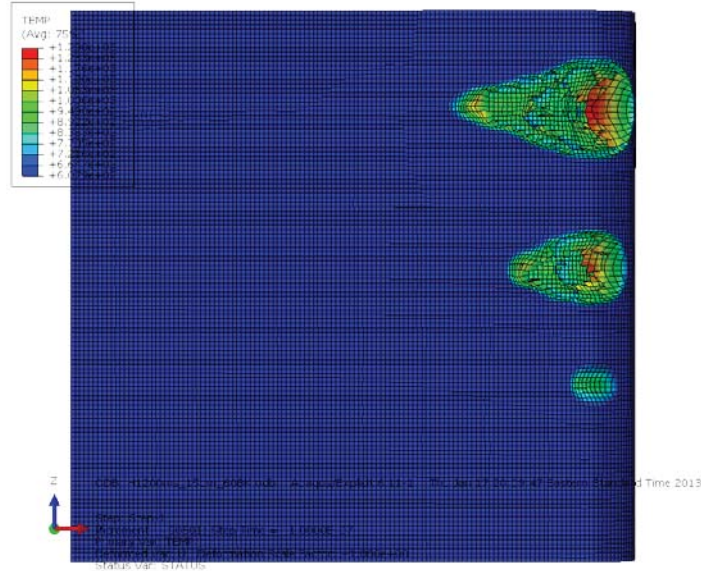


Figure A-13 Simulated Wear Patterns at 1200 m/s and 608 °K

$$V_{uA-v} = \# Asp_{uA} \sum_{n=1}^{n=5} \% Asp_n V_{SA-n-v}$$

n	$V_{SA-n-v}$ ( $mm^3$ )	#Asp / $mm^2$	%Asp <sub>n</sub>	$V_{uA-v}$ ( $mm^3/mm^2$ )
1	0.00E+00	601	25.0%	0.00E+00
2	0.00E+00	601	30.6%	0.00E+00
3	0.00E+00	601	27.8%	0.00E+00
4	4.95E-08	601	11.1%	3.31E-06
5	1.39E-07	601	5.6%	4.63E-06
$\Sigma V_{uA-v}$				7.94E-06

$$W_{uA} = 7.9E-06 \text{ mm}^3/mm^3$$

Table A-25 Normalized Wear at 1200 m/s

$$V_d = \sum_v W_{uA_v} \times l_{c_v} \times w_{c_v} \times D_{s_v} \times \%Cont_v$$

v	T	$l_c$	$w_c$	$D_s$	$W_{uA}$	%Cont	Interval Wear ( $mm^3$ )
(m/s)	(°K)	(mm)	(mm)	(mm)			
1200	608	24.5	90	1.E+05	7.94E-06	15.82%	398.9

Table A-26 Estimated Wear of the 1150 -1250 m/s Velocity Interval

### A.14 Results for the 1250-1350 m/s Interval

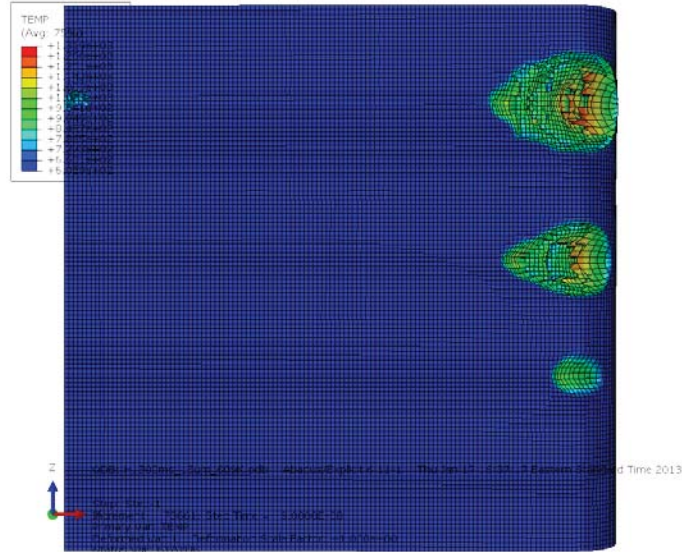


Figure A-14 Simulated Wear Patterns at 1300 m/s and 609 °K

$$V_{uA-v} = \# Asp_{uA} \sum_{n=1}^{n=5} \% Asp_n V_{SA-n-v}$$

1300m/s		609K		
n	$V_{SA-n-v}$ (mm <sup>3</sup> )	#Asp /mm <sup>2</sup>	%Asp <sub>n</sub>	$V_{uA-v}$ (mm <sup>3</sup> /mm <sup>2</sup> )
1	0.00E+00	601	25.0%	0.00E+00
2	0.00E+00	601	30.6%	0.00E+00
3	0.00E+00	601	27.8%	0.00E+00
4	4.72E-08	601	11.1%	3.15E-06
5	1.20E-07	601	5.6%	4.01E-06
$\Sigma V_{uA-v}$				7.16E-06

$$W_{uA} = 7.2E-06 \text{ mm}^3/\text{mm}^3$$

Table A-27 Normalized Wear at 1300 m/s

$$V_d = \sum_1^v W_{uA_v} \times l_{c_v} \times w_{c_v} \times D_{s_v} \times \%Cont_v$$

v	T	$l_c$	$w_c$	$D_s$	$W_{uA}$	%Cont	Interval Wear (mm <sup>3</sup> )
(m/s)	(°K)	(mm)	(mm)	(mm)			
1300	609	28.0	90	2.E+05	7.16E-06	15.57%	438.2

Table A-28 Estimated Wear of the 1250 -1350 m/s Velocity Interval

### A.15 Results for the 1350-1450 m/s Interval

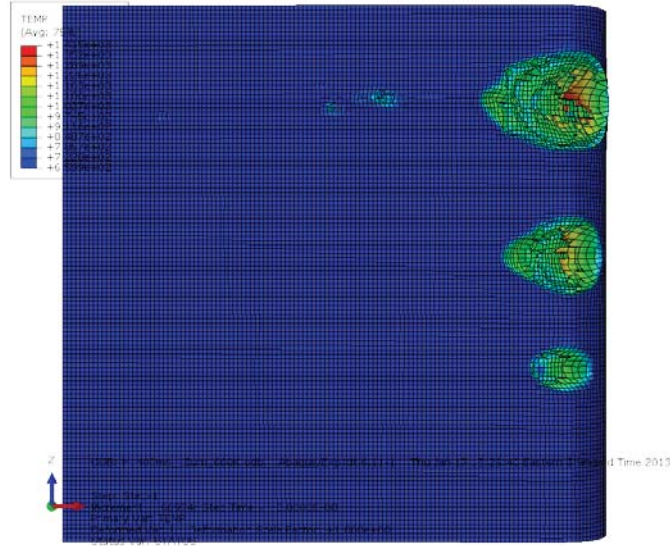


Figure A-15 Simulated Wear Patterns at 1400 m/s and 660 °K

$$V_{uA-v} = \# Asp_{uA} \sum_{n=1}^{n=5} \% Asp_n V_{SA-n-v}$$

n	$V_{SA-n-v}$ ( $mm^3$ )	#Asp / $mm^2$	%Asp <sub>n</sub>	$V_{uA-v}$ ( $mm^3/mm^2$ )
1	0.00E+00	601	25.0%	0.00E+00
2	0.00E+00	601	30.6%	0.00E+00
3	1.06E-08	601	27.8%	1.76E-06
4	5.13E-08	601	11.1%	3.42E-06
5	1.42E-07	601	5.6%	4.76E-06
$\Sigma V_{uA-v}$				9.94E-06
$W_{uA} =$				$9.9E-06 \text{ mm}^3/mm^3$

Table A-29 Normalized Wear at 1400 m/s

$$V_d = \sum_v W_{uA_v} \times l_{c_v} \times w_{c_v} \times D_{s_v} \times \%Cont_v$$

v	T	$l_c$	$w_c$	$D_s$	$W_{uA}$	%Cont	Interval Wear ( $mm^3$ )
(m/s)	(°K)	(mm)	(mm)	(mm)			
1400	660	35.0	90	2.E+05	9.94E-06	16.54%	870.6

Table A-30 Estimated Wear of the 1350 -1450 m/s Velocity Interval

## A.16 Results for the 1450-1530 m/s Interval

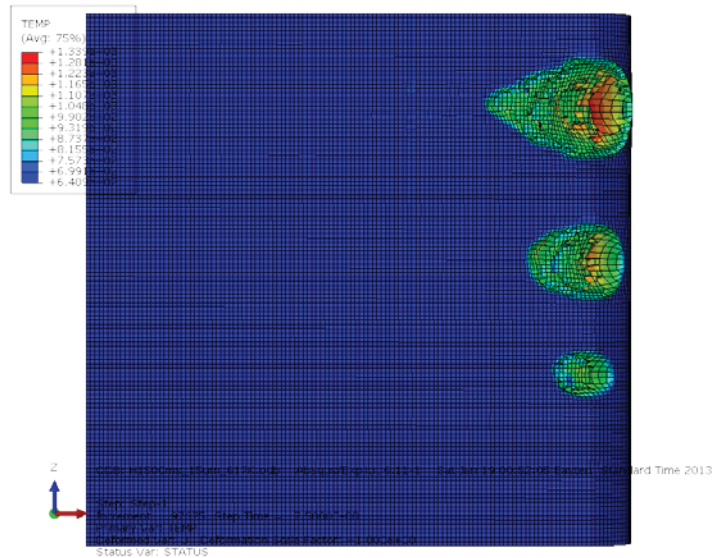


Figure A-16 Simulated Wear Patterns at 1500 m/s and 641 °K

$$V_{uA-v} = \# Asp_{uA} \sum_{n=1}^{n=5} \% Asp_n V_{SA-n-v}$$

n	$V_{SA-n-v}$ ( $mm^3$ )	#Asp / $mm^2$	%Asp <sub>n</sub>	$V_{uA-v}$ ( $mm^3/mm^2$ )
1	0.00E+00	601	25.0%	0.00E+00
2	0.00E+00	601	30.6%	0.00E+00
3	1.28E-08	601	27.8%	2.14E-06
4	5.88E-08	601	11.1%	3.92E-06
5	1.47E-07	601	5.6%	4.91E-06
			$\Sigma V_{uA-v}$	1.10E-05

$$W_{uA} = 1.1E-05 \text{ mm}^3/mm^3$$

Table A-31 Normalized Wear at 1500 m/s

$$V_d = \sum_v W_{uA} \times l_{c_v} \times w_{c_v} \times D_{s_v} \times \%Cont_v$$

v	T	$l_c$	$w_c$	$D_s$	$W_{uA}$	%Cont	Interval Wear ( $mm^3$ )
(m/s)	(°K)	(mm)	(mm)	(mm)			
1500	641	38.5	90	3.E+05	1.10E-05	16.86%	1730.7

Table A-32 Estimated Wear of the 1450 -1530 m/s Velocity Interval

### A.17 Results for the 1530-1450 m/s Interval

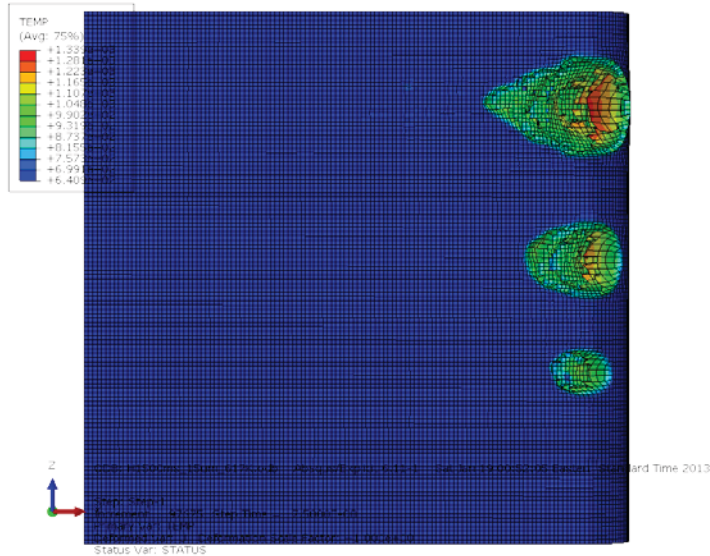


Figure A-17 Simulated Wear Patterns at 1500 m/s and 641 °K

$$V_{uA-v} = \# Asp_{uA} \sum_{n=1}^{n=5} \% Asp_n V_{SA-n-v}$$

n	$V_{SA-n-v}$ ( $mm^3$ )	#Asp / $mm^2$	%Asp <sub>n</sub>	$V_{uA-v}$ ( $mm^3/mm^2$ )
1	0.00E+00	601	25.0%	0.00E+00
2	0.00E+00	601	30.6%	0.00E+00
3	1.28E-08	601	27.8%	2.14E-06
4	5.88E-08	601	11.1%	3.92E-06
5	1.47E-07	601	5.6%	4.91E-06
			$\Sigma V_{uA-v}$	1.10E-05

$$W_{uA} = 1.1E-05 \text{ mm}^3/mm^3$$

Table A-33 Normalized Wear at 1500 m/s

$$V_d = \sum_v W_{uA_v} \times l_{c_v} \times w_{c_v} \times D_{s_v} \times \%Cont_v$$

v	$T$	$l_c$	$w_c$	$D_s$	$W_{uA}$	%Cont	Interval Wear ( $mm^3$ )
(m/s)	(°K)	(mm)	(mm)	(mm)			
1500	641	2.0	90	3.E+05	1.10E-05	6.11%	36.2

Table A-34 Estimated Wear of the 1530 -1450 m/s Velocity Interval

### A.18 Results for the 1450-1350 m/s Interval

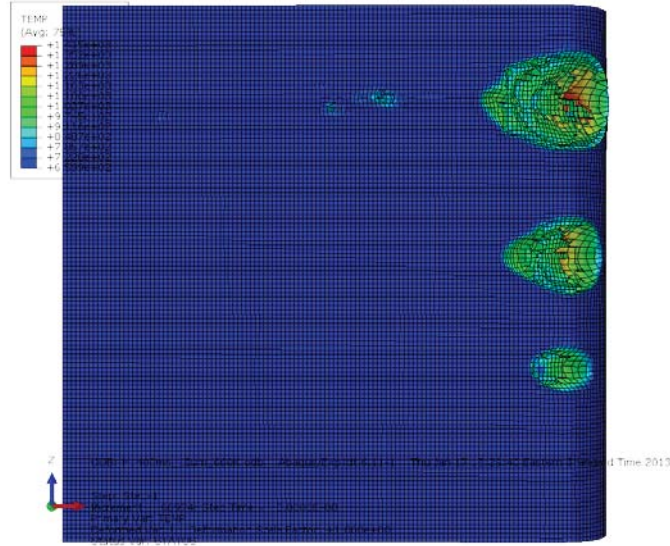


Figure A-18 Simulated Wear Patterns at 1400 m/s and 660 °K

$$V_{uA-v} = \# Asp_{uA} \sum_{n=1}^{n=5} \% Asp_n V_{SA-n-v}$$

n	$V_{SA-n-v}$ ( $mm^3$ )	#Asp / $mm^2$	%Asp <sub>n</sub>	$V_{uA-v}$ ( $mm^3/mm^2$ )
1	0.00E+00	601	25.0%	0.00E+00
2	0.00E+00	601	30.6%	0.00E+00
3	1.06E-08	601	27.8%	1.76E-06
4	5.13E-08	601	11.1%	3.42E-06
5	1.42E-07	601	5.6%	4.76E-06
$\Sigma V_{uA-v}$				9.94E-06
$W_{uA} =$				$9.9E-06 \text{ mm}^3/mm^3$

Table A-35 Normalized Wear at 1400 m/s

$$V_d = \sum_1^v W_{uA_v} \times l_{c_v} \times w_{c_v} \times D_{s_v} \times \%Cont_v$$

v	T	$l_c$	$w_c$	$D_s$	$W_{uA}$	%Cont	Interval Wear ( $mm^3$ )
(m/s)	(°K)	(mm)	(mm)	(mm)			
1400	660	6.0	90	3.E+05	9.94E-06	5.03%	75.6

Table A-36 Estimated Wear of the 1350 -1450 m/s Velocity Interval

### A.19 Results for the 1350-1250 m/s Interval

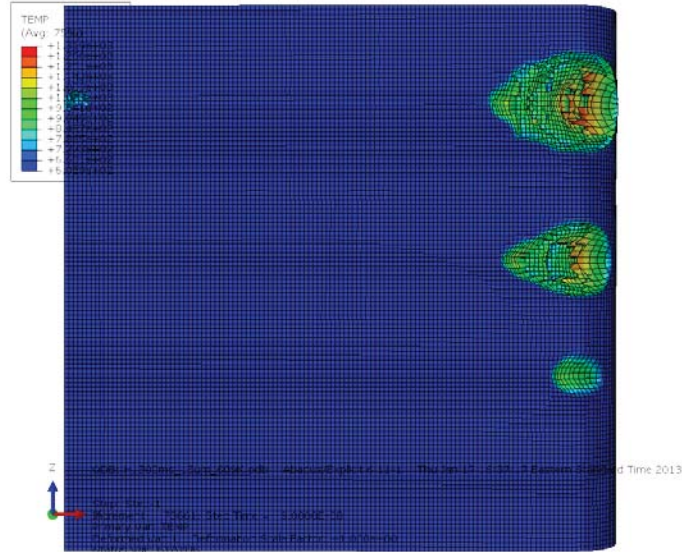


Figure A-19 Simulated Wear Patterns at 1300 m/s and 609 °K

$$V_{uA-v} = \# Asp_{uA} \sum_{n=1}^{n=5} \% Asp_n V_{SA-n-v}$$

1300m/s		609K		
n ( $\mu\text{m}$ )	$V_{SA-n-v}$ ( $\text{mm}^3$ )	#Asp / $\text{mm}^2$	%Asp <sub>n</sub>	$V_{uA-v}$ ( $\text{mm}^3/\text{mm}^2$ )
1	0.00E+00	601	25.0%	0.00E+00
2	0.00E+00	601	30.6%	0.00E+00
3	0.00E+00	601	27.8%	0.00E+00
4	4.72E-08	601	11.1%	3.15E-06
5	1.20E-07	601	5.6%	4.01E-06
$\Sigma V_{uA-v}$				7.16E-06

$$W_{uA} = 7.2\text{E-}06 \text{ mm}^3/\text{mm}^3$$

Table A-37 Normalized Wear at 1300 m/s

$$V_d = \sum_{v=1}^v W_{uA_v} \times l_{c_v} \times w_{c_v} \times D_{s_v} \times \%Cont_v$$

v	$T$	$l_c$	$w_c$	$D_s$	$W_{uA}$	%Cont	Interval Wear ( $\text{mm}^3$ )
(m/s)	(°K)	(mm)	(mm)	(mm)			
1300	609	10.0	90	3.E+05	7.16E-06	5.10%	85.5

Table A-38 Estimated Wear of the 1350 -1250 m/s Velocity Interval

## A.20 Results for the 1250-1150 m/s Interval

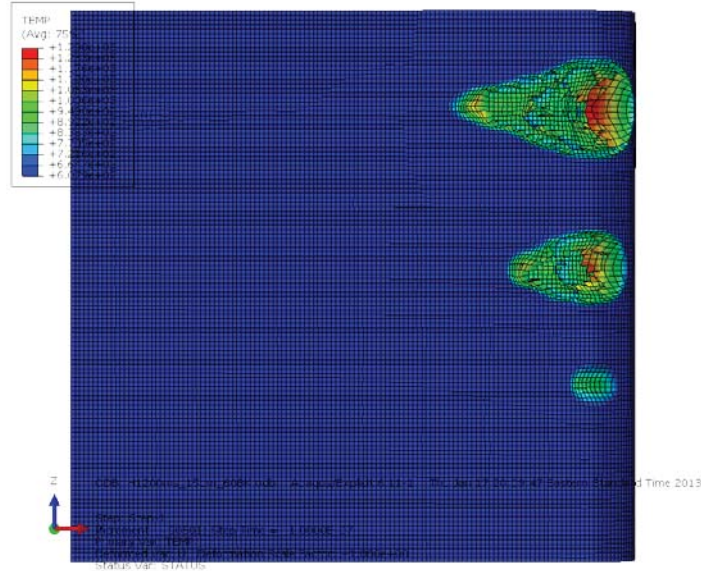


Figure A-20 Simulated Wear Patterns at 1200 m/s and 608 °K

$$V_{uA-v} = \# Asp_{uA} \sum_{n=1}^{n=5} \% Asp_n V_{SA-n-v}$$

n ( $\mu\text{m}$ )	$V_{SA-n-v}$ ( $\text{mm}^3$ )	#Asp / $\text{mm}^2$	%Asp <sub>n</sub>	$V_{uA-v}$ ( $\text{mm}^3/\text{mm}^2$ )
1	0.00E+00	601	25.0%	0.00E+00
2	0.00E+00	601	30.6%	0.00E+00
3	0.00E+00	601	27.8%	0.00E+00
4	4.95E-08	601	11.1%	3.31E-06
5	1.39E-07	601	5.6%	4.63E-06
$\Sigma V_{uA-v}$				7.94E-06

$$W_{uA} = 7.9E-06 \text{ mm}^3/\text{mm}^3$$

Table A-39 Normalized Wear at 1200 m/s

$$V_d = \sum_1^v W_{uA_v} \times l_{c_v} \times w_{c_v} \times D_{s_v} \times \%Cont_v$$

v (m/s)	T (°K)	$l_c$ (mm)	$w_c$ (mm)	$D_s$ (mm)	$W_{uA}$	%Cont	Interval Wear ( $\text{mm}^3$ )
1200	608	14.0	90	2.E+05	7.94E-06	5.36%	128.6

Table A-40 Estimated Wear of the 1250 -1150 m/s Velocity Interval

## A.21 Results for the 1150-1050 m/s Interval

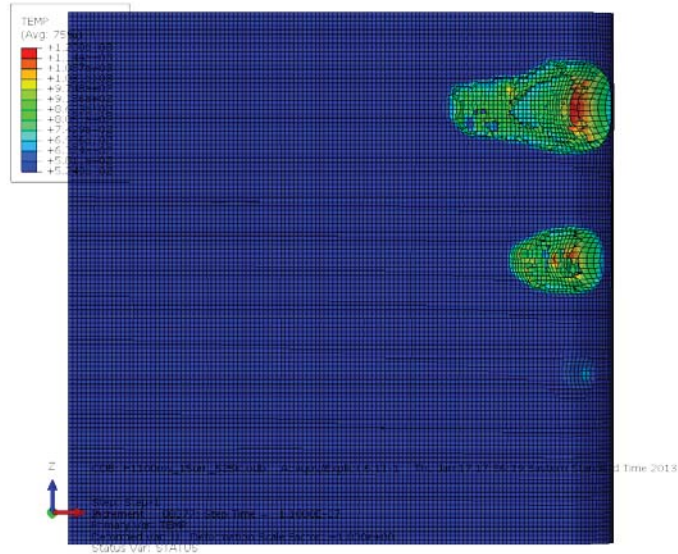


Figure A-21 Simulated Wear Patterns at 1100 m/s and 525 °K

$$V_{uA-v} = \# Asp_{uA} \sum_{n=1}^{n=5} \% Asp_n V_{SA-n-v}$$

n	$V_{SA-n-v}$ ( $mm^3$ )	#Asp / $mm^2$	%Asp <sub>n</sub>	$V_{uA-v}$ ( $mm^3/mm^2$ )
1	0.00E+00	601	25.0%	0.00E+00
2	0.00E+00	601	30.6%	0.00E+00
3	0.00E+00	601	27.8%	0.00E+00
4	3.65E-08	601	11.1%	2.43E-06
5	1.36E-07	601	5.6%	4.54E-06
$\Sigma V_{uA-v}$				6.98E-06

$$W_{uA} = 7.0E-06 \text{ mm}^3/mm^3$$

Table A-41 Normalized Wear at 1100 m/s

$$V_d = \sum_v W_{uA_v} \times l_{c_v} \times w_{c_v} \times D_{s_v} \times \%Cont_v$$

v	T	$l_c$	$w_c$	$D_s$	$W_{uA}$	%Cont	Interval Wear ( $mm^3$ )
(m/s)	(°K)	(mm)	(mm)	(mm)			
1100	525	18.0	90	2.E+05	6.98E-06	6.22%	154.6

Table A-42 Estimated Wear of the 1150 -1050 m/s Velocity Interval

## A.22 Results for the 1050-950 m/s Interval

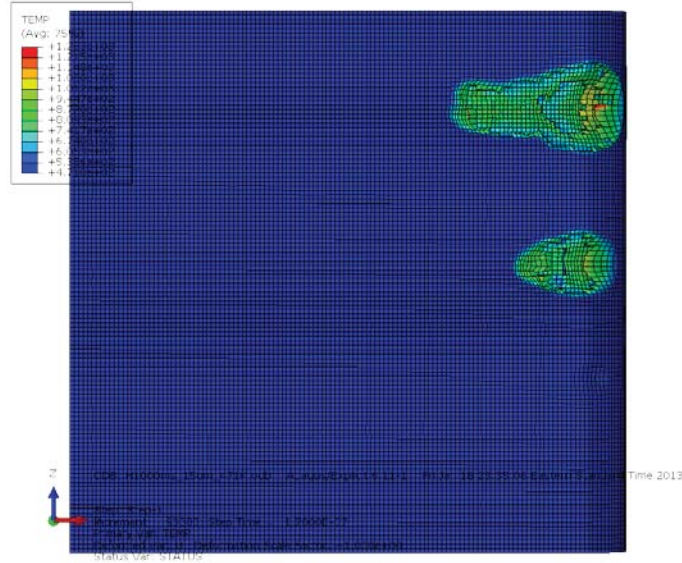


Figure A-22 Simulated Wear Patterns at 1000 m/s and 472 °K

$$V_{uA-v} = \# Asp_{uA} \sum_{n=1}^{n=5} \% Asp_n V_{SA-n-v}$$

n	$V_{SA-n-v}$ ( $mm^3$ )	#Asp / $mm^2$	%Asp <sub>n</sub>	$V_{uA-v}$ ( $mm^3/mm^2$ )
1	0.00E+00	601	25.0%	0.00E+00
2	0.00E+00	601	30.6%	0.00E+00
3	0.00E+00	601	27.8%	0.00E+00
4	2.77E-08	601	11.1%	1.85E-06
5	1.10E-07	601	5.6%	3.68E-06
$\Sigma V_{uA-v}$				5.53E-06

$$W_{uA} = 5.5E-06 \text{ mm}^3/mm^3$$

Table A-43 Normalized Wear at 1000 m/s

$$V_d = \sum_v W_{uA_v} \times l_{c_v} \times w_{c_v} \times D_{s_v} \times \%Cont_v$$

v	T	$l_c$	$w_c$	$D_s$	$W_{uA}$	%Cont	Interval Wear ( $mm^3$ )
(m/s)	(°K)	(mm)	(mm)	(mm)			
1000	471	23.0	90	3.E+05	5.53E-06	7.30%	175.6

Table A-44 Estimated Wear of the 1050 -950 m/s Velocity Interval

### A.23 Results for the 950-850 m/s Interval

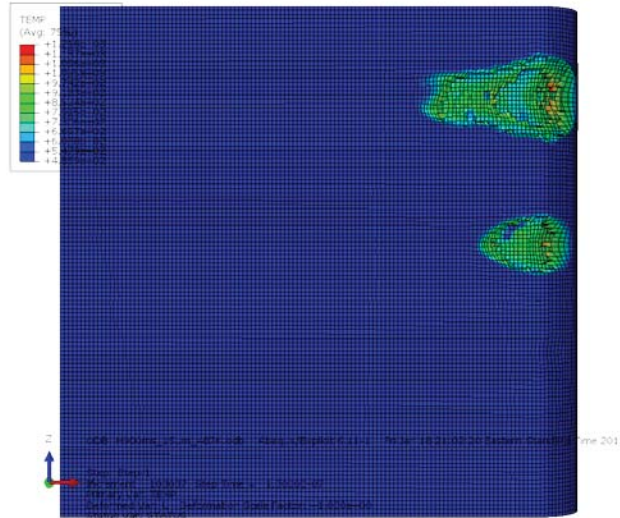


Figure A-23 Simulated Wear Patterns at 900 m/s and 486 °K

$$V_{uA-v} = \# Asp_{uA} \sum_{n=1}^{n=5} \% Asp_n V_{SA-n-v}$$

n	$V_{SA-n-v}$ ( $mm^3$ )	#Asp / $mm^2$	%Asp <sub>n</sub>	$V_{uA-v}$ ( $mm^3/mm^2$ )
1	0.00E+00	601	25.0%	0.00E+00
2	0.00E+00	601	30.6%	0.00E+00
3	0.00E+00	601	27.8%	0.00E+00
4	3.00E-08	601	11.1%	2.00E-06
5	1.22E-07	601	5.6%	4.09E-06
			$\Sigma V_{uA-v}$	6.09E-06
				$W_{uA} = 6.1E-06 \text{ mm}^3/mm^3$

Table A-45 Normalized Wear at 900 m/s

$$V_d = \sum_v W_{uA_v} \times l_{c_v} \times w_{c_v} \times D_{s_v} \times \%Cont_v$$

v	T	$l_c$	$w_c$	$D_s$	$W_{uA}$	%Cont	Interval Wear ( $mm^3$ )
(m/s)	(°K)	(mm)	(mm)	(mm)			
900	487	10.5	90	3.E+05	6.09E-06	7.17%	78.1

Table A-46 Estimated Wear of the 950 -850 m/s Velocity Interval

## A.24 Results for the 850-750 m/s Interval

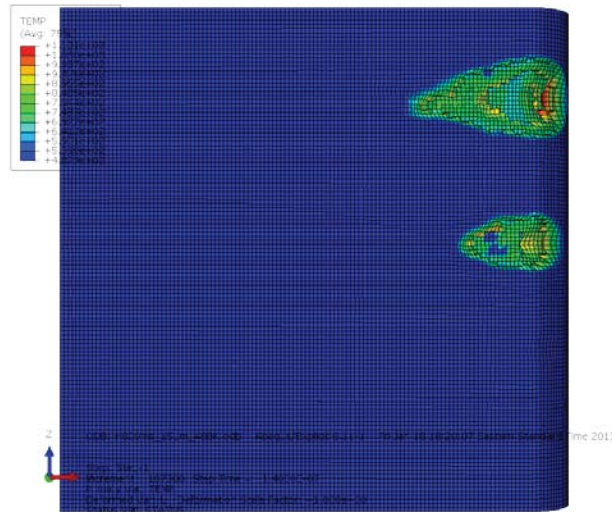


Figure A-24 Simulated Wear Patterns at 800 m/s and 488 °K

$$V_{uA-v} = \# Asp_{uA} \sum_{n=1}^{n=5} \% Asp_n V_{SA-n-v}$$

n	$V_{SA-n-v}$ ( $mm^3$ )	#Asp / $mm^2$	$\% Asp_n$	$V_{uA-v}$ ( $mm^3/mm^2$ )
1	0.00E+00	601	25.0%	0.00E+00
2	0.00E+00	601	30.6%	0.00E+00
3	0.00E+00	601	27.8%	0.00E+00
4	3.73E-08	601	11.1%	2.49E-06
5	1.18E-07	601	5.6%	3.95E-06
$\Sigma V_{uA-v}$				6.45E-06

$$W_{uA} = 6.4E-06 \text{ mm}^3/\text{mm}^3$$

Table A-47 Normalized Wear at 800 m/s

$$V_d = \sum_{v=1}^v W_{uA_v} \times l_{c_v} \times w_{c_v} \times D_{s_v} \times \% Cont_v$$

v	T (°K)	$l_c$ (mm)	$w_c$ (mm)	$D_s$ (mm)	$W_{uA}$	$\% Cont$	Interval Wear ( $mm^3$ )
800	488	19.9	90	4.E+05	6.45E-06	6.42%	207.2

Table A-48 Estimated Wear of the 850 -750 m/s Velocity Interval

## A.25 Results for the 750-622 m/s Interval

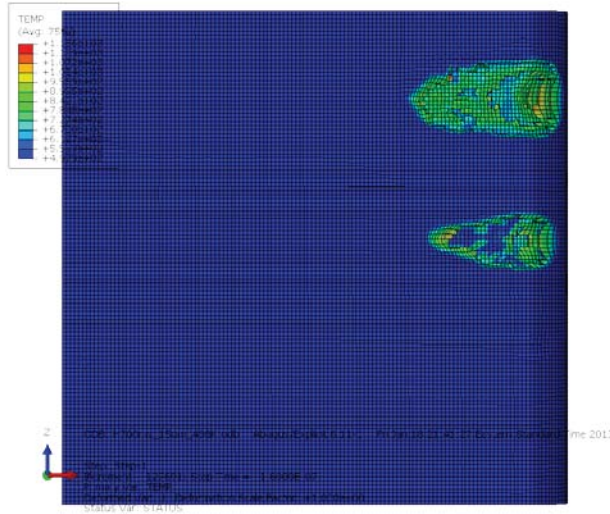


Figure A-25 Simulated Wear Patterns at 700 m/s and 498 °K

$$V_{uA-v} = \# Asp_{uA} \sum_{n=1}^{n=5} \% Asp_n V_{SA-n-v}$$

n	$V_{SA-n-v}$ ( $mm^3$ )	#Asp / $mm^2$	$\% Asp_n$	$V_{uA-v}$ ( $mm^3/mm^2$ )
1	0.00E+00	601	25.0%	0.00E+00
2	0.00E+00	601	30.6%	0.00E+00
3	0.00E+00	601	27.8%	0.00E+00
4	4.93E-08	601	11.1%	3.29E-06
5	1.34E-07	601	5.6%	4.49E-06
$\Sigma V_{uA-v}$				7.78E-06

$$W_{uA} = 7.8E-06 \text{ mm}^3/mm^3$$

Table A-49 Normalized Wear at 700 m/s

$$V_d = \sum_v W_{uA_v} \times l_{c_v} \times w_{c_v} \times D_{s_v} \times \% Cont_v$$

v	T	$l_c$	$w_c$	$D_s$	$W_{uA}$	$\% Cont$	Interval Wear ( $mm^3$ )
(m/s)	(°K)	(mm)	(mm)	(mm)			
700	498	38.6	90	6.E+05	7.78E-06	6.23%	659.9

Table A-50 Estimated Wear of the 650 -750 m/s Velocity Interval

## A.26 Results for the 650-622 m/s Interval

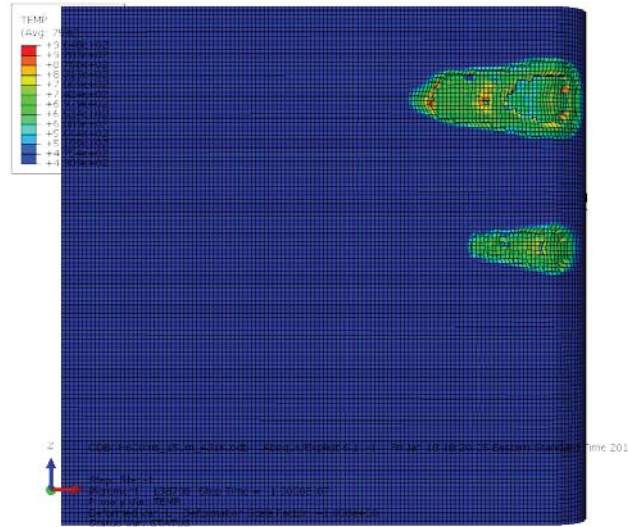


Figure A-26 Simulated Wear Patterns at 635 m/s and 432 °K

$$V_{uA-v} = \# Asp_{uA} \sum_{n=1}^{n=5} \% Asp_n V_{SA-n-v}$$

n	$V_{SA-n-v}$ ( $mm^3$ )	#Asp / $mm^2$	$\% Asp_n$	$V_{uA-v}$ ( $mm^3/mm^2$ )
1	0.00E+00	601	25.0%	0.00E+00
2	0.00E+00	601	30.6%	0.00E+00
3	0.00E+00	601	27.8%	0.00E+00
4	3.38E-08	601	11.1%	2.27E-06
5	1.27E-07	601	5.6%	4.21E-06
$\Sigma V_{uA-v}$				6.48E-06

$$W_{uA} = 6.5E-06 \text{ mm}^3/\text{mm}^3$$

Table A-51 Normalized Wear at 600 m/s

$$V_d = \sum_v W_{uA_v} \times l_{c_v} \times w_{c_v} \times D_{s_v} \times \% Cont_v$$

v	T	$l_c$	$w_c$	$D_s$	$W_{uA}$	$\% Cont$	Interval Wear ( $mm^3$ )
(m/s)	(°K)	(mm)	(mm)	(mm)			
635	450	46.7	90	1.E+05	6.48E-06	7.26%	175.8

Table A-52 Estimated Wear of the 650 -622 m/s Velocity Interval

## Appendix B. Example of the Abaqus Sliding Wear Report

The following is an example of a report requested to Abaqus to estimate the sliding wear. These reports directly provide the initial volume of each failed element (EVOL) and the cumulative volume of failed elements in each model part, assumed to be this part wear. It reports only the failed elements based in the binary STATUS variable, which has a value of 1 if the element is active or 0 if it has failed. The report is the one obtained from the simulations carried with an initial velocity of 25 m/s. The reports from all the other velocities had many more failed elements and therefore are much longer than this one. For this reason only one of such reports was included in this appendix.

\*\*\*\*\*

Field Output Report, written Mon Jun 28 10:43:38 2013

Source 1

ODB: C:/rbuentel/Documents/3DModel/MultiAsp/HHSTTFinal/H025ms\_15um\_297K.odb

Step: Step-1

Frame: Increment 0: Step Time = 0.0

Loc 1 : Whole element values from source 1

Output sorted by column "Element Label".

Field Output reported for whole element for part: SLIPERW4-1

Element Label	EVOL @Loc 1
44746	212.443E-12
44747	212.238E-12
45020	204.759E-12
45072	200.881E-12
45073	202.680E-12
45083	208.438E-12
45087	205.594E-12
45112	200.207E-12
45485	203.724E-12
45549	212.448E-12
45550	212.243E-12
45578	208.840E-12
45821	211.859E-12
45823	204.764E-12
45875	200.886E-12
45876	202.685E-12
45886	208.443E-12
45888	212.063E-12
45890	205.600E-12
45915	200.212E-12
46288	203.719E-12
46352	212.443E-12
46353	212.238E-12
46354	186.632E-12

46381 208.835E-12  
46597 192.582E-12  
46621 195.469E-12  
46624 211.854E-12  
46626 204.759E-12  
46678 200.881E-12  
46679 202.680E-12  
46689 208.438E-12  
46691 212.058E-12  
46693 205.594E-12  
46718 200.207E-12  
47091 203.719E-12  
47092 189.656E-12  
47155 212.443E-12  
47156 212.238E-12  
47157 186.632E-12  
47184 208.835E-12  
47400 192.582E-12  
47424 195.469E-12  
47427 211.854E-12  
47429 204.759E-12  
47481 200.881E-12  
47482 202.680E-12  
47492 208.438E-12  
47494 212.058E-12  
47496 205.594E-12  
47521 200.207E-12  
47894 203.719E-12  
47895 189.656E-12  
47958 212.443E-12  
47959 212.238E-12  
47960 186.632E-12  
47987 208.835E-12  
48203 192.582E-12  
48227 195.469E-12  
48230 211.854E-12  
48232 204.759E-12  
48284 200.881E-12  
48285 202.680E-12  
48295 208.438E-12  
48297 212.058E-12  
48299 205.594E-12  
48324 200.207E-12  
48697 203.719E-12  
48698 189.656E-12  
48761 212.443E-12  
48762 212.238E-12  
48763 186.632E-12  
48790 208.835E-12  
49006 192.582E-12  
49030 195.469E-12  
49033 211.854E-12  
49035 204.759E-12  
49087 200.881E-12  
49088 202.680E-12  
49098 208.438E-12  
49100 212.058E-12  
49102 205.594E-12  
49127 200.207E-12  
49564 212.448E-12  
49565 212.243E-12  
49593 208.840E-12  
49809 192.586E-12  
49836 211.859E-12  
49838 204.764E-12  
49890 200.886E-12  
49891 202.685E-12  
49901 208.443E-12

49903	212.063E-12
49905	205.600E-12
49930	200.212E-12
50367	212.443E-12
50396	208.835E-12
50639	211.854E-12
50641	204.759E-12
50693	200.881E-12
50694	202.680E-12
50706	212.058E-12
50708	205.594E-12
50733	200.207E-12
51199	208.835E-12
51444	204.759E-12
51496	200.881E-12
51497	202.680E-12
51511	205.594E-12
51536	200.207E-12

Total 22.4884E-09

Field Output reported for whole element for part: SLIPERW5-1

Element Label	EVOL @Loc 1
71157	221.516E-12
71158	216.335E-12
71900	211.675E-12
71952	221.510E-12
71953	216.330E-12
71991	227.084E-12
72418	212.799E-12
72665	222.924E-12
72695	211.680E-12
72747	221.516E-12
72748	216.335E-12
72786	227.090E-12
73213	212.794E-12
73240	205.654E-12
73460	222.919E-12
73488	203.038E-12
73490	211.675E-12
73542	221.510E-12
73543	216.330E-12
73557	207.137E-12
73581	227.084E-12
74006	196.962E-12
74007	196.186E-12
74035	205.659E-12
74255	222.924E-12
74283	203.043E-12
74285	211.680E-12
74337	221.516E-12
74338	216.335E-12
74350	199.261E-12
74352	207.142E-12
74376	227.090E-12
74801	196.957E-12
74802	196.181E-12
74803	212.794E-12
74830	205.654E-12
74839	210.371E-12
75050	222.919E-12
75078	203.038E-12
75080	211.675E-12

75132 221.510E-12  
75133 216.330E-12  
75145 199.256E-12  
75147 207.137E-12  
75171 227.084E-12  
75531 193.427E-12  
75596 196.962E-12  
75597 196.186E-12  
75598 212.799E-12  
75625 205.659E-12  
75634 210.376E-12  
75845 222.924E-12  
75873 203.043E-12  
75875 211.680E-12  
75927 221.516E-12  
75928 216.335E-12  
75938 193.579E-12  
75940 199.261E-12  
75942 207.142E-12  
75966 227.090E-12  
76326 193.423E-12  
76391 196.957E-12  
76392 196.181E-12  
76393 212.794E-12  
76420 205.654E-12  
76429 210.371E-12  
76640 222.919E-12  
76665 191.023E-12  
76668 203.038E-12  
76670 211.675E-12  
76722 221.510E-12  
76723 216.330E-12  
76733 193.574E-12  
76735 199.256E-12  
76737 207.137E-12  
76761 227.084E-12  
77121 193.423E-12  
77186 196.957E-12  
77187 196.181E-12  
77188 212.794E-12  
77215 205.654E-12  
77224 210.371E-12  
77435 222.919E-12  
77460 191.023E-12  
77463 203.038E-12  
77465 211.675E-12  
77517 221.510E-12  
77518 216.330E-12  
77528 193.574E-12  
77530 199.256E-12  
77532 207.137E-12  
77556 227.084E-12  
77916 193.427E-12  
77981 196.962E-12  
77982 196.186E-12  
77983 212.799E-12  
78010 205.659E-12  
78019 210.376E-12  
78230 222.924E-12  
78231 208.715E-12  
78255 191.027E-12  
78258 203.043E-12  
78260 211.680E-12  
78312 221.516E-12  
78313 216.335E-12  
78323 193.579E-12  
78325 199.261E-12  
78327 207.142E-12

78351	227.090E-12
78711	193.423E-12
78776	196.957E-12
78777	196.181E-12
78778	212.794E-12
78788	210.115E-12
78805	205.654E-12
78814	210.371E-12
79025	222.919E-12
79026	208.710E-12
79050	191.023E-12
79053	203.038E-12
79055	211.675E-12
79107	221.510E-12
79108	216.330E-12
79118	193.574E-12
79120	199.256E-12
79122	207.137E-12
79146	227.084E-12
79571	196.962E-12
79573	212.799E-12
79600	205.659E-12
79820	222.924E-12
79848	203.043E-12
79850	211.680E-12
79902	221.516E-12
79903	216.335E-12
79915	199.261E-12
79917	207.142E-12
79941	227.090E-12
80368	212.794E-12
80615	222.919E-12
80645	211.675E-12
80697	221.510E-12
80698	216.330E-12
80712	207.137E-12
80736	227.084E-12

Total 30.4188E-09

## **Appendix C. Theoretical Background**

The wear scenario simulated has to do with micro-level asperities colliding at high speeds. This scenario involves a complex wear problem that requires the understanding of several topics such as large displacements, large strains, large strain rates, viscoplastic flow stress, conservation equations, energy methods, finite element (FE) integration methods, shock waves, equations of state, adiabatic process, surface interactions, etc. This appendix will provide the pertinent theory for this problem. Most of this theory was obtained from the Abaqus Analysis User's Manual [31]. This theory will be presented summarizing the Abaqus Analysis User's Manual development [31]:

Section 1.1 -- Description, Mesh, and Formulation

Section 1.2 -- Deformation, Stress and Strain measures

Section 1.3 -- Conservation Equations & Virtual Work

Section 1.4 -- Elasto-Viscoplastic Material Behavior

Section 1.5 -- FE Concepts and Algorithms

Section 1.6 -- Mie -Gruneisen Equation of State Concepts

Section 1.7 -- Surface Characteristics and Interactions

Section 1.8 -- Experimentation and Extrapolation Concepts

It must be pointed out that many of these sections are missing the detailed background theory since each section could become an appendix itself. The theory presented only shows the important features utilized by this wear model. It is the intent of this appendix to include a great deal of information from many different references. These references will be included as at the appropriate point in the write up. This appendix is meant to be a good reference for students that may succeed after the author.

## **1.1 Description, Mesh and Formulation**

### **1.1.1 Types of Descriptions:**

When analyzing the time dependent material behavior it is necessary to describe the evolution of their translation and morphology throughout time. There are two main ways to describe this evolution, either using a Lagrangian or an Eulerian description.

#### ***1.1.1.1 Lagrangian Description:***

The Lagrangian or material description states motion as a function, of the material's original, reference, or undeformed state coordinates,  $\mathbf{X}$ , and time,  $t$ . Mathematically expressed as  $f(\mathbf{X}, t)$ , where the independent variables are the position coordinates of the original state ( $X_1, X_2$  and  $X_3$ ) and time,  $t$ .

#### ***1.1.1.2 Eulerian Description:***

The Eulerian or spatial description states motion as a function,  $f$ , of the material's current or deformed state coordinates,  $\mathbf{x}$ , and time,  $t$ . Mathematically expressed as  $f(\mathbf{x}, t)$ , where the independent variables are the position coordinates of the current state ( $x_1, x_2$  and  $x_3$ ) and time,  $t$ .

Usually one states the Eulerian coordinate system as fixed in space, where the material particles pass through this fixed system.

### **1.1.2 Types of Meshes:**

FE models divide a structure of interest into finite elements. These elements are composed of various points, called nodes. Each of these nodes connects to its contiguous nodes creating a web throughout the structure. This web is called a mesh. The mesh is programmed with all the necessary information to simulate how the structure will respond to the applied conditions. During the analysis this mesh carries this information throughout the structure. There are two main ways to mesh structures involving the motion of deformable materials; either with a Lagrangian or an Eulerian meshes [106].

### 1.1.2.1 Lagrangian Mesh

On a Lagrangian mesh the material is confined into each element of the mesh and therefore no other material can pass through it. The mesh deforms as the body deforms.

Figure C-1, shows a Lagrangian mesh, both the mesh nodes (green) and the points representing the confined material (purple) change position as the body deforms.

This figure, one can also observe the boundary nodes remain on the edge facilitating the application of boundary and interface conditions [106].

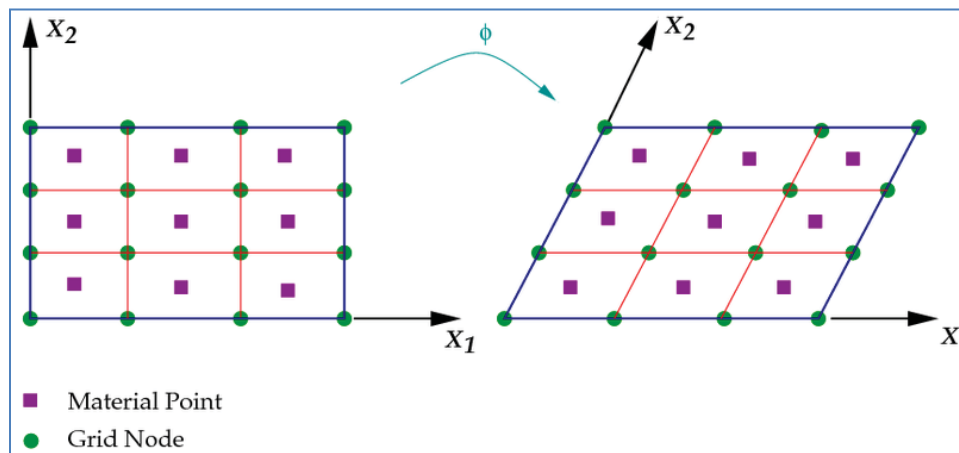


**Figure C-1 Lagrangian Mesh [106].**

The mesh of this 3D wear model is Lagrangian and it moves with the material throughout the micro-asperity collision event. This Lagrangian approach was followed based on the lessons learned from previous AFIT studies, carried out by Hale [232], and the FEA package selected to carry out the simulations, Abaqus.

### 1.1.2.2 Eulerian Mesh

The Eulerian mesh is a background mesh, fixed in space. For this type of mesh the nodes remain in their original position and the material particles flow through the mesh, as it deforms. Figure C-2, shows how the mesh nodes (green) remain fixed and the materials points (purple) flow through it. The position of a material point relative to the nodes varies with the motion.

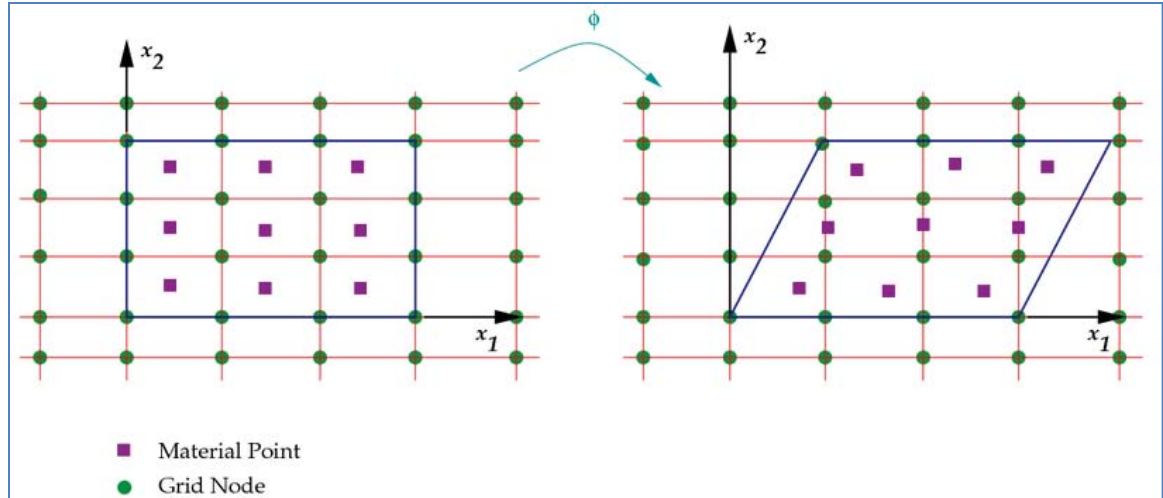


**Figure C-2 Eulerian Mesh [106].**

This type of mesh is not used for this 3D FE wear model; however it is used in the CTH hydrocode selected to carry out the sliding wear thermal analysis [66] and by some of the previous 2D wear models developed at AFIT [26, 46].

### 1.1.3 Types of FE Formulations

There are various ways to formulate, in FE, the motion of deformable materials throughout time. The formulas can be Lagrangian, Updated Lagrangian, Eulerian, or Lagrangian-Eulerian..

#### 1.1.3.1 Total Lagrangian Formulation:

This is a strictly Lagrangian approach used for structures modeled with Lagrangian meshes. In this formulation one traces material time dependent behavior with respect to the material (Lagrangian) coordinates,  $\mathbf{X}$ , and time,  $t$  [59]. This formulation involves only Lagrangian stress-strain measures such as the second Piola-Kirchhoff stress (section 1.2.17), the objective strain referred as the Green strain tensor (section 1.2.9) [59]. It becomes problematic for large deformations, especially in relating the stress to strain while satisfying the compatibility relations. Instead of using this approach, Abaqus typically uses the updated Lagrangian approach.

### ***1.1.3.2 Updated Lagrangian formulation:***

The Updated Lagrangian Formulation (ULF) is another way to analyze problems simulated with a Lagrangian mesh. This formulation traces material time dependent behavior with respect to the material (Lagrangian) coordinates,  $\mathbf{X}$ , and time,  $t$ , however, this formulation is typically expressed via Eulerian stress-strain measures. All the Lagrangian stress-strain measures are substituted, via transformations of tensors and mappings of configurations, with Eulerian stress-strain measures [59].

The ULF is conventionally used with a Lagrangian mesh but is expressed in Eulerian measures, such as the Cauchy stress (section 1.2.14), the rate of deformation (section 1.2.7), and the Jaumann stress rate (section 1.2.22). Its derivatives are with respect to the spatial (Eulerian) coordinates; and its integrals evaluated over the deformed or current (Eulerian) configuration [59].

In an ULF, the deformed configuration (Eulerian) at the end of the explicit time increment is taken as the initial or reference state (Lagrangian) for the subsequent time increment and this process is continually updated as the explicit time steps (section 1.5.2) proceed. In other words, one traces the material deformation by fixing an axis passing through the displaced point at the end of a time increment, (Eulerian coordinate system). Then, one uses this previously Eulerian point as the reference coordinate system (Lagrangian) for the next time increment [59].

For the formulations presented in this paper, it is important to understand that since the ULF is employed then one deals with incremental deformations. Therefore, one doesn't integrate over the entire deformed volume, one integrates only over the incremental volume of each explicit time step (section 1.5.2). In the ULF at each time step the initial, reference, Lagrangian Volume,  $V_0$ , is the deformed, Eulerian, current volume,  $V$ , of the previous step. In other words  $V_{0i}=V_{i-1}$  where "i" is the suffix that represents the explicit time step. In other words, in the ULF the "Lagrangian" original volume  $V_0$  of a step, it is certainly the Eulerian deformed volume  $V$  from the previous step.

The following sections will define both, the Lagrangian and Eulerian stress and strain measures (sections 1.2.9 through 1.2.17), how to transform these measures from

Eulerian to Lagrangian (Section 1.2.23) and vice versa, and the formulation required to develop the ULF (section 1.3.6). For example:

Section 1.2.23 will define the stress-strain work conjugates and will explain how their product is a scalar called the internal work,  $U_{int}$ . This scalar can be expressed in either Lagrangian or Eulerian measures as:

$$U_{int} = \int_{V_0} \boldsymbol{\varepsilon} \boldsymbol{\Sigma} dV_0 \quad \text{or} \quad U_{int} = \int_V \boldsymbol{\varepsilon} \boldsymbol{\sigma} dV \quad (\text{C-1})$$

where  $U_{int}$  is the internal work,  $\boldsymbol{\varepsilon}$  is the logarithmic strain,  $\boldsymbol{\Sigma}$  is the Second Piola-Kirchhoff stress tensor,  $\boldsymbol{\sigma}$  is the Cauchy stress tensor,  $V$  is the current deformed volume (Eulerian) and  $V_0$  is the reference volume (Lagrangian) [59]. Keep in mind that in an ULF the deformed volume at the end of a time step becomes the reference volume for the next time step.

Section 1.2.23 will also explain how using the Cauchy stress becomes problematic for large displacements, since in this case the stress is acting over an area with a changing volume. This section explains how one can substitute the Cauchy stress, for the product of the Kirchhoff stress,  $\boldsymbol{\tau}$ , (defined in 1.2.15), and the Jacobian matrix,  $J$ , (defined in section 1.2.4) to balance any volume change during the motion [59].

$$U_{int} = \int_V \boldsymbol{\varepsilon} \boldsymbol{\tau} J^{-1} dV \quad (\text{C-2})$$

Section 1.3.6 develops the formulation to apply these internal work scalars in the virtual work principle, expressed in an Updated Lagrangian form as:

$$\int_V \boldsymbol{\sigma} : \delta \mathbf{D} dV = \int_S \delta \mathbf{v} \cdot \mathbf{t} dS + \int_V \delta \mathbf{v} \cdot \mathbf{f} dV \quad (\text{C-3})$$

where  $V$  is the volume the current configuration (Eulerian),  $S$  is the surface surrounding the current volume,  $\boldsymbol{\sigma}$  is the Cauchy stress,  $\mathbf{D}$  is the strain rate or rate of deformation,  $\mathbf{v}$  is the velocity,  $\mathbf{t}$  is the traction vector, and  $\mathbf{f}$  is the body force per unit of current volume. Keep in mind that in an ULF the deformed volume at the end of a time step becomes the reference volume for the next time step [59].

This ULF is the one employed in this 3D wear model, built in Abaqus, with a Lagrangian mesh, to solve the system of equations for this problem.

### ***1.1.3.3 Eulerian and Lagrangian-Eulerian formulations:***

This 3D FE wear model was developed using a Lagrangian mesh and Abaqus uses the Updated Lagrangian Formulation to solve the simulations. The Eulerian and Lagrangian-Eulerian formulations mentioned next are only stated for completeness of the concepts presented in this document.

The Eulerian approach is stated as a function of the spatial coordinates and employs Eulerian stress-strain measures. On this approach the mesh is fixed in space and the material is passing through it. This Eulerian formulation is typically used for fluid mechanics [59]. The Lagrangian approach is typically used for deformation of solids.

In recent years, the Lagrangian and Eulerian approaches have been combined to develop Lagrangian-Eulerian methods to model large deformation of solids. Abaqus offers the capability to use an adaptive Lagrangian-Eulerian technique; however, for this model the technique wasn't used because it doesn't work properly with the element deletion feature employed in this model and presented in section 3.5.5.

## **1.2 Deformation, Stress and Strain Measures**

### **1.2.1 Displacement**

A displacement is a change in position and/or morphology of a continuum body. The displacement can be expressed in terms of a rigid-body displacement and a deformation. The rigid-body displacement is the translation and/or rotation of the body without changing its morphology. Deformation is the morphing in shape and/or size of the body from an initial state. Figure C-3 Body Displacement Representation [106] depicts the displacement of a continuum body [93].

### 1.2.2 Displacement Vector

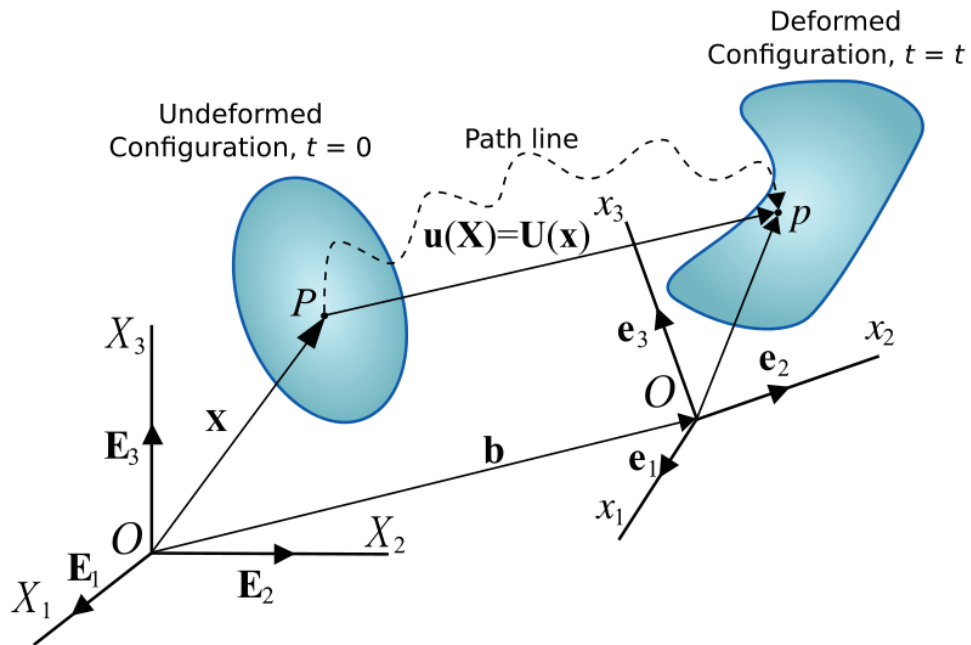


**Figure C-3 Body Displacement Representation [106]**

The displacement vector encompasses the magnitude and direction of the displacement of any point on a body. This vector represents the displacement of a material point from point  $P$ , in the original configuration, to point  $p$ , in the deformed configuration [106]. This displacement vector can be described in Lagrangian terms as:

$$\vec{u}(X, t) = \vec{b} + \mathbf{x}(X, t) - \mathbf{X} \quad (\text{C-4})$$

or in Eulerian terms as:

$$\vec{U}(\mathbf{x}, t) = \vec{b} + \mathbf{x} - \mathbf{X}(\mathbf{x}, t) \quad (\text{C-5})$$

where  $\vec{u}(X, t) = \vec{U}(\mathbf{x}, t)$  is the displacement vector between the points  $P$  and  $p$ ,  $\vec{b}$  is the vector between the origins of the original and current coordinate systems,  $\mathbf{X}$  are the coordinates of the original configuration (Lagrangian),  $\mathbf{x}$  are the coordinates of the deformed configuration (Eulerian), and  $t$  is time [93].

These equations can be simplified by superimposing both the undeformed and deformed coordinate systems. Doing so results in  $\vec{b}=0$  and these two equations can be reduced respectively to:

$$\bar{\mathbf{u}}(\mathbf{X}, t) = \mathbf{x}(\mathbf{X}, t) - \mathbf{X} \quad (\text{C-6})$$

$$\vec{\mathbf{U}}(\mathbf{x}, t) = \mathbf{x} - \mathbf{X}(\mathbf{x}, t) \quad (\text{C-7})$$

Displacements are used in FE models since it is easy to compute strains as a function of them. Many equations are given in terms of displacements, such as the displacement (section 1.2.5) and deformation gradient tensors (section 1.2.5), the Jacobian matrix (section 1.2.4), some strain measures, the virtual work, etc.

### 1.2.3 Deformation Gradient Tensor

The material deformation gradient tensor,  $\mathbf{F}$ , is a measure of the deformation of a material. This second-order tensor maps the material points on the original configuration to those points in the current configuration consisting of the same material. It quantifies the material shape and rotation changes. It doesn't provide information about where in space a material particle is (rigid-body translation), only about how it has deformed locally [93].

In a matrix form, the deformation gradient is given by:

$$\mathbf{F}_{ij} = \delta_{ij} + \frac{\partial u_i}{\partial X_j} = \begin{bmatrix} 1 + \frac{\partial u_1}{\partial X_1} & \frac{\partial u_1}{\partial X_2} & \frac{\partial u_1}{\partial X_3} \\ \frac{\partial u_2}{\partial X_1} & 1 + \frac{\partial u_2}{\partial X_2} & \frac{\partial u_2}{\partial X_3} \\ \frac{\partial u_3}{\partial X_1} & \frac{\partial u_3}{\partial X_2} & 1 + \frac{\partial u_3}{\partial X_3} \end{bmatrix} \quad (\text{C-8})$$

where  $u$  is the displacement,  $X$  is a component of the original coordinates, and  $\delta_{ij}$  is the Kronekor delta given by:

$$\delta_{ij} = \begin{cases} 1, & i = k \\ 0, & i \neq k \end{cases} \quad (\text{C-9})$$

The inverse of the deformation gradient tensor,  $\mathbf{F}^{-1}$ , is called the spatial deformation gradient tensor. Both of these tensors are used on many equations, including those to obtain the displacement gradient tensor (section 1.2.5), the Jacobian determinant (section 1.2.4),, to relate the different type of stresses, to obtain the strain rate and spin tensors (section 1.2.7), etc.

### 1.2.4 The Jacobian Determinant

The Jacobian is the determinant of deformation gradient. It is given by

$$J = \det(\mathbf{F}) \quad (\text{C-10})$$

where  $\mathbf{F}$  is the material deformation gradient tensor [31].

The Jacobian can be interpreted as a measure of the deformation in the structure given by the ratio between the material final and initial volume [59]:

$$J = \frac{dV}{dV_o} \quad (\text{C-11})$$

The Jacobian determinant is used in many equations including those to relate the Cauchy stress to the Kirchhoff stress (section 1.2.15) and those to obtain the Piola-Kirchhoff stresses (section 1.2.17).

### 1.2.5 Displacement Gradient Tensor

The material displacement gradient tensor is defined as the partial differentiation of the displacement vector with respect to the material coordinates. In matrix form is given by [93]:

$$\nabla_x \vec{u} = \mathbf{F} - \mathbf{I} = \begin{bmatrix} \frac{\partial u_1}{\partial X_1} & \frac{\partial u_1}{\partial X_2} & \frac{\partial u_1}{\partial X_3} \\ \frac{\partial u_2}{\partial X_1} & \frac{\partial u_2}{\partial X_2} & \frac{\partial u_2}{\partial X_3} \\ \frac{\partial u_3}{\partial X_1} & \frac{\partial u_3}{\partial X_2} & \frac{\partial u_3}{\partial X_3} \end{bmatrix} \quad (\text{C-12})$$

where  $\vec{u}$  is the displacement vector,  $\mathbf{X}$  are the material coordinates of the undeformed configuration (Lagrangian),  $\mathbf{F}$  is the deformation gradient tensor, and  $\mathbf{I}$  is the identity matrix of the same size with ones on the main diagonal and zeros elsewhere.

The spatial displacement gradient tensor is defined as the partial derivative of the displacement vector with respect to the Eulerian coordinates:

$$\nabla_x \vec{U} = \mathbf{I} - \mathbf{F}^{-1} = \begin{bmatrix} \frac{\partial U_1}{\partial x_1} & \frac{\partial U_1}{\partial x_2} & \frac{\partial U_1}{\partial x_3} \\ \frac{\partial U_2}{\partial x_1} & \frac{\partial U_2}{\partial x_2} & \frac{\partial U_2}{\partial x_3} \\ \frac{\partial U_3}{\partial x_1} & \frac{\partial U_3}{\partial x_2} & \frac{\partial U_3}{\partial x_3} \end{bmatrix} \quad (\text{C-13})$$

where  $\vec{U}$  is the displacement vector,  $\mathbf{F}^{-1}$  is the spatial deformation gradient tensor,  $\mathbf{I}$  the identity matrix and  $\mathbf{x}$  are the spatial coordinates of the deformed configuration (Eulerian) [93].

This tensor is used in the development of the necessary formula to obtain the equations used in this model such as those to define the velocity gradient vector (section 1.2.6), and the Jacobian determinant (section 1.2.4).

### 1.2.6 Velocity Gradient Vectors

From a Lagrangian viewpoint the velocity,  $\mathbf{v}$ , of a material particle is defined as:

$$\mathbf{v} = \frac{\partial \mathbf{x}}{\partial t} \quad (\text{C-14})$$

where  $\mathbf{x}$  are the spatial coordinates and  $t$  is time [93].

The partial differentiation of the spatial velocity vector with respect to the spatial coordinates yields the spatial velocity gradient tensor.

$$\mathbf{L} = \frac{\partial \mathbf{v}}{\partial \mathbf{x}} = \vec{\nabla}_x \mathbf{v} \quad (\text{C-15})$$

In matrix form is given by [31]:

$$L_{ij} = \begin{bmatrix} \frac{\partial v_1}{\partial x_1} & \frac{\partial v_1}{\partial x_2} & \frac{\partial v_1}{\partial x_3} \\ \frac{\partial v_2}{\partial x_1} & \frac{\partial v_2}{\partial x_2} & \frac{\partial v_2}{\partial x_3} \\ \frac{\partial v_3}{\partial x_1} & \frac{\partial v_3}{\partial x_2} & \frac{\partial v_3}{\partial x_3} \end{bmatrix} \quad (\text{C-16})$$

where  $\mathbf{v}$  is the spatial velocity vector and  $\mathbf{x}$  are the spatial or current coordinates [31].

When describing the time-dependent deformation of a body many calculations often require the time derivative of the deformation gradient. This derivative is called the material velocity gradient tensor, and is given by:

$$\dot{\mathbf{F}} = \frac{\partial \mathbf{F}}{\partial t} = \frac{\partial \mathbf{v}}{\partial \mathbf{X}} = \bar{\nabla}_{\mathbf{x}} \mathbf{v} \quad (\text{C-17})$$

In matrix form is given by [31]:

$$\dot{F}_{ij} = \begin{bmatrix} \frac{\partial v_1}{\partial X_1} & \frac{\partial v_1}{\partial X_2} & \frac{\partial v_1}{\partial X_3} \\ \frac{\partial v_2}{\partial X_1} & \frac{\partial v_2}{\partial X_2} & \frac{\partial v_2}{\partial X_3} \\ \frac{\partial v_3}{\partial X_1} & \frac{\partial v_3}{\partial X_2} & \frac{\partial v_3}{\partial X_3} \end{bmatrix} \quad (\text{C-18})$$

where  $\mathbf{v}$  is the spatial velocity vector and  $X$  are the material or reference coordinates [31]. The spatial velocity gradient tensor can be defined in terms of the material velocity tensor as:

$$\mathbf{L} = \dot{\mathbf{F}} \cdot \mathbf{F}^{-1} \quad (\text{C-19})$$

Moreover, the spatial velocity gradient tensor at each explicit time increment,  $i$ , can be expressed as:

$$\mathbf{L} = \frac{d}{dt} (\Delta \mathbf{F}) \cdot \Delta \mathbf{F}^{-1} \quad (\text{C-20})$$

where  $\Delta \mathbf{F}$  is the total deformation for that explicit time increment

This tensor can be decomposed in two parts. A symmetrical part called rate of deformation,  $\mathbf{D}$ , and an anti-symmetric part called spin tensor,  $\mathbf{W}$ . The rate of deformation is typically called in Abaqus the strain rate and is essential to carry out the Updated Lagrangian formulation. The spin tensor is responsible for pure rotation.

Mathematically their relations can be expressed as [31]:

$$\mathbf{L} = \mathbf{D} + \mathbf{W} \quad (\text{C-21})$$

$$\mathbf{D} = \frac{1}{2} (\mathbf{L} + \mathbf{L}^T) \quad (\text{C-22})$$

$$\mathbf{W} = \frac{1}{2} (\mathbf{L} - \mathbf{L}^T) \quad (\text{C-23})$$

The velocity gradient measure is used in many equations as the ones above to obtain the rate of deformation which is the main measure of the updated Lagrangian formulation used in Abaqus. The spin tensor is used to obtain the Jaumann stress rate defined in section 1.2.22.

### 1.2.7 Rate of Deformation

The materials behavior is generally history dependent, often called time-dependent material behavior, and therefore many constitutive equations appear in rate form. The rate of deformation,  $\mathbf{D}$ , is typically called in Abaqus the strain rate or the logarithmic strain rate, and can be expressed as [31]:

$$\dot{\boldsymbol{\varepsilon}} = \mathbf{D} = \frac{\partial \mathbf{v}}{\partial \mathbf{x}} = \frac{1}{2}(\mathbf{L} + \mathbf{L}^T) \quad (\text{C-24})$$

where  $\mathbf{L}$  is the velocity gradient.

This strain rate can be decomposed in two parts a volumetric and a deviatoric part as follow:

$$\dot{\boldsymbol{\varepsilon}}_{ij} = \frac{\dot{\boldsymbol{\varepsilon}}_{kk}}{3} + \dot{\boldsymbol{\varepsilon}}_{ij} \quad (\text{C-25})$$

where  $\dot{\boldsymbol{\varepsilon}}_{kk}/3$  is the volumetric strain rate, and  $\dot{\boldsymbol{\varepsilon}}$  is the deviatoric strain rate [31].

Abaqus uses the Updated Lagrangian formulation generally expressed in terms of the Cauchy stress and the rate of deformation measures. For all of the plasticity models in Abaqus, the rate of deformation tensor is considered the strain rate; the total strain components reported in the output are obtained by integrating the rate of deformation tensor in time, and also rotating the components to keep up with any material rotation that occurs.

The rate of deformation or strain rate measure can be decomposed in two parts.

$$\dot{\boldsymbol{\varepsilon}} = \mathbf{D} = \dot{\boldsymbol{\varepsilon}}_e + \dot{\boldsymbol{\varepsilon}}_{vp} \quad (\text{C-26})$$

where  $\dot{\boldsymbol{\varepsilon}}$  is the total strain rate,  $\dot{\boldsymbol{\varepsilon}}_e$  is the elastic strain rate, and  $\dot{\boldsymbol{\varepsilon}}_{vp}$  is the plastic strain rate [31].

### 1.2.8 Strain

Strain is defined as a measure of the amount of deformation a body experiences compared to its original size and shape. It is a normalized measure of deformation [93].

Strain measures are widely used in FE analysis because many formulas are in function of them and because it is easy to compute strains from displacements, which are the basic variable in the finite element models[31].

### 1.2.9 Green's Strain Tensor

The Green's strain tensor measures the changes in length and angle of a deformable solid, from a Lagrangian viewpoint. This Green's strain tensor is useful for problems involving large deformations. This strain tensor can be expressed in terms of the deformation gradient  $F$  as [93]:

$$\varepsilon_{ij}^G = \frac{1}{2}(F_{ki} \cdot F_{kj} - \delta_{ij}) \quad (C-27)$$

where  $F$  is the deformation gradient tensor and  $\delta_{ij}$  is the Kronekor delta.

The Green's strain tensor is useful for problems involving small strains, because, it can be computed directly from the deformation gradient. This wear problem involves large elasto-ciscoplastic strains, therefore green's strain is not uso seful, the most appropriate strain measure for tis problem is the logarithmic strain presented in the next section. The green strain concept was added to this paper for completeness of the theory.

### 1.2.10 Logarithmic Strain

This sliding wear problem involves large inelastic strains. The materials simulated behave in an elasto-viscoplastic manner. The yield stress for the type of ductile materials simulted are orders of magnitude smaller than their elastic modulus. For example for the VascoMax 300 steel the yield stresss is 2.17E6 kPa and its elastic modulus is 1.9E8 kPa.. Their stress-strain behavior can be better observed when plotted in a logarithmic scale, this fact implies that the most appropriate strain measure should be a logarithmic strain. This logarithmic strain is given by [31]:

$$\varepsilon = \ln(\sqrt{\mathbf{F} \cdot \mathbf{F}^T}) \quad (\text{C-28})$$

where  $\varepsilon$  is the logarithmic strain and  $\mathbf{F}$  is the deformation gradient tensor [31].

If one keeps the principal directions fixed in the original or material axes (no rotation), this logarithmic strain can be expressed for an explicit time increment as [31]:

$$\Delta\varepsilon = \ln(\sqrt{\Delta\mathbf{F} \cdot \Delta\mathbf{F}^T}) \quad (\text{C-29})$$

where  $\varepsilon$  is the logarithmic strain increment and  $\mathbf{F}$  is the deformation during that time increment [31].

In the absence of rotation, the rate of deformation is the logarithmic strain rate, wherefore integrating it over the time of the increment leads to the increment of the logarithmic strain [31].

$$\Delta\varepsilon = \int_{t_i}^{t_{i+1}} \mathbf{D} dt \quad (\text{C-30})$$

where  $\Delta\varepsilon$  is the logarithmic strain increment,  $\mathbf{D}$  is the rate of deformation,  $i$  is the time increment index, and  $t$  is time [31].

### 1.2.11 Equivalent Plastic Strain and Strain Rate

The equivalent plastic strain, for isotropic Von Mises plasticity (defined in section 1.4), is given by [31]:

$$\bar{\varepsilon}_{vp} = \varepsilon_{vp}|_0 + \int_0^t \sqrt{\frac{2}{3} \dot{\varepsilon}_{vp} : \dot{\varepsilon}_{vp}} dt \quad (\text{C-31})$$

where  $\bar{\varepsilon}_{vp}$  is the equivalent plastic strain,  $\dot{\varepsilon}_{vp}$  is the plastic strain rate,  $t$  is time,

$\varepsilon_{vp}|_0$  is the initial equivalent plastic strain (generally zero unless specified otherwise).

Similarly, the equivalent plastic strain rate for isotropic Von Mises plasticity (defined in section 1.4) can be calculated with [31]:

$$\dot{\bar{\varepsilon}}_{vp} = \sqrt{\frac{2}{3} \dot{\varepsilon}_{vp} : \dot{\varepsilon}_{vp}} \quad (\text{C-32})$$

where  $\dot{\bar{\varepsilon}}_{vp}$  is the equivalent plastic strain rate and  $\dot{\varepsilon}_{vp}$  is the plastic strain rate.

The Johnson and Cook plasticity equation (section 1.4.3) used in this 3D wear model to simulate the material viscoplastic behavior is a function of this equivalent plastic strain.

Section 1.5.3 explains how one can develop an algorithm to simulate the elasto-viscoplastic straining during a time step using this equation,

$$\left[ \bar{\epsilon}_{vp} \right]^{(i+1)} = \left[ \bar{\epsilon}_{vp} \right]^{(i)} + \sqrt{\frac{2}{3}} \left[ \dot{\epsilon}_{vp} \right]^{(i+1/2)} : \left[ \dot{\epsilon}_{vp} \right]^{(i+1/2)} \Delta t^{(i+1/2)} \quad (\text{C-33})$$

where  $\bar{\epsilon}_{vp}$  is the equivalent plastic strain,  $\dot{\epsilon}_{vp}$  is the plastic strain rate,  $t$  is time, and  $i$  is the time increment index.

This equivalent plastic strain rate is used in our model to simulate the material behavior via the Johnson and Cook's plasticity (section 1.4.3) and failure models (section 1.4.5). Both of the Johnson and Cook models employed in this 3D wear model to simulate the material plastic behavior and fracture are a function of this equivalent plastic strain.

### 1.2.12 Material Derivative

The material derivative, also called substantial derivative, is used to calculate the time rate of change of any physical quantity (such as velocity, temperature or density) for a material particle moving with a velocity,  $\mathbf{v}$  [93]. It relates the Lagrangian rate of change of a physical quantity to the sum of the local, or Eulerian rate of change, and the convective rate of change. This convective rate of change represents the contribution due to the change in the position of the material particle. The material derivative is defined as:

$$\underbrace{\frac{Da}{Dt}}_{\text{Lagrangian rate of change}} = \underbrace{\frac{\partial a}{\partial t}}_{\text{Eulerian rate of change}} + \underbrace{\mathbf{v} \cdot \nabla_x \mathbf{a}}_{\text{Convective rate of change}} \quad (\text{C-34})$$

where  $\mathbf{a}$  is a vector representing a physical quantity,  $t$  is time,  $\mathbf{v}$  is velocity,  $\nabla_x$  is the covariant derivative.

For example, if the physical quantity of interest is the density of a material, then the material derivative describes the density evolution with time, of a certain material portion, as it displaces [31]. The material derivative of density is:

$$\underbrace{\frac{D\rho}{Dt}}_{\text{Lagrangian rate of change in density}} = \underbrace{\frac{\partial \rho}{\partial t}}_{\text{Eulerian rate of change in density}} + \underbrace{\rho \cdot \nabla_x \mathbf{v}}_{\text{Convective rate of change in density}} \quad (\text{C-35})$$

This material derivative of density is used to manipulate the equations of conservation presented in section 1.3.

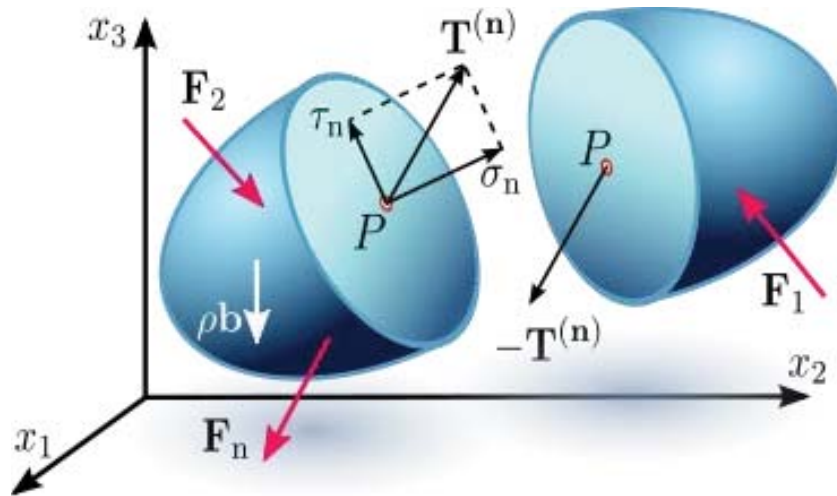


Figure C-4 Components of Stress [31]

### 1.2.13 Internal Traction Vector

The internal traction vector,  $\mathbf{T}^{(n)}$ , represents the stress acting on a cross-section of the deformed body across a surface  $S$ , with outer normal vector  $\mathbf{n}$ . The magnitude and direction of the traction vector depends on the applied loads ( $\mathbf{F}_n, \mathbf{F}_n, \dots, \mathbf{F}_n$ ). Figure C-4 illustrates how this vector may not be perpendicular to the surface plane however regardless if it is perpendicular or not, this stress can be expressed via two components: 1) The normal stress,  $\sigma_n$ , perpendicular to the plane, and 2) the shear stress,  $\tau_n$ , parallel to the plane [31].

The internal traction vector can be used to define the Cauchy stress (section 1.2.14) and also to formulate the principle of virtual work (section 1.3.6).

### 1.2.14 Cauchy or “True” Stress

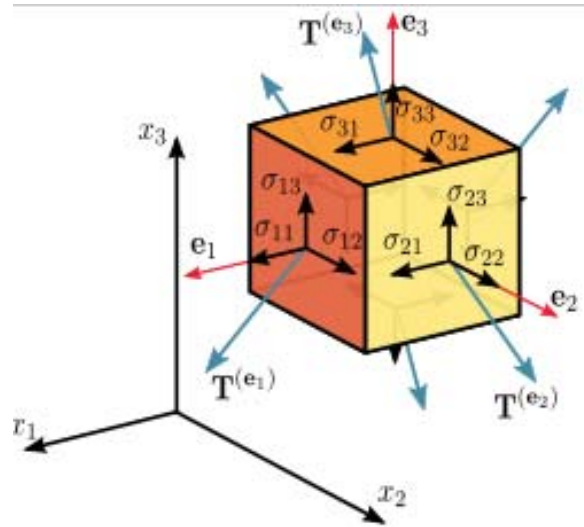


**Figure C-5 Cauchy’s Stress Tensor [99]**

The Cauchy Stress represents the stress in the deformed configuration. It is called the “true” stress because it corresponds to the true force per current or deformed area (Eulerian description) [31].

This measure assumes that the magnitude and direction of the stress vector,  $T^{(e_i)}$ , in any plane passing through a point can be calculated as a function of the stress vectors on three mutually perpendicular planes. Figure C-5 depicts this concept [31].

Cauchy’s stress theorem states that “there exists a second-order tensor field, called the Cauchy stress tensor, independent of  $n$ , such that  $T$  is a linear function of  $n$ .

This relation can be expressed as:

$$\mathbf{T} = n \cdot \boldsymbol{\sigma} \tag{C-36}$$

where  $\boldsymbol{\sigma}$  is the Cauchy stress and  $\mathbf{T}$  is the traction vector, and  $n$  the outward unit normal to the plane” [31].

The Cauchy stress tensor completely characterizes the internal forces acting on the deformed solid and it is considered the most practical stress measure for FE packages, as Abaqus [31].

The Cauchy stress tensor defines the state of stress at a point via nine components. This tensor can be expressed in a matrix form as [31].:

$$\boldsymbol{\sigma} = \sigma_{ij} = \begin{bmatrix} \mathbf{T}^{(e_1)} \\ \mathbf{T}^{(e_2)} \\ \mathbf{T}^{(e_3)} \end{bmatrix} = \begin{bmatrix} \sigma_{11} & \sigma_{12} & \sigma_{13} \\ \sigma_{21} & \sigma_{22} & \sigma_{23} \\ \sigma_{31} & \sigma_{32} & \sigma_{33} \end{bmatrix} \quad (\text{C-37})$$

where  $\mathbf{T}^{(e_i)}$  are the traction vectors in the plane perpendicular to the unit vector  $e_i$ .  $\sigma_{11}$ ,  $\sigma_{22}$ , and  $\sigma_{33}$  are the normal stresses, and  $\sigma_{12}$ ,  $\sigma_{13}$ ,  $\sigma_{21}$ ,  $\sigma_{23}$ ,  $\sigma_{31}$  and  $\sigma_{32}$  are shear stresses [31].

The Cauchy stress is based in the theory for small deformations with negligible changes in volume. Since, for large deformations the volume typically changes, then the increment of volume applied in the virtual work principle stated in terms of the Cauchy stress may not be constant during the motion. This fact can be accounted either by using the Kirchhoff stress or via the ULF that updates the incremental volume at the end of each small time step (see section 1.1.3.2). Abaqus employs the ULF using a Lagrangian mesh but typically stated in Eulerian terms of the Cauchy stress and the rate of deformation (section 3.11).

### 1.2.15 Kirchhoff stress

In a Lagrangian description there is no true concept of stress because the original state is still free of the applied forces that generate the deformation. The Kirchhoff stress,  $\boldsymbol{\tau}$ , is a measure of stress with respect to the original state (Lagrangian). It has no clear physical meaning. It is often used for the constitutive definitions of large strains [31].

Using the Cauchy stress becomes problematic for large displacements, since now the stress is acting over an area with a changing volume, therefore, one can substitute the Cauchy stress for the product of the Kirchhoff stress,  $\boldsymbol{\tau}$ , and the Jacobian matrix,  $J$ , (defined in section 1.2.4) to balance any volume change during the motion. This relation is given by:

$$\boldsymbol{\tau} = J\boldsymbol{\sigma} \quad (\text{C-38})$$

where  $J$  is the Jacobian determinant,  $\boldsymbol{\sigma}$  is the Cauchy stress, and  $\boldsymbol{\tau}$  is the Kirchhoff Stress.

### 1.2.16 First Piola-Kirchhoff Stress Tensor

The First Piola-Kirchhoff stress tensor,  $\mathbf{S}$ , is a Lagrangian measure, also called the nominal stress tensor. It can be considered as the internal force per unit of undeformed area acting within a solid. Is defined as:

$$\mathbf{S} = J\mathbf{F}^{-1}\boldsymbol{\sigma} \quad (\text{C-39})$$

where  $\mathbf{F}$  is the deformation gradient and  $J$  is the Jacobian [31].

It is a mathematical device to apply the force of the deformed configuration into the undeformed area, as depicted on the next figure [31]. It is used to help transform the equations of motion (section 1.3.3) from an Eulerian to a Lagrangian configuration.

The first Piola-Kirchhoff stress tensors relates the Eulerian and Lagrangian viewpoints for non-infinitesimal (or large) deformations, however, to define it one must know both the original and deformed configurations [106]. This Abaqus 3D wear model was developed with a Lagrangian mesh and uses an updated Lagrangian formulation. The Piola Kirchhoff's tensors are not used by Abaqus in the calculations required to solve this wear problem its definition were added just for completeness of the theory.

### 1.2.17 Second Piola-Kirchhoff Stress Tensor

The Second Piola-Kirchhoff stress tensor,  $\boldsymbol{\Sigma}$ , or material stress tensor is also a Lagrangian measure that can be imagined as the force per unit undeformed area, considering that the forces are acting upon the undeformed solid, rather than on the deformed solid [19]. It other words, introduces an imaginary force in the original configuration that corresponds, as a vector, into the real force during deformation. The next figure depicts this statement.

It is defined as:

$$\boldsymbol{\Sigma} = J\mathbf{F}^{-1}\boldsymbol{\sigma}\mathbf{F}^{-T} \quad (\text{C-40})$$

where  $\boldsymbol{\Sigma}$  is the Second Piola-Kirchhoff stress tensor,  $\mathbf{F}$  is the deformation gradient [104].

This Abaqus 3D wear model was developed with a Lagrangian mesh and uses an updated Lagrangian formulation. The Piola Kirchhoff's tensors are not used by Abaqus in the calculations required to solve this wear problem its definition were added just for completeness of the theory.

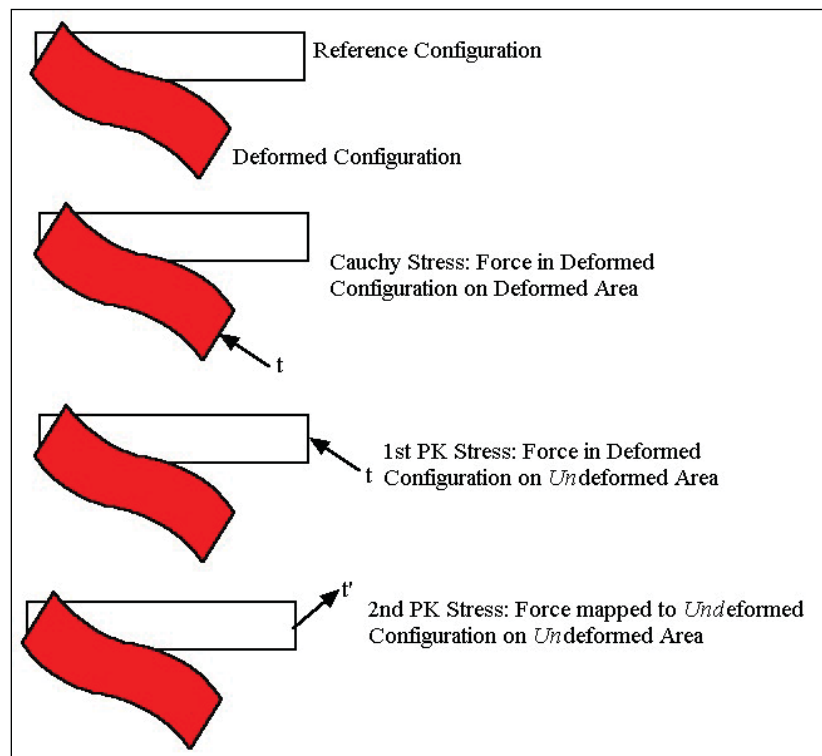
### 1.2.18 Stress Relations and Representation

Table C-1 presents the relations between these stress tensors:

$\sigma =$	$\sigma$	$J^{-1}\tau$	$J^{-1}SF^T$	$J^{-1}F\Sigma F^T$
$\tau =$	$J\sigma$	$\tau$	$SF^T$	$F\Sigma F^T$
$S =$	$J\sigma F^{-T}$	$\tau F^{-T}$	$S$	$F\Sigma$
$\Sigma =$	$JF^{-1}\sigma F^{-T}$	$F^{-1}\tau F^{-T}$	$F^{-1}S$	$\Sigma$

**Table C-1 Relations Between Stresses**

Figure C-6 attempts to graphically present the physical meaning of these stress measurements, however, it is necessary to understand that the Piola-Kirchhoff stress measures are mathematical devices with an untrue physical meaning.



**Figure C-6 Stress Tensors Representation [99]**

The Cauchy stress tensor can also be expressed as the sum of the hydrostatic stress tensor and the deviatoric stress tensor [31].

$$\boldsymbol{\sigma} = p\mathbf{I} + \boldsymbol{\sigma}' \quad (\text{C-41})$$

These two stress tensors are defined next.

### 1.2.19 Equivalent Hydrostatic Stress

In Abaqus the equivalent hydrostatic stress “is a measure of the pressure exerted by a state of stress and tends to change the volume of the stressed body” [31]. It is defined terms of the true Cauchy stresses by [31].

$$p = -\sigma_{kk} / 3 = -(\sigma_{11} + \sigma_{22} + \sigma_{33}) / 3 \quad (\text{C-42})$$

This hydrostatic stress is one of the necessary parameters to evaluate the material failure via the Johnson Cook (JC) dynamic failure criteria to be discussed next.

### 1.2.20 Deviatoric Stress

The deviatoric stress tends to distort the stressed body is incremental with time and summed. It is defined terms of the true Cauchy stresses by [31].

$$\boldsymbol{\sigma}' = \boldsymbol{\sigma} - p\mathbf{I} \quad (\text{C-43})$$

This deviatoric stress is one of the necessary parameters to evaluate the equation of energy for an adiabatic process, described in section 1.3.5.

### 1.2.21 Von-Von Mises stress

The Von-Von Mises stress represents the uniaxial equivalent of a multi-axial stress. It is based on the assumption that “if a material fails in a uniaxial tensile test then it is assumed to similarly fail under multi-axial loading” [31]. This stress is given by:

$$q = \sqrt{\frac{3}{2} \boldsymbol{\sigma}' : \boldsymbol{\sigma}'} \quad (\text{C-44})$$

The Von-Von Mises stress is used for many failure criterions [31]. It is one of the necessary parameters to evaluate the material failure via the Johnson Cook dynamic failure criterion summarized in section 1.3.

### 1.2.22 Jaumann Stress Rate

The Jaumann stress rate,  $\sigma^\nabla$  is based on the notion that the change of stress components consist of two parts: One corresponding to the change of stress in the material, and another due to convection, or circular motion, of the material. The Jaumann stress is defined as “the rate of change of the “true” Cauchy stress, referred to a set of axes which participate in the instantaneous rotation of the element” [31]. The Jaumann stress rate is given by:

$$\sigma^\nabla = \dot{\sigma} - J(W \cdot \sigma - \sigma \cdot W) \quad (C-45)$$

where  $W$  is the spin tensor defined in section 1.2.6 and  $J$  the Jacobian determinant defined in section 1.2.4 [31].

In Abaqus, most of the material models built with solid continuum elements employ this Jaumann stress rate. The Jaumann stress rate “provides to the FE method a convenient link between that material Lagrangian measures and the overall change in true (Cauchy) stress, which is the stress measure used by Abaqus for the equilibrium and virtual work equations. The Jaumann stress rate is the power conjugate of the rate of deformation” [31].

### 1.2.23 Strain Work Conjugates

FE methods often work with conjugate measures of motion and forces when setting up the mechanical problems. A stress is a work conjugate to a strain if their product results in an internal work scalar. These scalars are used in energy methods to help solve statistically indeterminate systems of equations. Statistically indeterminate systems of equations are those with not enough equations to solve for all the variables. An energy method often used to solve FE system of equations is the virtual work principle, described in section 1.3.6.

This Second Piola-Kirchhoff stress,  $\Sigma$ , is a work conjugate of Green’s strain,  $\epsilon$ . Both used to obtain the internal work in the Total Lagrangian formulation. The internal work equation in Lagrangian terms is given by:

$$U_{\text{int}} = \int_{V_0} \boldsymbol{\varepsilon} \boldsymbol{\Sigma} dV_0 \quad (\text{C-46})$$

where  $U_{\text{int}}$  is the internal work,  $\boldsymbol{\varepsilon}$  is the Green strain tensor,  $\boldsymbol{\Sigma}$  is the Second Piola-Kirchhoff stress tensor and  $V_0$  is the reference volume [31]

This Cauchy stress,  $\boldsymbol{\sigma}$ , is the work conjugate of the logarithmic strain,  $\boldsymbol{\varepsilon}$ . Both used to obtain the internal work in the Updated Lagrangian formulations used to solve this wear FE problem. The ULF incrementally updates the volume during an explicit time step (section 1.1.3.2). The internal work equation in ULF terms is given by:

$$U_{\text{int}} = \int_V \boldsymbol{\varepsilon} \boldsymbol{\sigma} dV \quad (\text{C-47})$$

where  $U_{\text{int}}$  is the internal work,  $\boldsymbol{\varepsilon}$  is the logarithmic strain,  $\boldsymbol{\sigma}$  is the Cauchy stress tensor and  $V$  is the current deformed volume [31].

For large deformations the volume may change, and therefore the increment of volume applied in this last internal work equation may not be constant during the motion. To account for issue, one can substitute the Cauchy stress for the product of the Kirchhoff stress by the Jacobian matrix that accounts for any volume change during the motion [106]:

$$U_{\text{int}} = \int_V \boldsymbol{\varepsilon} \boldsymbol{\tau} J^{-1} dV \quad (\text{C-48})$$

Table C-2 summarizes these work conjugate relations:

Measure of strain	Measure of stress	Formula	Equation
Green, $\boldsymbol{\varepsilon}^G$	2nd Piola-Kirchhoff, $\boldsymbol{\Sigma}$	$U_{\text{int}} = \int_{V_0} \boldsymbol{\Sigma} \boldsymbol{\varepsilon}^G dV_0$	(C-49)
Logarithmic, $\boldsymbol{\varepsilon}$	Cauchy stress, $\boldsymbol{\sigma}$	$U_{\text{int}} = \int_V \boldsymbol{\varepsilon} \boldsymbol{\sigma} dV$	(C-50)
Green, $\boldsymbol{\varepsilon}^G$	Kirchhoff, $\boldsymbol{\tau}$	$U_{\text{int}} = \int_V \boldsymbol{\varepsilon}^G \boldsymbol{\tau} J^{-1} dV$	(C-51)

**Table C-2 Stress and Strain Conjugates**

The work scalars obtained using the above conjugate relations can be used in energy methods to help solve statically indeterminate problems where one has more equations to solve than variables. The FE analysis of the sliding wear involves this kind

of problems and for this 3D FE Abaqus model the work conjugate relations are used to solve the problem via energy methods such as the virtual work principle, described in detail in section 1.3.6.

### **1.3 Conservation Laws and Equilibrium**

#### **1.3.1 Conservation Laws**

All materials are expected to satisfy the three conservation laws of equilibrium throughout their time dependent behavior. The exact solution of our wear problem requires equilibrium to be maintained at all times over any volume. However, the FE method approximates this requirement with a weaker solution, that equilibrium must be maintained in an average sense over a finite number of divisions of the body volume [106].

The conservation laws can be expressed using either the Lagrangian or Eulerian description. The definitions and equations for these conservation laws are:

#### **1.3.2 Conservation of Mass:**

This 3D FE wear model was built using a Lagrangian mesh and its mass is conserved automatically because each element represents a fixed portion of material, however this equation is used to calculate the incremental density changes..

The total mass,  $M$ , of a body is unchanged (constant) during motion [106]. The mass at an initial time,  $t_0$ , is equal to that at any other time,  $t$ , and i.e.

$$M = \int_{V_0} \rho_0 dV_0 = \int_V \rho dV = \text{constant} \quad (\text{C-52})$$

where  $M$  is the total mass,  $\rho$  is the density,  $\rho_0$  is the initial density,  $V$  is the current volume,  $V_0$  is the initial volume. Recalling that since this model is using a ULF then the volume is incrementally updated for each time step (section 1.1.3.2) [106].

### 1.3.2.1 Lagrangian (material) form of the Conservation of Mass equation

Recalling the Jacobian determinant,  $J$ , defined in section 1.2.4, one can substitute in the previous equation the current volume in terms of this Jacobian and the reference volume to get:

$$\int_{V_0} \rho_0 dV_0 = \int_{V_0} \rho J dV_0 \quad (C-53)$$

Since this equation is valid for an arbitrary volume, one can write it in short as:

$$\rho_0 = \rho J \quad (C-54)$$

The following relations derived from this Lagrangian form of the conservation of mass equations will be used in the next section to transform the conservation of momentum equations from a Lagrangian to an Eulerian configuration [106]:

$$\rho_0 dV_0 = \rho DV = \rho J dV_0 = const \quad \text{and} \quad J = \frac{\rho_0}{\rho} = \frac{dV}{dV_0} \quad (C-55)$$

### 1.3.2.2 Eulerian form of the Conservation of Mass equation

Deriving the mass equation against time, one gets the time rate of the total mass in the volume [106]:

$$\frac{\partial M}{\partial t} = \int_V \frac{\partial \rho}{\partial t} dV \quad (C-56)$$

where  $M$  is the total mass,  $\rho$  is the density,  $V$  is the current volume, and  $t$  is time.

Recalling that since this model is using a ULF one doesn't integrate over the entire deformed volume, one integrates only over the incremental volume of each explicit time step (section 1.1.3.2) [106].

Defining the flux of the mass through the surface and the rate of mass inflow as:

$$\text{flux} = \text{rate of mass outflow} = \int_S \rho \vec{v} \cdot \vec{n} dS \quad (C-57)$$

$$\text{rate of mass inflow} = -\int_S \rho \vec{v} \cdot \vec{n} dS = -\int_V \nabla \cdot (\rho \vec{v}) dV \quad (C-58)$$

where  $\rho$  is the density,  $\rho_0$  is the initial density,  $\vec{v}$  is the velocity vector,  $\vec{n}$  is the normal unity vector to the surface  $S$ .

Assuming that no mass is created inside the volume; then the time rate of mass must be equal to the rate of flux of the mass through the surface. So:

$$\int_V \frac{\partial \rho}{\partial t} dV = - \int_V \nabla \cdot (\rho \vec{v}) dV, \text{ or rearranging: } \int_V \left( \frac{\partial \rho}{\partial t} + \nabla \cdot (\rho \vec{v}) \right) dV = 0 \quad (\text{C-59})$$

Since this equation must be valid for any volume then it can be expressed as:

$$\frac{\partial \rho}{\partial t} + \nabla_x \cdot (\rho \vec{v}) = 0 \quad \text{or} \quad \frac{\partial \rho}{\partial t} + v_i \frac{\partial \rho}{\partial x_i} + \rho \frac{\partial v_i}{\partial x_i} = 0 \quad (\text{C-60})$$

Using the material derivative of density, defined in section 1.2.12, one can express this equation on an Eulerian form [106]:

$$\frac{D\rho}{Dt} + \rho \nabla_x \cdot \vec{v} = 0 \quad \text{or} \quad \frac{D\rho}{Dt} + \rho \frac{\partial v_i}{\partial x_i} = 0 \quad (\text{C-61})$$

This conservation law has to be satisfied anytime material motion or deformation occurs, however, this 3D FE wear model was built using a Lagrangian mesh and its mass is conserved automatically because each element represents a fixed portion of material.

### 1.3.3 Conservation of Linear Momentum

#### 1.3.3.1 Conservation of Linear Momentum in Eulerian form

Based upon Newton's second law the rate of change momentum of a given amount of mass is [106].

$$\int_S t_i dS + \int_V f_i dV = \frac{D}{Dt} \int_V \rho v_i dV \quad (\text{C-62})$$

where  $t$  is the surface traction per unit of current area,  $V$  is the volume the current configuration,  $S$  is the surface bounding this volume,  $\rho$  is density,  $v$  is the velocity, and  $f$  is the body force per unit of current volume. Recalling that since this model is using a ULF one doesn't integrate over the entire deformed volume, one integrates only over the incremental volume of each explicit time step (section 1.1.3.2) [106].

The first term can be substituted with the Cauchy relation described in section 1.2.15 and then one can apply the divergence theorem to get [106].

$$\int_S t_i dS = \int_S \sigma_{ji} n_j dS = \int_V \frac{\partial \sigma_{ji}}{\partial x_j} dV \quad (\text{C-63})$$

The third term can be substituted using the material time derivative of a volume integral presented in section 1.2.12:

$$\frac{D}{Dt} \int_V \rho v_i dV = \int_V \rho \frac{Dv_i}{Dt} dV \quad (C-64)$$

Replacing these two terms in the original equation one gets [106]

$$\int_V \frac{\partial \sigma_{ji}}{\partial x_j} dV + \int_V f_i dV = \int_V \rho \frac{Dv_i}{Dt} dV \quad (C-65)$$

Since this equation must hold for any arbitrarily volume, one can simplify it to obtain which is called the Cauchy equations of motion [106].

$$\frac{\partial \sigma_{ji}}{\partial x_j} + f_i = \rho \frac{Dv_i}{Dt} \quad (C-66)$$

where  $\sigma$  is the Cauchy stress tensor,  $\rho$  is the density,  $v$  is velocity,  $f$  is the body force per unit of volume, and  $t$  is time.

The Cauchy equations of motion consist of three partial differential equations and a total of six unknown components of stress. These equations are often not enough to determine the stress distribution. To do so additional equations must be considered, i.e. displacement versus strain relations (kinematic relations) or stress versus strain relations (constitutive equations) [106]. The Cauchy equations of motion are important to develop the weak solution to this FE problem expressed. The Virtual Work principle, explained and developed in section 1.3.6, is based on these conservation of linear momentum equations [106].

### ***1.3.3.2 Conservation of Linear Momentum in Lagrangian form***

The Cauchy equations of motion apply to the current deformed configuration. These equations of motion can be transformed to the Lagrangian configuration using the following relations [106].

- The relationship between the first Piola-Kirchhoff and the Cauchy stresses:

$$\sigma_{ji} = \frac{\rho}{\rho_0} F_{jr} S_{ri} \quad (C-67)$$

where  $S$  is the 1<sup>st</sup> PK stress tensor,  $\rho$  is the density,  $\rho_0$  is the reference density, and  $F$  is the deformation gradient matrix [104].

- The relations derived from the conservation of mass principle, described in section 1.2:

$$\rho dV = \rho J dV_0 = \rho_0 dV_0 \quad \text{and} \quad \int_V \rho \frac{Dv}{Dt} dV = \int_{V_0} \rho_0 \frac{dv_i}{dt} dV_0 \quad (\text{C-68})$$

where  $\rho$  is the density,  $\rho_0$  is the reference density,  $J$  is the Jacobian  $V$  is the current volume,  $V_0$  is the reference volume, and  $t$  is time [104].

- The divergence theorem relation:

$$\int_{S_0} S_{ji} n_j dS_0 = \int_{V_0} \frac{\partial S_{ji}}{\partial X_j} dV_0 \quad (\text{C-69})$$

where  $S_{ji}$  is the 1<sup>st</sup> PK stress tensor,  $S_0$  is the reference surface,  $V_0$  is the reference volume,  $n$  is the normal unit vectorm, and  $X$  are the material coordinates.

Recalling these relations one can transform the Eulerian equation in terms of the Cauchy stress:

$$\int_V \frac{\partial \sigma_{ji}}{\partial x_j} dV + \int_V f_i dV = \int_V \rho \frac{Dv_i}{Dt} dV \quad (\text{C-70})$$

into a Lagrangian equation in terms of the first Piola-Kirchhoff .

$$\int_{V_0} \frac{\partial S_{ji}}{\partial X_j} dV_0 + \int_{V_0} f_{i0} dV_0 = \int_{V_0} \rho_0 \frac{dv_i}{dt} dV_0 \quad (\text{C-71})$$

where  $S$  is the 1<sup>st</sup> PK stress tensor,  $\sigma$  is Cauchy's stress tensor,  $\rho$  is the density,  $\rho_0$  is the reference density,  $v$  is velocity,  $f$  is the body force per unit of volume,  $v$  is the velocity, and  $V$  is the current volume,  $V_0$  is the reference volume, and  $t$  is time [104].

Recalling that since this model is using a ULF one doesn't integrate over the entire deformed volume, one integrates only over the incremental volume of each explicit time step (section 1.1.3.2).

Realizing that this equation must hold for any volume one can get the Cauchy equations of motion expressed in referential coordinates by means of the first Piola-Kirchhoff strain tensor.

$$\frac{\partial S_{ji}}{\partial X_j} + f_{i0} = \rho_0 \frac{dv_i}{dt} \quad (C-72)$$

Using the relation between the first and second Piola-Kirchhoff stresses,  $S_{ji} = \Sigma_{jr} F_{ir}$ , one could rewrite these equations in terms of the second Piola-Kirchhoff stress tensor as:

$$\frac{\partial}{\partial X_j} (\Sigma_{jr} F_{ir}) + f_{i0} = \rho_0 \frac{dv_i}{dt} \quad (C-73)$$

where  $\Sigma$  is the 2<sup>nd</sup> PK stress tensor,  $\rho_0$  is the reference density,  $v$  is the velocity,  $f$  is the body force per unit of volume,  $F$  is the deformation gradient matrix and  $t$  is time [106].

These conservation of linear momentum equations in Lagrangian terms are not used by Abaqus. They are included on this dissertation only for completeness of the theory.

### 1.3.4 Conservation of Angular Momentum

The conservation of angular momentum principle states that equilibrium requires that the summation of moments, with respect to any point, to be zero. Expressing it mathematically:

$$\int_S (\mathbf{X} \times \mathbf{t}) dS + \int_V (\mathbf{X} \times \mathbf{f}) dV = 0 \quad (C-74)$$

where  $t$  is the surface traction per unit of current area,  $V$  is the volume the current configuration,  $S$  is the surface bounding this volume,  $f$  is the body force per unit of current volume and  $X$  are the material coordinates [106].

Evaluating equilibrium by taking moments about the origin leads to realize that the stress tensor is symmetric, and has only six independent stress components, instead of nine. This stress tensor symmetry is mathematically expressed as::

$$\sigma = \sigma^T \quad (C-75)$$

The symmetry of the true stress matrix is called Cauchy's second law of motion. A benefit of this law is that moment equilibrium is automatically satisfied and one needs only to consider translational equilibrium [106].

### 1.3.5 Conservation of Energy

There are many ways to express the conservation of energy principle. The equation for conservation of energy used by Abaqus to aid in the solution of this problem equates the increase in internal energy per unit mass,  $U_m$ , to the rate at which work is being done by the stresses plus the rate at which heat is being added. In the absence of heat conduction the energy equation can be written as:

$$\rho \frac{\partial U_m}{\partial t} = (p - p_{bv}) \frac{1}{\rho} \frac{\partial \rho}{\partial t} + \boldsymbol{\sigma}' : \dot{\boldsymbol{\epsilon}} + \rho \dot{Q} \quad (\text{C-76})$$

where  $\rho$  is density,  $U_m$  is internal energy per unit of mass,  $p_{bv}$  is the pressure due to bulk viscosity,  $\boldsymbol{\sigma}'$  is the deviatoric stress tensor and  $\dot{\boldsymbol{\epsilon}}$  is the deviatoric strain rate and  $\dot{Q}$  is the heat rate per unit of mass, and  $p$  is pressure [106].

The equation of state, defined in section 1.6, is used to aid in the solution of this energy equation by relating the pressure to the current density and the internal energy per unit of mass.

#### 1.3.5.1 Adiabatic Assumption

The adiabatic stress analysis is commonly used to simulate high-speed processes linked to large inelastic strains. In these types of processes the heating of the material due to its plastic deformation is an important thermal effect, because it has little time to diffuse and therefore produces a local rise in temperature. This temperature increase is calculated directly at the material integration and used for any subsequent calculations [31].

For an adiabatic process the energy equation can be simplified to:

$$\rho c_v \frac{\partial T}{\partial t} = (p - p_{bv}) \frac{1}{\rho} \frac{\partial \rho}{\partial t} + \boldsymbol{\sigma}' : \dot{\boldsymbol{\epsilon}} \quad (\text{C-77})$$

where  $\rho$  is density,  $c_v$  is the specific heat at a constant volume,  $T$  is temperature,  $p$  is pressure,  $p_{bv}$  is the pressure due bulk viscosity,  $\boldsymbol{\sigma}'$  is the deviatoric stress tensor, and  $\dot{\boldsymbol{\epsilon}}$  is the deviatoric [31].

This equation was derived from the equation of energy presented in section 1.3.5 substituting on it, the following specific heat relation and realizing that in an adiabatic process the heat flow can be neglected. The EOS aids on the solution of this equation by calculating the pressure at each time increment. The conservation of mass equation helps it by providing the current density and based on the equations of motion one can obtain the deviatoric stress and strain rate.

Under an adiabatic assumption the heat is generated in an element by plastic work. The resulting temperature rise then can be computed using the specific heat of the material [31]. The specific heat is defined as “the amount of heat required to increase the temperature of a unit mass by one degree” [104]. For a process where the heat is supplied keeping the pressure constant the specific heat is:

$$c_p = \left. \frac{\partial U_m}{\partial T} \right|_p \quad (C-78)$$

In Abaqus an adiabatic condition is always assumed for materials modeled with an EOS. This condition is assumed irrespective of whether an adiabatic step has been specified [31]. For this 3D wear model an adiabatic analysis was selected because at the micron-level the wear process is extremely rapid and therefore, the heat has little time to diffuse. Furthermore, the Johnson-Cook plasticity criterion is tailored for high-strain-rate transient dynamic applications and its temperature changes are typically computed by assuming adiabatic conditions.

### 1.3.6 Virtual Work

The exact solution to problems involving time dependent material deformation requires equilibrium to be maintained at all times over any arbitrary volume of the body. For many of these problems the analytical solution is statically indeterminate because it has more equations to solve than variables. To solve these kind of problems the FE method: “approximates this equilibrium requirement by replacing it with a weaker equilibrium requirement, that equilibrium must be maintained in an average sense over a finite number of divisions of the volume of the body” [31].

The FE models approximate the equilibrium by introducing into the “weak formulation” the Cauchy’s equations of motion, developed in section 1.3.3:

$$\left(\frac{\partial}{\partial X}\right) \cdot \boldsymbol{\sigma} + \mathbf{f} = \mathbf{0} \quad (\text{C-79})$$

The weaker equation is obtained by integrating the dot product of the three pointwise equilibrium force equations by an arbitrary, “test function,” continuous over the entire volume [31]. . The test function commonly used is the “virtual” velocity field,  $\delta \mathbf{v}$ , which is completely arbitrary but whose variations are restricted to a finite number of nodal values and must follow any prescribed kinematic constraints. The result from this dot product is a single scalar at each material point that is then integrated over the entire body[31]. This virtual work principle can be mathematically expressed as:

$$\int_V \left[ \left(\frac{\partial}{\partial X}\right) \cdot \boldsymbol{\sigma} \right] \cdot \delta \mathbf{v} \, dV + \int_V \mathbf{f} \cdot \delta \mathbf{v} \, dV = \mathbf{0} \quad (\text{C-80})$$

where  $V$  is the volume the current configuration,  $X$  are the material coordinates,  $\boldsymbol{\sigma}$  is the Cauchy stress,  $\mathbf{v}$  is the velocity, and  $\mathbf{f}$  is the body force per unit of current volume. Recalling that since this model is using a ULF one doesn’t integrate over the entire deformed volume, one integrates only over the incremental volume of each explicit time step (section 1.1.3.2) [31].

Applying to this equation the chain rule to the first term one gets:

$$\int_V \left[ \left(\frac{\partial}{\partial X}\right) \cdot \boldsymbol{\sigma} \cdot \delta \mathbf{v} - \boldsymbol{\sigma} : \left(\frac{\partial \delta \mathbf{v}}{\partial X}\right) \right] dV + \int_V \mathbf{f} \cdot \delta \mathbf{v} \, dV = \mathbf{0} \quad (\text{C-81})$$

Redistributing:

$$\int_V \left[ \left(\frac{\partial}{\partial X}\right) \cdot \boldsymbol{\sigma} \cdot \delta \mathbf{v} \right] dV - \int_V \boldsymbol{\sigma} : \left(\frac{\partial \delta \mathbf{v}}{\partial X}\right) dV + \int_V \mathbf{f} \cdot \delta \mathbf{v} \, dV = \mathbf{0} \quad (\text{C-82})$$

Applying Gauss's theorem to rewrite a surface integral as a volume integral:

$$\int_S [\mathbf{n} \cdot \boldsymbol{\sigma} \cdot \delta \mathbf{v}] \, dS - \int_V \boldsymbol{\sigma} : \left(\frac{\partial \delta \mathbf{v}}{\partial X}\right) dV + \int_V \mathbf{f} \cdot \delta \mathbf{v} \, dV = \mathbf{0} \quad (\text{C-83})$$

Substituting the definition of Cauchy stress, 1.2.14:

$$\int_V \boldsymbol{\sigma} : \left(\frac{\partial \delta \mathbf{v}}{\partial X}\right) dV = \int_S \delta \mathbf{v} \cdot \mathbf{t} \, dS + \int_V \mathbf{f} \cdot \delta \mathbf{v} \, dV = \mathbf{0} \quad (\text{C-84})$$

Recalling the definitions of the velocity gradient, rate of deformation and spin tensor in the current configuration presented in section 1.2.6:

$$\frac{\partial \mathbf{v}}{\partial \mathbf{X}} = \mathbf{L} = \mathbf{D} + \mathbf{W} \quad \text{where} \quad \mathbf{D} = \frac{1}{2}(\mathbf{L} + \mathbf{L}^T) \quad \text{and} \quad \mathbf{W} = \frac{1}{2}(\mathbf{L} - \mathbf{L}^T) \quad (\text{C-85})$$

Since  $\boldsymbol{\sigma}$  is symmetric and the spin tensor antisymmetric then:

$$\boldsymbol{\sigma} : \delta \mathbf{W} = \frac{1}{2} \boldsymbol{\sigma} : \delta \mathbf{L} - \frac{1}{2} \boldsymbol{\sigma} : \delta \mathbf{L} = 0 \quad (\text{C-86})$$

Using these relations one can conclude that:

$$\boldsymbol{\sigma} : \frac{\partial \delta \mathbf{v}}{\partial \mathbf{X}} = \boldsymbol{\sigma} : \delta \mathbf{D} + \boldsymbol{\sigma} : \delta \mathbf{W} = \boldsymbol{\sigma} : \delta \mathbf{D} \quad (\text{C-87})$$

Substituting the last term in equation 3.81 and rearranging one obtains the virtual work equation in the classical form

$$\int_V \boldsymbol{\sigma} : \delta \mathbf{D} \, dV = \int_S \delta \mathbf{v} \cdot \mathbf{t} \, dS + \int_V \delta \mathbf{v} \cdot \mathbf{f} \, dV \quad (\text{C-88})$$

where  $V$  is the volume the current configuration,  $S$  is the surface surrounding the current volume,  $\boldsymbol{\sigma}$  is the Cauchy stress,  $\mathbf{D}$  is the strain rate or rate of deformation,  $\mathbf{v}$  is the velocity, and  $\mathbf{f}$  is the body force per unit of current volume. Recalling that since this model is using a ULF one doesn't integrate over the entire deformed volume, one integrates only over the incremental volume of each explicit time step (section 1.1.3.2) [31].

The physical interpretation of this virtual work principle is that: “The rate of work done by the external forces subjected to any virtual velocity field is equal to the rate of work done by the equilibrating stresses on the rate of deformation (or strain rate) of the same virtual velocity field.” [31].

It is important to note that this principle formulated in an Updated Lagrangian form is the “weaker equilibrium requirement” used to solve this 3D FE wear model.

## **1.4 Elasto-Viscoplastic Behavior**

### **1.4.1 Hooke's Law of Elasticity**

Hooke's law of elasticity states that the displacement of a spring,  $\Delta$ , is in direct proportion,  $k$ , to the applied load,  $F$  [106].

$$F = k\Delta \quad (C-89)$$

This law relates the elastic tensile stress and strains of materials and many materials obey this law up to the material's elastic limit. In strain-stress terms this law states that the materials tensile stress,  $\sigma$ , is linearly proportional to its displacement per unit of length (strain),  $\epsilon$ . In a mathematical form as:

$$\sigma = \mathbf{D}_E \epsilon_e \quad (C-90)$$

where  $\mathbf{D}_E$  is the stress-strain or elasticity matrix. This matrix is generally given in terms of the material modulus of elasticity,  $E$ , and Poisson's ratio,  $\nu$  [106].

Hooke's law is used in the 3D wear model to simulate the material's elastic response Figure C-7 shows how this law is used in the algorithm for elasto-viscoplastic straining during the explicit time step. It is also used for the penalty method, explained in section 1.7.3.

## 1.4.2 Viscoplasticity

This 3D wear model is based on a micro level collision. As this collision evolves the amount of deformation surpasses the elastic region and therefore viscoplasticity needs to be considered.

In continuum mechanics, the theory of viscoplasticity describes the rate-dependent inelastic behavior of solids. A material is rate-dependence, or viscous, when its deformation depends on the rate at which the loads are applied. When the material undergoes unrecoverable deformations it is said to be inelastic, or plastic [106].

Viscoplasticity formulations are commonly used to solve problems dealing with permanent deformations, collapse of structures, stability, crash simulations, systems exposed to high temperatures, and dynamic problems of systems exposed to high strain rates [31].

Viscoplasticity formulations are often based in the viscoplastic strain rate,  $\dot{\epsilon}_{vp}$ . Deriving equation 3.87, with respect to time, one gets  $\dot{\sigma} = \mathbf{D}_E \dot{\epsilon}_e$ . Substituting this result on equation 3.31,  $\mathbf{D} = \dot{\epsilon}_e + \dot{\epsilon}_{vp}$  and rearranging one arrives to

$$\mathbf{D} = \dot{\sigma} \mathbf{D}_E^{-1} + \dot{\epsilon}_{vp} \quad (C-91)$$

where  $\dot{\epsilon}_{vp}$  is the plastic strain,  $\mathbf{D}$  is the strain rate,  $\dot{\sigma}$  is the stress rate, and  $\mathbf{D}_E$  is the elasticity matrix [31].

The complex dynamic sliding wear problem attempted to be solved via this 3D FE wear model involves large permanent deformations, high strain rates and high temperatures, therefore, a constitutive viscoplastic model was selected for it.

For this 3D wear model the viscoplastic behavior was considered in three parts. The first part defines the uniaxial plasticity yield stress. The second part incorporates a plasticity flow rule. The third and last part applies a material failure criterion. Each one of these parts will be discussed in the next sections.

### 1.4.3 Johnson-Cook Viscoplastic Model

In viscoplasticity, the development of a mathematical model goes back to 1910 with Andrade's law. Many empirical and semi-empirical models are currently used to approximate plasticity. Some of the most popular models include: the Johnson–Cook , the Steinberg–Cochran–Guinan–Lund, the Zerilli–Armstrong, the Mechanical Threshold Stress, and the Preston–Tonks–Wallace model [106].

The Johnson–Cook model is an empirical, phenomenological model, widely used and available in Abaqus. It was selected for this 3D wear model because: 1) it provides a reasonable simulation of the viscoplastic behavior, 2) it is available in Abaqus (the FE package of choice), 3) it accounts for both temperature and plastic strain rate effects, 4) the necessary JC parameters for the materials of interest were already obtained in previous wear studies, and 5) because it can be used in conjunction with the Johnson–Cook’s dynamic failure model [31].

The Johnson-Cook’s viscoplastic model was developed in 1983 by G. R. Johnson and W. H. Cook. It is a phenomenological model based on Split-Hopkinson bar tests [31]. This model is suitable for high-strain-rate deformation of many materials, including most metals. It is suitable for problems where the strain rate varies over a large range and the temperature changes due to plastic deformation caused by thermal softening. It is often employed in adiabatic transient dynamic simulations [31]. The Johnson-Cook hardening model assumes the dynamic flow stress to be of the form:

$$\bar{\sigma}_y = [A + B(\bar{\epsilon}_p)^n][1 + CLn(\frac{\dot{\bar{\epsilon}}_p}{\dot{\bar{\epsilon}}_0})][1 - (\frac{T - T_0}{T_m - T_0})^m] \quad (C-92)$$

where  $\bar{\sigma}_y$  is the static yield stress,  $\bar{\epsilon}_p$  is the equivalent plastic strain,  $\dot{\bar{\epsilon}}_p$  is the equivalent plastic strain rate,  $\dot{\bar{\epsilon}}_0$  is the equivalent plastic strain rate,  $T$  is the current temperature,  $T_m$  is the melting temperature,  $T_0$  is the transition temperature,  $A$  is the initial yield stress,  $B$  is the hardening modulus,  $C$  is a strain rate dependent coefficient,  $m$  is the thermal softening coefficient, and  $n$  is the work-hardening exponent [31].

The first set of brackets represents the static yield stress obtained at the reference temperature and strain rate:

$$\frac{\dot{\bar{\epsilon}}_p}{\dot{\bar{\epsilon}}_0} = 1 \text{ and } \frac{T - T_0}{T_m - T_0} = 0 \quad (C-93)$$

The second and third sets of brackets represent the effects of strain rate and temperature, respectively. At the melting temperature the stress goes to zero.

The third bracket contains a term commonly referred as the homologous temperature, given by

$$T^* = \frac{T - T_0}{T_m - T_0} \quad (C-94)$$

where  $T$  is the current temperature,  $T_m$  is the melting temperature,  $T_0$  is the transition [31].

Section 1.9 presents the tests executed to derive the JC plasticity parameters for both of the materials used in this model.

#### 1.4.4 Johnson-Cook Flow Rule

According to the viscoplastic theory, viscoplastic flow occurs beyond the yield stress [31]. There are many flow rules trying to define the viscoplastic behavior of materials, some of the most popular include the Prandtl-Reuss flow for the perfectly plastic material behavior, the Von Mises flow governed by the Von Mises yield condition, and the Tresca flow governed by the Tresca yield criterion [31].

The flow rule used in this 3D wear model is based on the Johnson-Cook plasticity and can be expressed as:

$$\begin{aligned}\dot{\bar{\varepsilon}}_{vp} &= \dot{\varepsilon}_0 \exp\left[\frac{1}{C}(R-1)\right] & \text{for } \bar{\sigma}_y \geq \bar{\sigma}^0 & \text{(yield has occurred)} \\ \dot{\bar{\varepsilon}}_{vp} &= 0 & \text{for } \bar{\sigma}_y < \bar{\sigma}^0 & \text{(yield has not occurred)}\end{aligned}\quad (C-95)$$

where  $\dot{\bar{\varepsilon}}_{vp}$  is the equivalent plastic strain rate,  $\dot{\varepsilon}_0$  is the reference strain rate, generally  $\dot{\varepsilon}_0 = 1$ ,  $C$  is the JC strain rate dependent coefficient,  $R = R(\bar{\varepsilon}_{vp})$  is the ratio of the yield stress at non zero strain to the static yield stress, so that  $R(\dot{\varepsilon}_0) = 1$ , and  $\bar{\sigma}^0$  is the static yield stress [31].

The static yield stress is given by [31]:

$$\bar{\sigma}_y = [A + B(\bar{\varepsilon}_p)^n] \left[1 - \left(\frac{T - T_0}{T_m - T_0}\right)^m\right] \quad (C-96)$$

Figure C-7 shows how these last two equations are used in the algorithm for viscoplastic straining during an explicit time step.

#### 1.4.5 Johnson-Cook Dynamic Failure Criterion

Material failure is defined as “the loss of load carrying capacity of a material” [31]. Several criteria have been developed to attempt to predict when failure will occur.

The Johnson-Cook dynamic failure criterion was introduced by G. R. Johnson and W. H. Cook in 1985 to express the fracture strain as a function of strain rate, temperature and pressure. It is a phenomenological model based on the results of Split-Hopkinson bar tests, that attempts to predict when failure will occur based on what happened in the experimental data [31]. This criterion is suitable only for high-strain-rate deformation of metals, and it is generally appropriate for truly dynamic situations [31]. The criterion is based on the value of the equivalent plastic strain at element integration points. Johnson and Cook assumed failure occurs when the damage parameter  $\omega_{JC}$  exceeds 1.  $\omega_{JC}$  is defined in terms of the equivalent plastic strain as:

$$\omega_{JC} = \sum \frac{\Delta \bar{\varepsilon}_p}{\bar{\varepsilon}_f} \quad (C-97)$$

where  $\Delta \bar{\varepsilon}_p$  is the increment of the equivalent plastic strain and  $\bar{\varepsilon}_f$  is the strain at failure re-evaluated at each time increment[31].

The strain at failure is assumed to be of the form:

$$\bar{\varepsilon}_f = [d_1 + d_2 \exp(d_3 \frac{p}{q})][1 + d_4 \ln(\frac{\dot{\varepsilon}_p}{\dot{\varepsilon}_0})][1 + d_5 (\frac{T - T_0}{T_m - T_0})] \quad (C-98)$$

where  $\dot{\varepsilon}_p$  is the plastic strain rate,  $\dot{\varepsilon}_0$  is the reference strain rate,  $T$  is the current temperature,  $T_m$  is the melting temperature,  $T_0$  is the transition temperature,  $p$  is the pressure stress,  $q$  is the Von Mises stress, and  $d_1$  through  $d_5$  are the models' fracture constants [31].

The first set of brackets in this equation represents the strain to fracture as a function of the triaxiality increases. The term  $p/q$  used in this bracket is called triaxiality or the hydrostatic tensile stress and is defined as the ratio of the hydrostatic pressure over the Von Mises stress. The second bracket represents the effect of an increased strain rate on the material ductility. The third bracket represents the thermal softening as a function of the homologous temperature [31].

The JC dynamic failure criterion is used in this 3D FE wear model as a damage initiation criterion. Section 1.3 presents the tests executed to derive the JC fracture parameters.

#### 1.4.6 Damage Evolution Criterion

The Abaqus damage evolution criterion assumes that damage progressively degrades the material stiffness, leading to failure. For this model, the equivalent plastic displacement necessary to fail,  $\bar{u}_{pf}$ , was introduced as an input. The damage evolution is assumed to follow a linear relation between the equivalent plastic displacement,  $\bar{u}_p$ , and the damage variable,  $d$ . At the onset of damage  $\bar{u}_p = 0$ , and there is no stiffness degradation ( $d=0$ ). After the damage initiation point the rate of change of the equivalent plastic displacement,  $\dot{\bar{u}}_p$ , is calculated with [31]:

$$\dot{\bar{u}}_p = L \dot{\varepsilon}_p \quad (C-99)$$

where  $L$  is the characteristic length of the element, and  $\dot{\varepsilon}_p$  is the equivalent plastic strain

At failure  $\bar{u}_p = \bar{u}_{pf}$  and the stiffness is fully degraded ( $d=1$ ). The damage variable varies as a function of time according to [31]:

$$\dot{d} = \frac{\dot{\bar{u}}_p}{\bar{u}_{pf}} = \frac{L\dot{\bar{\epsilon}}_p}{\bar{u}_{pf}} \quad (\text{C-100})$$

where  $\dot{d}$  is the rate of change of the damage variable,  $\dot{\bar{\epsilon}}_p$  is the equivalent plastic strain rate,  $L$  is the element characteristic length, and  $\bar{u}_{pf}$  is the plastic displacement at the failure point. After reaching the damage initiation point the stress decreases according to [31]:

$$\sigma = \bar{\sigma}(1 - d_{EC}) \quad (\text{C-101})$$

where  $\sigma$  is the flow stress,  $\bar{\sigma}$  is the JC flow stress due to an undamaged response, and  $d_{EC}$  is the damage evolution criterion variable. This variable represents the material's stiffness degradation. When  $d_{EC} = 0$  the material has no stiffness degradation. When  $d_{EC} = 1$  the material stiffness is completely degraded and fracture is assumed to occur [31]. For this 3D FE wear model once fracture occurs then the element is deleted from the mesh.

## **1.5 Finite Element (FE) Concepts**

FE is an analysis technique to approximate the solutions to structural problems as an alternative to find the analytical solution. To find the analytic solution, the unknown quantities are obtained from mathematical functions valid at an infinite number of locations in the object under study, if this object has irregular geometries or discontinuities stating and solving these functions becomes very hard. As an alternative numerical methods provide only approximate values of the unknown quantities at discrete points in the object [31].

FE models divide a structure of interest into finite elements. For each of these elements, approximate functions are used to represent the unknown quantities. These elements are composed of various points, called nodes. Each of these nodes connects to its contiguous nodes creating a web throughout the structure. This web is called a mesh. The mesh is programmed with all the necessary information to simulate how the structure will respond to the applied conditions. During the analysis all the element functions are combined to produce a set of simultaneous algebraic equations. The number of functions

depends on the number of elements. The solution of these large-order systems of equations provides the approximate solution to the structural problem [84].

### 1.5.1 FE Analysis (FEA) Package

FEA packages, programmed to solve large-order systems of equations, became common with the blooming of fast computers and can help to simulate the effects of applied loads, vibrations, fatigue, and heat transfer. FEA packages, such as Abaqus, are very useful to simulate scenarios subject to high-stress applications, such as the collision of asperities studied in this research [31].

The FEA packages generally approach the motion of deformable materials in two main ways, either using Lagrangian or Eulerian meshes.

### 1.5.2 Explicit Dynamic Analysis

The explicit dynamics analysis in the Abaqus FEA package is based on the application of an explicit integration rule combined with the use of diagonal element mass matrices. The explicit integration through time is carried by using many small time increments and doesn't require iterations [31]. The equations of motion (for displacement, velocity and acceleration) are integrated using the explicit central difference integration rule.

$$\begin{aligned}
 \mathbf{u}^{(i+1)} &= \mathbf{u}^{(i)} + \Delta t^{(i+1)} \dot{\mathbf{u}}^{(i+1/2)} \\
 \dot{\mathbf{u}}^{(i+1/2)} &= \dot{\mathbf{u}}^{(i-1/2)} + \frac{\Delta t^{(i+1)} + \Delta t^{(i)}}{2} \ddot{\mathbf{u}}^{(i)} \\
 \ddot{\mathbf{u}}^{(i)} &= \mathbf{M}^{-1} \cdot (\mathbf{F}^{(i)} - \mathbf{P}^{(i)})
 \end{aligned} \tag{C-102}$$

where  $\mathbf{u}$  is the displacement,  $\dot{\mathbf{u}}$  is velocity,  $\ddot{\mathbf{u}}$  is acceleration,  $i$  is the increment number,  $i \pm 1/2$  are the mid-increment values,  $t$  is time,  $\mathbf{M}$  is the diagonal mass matrix,  $\mathbf{F}$  is the applied load vector, and  $\mathbf{P}$  is the internal force vector [31]. The internal vector is given by:

$$\mathbf{P} = \int_V \mathbf{B}^T : \boldsymbol{\sigma} dV \tag{C-103}$$

where and  $\mathbf{B}$  is a strain-displacement, and  $V$  is the volume of the material at the “current” point in time [31].

The explicit integration gains computational efficiency through the use of the diagonal element mass matrix,  $\mathbf{M}$ , since the inversion of it,  $\mathbf{M}^{-1}$ .  $\mathbf{M}^{-1}$  is used to compute the accelerations at the beginning of the increment [31].

The explicit integration is based in the fact that the kinematic state can be evaluated using known values of the velocity,  $\dot{\mathbf{u}}^{(i-\frac{1}{2})}$ , and acceleration,  $\ddot{\mathbf{u}}^{(i)}$ , from the previous increment. To start the integration the initial value of the mean velocity,  $\dot{\mathbf{u}}^{(-\frac{1}{2})}$ , needs to be defined. This value is defined in Abaqus by default as [31]:

$$\dot{\mathbf{u}}^{(-1/2)} = \dot{\mathbf{u}}^{(0)} + \frac{\Delta t^{(0)}}{2} \ddot{\mathbf{u}}^{(0)} \quad (\text{C-104})$$

### 1.5.3 FE Elasto Viscoplastic Straining Algorithm

The following strain increment equation can be used to create a FEA elasto-viscoplastic straining algorithm for an explicit integration method.

$$[\boldsymbol{\varepsilon}_{vp}]^{(i+1)} = [\boldsymbol{\varepsilon}_{vp}]^{(i)} + \sqrt{\frac{2}{3}} [\dot{\boldsymbol{\varepsilon}}_{vp}]^{(i+1/2)} : [\dot{\boldsymbol{\varepsilon}}_{vp}]^{(i+1/2)} \Delta t^{(i+1/2)} \quad (\text{C-105})$$

The flow chart presented in Figure C-7 employs many of the equations defined previously. This FE a basic viscoplastic algorithm can be implemented, using the dynamic explicit integration procedure in conjunction with the JC plasticity criterions. The algorithm employed by this model is far more complex, but this one provides a general idea of the flow to the reader.

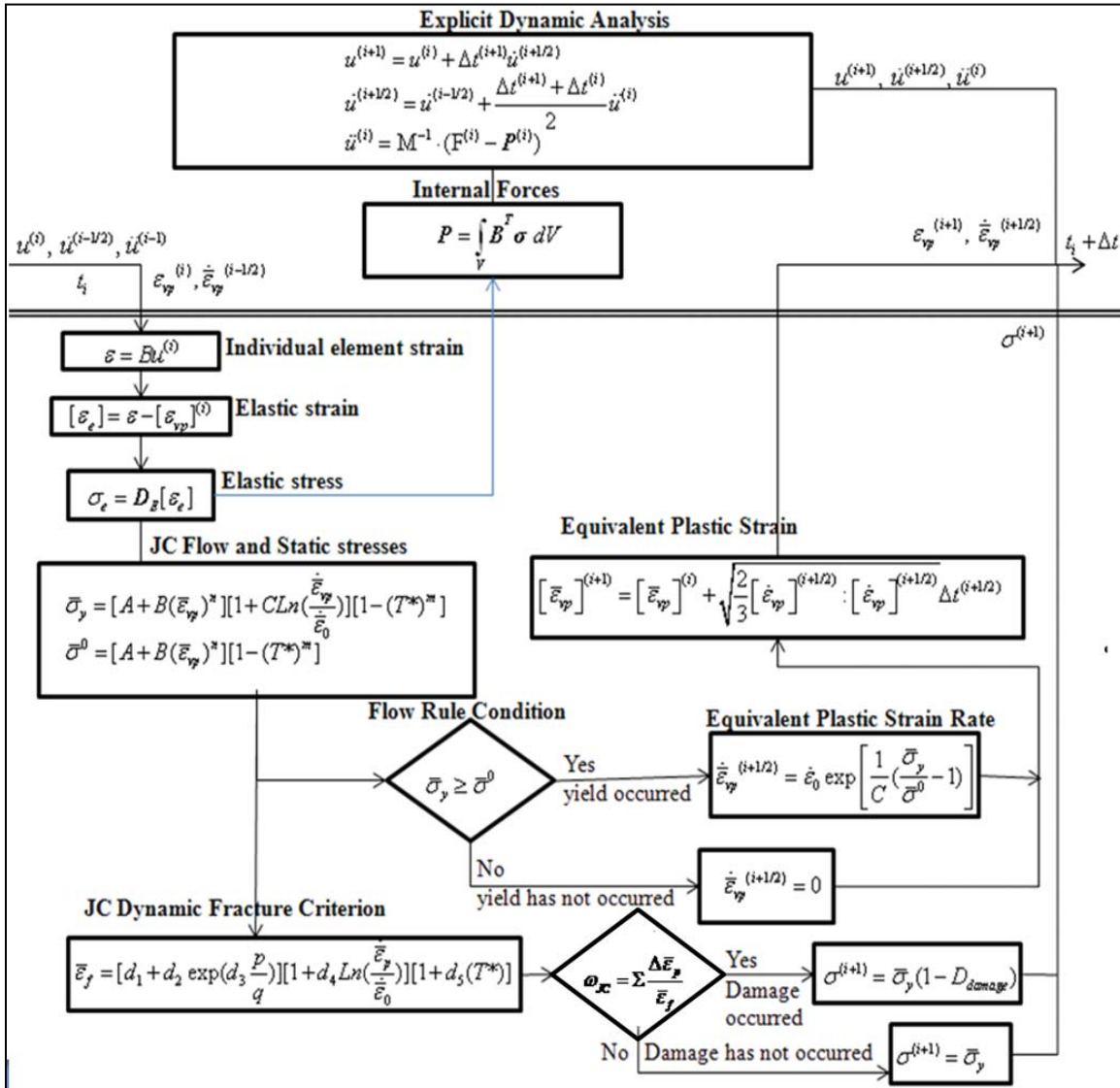


**Figure C-7 Algorithm Elasto-Viscoplastic Straining During a Time Step**

where  $\mathbf{M}$  is the global mass matrix,  $\mathbf{F}$  are the external load matrix,  $\mathbf{P}$  is the internal nodal forces,  $\boldsymbol{\varepsilon}$  is the individual element strain,  $\mathbf{B}$  is a strain-displacement matrix,  $\mathbf{D}_E$  is the

elasticity matrix,  $\varepsilon_e$  is the elastic strain,  $\bar{\sigma}_y$  is the yield stress,  $\varepsilon_{vp}$  is the plastic strain,  $\dot{\varepsilon}_{vp}$  is the equivalent viscoplastic strain rate,  $\dot{\varepsilon}_0$  is the reference strain rate,  $T$  is the current temperature,  $T_m$  is the melting temperature,  $T_0$  is the transition temperature,  $A$  is the initial yield stress,  $B$  is the hardening modulus,  $C$  is a strain rate dependent coefficient,  $m$  is the thermal softening coefficient, and  $n$  is the work-hardening exponent,  $\varepsilon_f$  is JC failure strain,  $p$  is the pressure stress,  $q$  is the Von Mises stress, and  $d_1$  through  $d_5$  are the models' fracture constants.

### 1.6 Mie-Gruneisen Equation of State

This 3D wear model deals with high-speed collisions that may generate shock waves therefore an EOS was considered to determine the pressure in a shock-compressed solid and the internal energy of the material. The EOS aids to solve the adiabatic equation of energy used in this model by providing the pressure,  $p$  in terms of the internal energy,  $U$  and the density,  $\rho$ . For this model the rise in temperature is calculated directly at the material integration points in accordance with the conservation of energy equation under adiabatic conditions aided by the EOS. By using this Mie-Gruneisen EOS the shock Hugoniot curve is taken as a reference, simulating the wave propagation more precisely.

Mie-Gruneisen EOS is generally used for problems involving high velocities [31]. On its linear form is given by:

$$p - p_H = \Gamma \rho (U - E_H) \quad (\text{C-106})$$

where  $p$  is pressure,  $p_H$  is the Hugoniot pressure,  $\Gamma$  is the Gruneisen ratio,  $\rho$  is density,  $U$  is the internal energy, a  $E_H$  is the Hugoniot specific energy [31].

The  $\Gamma$  Gruneisen ratio is defined by:

$$\Gamma = \Gamma_0 \frac{\rho_0}{\rho} \quad (\text{C-107})$$

where  $\Gamma_0$  is a material property and  $\rho_0$  is the reference density [31].

The Hugoniot specific energy  $E_H$  is defined by [31]:

$$E_H = p_H \frac{\eta}{2\rho_0} \quad (\text{C-108})$$

The nominal compressive strain  $\eta$  is given by [31]:

$$\eta = 1 - \frac{\rho_0}{\rho} \quad (\text{C-109})$$

The Hugonit pressure  $p_H$  can be stated as [31]:

$$p_H = \frac{\rho_0 c_0^2 \eta}{(1 - s\eta)^2} \quad (\text{C-110})$$

where  $c_0$  is the reference speed of sound and  $s$  is a parameter that relates the linear shock velocity  $U_s$  and the particle velocity  $U_p$  by equation [31].

$$U_s = c_0 + sU_p. \quad (\text{C-111})$$

If one substitutes these four equations on the linear form of the Mie-Gruneisen EOS and rearrange it in terms of pressure, one arrives to the form of the EOS used by Abaqus [31]:

$$p = \frac{\rho_0 c_0^2 \eta}{(1 - s\eta)^2} \left(1 - \frac{\Gamma_0 \eta}{2}\right) + \Gamma_0 \rho_0 U \quad (\text{C-112})$$

This 3D wear model incorporates this EOS to aid in the solution of the system of equations. One of its disadvantages is that it is unable to handle material phase changes, e.g. melting due to large internal pressure and/or temperatures, however, for this model this is not considered an issue because the elements that reach its melting point are considered as failed elements and are removed from the mesh and from any further calculations.

## **1.7 Surface Interactions**

### **1.7.1 Surface Roughness**

Based on the results from previous wear studies this 3D FE model focuses on characterizing an asperity collision at the micro-mechanical level. Specifically at one of the contact points between the two sliding surfaces. In order to simulate this scenario it is

critical to understand the surface roughness parameters, specifically what is an asperity, what is a valley, how can one measure them, and how are they distributed.

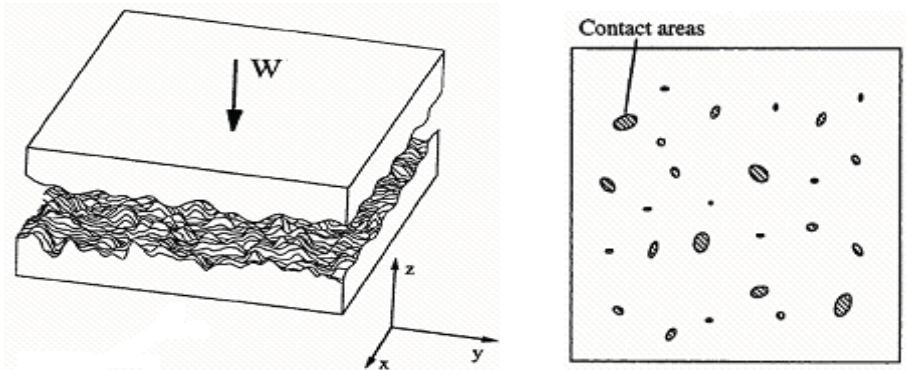


**Figure C-8 Schematic of Surfaces in Contact and their Contact Points [12]**

When two supposedly flat surfaces as those depicted in Figure C-8 (left) become into contact, this contact occurs only at discrete contact points, as shown in Figure C-8 (right). These contact areas have in their vicinity regional stresses that oppose the applied load. If one of these surfaces slides over the other one, deformation occurs around these contact spots and the material failure is reached, sliding wear occurs. Thus, one can model sliding wear at the micro-mechanical level attempting to replicate the interactions between the two surfaces, at these contact points [12].

Roughness is a measure of the surface texture. It can be quantified by the vertical deviations from an ideal horizontal surface, or mean line. If these deviations are large, the surface is rough; if they are small the surface is smooth [12].

Roughness can be characterized by many parameters a commonly used parameter is amplitude. Amplitude parameters can provide us statistical information about the shape of the height distribution histogram. The high points on the histogram are called asperities or peaks, and the low points are called valleys. Moreover, the asperities can be defined as microscopic projections on surfaces resulting from surface finishing processes [12].

In this model, one accounts for the surface roughness based on amplitude parameters, the average roughness,  $R_a$ :

$$R_a = \frac{1}{n} \sum_1^n |y_i| \quad (\text{C-113})$$

where  $n$  is the number of points on the profile and  $y_i$  is the vertical distance from the mean line.

This formula assumes a filtered roughness profile and an already calculated mean line. Typically the roughness is filtered to separate form error, waviness, and roughness resulting from a measurement.

The dimensions of the asperities modeled were based on average asperity size measurements taken on specimens of the materials.

To extrapolate the model results a spatial parameter, the number of asperities per unit of area was employed. This parameter is given by:

$$\# Asp_{uA} = \frac{\text{Number of asperities}}{M \times N} \quad (\text{C-114})$$

where  $M$  and  $N$  are the width and length of the rectangular microscopical image.

This value is used to extrapolate the wear due to a single asperity into the average wear due multiple asperities assuming the density of the asperities is such, that the distance between surface contact points is large enough that one can consider wear due to a single asperity collision as an isolated event. Thus, any consecutive collisions are then considered as only replicates of this single asperity collision scenario.

Section 1.4 presents the experimentation required to obtain the surface roughness parameters to be used in this 3D wear model. Sections 5 shows how the asperity size parameters are incorporated into the model geometry to characterize sliding the micro-mechanical wear.

### **1.7.2 Friction**

Friction is important for this investigation since the 3D wear model is based on the dry sliding between two objects at the micro-mechanical level, and therefore the forces generated by this relative motion need to be considered.

Friction is defined as the force resisting the relative motion of solid surfaces, fluid layers, and/or material elements sliding against each other [37]. This section presents the required frictional background.

Charles-Augustine de Coulomb developed a model to calculate the force of dry friction using the following governing equation:

$$F_f \leq \mu F_n \quad (\text{C-115})$$

where  $F_f$  is the force of friction exerted by each surface on the other,  $\mu$  is an empirical coefficient of friction, and  $F_n$  is the normal force exerted by each surface on the other.

In the article “Frictional Interactions in High-speed Sliding Contact”, Chad A. Burton and Robert A. Brockman, they state that the “friction coefficient is an empirical parameter that accounts for sources of resistance to relative motion on a scale smaller than that represented explicitly in one’s model ...”. They suggest that all the frictional resistance arising from surface waviness, asperities, and smaller microstructural features must be bundled into a specified value of  $\mu$ . If the model has details about surface waviness or asperities, then the appropriate value of the friction coefficient must change: the features represented explicitly in the model, produce additional frictional resistance that was previously accounted by the value of  $\mu$  at the higher level. They conclude that the value of  $\mu$  does not disappear, since smaller-scale features will still contribute to sliding friction but will not be manifested in the model physics automatically [20]. The Figure C-9 shows a notional depiction of this concept of the qualitative dependence of

friction coefficient on model length scale.

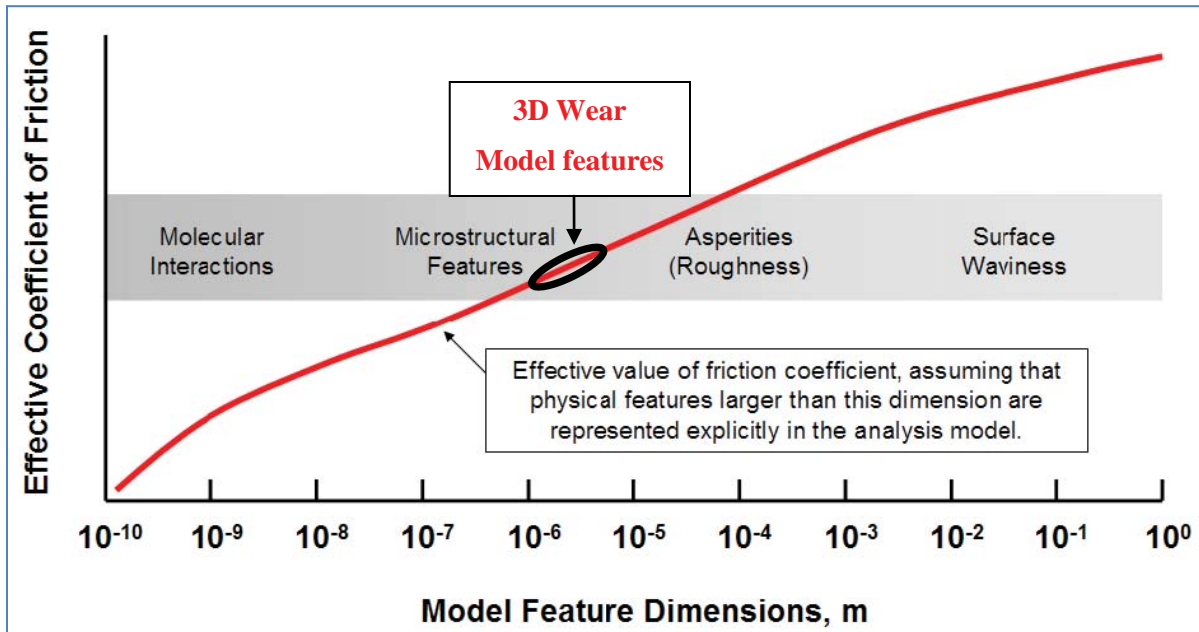


**Figure C-9 Qualitative Dependence of Friction Coefficient on Length Scale**

The 3D wear model takes into consideration roughness features at the asperity level, in fact it focuses on the collision of these asperities. The size range of the asperities to be modeled is 2-10 micro-meters. Thus, considering this fact, the effective Coefficient Of Friction (COF) to be used for it should be a fraction of that obtained at macro-level experiments, however due to the lack of experimental data available, the COF employed on it was based on Montgomery's steel-on-steel investigations [81].

### 1.7.3 Penalty Method

During a collision, as the one simulated in this research's 3D wear model, the contact between the two bodies needs to be considered. Specifically, once they start to interpenetrate the external boundaries of each other.

The penalty method is an algorithm to simulate a rigid body contact that permits some relative motion of the surfaces, an elastic slip. This method applies virtual springs (stiffness) to the surfaces in contact [31]. The penalty method, predicts the updated geometry using the basic central difference algorithm, looks for contact conditions that are active or violated, and then corrects them by doing two things:

(1) Adjusting the location of the nodes and their velocities to ensure the contact constraint is satisfied, while conserving momentum in the process [31]; and

(2) Applying restoring forces to maintain the contact constraint. The restoring forces are determined via the properties of the materials in contact, so the appropriate penalty stiffness can be applied without wrecking the critical time step. These restoring forces are proportional to the length of sudden interpenetration [31]. Figure C-10 shows a graphical depiction of this method.

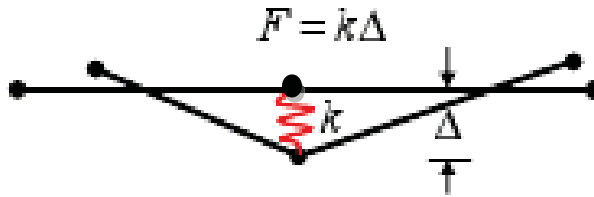


**Figure C-10 Schematic of the Penalty Method Equivalent Stiffness**

The penalty becomes greater as the material penetration  $\Delta$  increases, which is physically equivalent to a compression of a spring.

The potential energy  $\Pi_{sp}$ , resulting when applying the penalty methods and is given by:

$$\Pi_{sp} = \frac{1}{2} k \Delta^2 \quad (C-116)$$

This penalty term then can be easily incorporated to enforce the constraint by adding it to the potential energy function,  $\Pi_p$ , of the system. This energy is then accounted for in the energy method used to solve the statistically indeterminate systems of equations [31].

## **1.8 Experimentation and Extrapolation Concepts**

### **1.8.1 Archard's Wear Rate Model**

Archard's [4] approach to obtain wear rates is important for this research because it has proven to be successful for low-velocities problems. This model was used on previous high-speed wear investigations to develop a scaling factor used to extrapolate

low-speed proven results to high-speed predictions. For this research the dimensionless normalized results obtained with Archard's model will be used for comparison purposes.

In 1956, Archard [4] experimented with a pin on disk system to study the wear of metals under dry conditions. They employed a low speed rotating disk with a pin over its surface. They researched the material wear effects due to the load applied to the pin and due to the disk low velocity rotation. They related wear rates, normal loads and material hardness via the following equation:

$$\tilde{Q} = W_{uA} = k_A \tilde{p} \quad (\text{C-117})$$

where  $\tilde{Q}$  is the dimensionless normalized wear rate also called the wear rate per unit of area,  $W_{uA}$ ,  $k_A$  is Archard's Wear Coefficient,  $\tilde{p}$  is the normalized pressure given by

$$\tilde{p} = \frac{F_n}{A_n H} \quad (\text{C-118})$$

where  $F_n$  is the normal force,  $A_n$  is the apparent contact area, and  $H$  is the indentation hardness.

Delamination occurs when materials separates in layers. Archard's wear coefficient  $k_A$ , can be estimated with the following delamination theory formula, based on plastic shear strain accumulation around material inclusions.

$$k_A = \frac{2\gamma_0 f_v}{f_A^*} \quad (\text{C-119})$$

where  $\gamma_0$  is the accumulated plastic shear strain,  $f_v$  is the volume fraction of inclusions, and  $f_A^*$  is the critical area fraction of voids.

Archard's experiments were based on low speed sliding wear. Archard's model was considered inappropriate for this high speed sliding wear problem since this problem deals with velocities up to 1,530 m/s and Archard's experiments were executed at a relatively low velocities around 10 m/s [4].

### 1.8.2 Wear Rates and Total Sliding Wear.

Wear rate is defined as the volume of material removed per unit of time or per unit of sliding distance [12]. For this research, the wear rates are considered in terms of sliding distance, unless otherwise noted. The equation for a dimensional wear rate is

$$W = V_d / D_s \quad (C-120)$$

where  $W$  is the wear rate,  $V_d$  is the volume of material removed or damaged, and  $D_s$  is the sliding distance.

The wear rates can be normalized to become dimensionless by dividing them by the area of contact,  $A_c$ . These wear rates per unit of area can be calculated by:

$$W_{uA} = W / A_c \left( \frac{V_d [mm^3]}{D_s [mm] \cdot A_c [mm^2]} \right) \quad (C-121)$$

Dimensionless wear rates are the most practical because they can be applied regardless of the dimensions of the system. Section 6.4 explains why in this problem dimensionless wear rates are necessary since the area of contact varies.

For a rectangular shape the  $A_c$  is given by:

$$A_c = l_c \times w_c \quad (C-122)$$

where  $l_c$  and  $w_c$  are the length and width of the area in contact, assumed to be rectangular.

The sliding distance,  $D_s$ , is a function of the horizontal distance traveled,  $D$ , and the percent of distance in contact,  $\%Cont$ , or:

$$D_s = D \cdot \%Cont \quad (C-123)$$

To estimate wear, one can arrive to the following equation by combining and rearranging the previous three equations.

$$V_d = W_{uA} \times l_c \times w_c \times D_s \times \%Cont \quad (C-124)$$

Since generally the wear rates are a function of the sliding velocity then, if the velocity is not constant, one can estimate the total wear by dividing the velocity profile into a number,  $n$ , of discrete velocity ranges, evaluating the wear at each range, and then adding them all. In other words:

$$V_d = \sum_1^n W_{uA_n} \times l_{c_n} \times w_{c_n} \times D_{s_n} \times \%Cont_n \quad (C-125)$$

where  $V_d$  is the total wear,  $W_{uA_n}$  are the normalized wear rates,  $l_{c_n}$  is the length in contact,  $w_{c_n}$  is the width in contact,  $D_{s_n}$  is the sliding distance in contact,  $\%Cont_n$  is the percent of distance in contact and the suffix  $n$  denotes the discrete velocity range number.

Section 5.11 summarizes how this equation will be used in conjunction with the normalized wear values to calculate the total mechanical sliding wear.

### **1.8.3 Split Hopkinson Bar (SHB) Tests**

This section provides the background information of the SHB test experiments required to obtain some of the parameters necessary for this model. Although the apparatus presented was not be physically operated by the student, understanding their theory and providing an overview of their operation is important.

The Hopkinson Pressure Bar was developed by Bertram Hopkinson in 1914 to measure stress pulse propagation in a metal bar. In 1949 H. Kolsky refined the technique by using two bars in series, setup known as the split-Hopkinson bar, to measure stress and strain, incorporating oscilloscopes with electrical condenser units to measure the pressure wave propagation in the pressure bars. Later modifications have allowed for tensile, compression, impact, and torsion testing [24]. Figure C-11, is a picture of the UDRI SHB test apparatus. Figure C-12 shows a schematic of the apparatus and Figure C-13 zooms into the schematic of the test specimen.

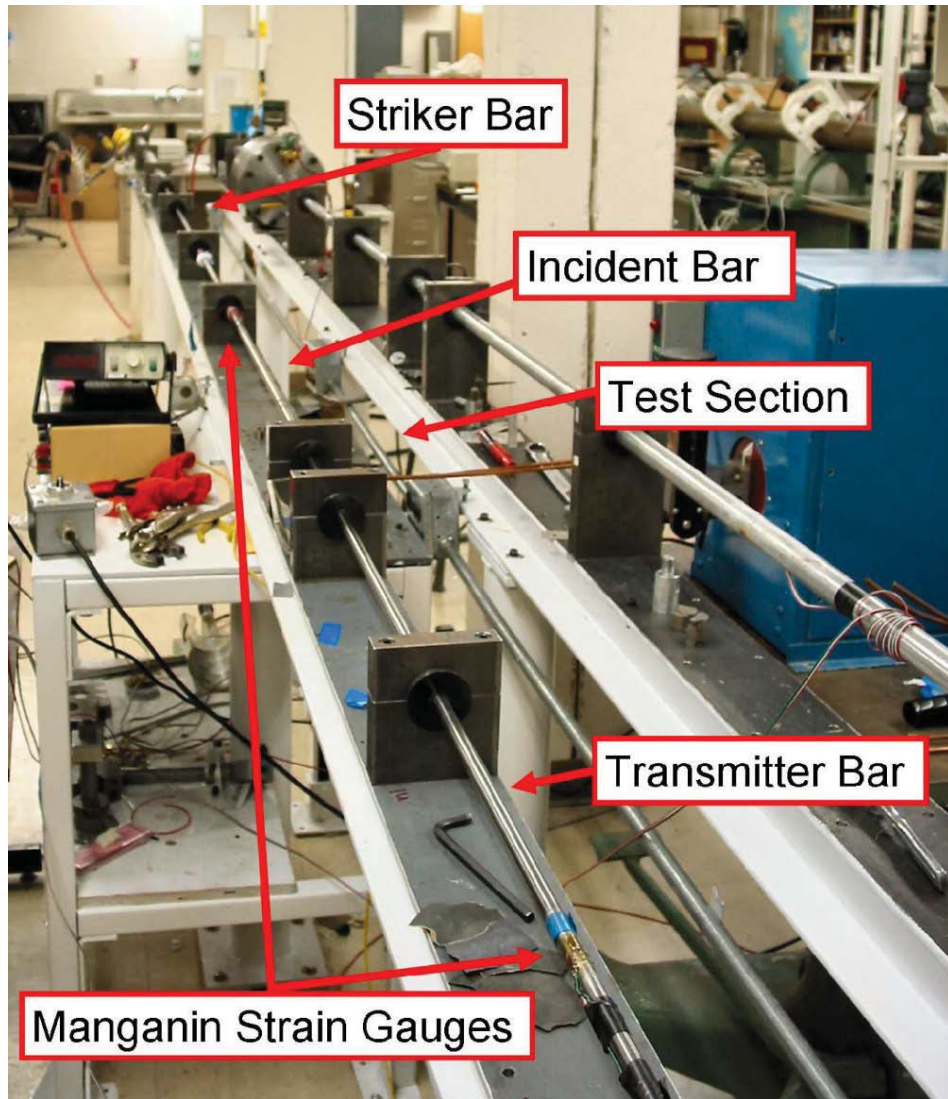


**Figure C-11 UDRI Split Hopkinson Bar Test Apparatus [24].**

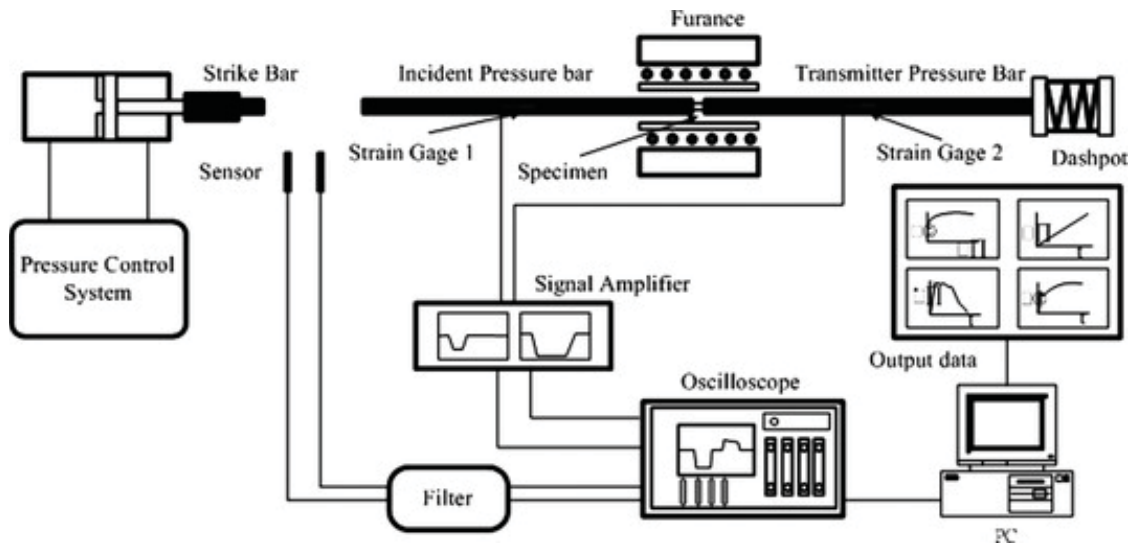


Figure C-12 Split Hopkinson Bar Test Apparatus for Direct Impact Tests [57]

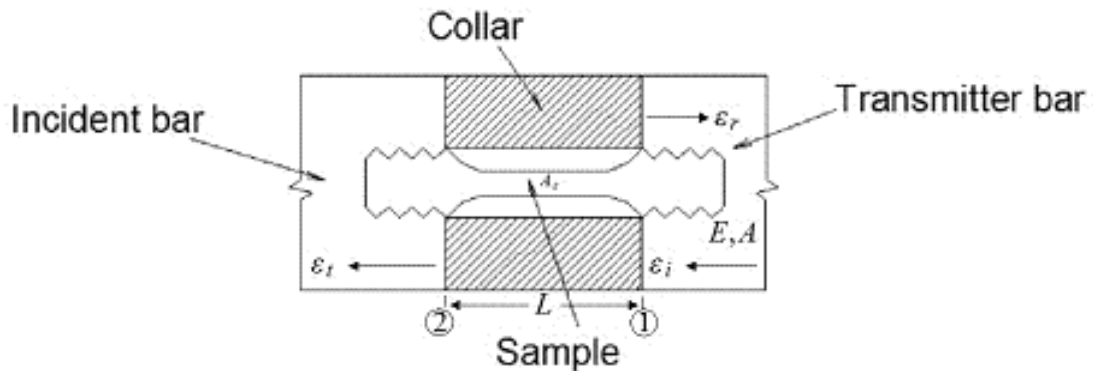
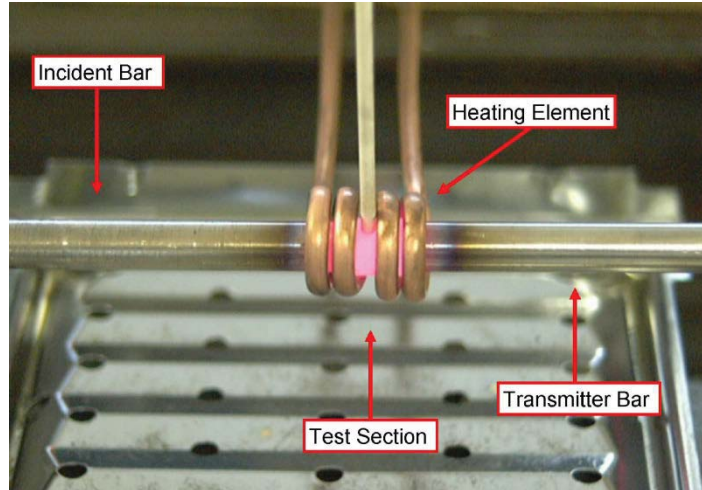


Figure C-13 Schematic of SHB Test Specimen [24].

This SHB tests can be carried out to obtain data at different temperatures by pre-heating the specimen to the temperature of interest with the aid of a heating element as the one presented in the Figure C-14 [24].



**Figure C-14 SHB Test Apparatus Heating Element [24].**

For the SHB direct impact tests the striker bar hits the incident bar, this impact creates a stress wave that propagates through the incident bar at the material's sound speed. A collar made from the same material used for the bars is surrounds the specimen to let it withstand the compression from the stress wave. This facilitates the pulse to be transmitted through the test specimen without a significant loss of the wave intensity. The incident wave loses the specimen's collar as it passes through it. The free end then reflects the compression wave as a tension wave because it cannot support the stress. This wave travels through the transmitter bar, back to the specimen (now without a collar) [24]. The transmitted strain pulse,  $\varepsilon_t$ , is measured with a strain gage placed on the incident bar (Strain gage 1 in Figure C-12. The reflected strain pulse,  $\varepsilon_r$  is measured with a strain gage placed on the transmitter bar (Strain gage 2 in Figure C-12. From the strain data gathered by these two gages the stresses can be calculated as follow [57]:

First, the stress pulse are assumed to be

$$\sigma = \rho c_o V_s \tag{C-126}$$

where  $\rho$  is the material density,  $c_o$  is the material sound speed, and  $V_s$  is the striker bar velocity measured using laser breaks.

The elastic wave speed can be calculated with:

$$c_o = \sqrt{\frac{E}{\rho}} \tag{C-127}$$

where  $E$  is the striker bar elastic modulus.

The displacements at the ends of the specimen are evaluated with:

$$u_1 = \int_0^t c_0 \varepsilon_1 dt = c_0 \int_0^t (\varepsilon_i - \varepsilon_r) dt \quad (C-128)$$

$$u_2 = \int_0^t c_0 \varepsilon_2 dt = c_0 \int_0^t \varepsilon_t dt \quad (C-129)$$

where  $u_{1,2}$  are the displacements at ends 1 and 2 of,  $\varepsilon_{1,2}$  are the strains at ends 1 and 2,  $c_0$  is the material sound speed and  $\varepsilon_i$ ,  $\varepsilon_t$ , and  $\varepsilon_r$  are the incident, transmitted and reflected strain pulses [57].

Knowing that  $\varepsilon = \partial u / \partial x$ , one evaluates the specimen strain,  $\varepsilon_s$ , with:

$$\varepsilon_s = \frac{u_1 - u_2}{L} \quad (C-130)$$

where  $L$  is the length of the specimen and  $u_{1,2}$  are the displacements at ends 1 and 2 [57].

Combining these three equations one can express the specimen strain as:

$$\varepsilon_s = \frac{c_0}{L} \int_0^t (\varepsilon_i - \varepsilon_r - \varepsilon_t) dt \quad (C-131)$$

The pressures on the specimen's ends are given by:

$$P_1 = EA(\varepsilon_i + \varepsilon_r) \quad (C-132)$$

$$P_2 = EA\varepsilon_t \quad (C-133)$$

where  $E$  is Young's modulus of elasticity and  $A$  is the specimen's cross area [57].

Assuming that the forces on both ends of the specimen are equal,  $P_1 = P_2$ , then by combining the last two equations one arrives to [57]:

$$\varepsilon_t = \varepsilon_i + \varepsilon_r \quad (C-134)$$

Substituting this equation into 3.112 one arrives to:

$$\varepsilon_s = \frac{c_0}{L} \int_0^t [\varepsilon_i - \varepsilon_r - (\varepsilon_i + \varepsilon_r)] dt = \frac{-2c_0}{L} \int_0^t \varepsilon_r dt \quad (C-135)$$

Deriving this equation one can calculate the specimens stress rate:

$$\dot{\varepsilon}_s = \frac{-2c_o}{L} \varepsilon_r \quad (\text{C-136})$$

Knowing that  $\sigma = E\varepsilon$ , one can express the specimen stress as:

$$\sigma_s = E\varepsilon_s \quad (\text{C-137})$$

Understanding the methods required to phenomenologically obtain the material's properties, both elastic and plastic at varying strain rates, was required. The stress and strain measurements derived from these experiments can be used to develop the constitutive models that approximate the material's characteristics. For this research the stress-strain curves obtained from these types of experiments, executed at various strain rates and temperatures, were used to obtain the Johnson-Cook's plasticity model parameters. The maximum strain-rate that can be generated in the SHB scenario is on the order of  $10^3/\text{sec}$  [24].

#### 1.8.4 Flyer Impact Plate Tests (FIPT)

To cover the maximum range of strain-rates when developing the Johnson-cook constitutive model, two major tests are typically conducted. The traditional SHB test that can generate the parameters for strain-rates up to  $10^3/\text{sec}$  and the flyer impact plate tests to extend it beyond those that. The FIPT can be used for uniaxial strain-rates ranging from  $10^4/\text{sec}$  to  $10^6/\text{sec}$  [24].

On these experiments a flyer plate is launched in a gun barrel towards a stationary target plate. The flyer plate is carried on a projectile known as a sabot, and is launched at velocities ranging from a few meters per second up to several kilometers per second using a variety of gas and powder. A picture of the flyer plate apparatus and a schematic of the simple plate impact experiment are shown in Figure C-15. Once the impact occurs, normal uniaxial-strain compressive waves will be propagated in both the flyer and the target. The target plate is expected to deform inelastically during the experiment. If the impact velocity is sufficiently high, one or both of the propagating waves within the plates will be inelastic. At velocities just above the velocity required to cause yield of the target material, both elastic and plastic waves will propagate into the target, with the elastic precursor propagating at a higher wave speed. The magnitude of the elastic

precursor wave is known as the Hugoniot elastic limit (HEL). The flyer plate experiments can be tailored to yield both the HEL and the peak stresses at given impact velocities [24].

The elastic precursor wave travels at the material sound speed. The plastic deformation wave travels at a slower speed behind the elastic precursor. At a particular point in the material, the peak stress is the summation of the plastic and elastic deformation waves, until the elastic release wave returns from the far-field boundary. The main reason that the HEL is used to estimate the flow stress at a given strain-rate is that uniaxial strain simulations of the impact event will rely on the material constitutive model to adjust the magnitude of the HEL and thereby the total peak stress. These high speed tests can provide the stress measurements with respect to time for a given impact [24].

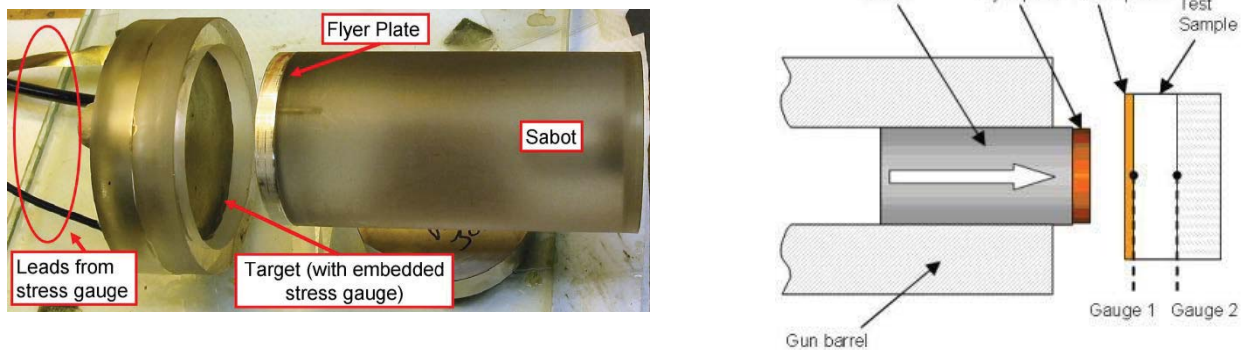


**Figure C-15 Flyer Plate Test Apparatus and Schematic [24].**

### **1.9 Appendix Summary**

In summary, this appendix is an attempt to present as much as practical, all of the methods and functions used to develop this FE wear model. As stated at the beginning of the appendix “each section could be a appendix in its self”. It was felt that the order of the important concepts should be presented before the concepts and functions were used. In addition, some concepts that are not used were presented for completeness of the theory. Finally one must realize many of the equations are incremental and though they were not show explicitly, the mean was stated. The concept of displacement for example comes from integrating the velocity with respect to time and the velocity is based on

integrating acceleration with respect to time. The explicit method used in Abaqus characterizes each node and balances force.

## Appendix D. Input Parameters Determination

This appendix presents a summary of the processes required to derive this 3D FE wear model input parameters. These parameters were obtained from previous studies such as those conducted by Montgomery's to obtain the coefficient of friction, by Johnson and Holmquist for the J-C parameters, and by Dr. Voyiadjis for the surface characterization parameters. None of these experiments were carried out by the author. This appendix presents only a brief overview of the experiments required to obtain the parameters for each of the algorithms employed by this 3D FE wear model. The references included in each section will point the documents containing the details of each experimentation.

### 1.1 Johnson-Cook Plasticity Parameters for Low-Strain-Rate Scenarios

In 2005, Z. A. Kennan [57] conducted Split Hopkinson bar tests, at the University of Dayton Research Institute (UDRI). He conducted these tests using AISI-1080 and VascoMax 300 steel specimens submitted to various strain rates and temperatures to develop the constitutive model for each of these two materials. The dimensions of the specimens employed on these experiments are depicted in Figure D-1.

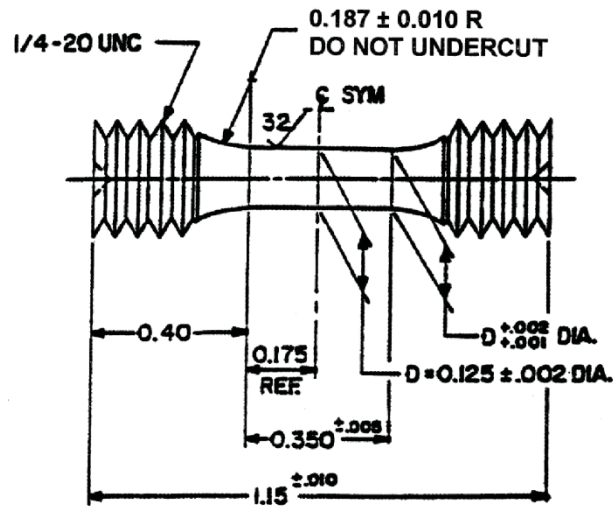


Figure D-1 SHB Specimen Dimensions (inches) [57]

The AISI-1080 Steel results from the SHB Tests are presented in Table D-1.

Test No.	Test Temp (°F)	Strain Rate (s <sup>-1</sup> )	Flow Stress at $\epsilon \sim .06$ (GPa)
Q1, Q2	70	~1	1.048
3, 4	70	~500	1.22
11, 12	300	~500	1.01
16, 17	500	~500	.89
18, 20	750	~500	1.00
6, 7	70	~1000	1.27
13, 14	300	~1000	.88
23, 24	500	~1000	.75
22, 31	750	~1000	.99
25, 26	70	~1500	1.18
33, 34	300	~1500	1.26
27, 28	500	~1500	1.12
36, 38	750	~1500	.82

**Table D-1 SHB Test Results for AISI-1080 Steel [57]**

UDRI obtained the quasi-static data presented in Figure D-2 from two tensile strength tests. In both, the AISI-1080 steel displayed a typical strain-hardening curve and very little necking, as one can see in Figure D-2 [57].

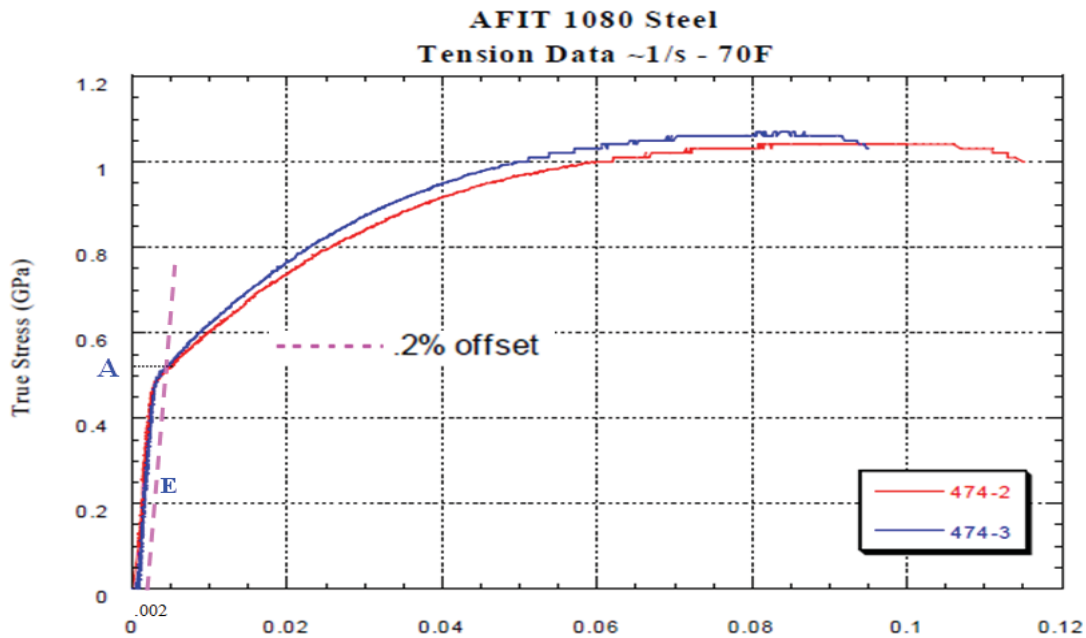


**Figure D-2 Stress-Strain Curves for AISI-1080 Steel [57]**

The data from these quasi-static tests was used to obtain the material elastic Modulus. The slope of the elastic region represents the elastic modulus,  $E$ . For these tests the average  $E$  was determined to be 203 GPa [57].

This data was also used to obtain the parameters  $A$ ,  $B$  and  $n$  of the Johnson-Cook plasticity equation, presented in section 1.4.3:

$$\bar{\sigma}_y = [A + B(\bar{\epsilon}_p)^n][1 + CLn(\frac{\dot{\bar{\epsilon}}_p}{\dot{\bar{\epsilon}}_0})][1 - (\frac{T - T_0}{T_m - T_0})^m] \quad (D-1)$$

where  $\bar{\sigma}_y$  is the static yield stress,  $\bar{\epsilon}_p$  is the equivalent plastic strain,  $\dot{\bar{\epsilon}}_p$  is the equivalent plastic strain rate,  $\dot{\bar{\epsilon}}_0$  is the equivalent plastic strain rate,  $T$  is the current temperature,  $T_m$  is the melting temperature,  $T_0$  is the transition temperature,  $A$  is the initial yield stress,  $B$  is the hardening modulus, and  $C$  is a strain rate dependent coefficient [57].

The JC parameter  $A$ , was determined by applying the 0.2% offset yield limit rule typically used on steels to determine their Yield stress. Their offset is depicted by the pink line in the previous figure and its intersection point, represents the yield stress (JC parameter  $A$ ). The average from both tests was 0.525 GPa [57].

To obtain the Johnson-Cook strain hardening factor,  $B$ , and the strain hardening index,  $n$ , the plastic region of the quasi-static curves was defined in terms of the Effective Stress Difference (ESD) and the plastic strain. The ESD, or stress after the yield stress, can be calculated simply by subtracting to the total stress from the yield stress. The plastic strain can be calculated as the total strain minus the elastic strain. Plotting the log of the ESD and plastic strain allows one to apply a linear fit. The logarithmic plots for test 474-2 are presented in Figure D-3 and for test 474-3 in Figure D-4 [57].

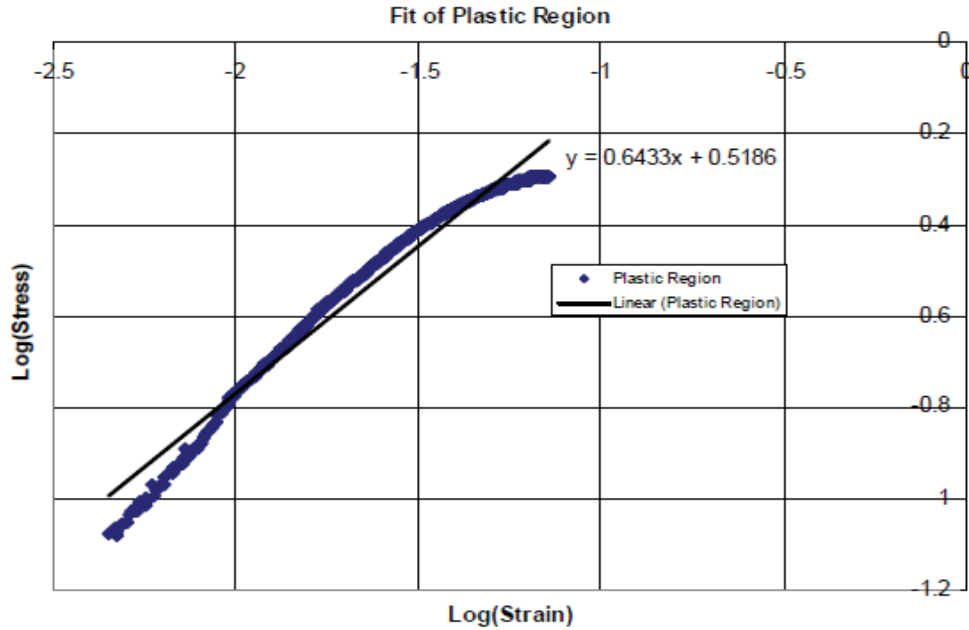


**Figure D-3 Strain Hardening Factor “B” and Index “n” for Test 474-2 [57]**

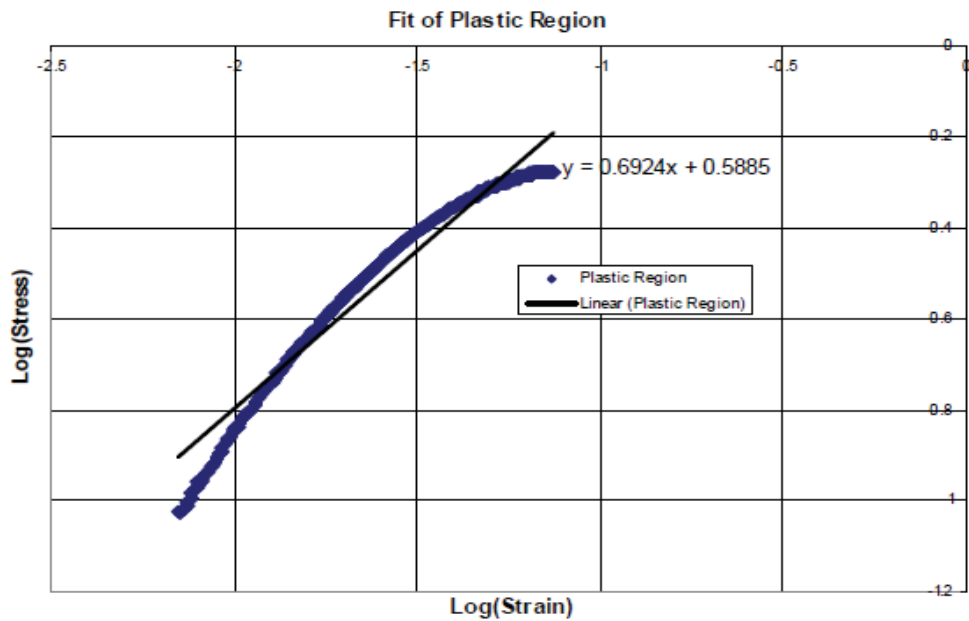


**Figure D-4 Strain Hardening Factor “B” and Index “n” for Test 474-3 [57]**

The JC strain hardening factor B is determined by the intersection of these log plots with the Y axis, in these cases the intersection values are 0.5186 and 0.5885. Converting these logarithmic values of B one gets: For test 474-2,  $B=10^{0.5186}=3.300$  and for test 474-3,  $B=10^{0.5885}=3.877$ . Their average was determined to be  $B=3.59$  GPa.

The JC strain hardening index,  $n$ , is the slope of these logarithmic plots, therefore  $n=0.6433$  for the 474-2 test and  $n=0.6924$  for the 474-3 test. Their average  $n=0.67$ .

The strain rate sensitivity parameter,  $C$ , can be found from SHB tests conducted at room temperature, 25 °C and various strain rates. Kennan [57] carried these experiments at four arbitrary different strain rates: 1/s, 500/s, 1000/s, and 1500/s. To find the  $C$  coefficient, he followed these steps [57]:

(1) Selected a strain that represents the plastic area of interest, high to facilitate calculations but away from the fracture point, Kennan selected a strain of 0.62,

(2) From experiments at various strain rates, he created a series of points by dividing the JC dynamic stress (defined in section 1.4.3) at the strain of interest by the static stress (defined in section 1.4.4) and given by:

$$\bar{\sigma}_y = [A + B(\bar{\epsilon}_p)^n] \left[ 1 - \left( \frac{T - T_0}{T_m - T_0} \right)^m \right] \quad (D-2)$$

(3) Plotted on a logarithmic scale the ratio of the dynamic stress over the static stress versus the strain rate, (3) applied a least square fit to the test points, and

(4) Obtained the slope of the least square fit, which is the  $C$  coefficient [57].

Table D-2 shows the data that Kennan employed to obtain the strain rate sensitivity of the AISI-1080 steel and Figure D-5 presents the plot he used.. The chosen strain was 0.62 and the average  $C$  was determined to be 0.029 [57].

Strain Rate	Test Number	Stress at E=.062	Avg Stress	Dynamic/Static Stress	Ln(Strain Rate)
1	1	1.0000	1.0200	1.0000	0.0000
1	2	1.0400			
500	3	1.2107	1.2227	1.1987	6.2146
500	4	1.2347			
1000	6	1.2971	1.2686	1.2437	6.9078
1000	7	1.2401			
1500	25	1.1759	1.1792	1.1561	7.3132
1500	26	1.1825			

**Table D-2 Strain Rate Data [57]**

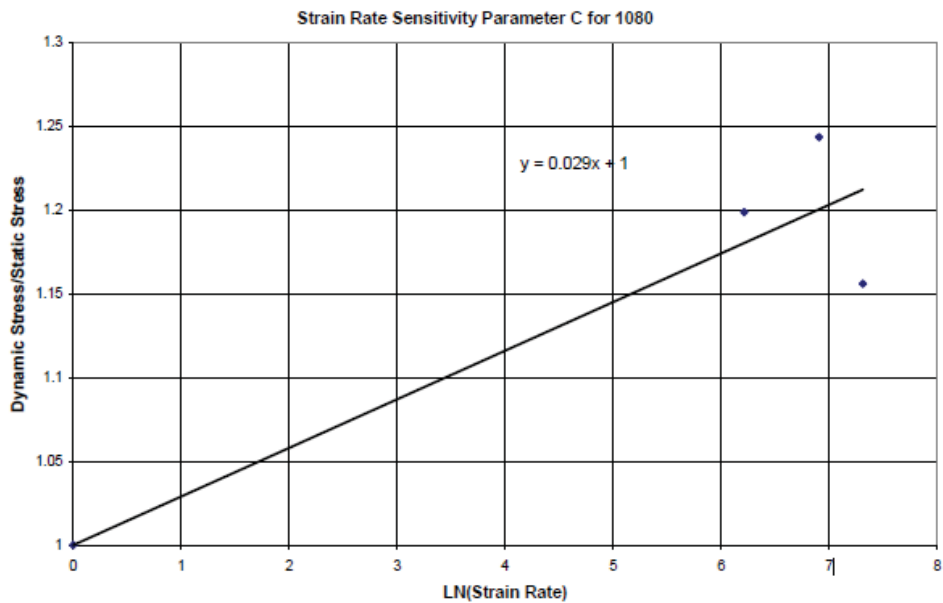


**Figure D-5 Strain Rate Sensitivity, “C”, of AISI-1080 Steel [57]**

Finally, the thermal softening coefficient,  $m$ , was determined from test data at varying temperatures and a fix strain–rate. To find this factor one follows these steps: (1) Calculate one minus ratio of the dynamic stress over the static stress, (2) calculate the homologous temperature defined in section 1.4.3, (2) plot in a logarithmic scale the relation between these two values, (3) apply least square fit to the test points (4) Obtain the slope of the least square fit, which is the  $m$  thermal coefficient [57].

Table D-3 and Figure D-6 show the data and plot employed to obtain the thermal softening coefficient of the AISI-1080 steel.  $m$  was determined to be 0.75.

Strain Rate 500

Dynamic Stress 1.222702

Test Number	Strain	Stress	Interpellation	Interp. Stress	Temp	Log(1-[Dyn. Stress(T) / Dyn. Stress(RT)])	T*	Log(T*)
3 and 4				1.2	70	-1.7313	0.0040	-2.3962
11	0.0619	1.0120	126.1905	1.0297	300	-0.8017	0.0964	-1.0160
	0.0623	1.0650						
12	0.0619	0.9935	1.0714	0.9936	300	-0.7273	0.0964	-1.0160
	0.0624	0.9941						
16	0.0617	0.8417	84.2308	0.8678	500	-0.5372	0.1767	-0.7527
	0.0622	0.8855						
17	0.0618	0.9043	-21.5625	0.8989	500	-0.5771	0.1767	-0.7527
	0.0624	0.8905						
18	0.0617	1.0200	106.6667	1.0520	750	-0.8551	0.2771	-0.5574
	0.0622	1.0680						
20	0.0618	0.9332	86.6667	0.9479	750	-0.6484	0.2771	-0.5574
	0.0623	0.9722						

Table D-3 Temperature Dependent Data [57]

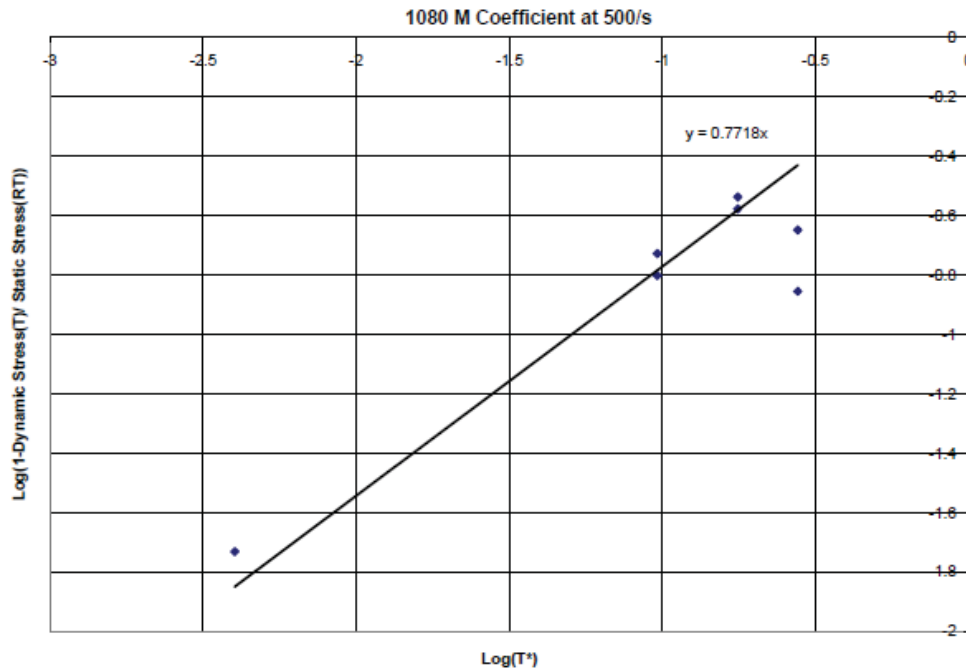


Figure D-6 Thermal Softening Coefficient “m” for the AISI-1080 Steel [57]

To verify the effectiveness of the constitutive model over a wide range of dynamic loadings, Kennan plotted the flow stresses versus the strain rates of both the experimental and JC constitutive model. In Kennan’s plot, presented in Figure D-7, one

can see that in deed the Johnson-Cook model followed the relationship between temperature and flow stress [57].

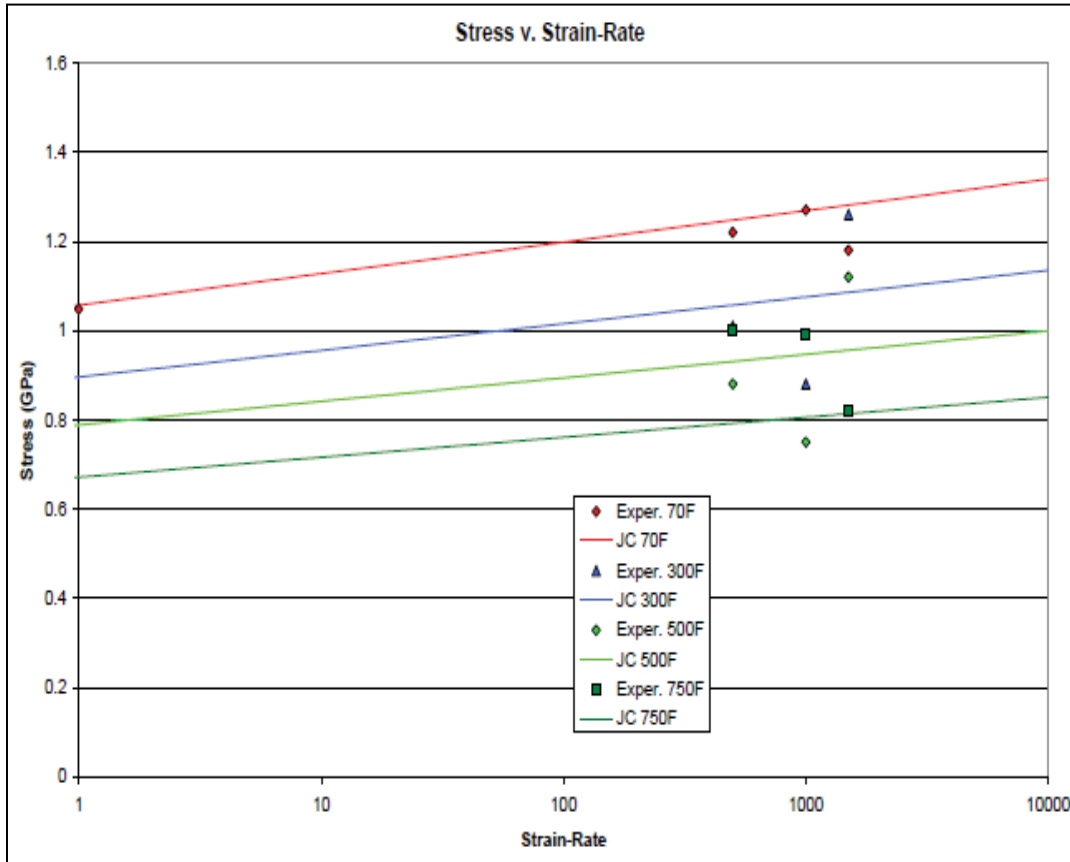


Figure D-7 Stress-Strain Rate Curves for AISI-1080 Steel [26]

The VascoMax300 SHB tests results are summarized in the next table.

Test No.	Test Temp (°F)	Strain Rate (s <sup>-1</sup> )	Flow Stress at $\epsilon \sim .01$ (GPa)
Q1, Q2	70	~1	2.15
3, 4	70	~500	2.2
15, 16	500	~500	1.78
19, 20	750	~500	1.75
17, 18	1000	~500	1.4
1, 2	70	~1000	2.18
9, 28	500	~1000	1.88
10, 11	750	~1000	1.63
12, 13	1000	~1000	1.33
6, 7	70	~1500	2.38
21, 23	500	~1500	1.95
24, 25	750	~1500	1.68
26, 27	1000	~1500	1.65

**Table D-4 SHB Test Results for Vascomax300 Steel [57]**

Figure D-8 shows the quasi-static curves of this VascoMax300 steel. On it one can see that the material shows little strain hardening, brittle failure and necking. Kennan corrected the necking phenomenon, by assuming incompressible material characteristics. Figure D-8 displays both, the uncorrected and corrected stress-strain curves [25]. Similar characteristics were observed over all the strain rates and temperatures.

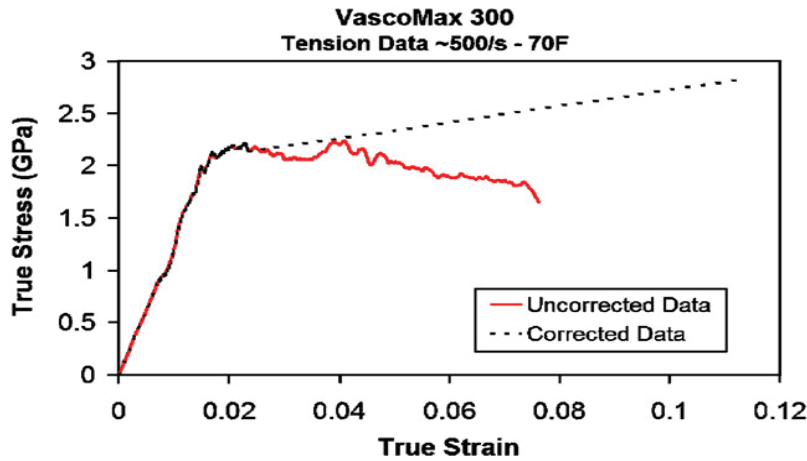


**Figure D-8 Stress-Strain Curves for VascoMax 300 [26]**

From the corrected plot Kennan derived all the JC parameters for the Vascomax300 material following the same methodology explained above for the AISI-1080 steel. The JC parameters for this material were determined to be  $A=2.1$  GPa,  $B=0.124$  GPa,  $C=0.03$ ,  $m=0.8$ , and  $n=0.3737$  [26].

In Figure D-9, one can see how the Johnson-Cook model, using these parameters, did follow the relationship between temperature and flow stress.

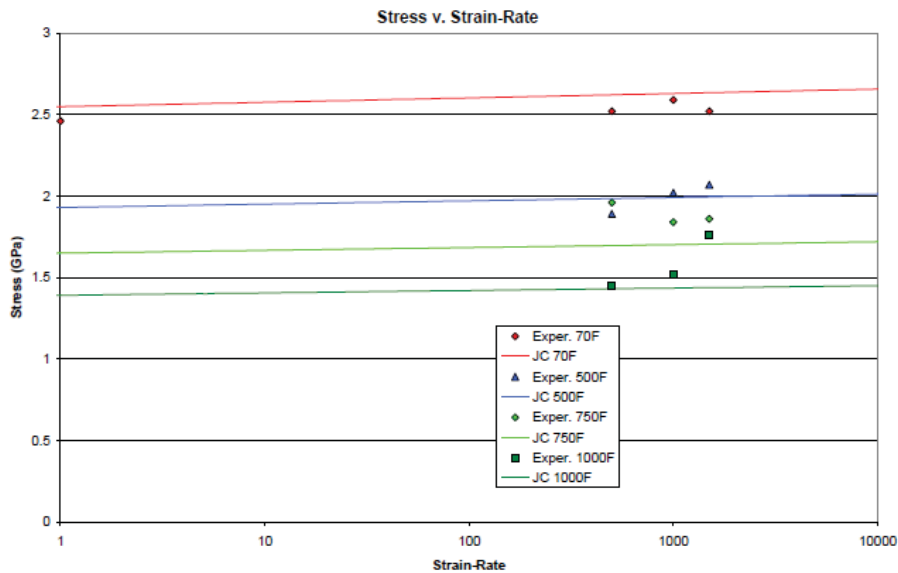


**Figure D-9 Stress-Strain Rate Curves for VascoMax 300 [26]**

The JC parameters obtained from the SHB tests of the AISI-1080 and VascoMax300 steels are summarized in Table D-5.

<b>Materials</b>	<b>A</b> <i>(GPa)</i>	<b>B</b> <i>(GPa)</i>	<b>C</b>	<b>m</b>	<b>n</b>
<b>VascoMax 300</b>	2.17	.124	0.0046	0.95	0.3737
<b>AISI-1080 Steel</b>	0.525	3.59	0.029	0.7525	0.6

**Table D-5 JC Plasticity Parameters Obtained from SHB Tests**

### **1.2 Johnson-Cook Plasticity Parameters for High-Strain-Rate Scenarios**

In 2006, Cinnamon [27] conducted various tests to AISI-1080 Steel and VascoMax 300 specimens to characterize the behavior of both of these materials at various high strain rates and temperatures.

The JC parameters determined by Kennan [57] using the SHB tests can be used in the mid-strain-rate regimen. However, since this research deals with a high strain-rate wear scenario, in order to determine the appropriate parameters various flyer plate experiments had to be conducted to adapt the J-C model to the high-strain-rate regimen [27]. These tests were carried out at the University of Dayton Research Institute (UDRI) and summarized in Table D-6.

Test	Flyer	Velocity	Target
7-1874	3 mm VascoMax 300	685 m/s	2 mm + gauge + 12 mm VascoMax 300
7-1875	3 mm 1080 Steel	669 m/s	2 mm + gauge + 12 mm 1080 Steel
7-1876	3 mm VascoMax 300	450 m/s	2 mm + gauge + 12 mm VascoMax 300
7-1877	3 mm 1080 Steel	437 m/s	2 mm + gauge + 12 mm 1080 Steel
7-1878	3 mm VascoMax 300	891 m/s	6 mm VascoMax 300 + gauge + 12 mm PMMA
7-1879	3 mm 1080 Steel	891 m/s	6 mm 1080 Steel + gauge + 12 mm PMMA

**Table D-6 Summary of UDRI Flyer Plate Tests [57]**

To tailor the JC plasticity parameters for high-strain-rate scenarios, an Eulerian-Lagrangian hydrocode called CTH, was chosen to simulate the flyer plate impacts through a 1-D model. Cinnamon followed these steps: First, He compared against the flyer-plate experimental data against the results from the CTH simulations carried out with the JC parameters obtained from the SHB tests. Figure D-10 and Figure D-11 show the comparison for tests 7-1878 and 7-1879. In them, one can see how the JC models

using the SHB parameters under-predict the flow stress at high-strain-rates, therefore the parameters had to be adjusted with the flyer plate experiments data, to effectively tailor them to the high strain-rate impacts [26].

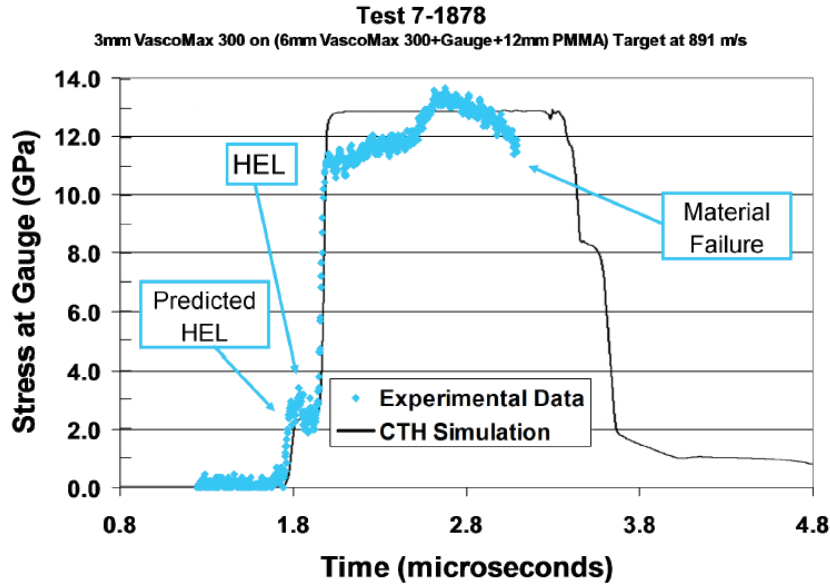


Figure D-10 Flyer Test Results vs. Model of VascoMax300 [26]

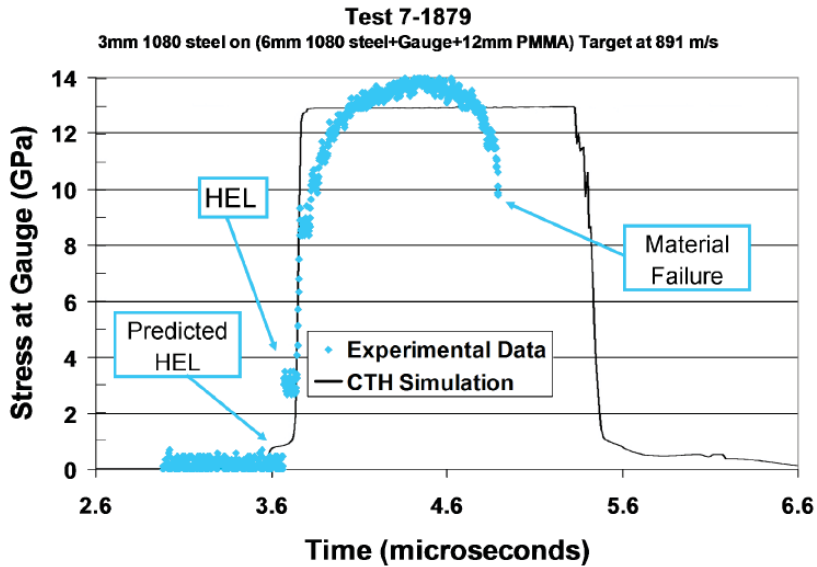


Figure D-11 Flyer Test Comparison vs. Original Model of AISI-1080 [26]

The JC parameters were adjusted between the CTH simulations, in an iteration process to calibrate the simulations based on the flyer plate test data. In other words, the parameters were iteratively adjusted until finding a "best-fit" match to the flyer tests data.

Figure D-12 and Figure D-13 show the "best-fit" CTH simulations for VascoMax 300 (test 1878) and AISI-1080 (test 1979). These plots depict the simulation of the flow stress as a function of time [26].

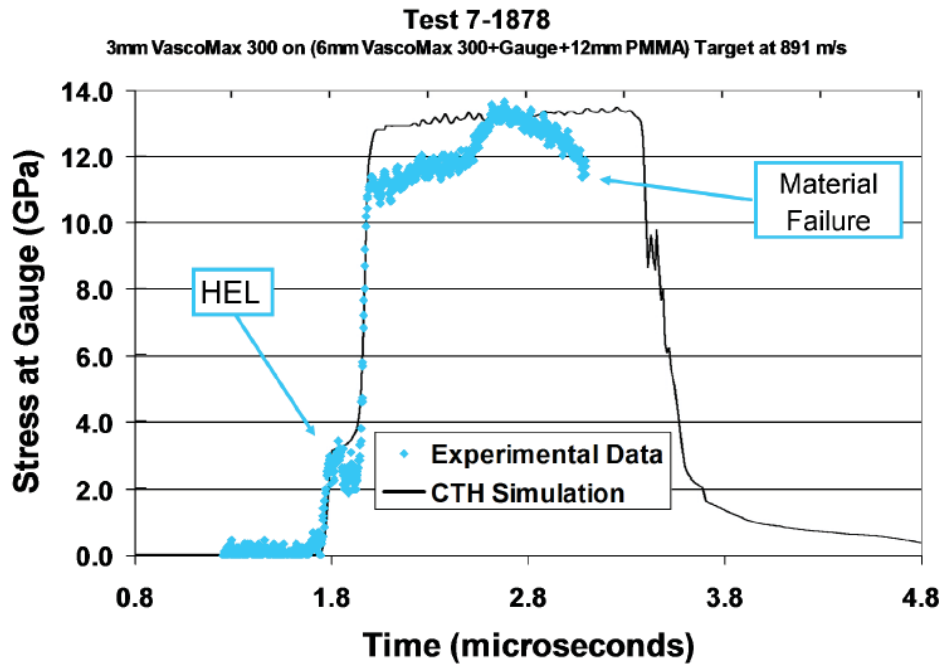
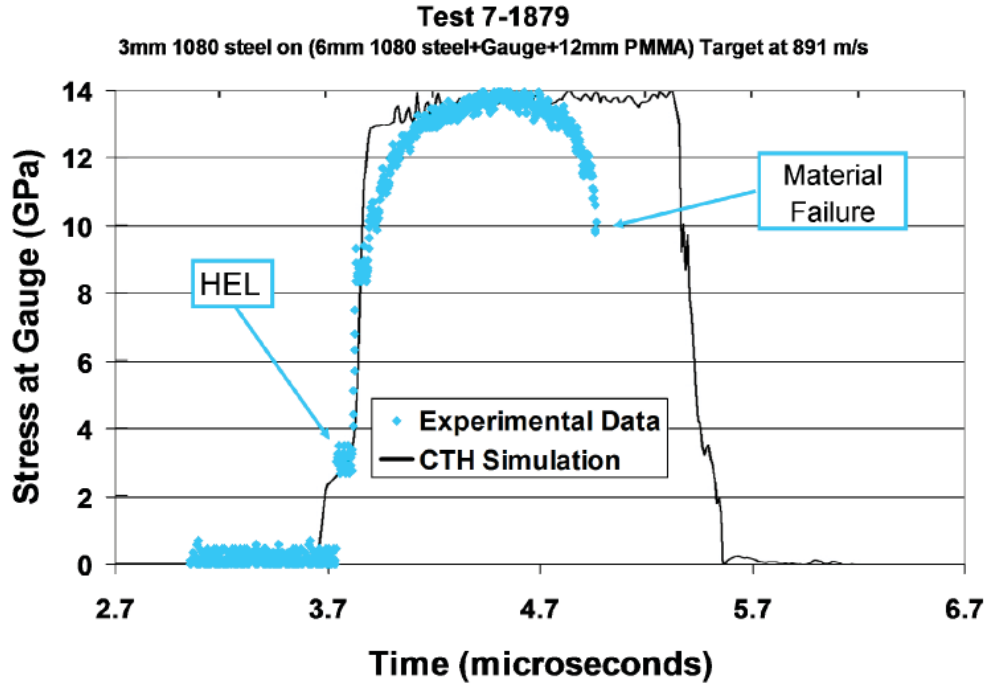


Figure D-12 Flyer Test Results vs. "Best Fit" Model of VascoMax300 [26]



**Figure D-13 Flyer Test Results vs. “Best Fit” Model of AISI-1080 [26]**

Table D-7 summarizes the constants obtained for both CTH models, once adjusted to “best fit” the flyer plate stress data. These JC parameters were the ones fed into this research 3D FE wear model.

<b>Materials</b>	<b><i>A</i> (GPa)</b>	<b><i>B</i> (GPa)</b>	<b><i>C</i></b>	<b><i>m</i></b>	<b><i>n</i></b>
<b>VascoMax 300</b>	2.1	.124	0.03	0.8	0.3737
<b>AISI-1080 Steel</b>	0.7	3.6	0.017	0.25	0.6

**Table D-7 JC Plasticity Parameters Refined with Flyer Tests**

### 1.3 Johnson-Cook Failure Parameters Determination

Fracture theory typically predicts that the failure will occur due to the coalescence of voids at the center of the specimen, as shown in Figure D-14 [40]. For this reason Johnson and Cook developed a failure criterion based on the stress state and plastic strain at fracture projected in this interior point.

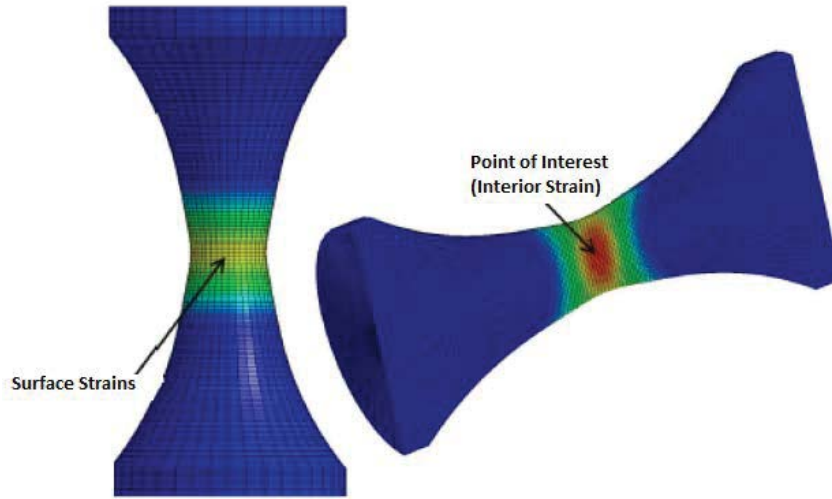


**Figure D-14 Fracture Point of Interest [40]**

This JC Dynamic failure criterion, presented in section 1.4.5, is given by:

$$\bar{\epsilon}_f = [d_1 + d_2 \exp(d_3 \frac{p}{q})][1 + d_4 \ln(\frac{\dot{\epsilon}_p}{\dot{\epsilon}_0})][1 + d_5 (\frac{T - T_0}{T_m - T_0})] \quad (D-3)$$

The triaxiality term  $p/q$ , is also called the hydrostatic tensile stress. It is defined as the ratio of the hydrostatic pressure,  $p$ , over the Von Mises stress,  $q$ . This JC fracture criterion is based on the triaxiality and therefore to obtain the parameters for it, one must first find out the triaxiality at the SHB test specimen's center point. Since, to the best of the author's knowledge, there is no instrumentation to measure the triaxiality at this interior point then, an alternative way is to obtain this it from FE simulations. The simulations are carried using the Johnson-Cook data from the plasticity tests. They are intentionally ran without a failure model and then the results are manually truncated to match the experimental data at the failure point.

The next few subsections will describe how Hammer [40] obtained these JC Dynamic failure criterion parameters:

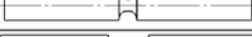
### ***2.1.2.1 Experimentation***

Hammer [40] carried out the various experiments to obtain the JC failure parameters for the Ti-gAl-4V alloy. He submitted material specimens to Quasi-static and high strain rate tension, compression, and torsion (shear) tests. He then used the procedures described in section 1.9 to derive the JC plasticity parameters from these experiments. He concluded that for the Ti-gAl-4V alloy:  $A=1002\text{MPa}$ ,  $B=431\text{MPa}$ ,  $n=0.5$ ,  $C=0.023$ , and  $m=0.69$ .

### ***2.1.2.2 Abaqus SHB Simulations***

To obtain the fracture parameters, Hammer introduced these parameters into an Abaqus SHB test model to simulate plane stress, axisymmetric, plane strain, and combined loading tests. Carrying out experiments with different test specimens spreads out the range of the strain failure points necessary to develop the fracture criterion. A wider strain failure range aids to increase the accuracy of the criterion [41].

These simulations were intentionally ran without a failure model and the results were manually truncated to match the experimental data at the failure point. The triaxiality, on the center of the simulated specimens, was recorded at the truncated point, to determine the JC failure criterion. Table D-6 shows the stress triaxiality at these truncated points, obtained at the reference strain rate of  $1\text{ s}^{-1}$  and reference temperature of  $25\text{ }^{\circ}\text{C}$ .

Test No.	Geometry Type	Geometry	Failure Strain	Stress Triaxiality
SG1	Plane Stress		0.59	0.400
SG2			0.44	0.431
SG3			0.43	0.489
SG4			0.14	0.583
SG5	Axisymmetric		0.31	0.369
SG6			0.31	0.492
SG7			0.32	0.564
SG8			0.27	0.618
SG9			0.27	0.751
SG10			0.22	0.956
SG11	Plane Strain		0.21	0.470
SG12			0.22	0.660
SG13			0.21	0.768
LR1	Combined Loading		0.29	0.252
LR2			0.51	0.150
LR3			0.43	0.00
LR4			0.42	-0.148

**Table D-8 Ductile Fracture Simulations Results of the Ti-6Al-4V [41]**

### 2.1.2.3 Johnson-Cook Failure Parameters $d_1$ , $d_2$ , and $d_3$

Hammer determined the stress state dependence parameters ( $d_1$ ,  $d_2$ , and  $d_3$ ) following these steps [41]:

1) Plotting the failure strain points against the triaxiality obtained from the truncated simulations, as shown in Figure D-15. 2.

2) Finding a curve to fit the data aided by computer software. He determined that the parameters for the first bracket of the JC failure equation are:  $d_1 = -0.081$ ,  $d_2 = 1.18$  and  $d_3 = -0.15$ . The equation with these parameters is represented by the green line in Figure D-15 and is stated as:

$$\left[ d_1 + d_2 \exp\left(d_3 \frac{P}{q}\right) \right] = \left[ -0.081 + 1.18 \exp(-0.15 \frac{P}{q}) \right] \quad (D-4)$$

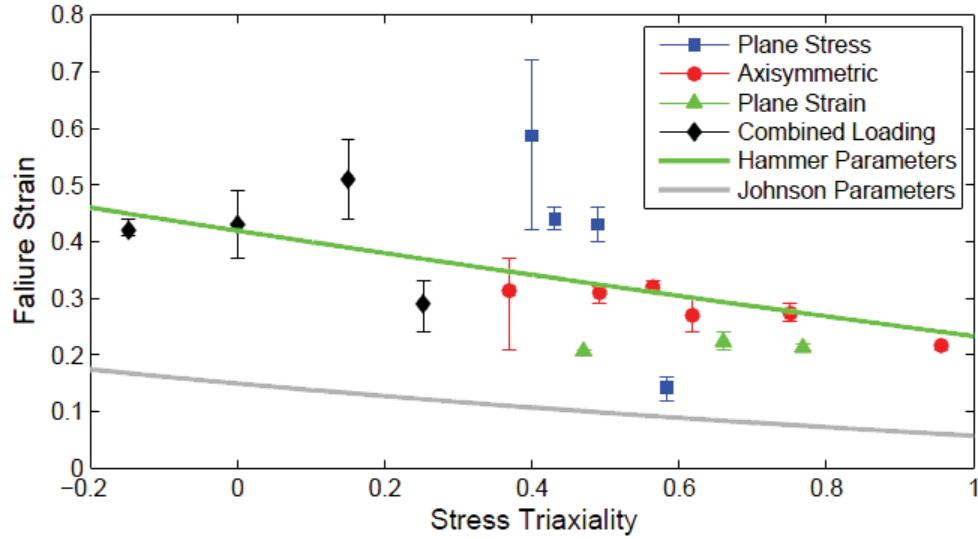


**Figure D-15 Johnson-Cook Predictions vs. Experimental Data [40]**

The gray line in Figure D-15 represents the results from the equation using the parameters obtained by Johnson and Holmquist. Johnson-Holmquist determined the parameters to be  $d_1 = -0.09$ ,  $d_2 = 0.25$  and  $d_3 = 0.5$  [53].

#### **2.1.2.4 Johnson-Cook Failure Parameter $d_4$**

To obtain the strain dependent parameter,  $d_4$ , present in the second bracket of the JC failure equation, Hammer first obtained the strain dependent fracture points from the strain-rate dependence experiments, presented in Figure D-16

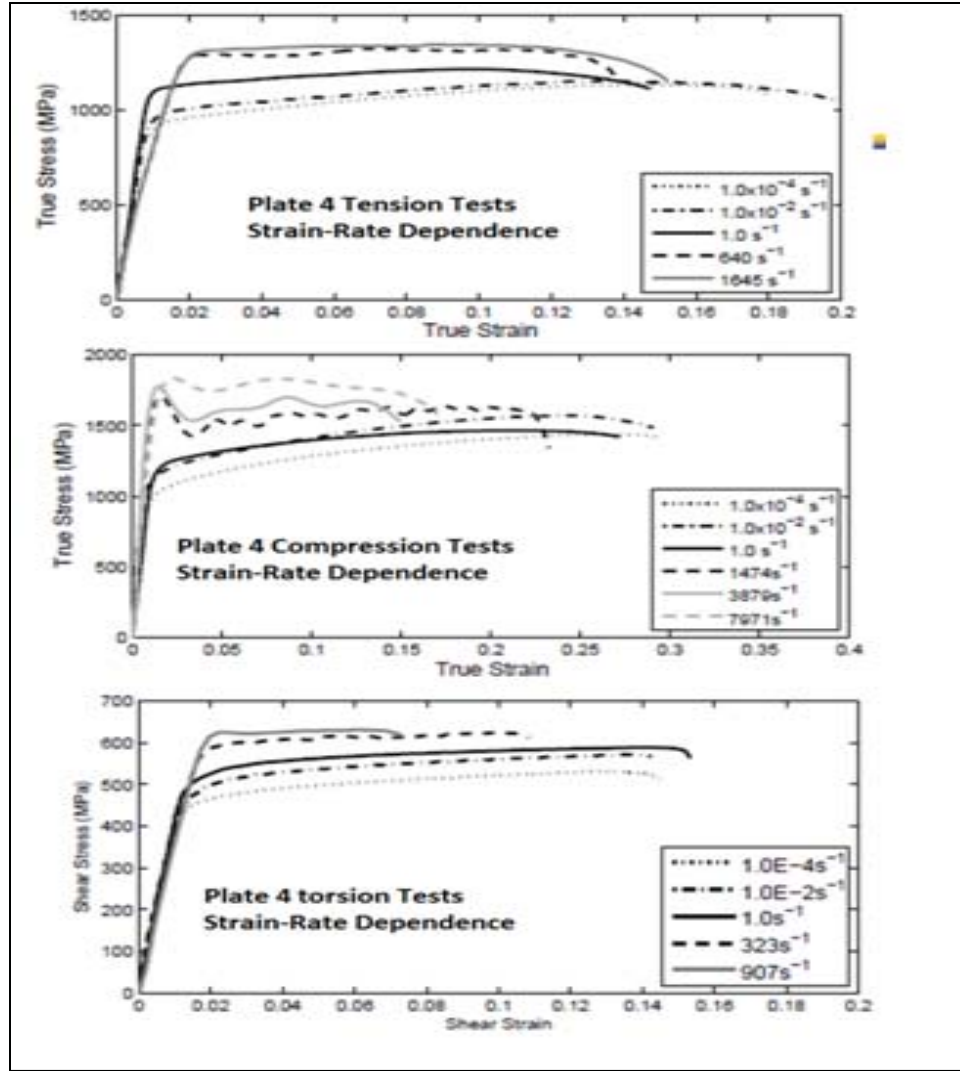


Figure D-16 Strain Rate Dependent Data [41]

He then normalized these fracture strains obtained at the reference temperature and assuming a reference triaxiality of  $p/q \sim 0.4$  (based on the mean triaxiality results from the tests presented in Table D-6 [41]). The normalized strain he used to obtain the strain rate parameter is given by:

$$\frac{\bar{\varepsilon}_f}{\varepsilon_r} = \left[ 1 + d_4 \ln\left(\frac{\dot{\varepsilon}_p}{\dot{\varepsilon}_0}\right) \right] \quad \text{where} \quad \varepsilon_r = \left[ d_1 + d_2 \exp\left(d_3 \frac{p}{q}\right) \right] \left[ 1 + d_5 \left( \frac{T - T_0}{T_m - T_0} \right) \right] \quad (\text{D-5})$$

He substituted in this equation the reference triaxiality, the reference temperature, and the parameters already obtained  $d_1$ ,  $d_2$  and  $d_3$  and to get:

$$\varepsilon_r = [-0.081 + 1.18 \exp(-0.15 \times 0.4)][1 + 0] = 1.03 \quad (D-6)$$

He divided the values of the strain dependent fracture points by 1.03 to normalize them and plotted these normalized strain fracture points, as shown in Figure D-17.

Hammer then obtained  $d_4$  by fitting a curve through these points, the green curve of Figure D-17. He determined that  $d_4 = -0.012$  for the Ti-6Al-4V alloy [41].

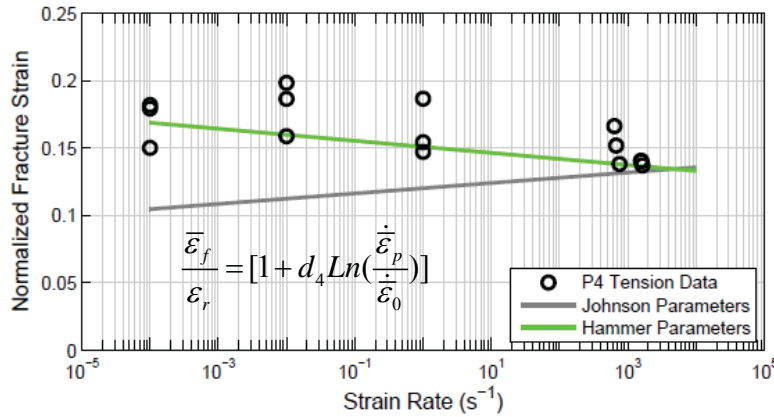


**Figure D-17 Strain Rate Sensitivity for Ti-6Al-4V [40]**

The gray line in this figure represents the curve with the parameters obtained by Johnson and Holmquist [53]. Johnson-Holmquist determined that  $d_4 = 0.014$ .

### 2.1.2.5 Johnson-Cook Failure Parameter $d_5$

Finally, Hammer determined  $d_5$  by from the experimental temperature dependent data, shown in Figure D-18 as follow:

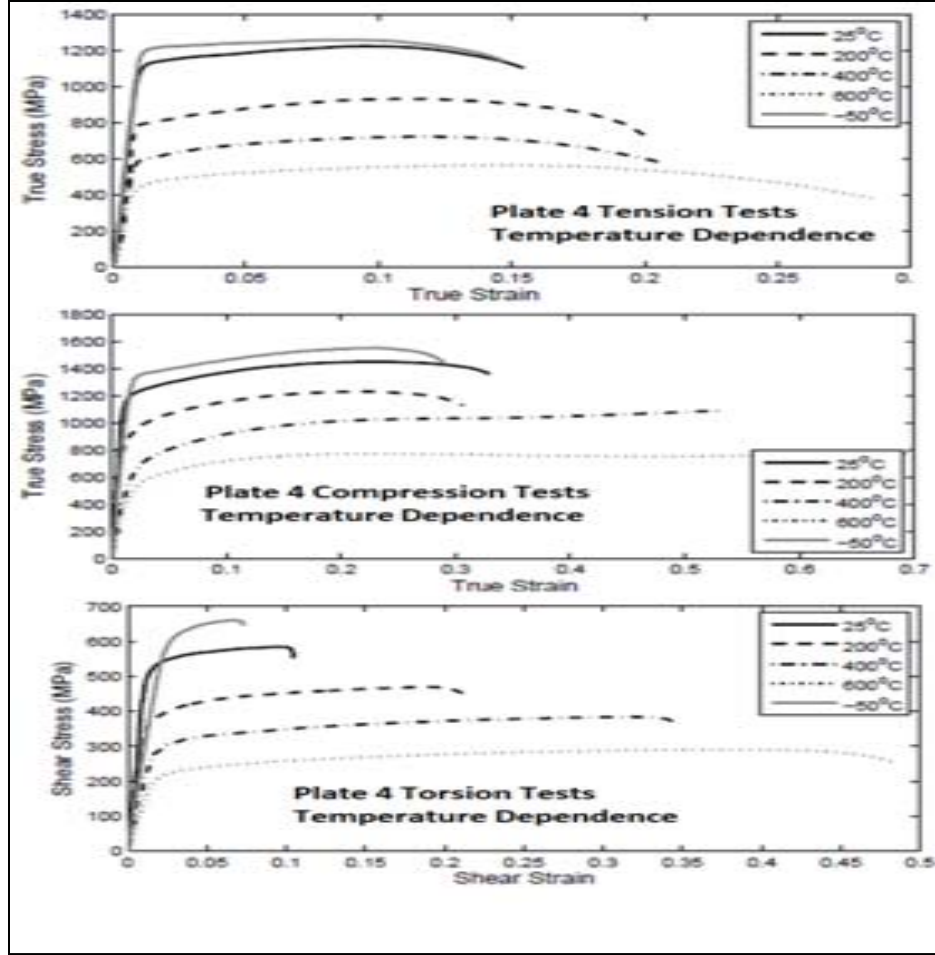


Figure D-18 Temperature Dependent Data [40].

Hammer [41] normalized these fracture strains obtained at the reference strain rate of  $1s^{-1}$  and at the reference triaxiality of  $p/q \sim 0.4$  (based on the mean triaxiality results from the tests presented in Table D-6. The normalized strain he used to obtain  $d_5$  is given by:

$$\frac{\bar{\epsilon}_f}{\epsilon_r} = [1 + d_5 (\frac{T - T_0}{T_m - T_0})] \text{ where } \epsilon_r = [d_1 + d_2 \exp(d_3 \frac{p}{q})][1 + d_4 \ln(\frac{\dot{\epsilon}_p}{\dot{\epsilon}_0})] \quad (D-7)$$

He substituted in this equation the reference triaxiality, the reference strain rate, and the parameters already obtained  $d_1$ ,  $d_2$  and  $d_3$  and to get:

$$\epsilon_r = [-0.081 + 1.18 \exp(-0.15 \times 0.4)][1 + 0.14 \ln(1)] = 1.03 \quad (D-8)$$

He then divided the values of temperature dependent fracture points by 1.03 to normalize them and plotted points against the homologous temperature, as shown in Figure D-19. The homologous temperature is 0 at the reference temperature of 25 °C, 0.14 at 200 °C, 0.3 at 400 °C and 0.44 at 600 °C.

Finally,  $d_5$  was determined by fitting a curve through these points. Hammer determined  $d_5$  was 2.1 for the Ti-6Al-4V alloy, the green curve in Figure D-19 represents the fitting curve using this value.

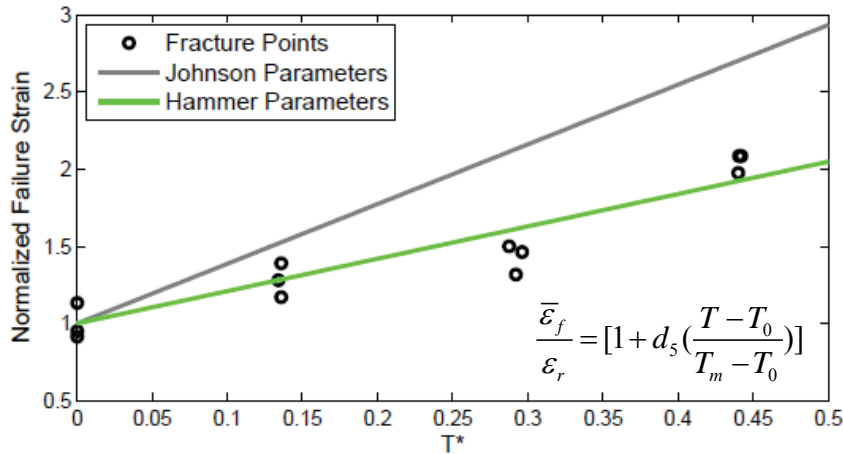


**Figure D-19 Strain Rate Sensitivity for Ti-6Al-4V [40]**

The gray line represents the curve using the parameters obtained by Johnson and Holmquist [53]. Johnson-Holmquist determined that  $d_5= 3.87$ .

Due to the lack of the required experimental data required to obtain the parameters for the VascoMax300 and AISI-1080 steel, the parameters determined by Johnson-Holmquist [53] for the Ti-6Al-4V and AISI1045 steel were used instead for this 3D FE wear model. Table D-9 summarizes these input parameters:

Materials	Parameters of materials with similar properties:	$d_1$	$d_2$	$d_3$	$d_4$	$d_5$
VascoMax 300	Ti-6Al-4V <sup>[31]</sup>	-0.09	0.25	0.5	0.014	3.87
AISI-1080 Steel	AISI Steel 1045 <sup>[31]</sup> .	0.7	3.6	0.17	0.25	0.6

**Table D-9 JC Dynamic Failure Parameters**

### 1.4 Mie-Gruneisen Equation of State (EOS)

The concepts related to the Mie-Gruneisen Equation of State are presented in Appendix A, Section [1.4]. This EOS is generally used for problems involving impact at high velocities, ranging from 100 m/s to 2,000 m/s [31], therefore it is used for this research high-speed sliding simulations.

An accurate description of the shock wave propagation is important in simulations involving impact. The benefit of the Mie-Gruneisen EOS is that the shock Hugoniot curve is taken as a reference. During simulations this experimental fit is followed and describes the propagation more precisely.

The necessary material properties to implement this relationship in Abaqus were obtained from materials with similar properties. These materials were available in AFIT's CTH database and summarized in Table D-10. CTH is an Eulerian-Lagrangian hydrocode developed by Sandia National Laboratory.

<b>Materials</b>	<b>Parameters of materials with similar properties:</b>	$c_0$ (km/s)	$s$	$\Gamma_0$
<b>VascoMax 300</b>	VascoMax250 <sup>[CTH]</sup>	4.605	1.456	1.65
<b>AISI-1080 Steel</b>	CTH Iron-Alpha <sup>[CTH]</sup>	3.980	1.580	1.6

**Table D-10 Mie-Gruneisen EOS Parameters**

### 1.5 Friction Experimentation

Montgomery's experimental frictional data was used in the present research as the frictional relationship between the two sliding parts, therefore, providing an overview of this experimentation is important.

Between 1946 and 1956 the U.S Army conducted extensive experiments to collect friction and wear data at sliding speeds, up to 1800ft/s. To do so, they used a sophisticated high-speed pin-on disk apparatus [81].

Montgomery [81] used this data to obtain empirical coefficients of friction,  $\mu$ . The experimental data points from his investigations of steel-on-steel sliding allowed us to relate the friction coefficient to the pressure velocity factor,  $Pv$ . In order to do so these

experimental points were exponentially fitted to a curve. From this curve was derived the following equation, which is in terms of millimeters and MPa units.

$$\mu = \begin{cases} 0.269e^{-3.409 \times 10^{-7} P_v} + 0.307e^{-6.08 \times 10^{-9} P_v} & : 0 < P_v < 4.45 \times 10^8 \\ 0.02 & : P_v \geq 4.45 \times 10^8 \end{cases} \quad (D-9)$$

As one can notice on this equation, once the pressure velocity exceeds  $4.45 \times 10^8$  MPa mm/s, the coefficient of friction becomes constant, which corresponds to Montgomery's observations at high pressure velocities [81]. Montgomery's experimental data is plotted and presented in Figure D-20.

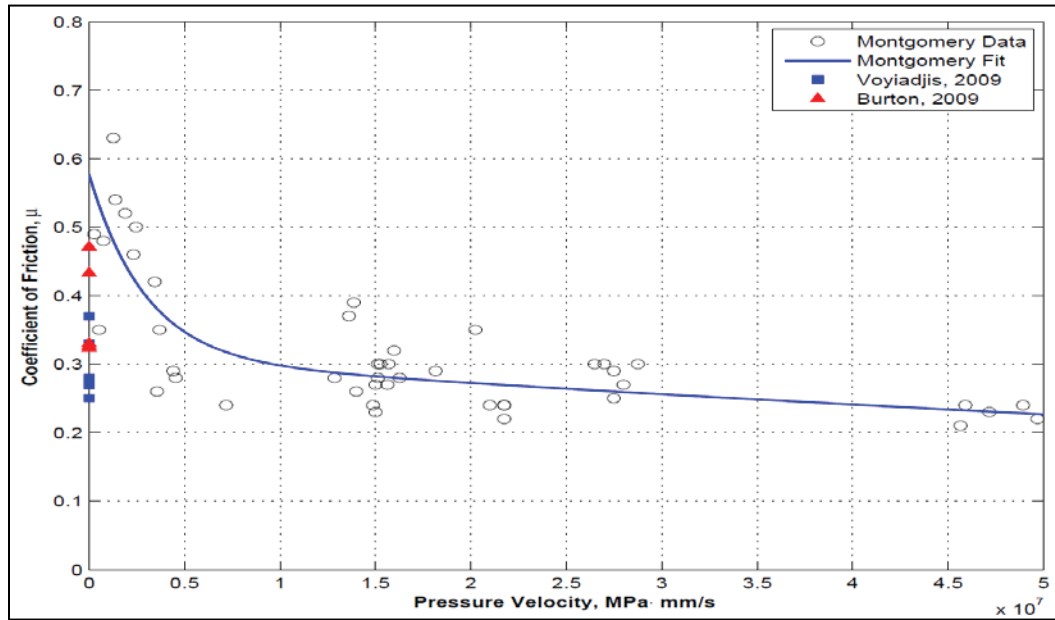


**Figure D-20 Montgomery's Coefficient of Friction [81]**

## 1.6 Initial Temperature Experimentation

Considering that the higher the initial temperature the softer the initial state of the colliding asperity, one needs to input appropriate temperatures into the model. The initial temperatures introduced into the model were determined by Le [66]. Le carried out a thermal analysis developed from the high-speed sliding of a traveling slipper over the Holloman High Speed Test Track. The goal of her research was to characterize the amount of heat flow going into the slipper as it slid and to predict the melt wear [66].

Le's heat transfer analysis assumed one-dimensional heat conduction into the slipper, due to the frictional energy produced by the relative motion between the slipper and the rail. This frictional energy in the form of heat then translates into high temperatures which eventually reach the point of melt [66].

Le investigated how much melt wear was produced by considering the partition fraction of heat entering into the slipper. She used different partition fraction functions, some assumed that the slipper was always in contact with the rail and others that bounced due to the aerodynamics and imperfections on the system. The total melt wear predicted using these functions was between 2-3%, however, these results depended heavily on the partition function used. The investigation to determine the actual partition formulation for this wear problem is still ongoing. Le's [66] preliminary results are reasonable and in general agreement with wear theory. The skin temperatures, as a function of the DADS percent of contact, introduced into this model are based on Le's preliminary results:

Velocity (m/s)	Skin Temperature (°K)	DADS %Contact
25	299.2	0.89
100	317.5	0.73
200	328.9	0.47
300	364.1	0.3
400	399.1	0.27
500	429.8	0.29
600	440.2	0.25
700	506.7	0.19
800	495.7	0.24
900	494.9	0.25
1000	479.5	0.24
1100	532.5	0.19
1200	615.5	0.16
1300	615.9	0.16
1400	666.4	0.17
1500	646.5	0.17

**Table D-11 Thermal Analysis Results [66]**

## 1.7 Appendix Summary

This appendix presented only a brief overview of the experiments required to obtain the parameters for the algorithms employed by this 3D FE wear model. The references included in each section pointed the documents containing the details of these experiments. The following table summarizes the input-parameters for this model:

	<b>AISI-1080 Steel</b>	<b>VascoMax300 Steel</b>
<b>Shear Modulus (kPa)</b>	7.984E+7	7.389E+7
<b>JC Plasticity A (kPa)</b>	5.25E+5	2.17E+6
<b>JC Plasticity B (kPa)</b>	3.59E+6	1.24E+5
<b>JC Plasticity n</b>	0.67	0.37
<b>JC Plasticity C</b>	0.029	0.03
<b>JC Plasticity m</b>	0.75	.8
<b>JC D. Fracture d<sub>1</sub></b>	0.06	-0.09
<b>JC D. Fracture d<sub>2</sub></b>	3.31	0.27
<b>JC D. Fracture d<sub>3</sub></b>	1.96	0.48
<b>JC D. Fracture d<sub>4</sub></b>	0.002	0.014
<b>JC D. Fracture d<sub>5</sub></b>	0.58	3.87
<b>Eq. Plastic displacement to fail (mm)</b>	0.00001	0.00001
<b>MG EOS c<sub>0</sub> (mm/s)</b>	4.16E6	3.98E6
<b>MG EOS s</b>	1.195	1.58
<b>MG EOS <math>\Gamma_0</math></b>	1.63	1.6
<b>Melting Temperature T<sub>m</sub> ( °K)</b>	1670	
<b>Initial Temperature T<sub>0</sub> ( °K)</b>	293	See Table IV-12
<b>Density (kg/mm<sup>3</sup>)</b>	7.8E-6	8E-6
<b>Poison's ratio</b>	0.27	0.283
<b>Specific Heat C<sub>v</sub> (mm<sup>2</sup>/ °Ks<sup>2</sup>)</b>	4.9E+8	4.5E+8 and 7.0E+8
<b>Avg. Asperity Size R<sub>a</sub> (um)</b>	2.5	6.1
<b>Asperity Distribution</b>	See Figure D-21	N/A
<b>Coefficient of Friction</b>	Given by Equation IV-9	

**Table D-12 3D FE Wear Model Input Parameters**

## Bibliography

1. Adams, B., “*Simulations of ballistic impacts on armored civil vehicles,*” MT 06.03 Eindhoven University of Technology, June 2003
2. Archard, J. F. “*Contact and Rubbing of Flat Surfaces,*” *Journal of Applied Physics*, 24(8): 981–988, August 1953.
3. Archard, J. F. “*The Temperature of Rubbing Surfaces,*” *Wear*, 2(6):438–455, October 1959.
4. Archard, J. F. and W. Hirst. “*The Wear of Metals Under Unlubricated Conditions,*” *Proceedings of the Royal Society of London. Series A, Mathematical and Physical Sciences*, 236(1206):397–410, 1956.
5. Ashby, M. F. and S. C. Lim. “*Wear-Mechanism Maps,*” *Scripta Metallurgica et Materialia*, 24(5):805–810, May 1990.
6. *ASTM. Standard Terminology Relating to Wear and Erosion, G-40-01.* ASTM International, West Conshohocken, Pennsylvania, 2001.
7. ATI Allvac, Inc., 2020 Ashcroft Ave, PO Box 5030, Monroe, North Carolina, 28110. *VascoMax Technical Data Sheet*, June 2008. [www.allvac.com](http://www.allvac.com).
8. Bayer, R. G. *Wear Analysis for Engineers.* HNB Publishing, New York, 2002.
9. Bayer, R.G. *Engineering Design for Wear.* Marcel Dekker, Inc., New York, 2004.
10. Bayer, R. G. *Mechanical Wear Fundamentals and Testing.* Marcel Dekker, Inc., New York, 2004.
11. Benabdallah, H. and D. Olender. “*Finite Element Simulation of the Wear of Polyoxymethylene in Pin-on-disc Configuration*” *Wear*, 261(11-12):1213–1224, December 2006.
12. Bhushan, B. *Introduction to Tribology.* John Wiley & Sons, New York, 2002.

13. Bogdanovich, P. N. and D. V. Tkachuk. “*Thermal and Thermomechanical Phenomena in Sliding Contact,*” *Journal of Friction and Wear*, 30(3):153–163, 2009.
14. Boley, B. A. and J. H. Weiner. *Theory of Thermal Stresses*. Dover Publications, Inc., New York, 1997.
15. Bowden, F. P. and E. H. Freitag. “*The Friction of Solids at Very High Speeds. I. Metal on Metal. II. Metal on Diamond,*” *Proceedings of the Royal Society of London. Series A, Mathematical and Physical Sciences*, 248:350–367, November 1958.
16. Bowden, F. P. and P. A. Persson. “*Deformation, Heating and Melting of Solids in High-speed Friction,*” *Proceedings of the Royal Society of London. Series A, Mathematical and Physical Sciences*, 260:433–458, March 1961.
17. Bowden, F. P. and K. E. W. Ridler. “*Physical Properties of Surfaces. III. The Surface Temperature of Sliding Metals. The Temperature of Lubricated Surfaces,*” *Proceedings of the Royal Society of London. Series A, Mathematical and Physical Sciences*, 154(883):640–656, May 1936.
18. Bowden, F. P. and P. H. Thomas. “*The Surface Temperature of Sliding Solids,*” *Proceedings of the Royal Society of London. Series A, Mathematical and Physical Sciences*, 223(1152):29–40, April 1954.
19. Bower, A. F. *Applied Mechanics of Solids*. CRC press, 2009.
20. Burton, C.A. and R.A. Brockman. “*Frictional Interactions in High-speed Sliding Contact.*” *Proceedings of the 50th AIAA/ASME/ASCE/AHS/ASC Structures, Structural Dynamics and Materials Conference*. AIAA, Palm Springs, California, 4-7 May 2009.
21. Cameron, G. and A. Palazotto. “*An Evaluation of High Velocity Wear,*” *Wear*, 265(7-8):1066–1075, September 2008.
22. Cameron, G. J. *An Evaluation of High Velocity Wear*, AFIT/GAE/ENY/07M06. Master’s Thesis, Air Force Institute of Technology, Wright-Patterson AFB, OH, 2007.
23. Chmiel, A. J. *Finite Element Simulation Methods for Dry Sliding Wear*, AFIT/GAE/ENY/08-M03. Master’s thesis, Air Force Institute of Technology, Wright Patterson AFB, OH, 2008.

24. Cinnamon, J. D. *Analysis and Simulation of Hypervelocity Gouging Impacts* AFIT/DS/ENY/06-01. Ph.D. Dissertation, Air Force Institute of Technology, Wright-Patterson AFB, OH, 2006.
25. Cinnamon, J. D. and A. N. Palazotto. “*Metallographic Examination and Validation of Thermal Effects in Hypervelocity Gouging,*” *Journal of Pressure Vessel Technology*, 129(1):133–141, January 2007.
26. Cinnamon, J. D., A. N. Palazotto, and N. S. Brar. “*Further Refinement of Material Models for Hypervelocity Gouging Impacts.*” Proceedings of the 47th AIAA/ASME/ASCE/AHS/ASC Structures, Structural Dynamics and Materials Conference. AIAA, Newport, Rhode Island, 1-4 May 2006.
27. Cinnamon, J. D., A. N. Palazotto, and Z. Keenan. “Material Characterization and Development of a Constitutive Relationship for Hypervelocity Impact of 1080 Steel and VascoMax 300,” *International Journal of Impact Engineering*, 33(112):180–189, December 2006.
28. Cinnamon, J.D., A.N. Palazotto, and A.G. Szmerekovsky. “Further Refinement and Validation of Material Models for Hypervelocity Gouging Impacts,” *AIAA Journal*, 46(2):317–327, 2008.
29. Cinnamon, J. D., A. N. Palazotto, A. G. Szmerekovsky, and R. J. Pendleton. “*Further Investigation of a Scaled Hypervelocity Gouging Model and Validation of Material Constitutive Models.*” Proceedings of the 47th AIAA/ASME/ASCE/AHS/ASC Structures, Structural Dynamics and Materials Conference. AIAA, Newport, Rhode Island, 1-4 May 2006.
30. Cowan, R. S. and W. O. Winer. “*Frictional Heating Calculations.*” *Friction, Lubrication, and Wear Technology: ASM Handbook*, Volume 18, 39–44. ASM International, 1992.
31. Dassault Systèmes. ABAQUS v6.10.2 Analysis User’s Manual. Dassault Systèmes, Providence, Rhode Island, 2010.
32. Dean, J., C.S. Dunleavy, P.M. Brown, T.W. Clyne. “Energy absorption during projectile perforation of thin steel plates and the kinetic energy of ejected fragments”, *International Journal of Impact Engineering* 1–9, 2009

33. Duan, C. Z., T. Dou, Y. J. Cai, and Y. Y. Li, "Finite Element Simulation and Experiment of Chip Formation Process during High Speed Machining of AISI 1045 Hardened Steel" *International Journal of Recent Trends in Engineering*, Vol 1, No. 5, May 2009
34. El-Tobgy, M.S., E. Ng, M.A. Elbestawi, "*Finite element modeling of erosive wear*," *International Journal of Machine Tools & Manufacture* 45 (2005) 1337–1346, January 2005
35. Farrell, R. M. and T. S. Eyre. "The Relationship Between Load and Sliding Distance in the Initiation of Mild Wear in Steels," *Wear*, 15(5):359–372, May 1970.
36. Ford, I. J. "Roughness effect on friction for I multi-asperity contact between surfaces", Harwell Laboratory, Didcot, Oxon, UK August 1993.
37. Glossary of Terms and Definitions in the Field of Friction, Wear and Lubrication (Tribology ), Research Group on Wear of Engineering Materials, OECD, Paris, 1969.
38. Hale, C.S., *Consideration of Wear Rates at High Velocity* AFIT/DS/ENY/10-08. Ph.D. Dissertation, Air Force Institute of Technology, Wright-Patterson AFB, OH, October 2008.
39. Hale, C.S., A. N. Palazotto, G. J. Cameron, and G. J. Chmiel "Consideration of Wear at High Velocities." *Structural Dynamics and Materials Conference*. AIAA, Schaumburg, IL, 7-10 April 2008
40. Hall, A. M. and C. J. Slunder. *The Metallurgy, Behavior, and Application of the 18-Percent Nickel Maraging Steels*. Technical Report NASA SP-5051, National Aeronautics and Space Administration, Washington, D.C., 1968.
41. Hammer, J. T. *Plastic Deformation and Ductile Fracture of Ti-6Al-4V under Various Loading Conditions*. M.S. Thesis, Ohio State University, OH, 2012.
42. *Holloman High Speed Tests Track*. Design Manual Technical Report, 846th Test Squadron, 46th Test Group, Holloman AFB, New Mexico, 2004
43. Hooputra, H., H. Gese, H. Dell, and H. Werner, "A comprehensive failure model for crashworthiness simulation of aluminum extrusions." *International Journal of Crashworthiness*, 9:5, 449-464, 2004

44. Hooser, M. D. "*Simulation of a 10,000 Foot per Second Ground Vehicle.*" Proceedings of the 21st AIAA Advanced Measurement Technology and Ground Testing Conference. AIAA, Denver, Colorado, 19-22 June 2000.
45. Hooser, M.D. and A. Schwing. "*Validation of Dynamic Simulation Techniques at the Holloman High Speed Test Track.*" Proceedings of the 38th AIAA Aerospace Sciences Meeting and Exhibit. AIAA, Reno, Nevada, 10-13 January 2000.
46. Huber, D. A., *The Use of Various Failure Criteria As Applied To High Speed Wear* AFIT/DS/ENY/11-D01. Thesis, Air Force Institute of Technology, Wright-Patterson AFB, OH, December 2011.
47. Hutchings, I. M. "*The Challenge of Wear.*" Wear -Materials, Mechanisms and Practice, Tribology in Practice Series, 1-7. Chichester, England: John Wiley & Sons, 2005.
48. Hypersonic Upgrade Program (HUP) Super Roadrunner Over/Under Data Report, Mission 80X-G1. Technical Report, 846th Test Squadron, 46th Test Group, Holloman AFB, New Mexico, 2004
49. Incropera, F. P. and D. P. DeWitt. *Fundamentals of Heat and Mass Transfer.* John Wiley & Sons, New York, 1990.
50. Janna, W. S. *Engineering Heat Transfer.* CRC Press, Boca Raton, 2009.
51. Johnson, G.R. and W.H.Cook. "A Constitutive Model and Data for Metals Subjected to Large Strains, High Strain Rates and High Temperatures." Proceedings of the 7th International Symposium on Ballistics. April 1983.
52. Johnson, G.R. and W.H.Cook. "Fracture Characteristics of Three Metals Subjected to Various Strains, Strain rates, Temperatures and Pressures." Engineering Fracture Mechanics Vol. 21, No. I, pp. 3148. 1985.
53. Johnson, G.R. and Holmquist, T.J., "Test Data and Computational Strength and Fracture Model Constants for 23 Materials Subjected to Large Strains, High Strain Rates, and High Temperatures," Los Alamos National Laboratory, LA-11463-MS, 1989.

54. Johnson, R. L., M. A. Swikert, and E. E. Bisson. *Friction at High Sliding Velocities*. Technical Report NACA-TN-1442, Flight Propulsion Research Laboratory, National Advisory Committee for Aeronautics, Cleveland, Ohio, October 1947.
55. Kato, K. “*Classification of Wear Mechanisms/Models.*” *Wear -Materials, Mechanisms and Practice, Tribology in Practice Series*, 9–20. Chichester, England: John Wiley & Sons, 2005.
56. Kay,G., “*Failure Modeling of Titanium 6Al-4V and Aluminum 2024-T3 With the Johnson-Cook Material Model*”, Report No DOT/FAA/AR-03/57, Office of Aviation Research Washington, D.C. 20591, September 2003.
57. Kennan, Zachary. “*Determination of the Constitutive Equations for 1080 Steel and VascoMax 300*”, AFIT/GAE/ENY/05-J05. Master’s thesis, Air Force Institute of Technology, Wright-Patterson AFB, OH, May 2005.
58. Korkegi, R.H.and R.A.Briggs. “*The Hypersonic Slipper Bearing –A Test Track Problem,*” *Journal of Spacecraft & Rockets*, 6(2):210–212, 1969.
59. Krenk, S., *Non-linear Modeling and Analysis of Solids and Structures*, Cambridge University Press, UK, 2009
60. Krupovage, D. J. *Rail Friction & Slipper Wear on the Holloman High Speed Test Track*. Technical Report, Test Track Division, 6585th Test Group, Holloman AFB, New Mexico, October 1987.
61. Krupovage, D. J., L. C. Mixon, and J. D. Bush. *Design Manual for Dual Rail, Narrow Gage, and Monorail Rocket Sleds*. Technical Report, Test Track Division, 6585th Test Group, Holloman AFB, New Mexico, 1991.
62. Krupovage, D. J. and H. J. Rasmussen. *Hypersonic Rocket Sled Development*. Technical Report AD-TR-82-41, Test Track Division, 6585th Test Group, Holloman AFB, New Mexico, September 1981.
63. Laird, D. J. *The Investigation of Hypervelocity Gouging*, AFIT/DS/ENY/02-01. Ph.D. Dissertation, Air Force Institute of Technology, Wright-Patterson AFB, OH, 2002.
64. Laird, D. J. and A. N. Palazotto. “*Effect of Temperature on the Process of Hypervelocity Gouging,*” *AIAA Journal*, 41(11):2251–2260, 2003.

65. Laird, D. J. and A. N. Palazotto. “*Gouge Development During Hypervelocity Sliding Impact*,” International Journal of Impact Engineering, 30(2):205–223, January 2004.
66. Le, K. H., *A Study of the thermal Environment Developed by a Traveling slipper at high Velocity* AFIT/DS/ENY/13-M-20. Thesis, Air Force Institute of Technology, Wright-Patterson AFB, OH, 2012.
67. Lesquois, O., J. J. Serra, P. Kapsa, S. Serror, and C. Boher. “*Degradations in a High-Speed Sliding Contact in Transient Regime*,” Wear, 201(1-2):163–170, December 1996.
68. Lim, S. C. “*Recent Developments in Wear-Mechanism Maps*,” Tribology International, 31(1-3):87–97, January 1998.
69. Lim, S. C. and M. F. Ashby. “*Wear-Mechanism Maps*,” Acta Metallurgica, 35(1):1–24, January 1987.
70. Lim, S. C., M. F. Ashby, and J. H. Brunton. “*The Effects of Sliding Conditions on the Dry Friction of Metals*,” Acta Metallurgica, 37(3):767–772, March 1989.
71. Lodygowski, A., G.Z. Voyiadjis, B. Deliktas, and A. Palazotto, *Non-local and numerical formulations for dry sliding friction and wear at high velocities*, International Journal of Plasticity 0749-6419, October 2010.
72. Loikkanen, M. J., M. Buyuk, C. D. Kan, and N. Meng, “A Computational and experimental Analysis of Ballistic Impact to Sheet Metal Aircraft Structures.” European LS-DYNA Users Conference, March 2005.
73. MatWeb LLC 2011. Retrieved March 3, 2013 from <https://http://www.matweb.com/search/DataSheet.aspx?MatGUID=bee590cc47254e378f4dc719f995898a>
74. Meador, Stephen P. *Consideration of Wear at High Velocities*, AFIT/GAE/ENY/10-M16. Master’s thesis, Air Force Institute of Technology, Wright Patterson AFB, OH, 2010.
75. Meyers, M. A. *Dynamic Behavior of Materials*. John Wiley & Sons, New York, 1994.

76. Minto, D. W. “*Recent Increases in Hypersonic Test Capabilities at the Holloman High Speed Test Track.*” Proceedings of the 38th AIAA Aerospace Sciences Meeting and Exhibit. AIAA, Reno, Nevada, 10-13 January 2000.
77. Minto, D. W. “*The Holloman High Speed Test Track Hypersonic Upgrade Program Status.*” Proceedings of the 22nd AIAA Aerodynamic Measurement Technology and Ground Testing Conference. AIAA, Saint Louis, Missouri, 24-26 June 2002.
78. Molinari, A., Y.Estrin, and S.Mercier. “Dependence of the Coefficient of Friction on the Sliding Conditions in the High Velocity Range,” *Journal of Tribology*, 121(1):35–41, January 1999.
79. Molinari, J. F., M. Ortiz, R. Radovitzky, and E. A. Repetto. “*Finite-Element Modeling of Dry Sliding Wear in Metals,*” *Engineering Computations*, 18(3/4):592–610, 2001.
80. Montgomery, R. S. “*Muzzle Wear of Cannon,*” *Wear*, 33(2):359–368, July 1975.
81. Montgomery, R.S. “*Friction and Wear at High Sliding Speeds,*” *Wear*,36(3):275– 298, March 1976.
82. Montgomery, R. S. “*Surface Melting of Rotating Bands,*” *Wear*, 38(2):235–243, July 1976.
83. Odeshi, A.G., M.N, Bassim, S. Al-Ameeri, and Q. Li. “*Dynamic shear band propagation and failure in AISI 4340 steel.*” *Journal of Materials Processing Technology* 169 (2005): 150-155.
84. Owen, D. R., Hinton, E., *Finite Elements in Plasticity.* Department of Civil Engineering, University College of Swansea, U. K. 1980.
85. Palazotto, Anthony N. and Stephen P. Meador. “*Consideration of Wear at High Velocities Using a Hydrocode*”. AIAA, Accepted for publication 2011.
86. P̃odra, P. and S. Andersson. “*Simulating Sliding Wear with Finite Element Method,*” *Tribology International*, 32(2):71–81, January 1999.
87. Philippon, S., G. Sutter, and A. Molinari. “*An Experimental Study of Fiction at High Sliding Velocities,*” *Wear*, 257(7-8):777–784, October 2004.

88. Poizat, C., L. Campagne, L. Daridon, S. Ahzi, C. Husson, and L. Merle, *Modeling and Simulation of Thin Sheet Blanking using damage and rupture criteria*, International Journal of Forming Processes. Volume 8 (1): 29-47, 2005.
89. Polyzois, I., *Finite Element Modeling of the Behavior of Armor Materials Under High Strain Rates and Large Strains*, Thesis, Department of Mechanical and Manufacturing Engineering, University of Manitoba, Winnipeg, Manitoba, Canada, 2010.
90. Raftenberg, M. N., "A Shear Banding Model for Penetrations Calculations", Army Research Laboratory, Report ARL-TR-2221, Aberdeen Proving Ground, MD, April 2000.
91. Rajagopalan, S., M. A. Irfan, and V. Prakash. "Novel Experimental Techniques for Investigating Time Resolved High Speed Friction," *Wear*, 225-229(Part 2):1222–1237, April 1999.
92. Rohrbach, K. and M. Schmidt. "Maraging Steels." Properties and Selection: Irons, Steels, and High-Performance Alloys: Metals Handbook, Volume 1, 793–800. ASM International, 1990.
93. Saada, A. S., *Elasticity Theory and Applications*. Krieger Publishing Co. Malabar, Fl. 1993.
94. Saka, N., A.M. Eleiche, and N.P. Suh. "Wear of Metals at High Sliding Speeds," *Wear*, 44(1):109–125, August 1977.
95. Schmidt, M. and K. Rohrbach. "Heat Treating of Maraging Steels." Heat Treating: ASM Handbook, Volume 4, 219–228. ASM International, 1991.
96. The Sherwin-Williams Company, 101 Prospect Avenue N.W., Cleveland, OH 44115. Macropoxy® 646-100 *Fast Cure Epoxy, Mill White, Material Safety Data Sheet*, August 2009. Protective.sherwin-williams.com. Smith, W. F. Principles of Materials Science and Engineering. McGraw-Hill, Inc., New York, second edition, 1990.
97. Suh, N.P. "The Delamination Theory of Wear," *Wear*, 25(1):111–124, July 1973.
98. Suh, N.P., S. Jahanmir, E.P. Abrahamson II, and A.P. Turner. "Further Investigation of the Delamination Theory of Wear," *Journal of Lubrication Technology*, 96, October 1974.

99. Szmerekovsky, A. G. *The Physical Understanding of the Use of Coatings to Mitigate Hypervelocity Gouging Considering Real-Test Sled Dimensions* AFIT/DS/ENY/04-06. Ph.D. Dissertation, Air Force Institute of Technology, Wright-Patterson AFB, OH, 2004.
100. Szmerekovsky, A. G. and A. N. Palazotto. "Structural Dynamic Considerations for a Hydrocode Analysis of Hypervelocity Test Sled Impacts," *AIAA Journal*, 44(6):1350–1359, 2006. 75.
101. Szmerekovsky, A.G., A.N. Palazotto, and J.D. Cinnamon. "*An Improved Study of Temperature Changes During Hypervelocity Sliding High Energy Impact.*" Proceedings of the 47th AIAA/ASME/ASCE/AHS/ASC Structures, Structural Dynamics and Materials Conference. AIAA, Newport, Rhode Island, 1-4 May 2006.
102. Voyiadjis, G.Z., A. Lodygowski, and B. Deliktas. *Non-Local Coupling of Friction and Damage I High Velocity Wear*. Technical Report, Louisiana State University, Baton Rouge, Louisiana, 2009.
103. Voyiadjis, G.Z., Deliktas, B., Lodygowski, A., Palazotto, A.N., Philippon, S., Rusinek, A., Faure, L., Chevrier, P., 2009a. *High rate and frictional effects in wear of metals using strain gradient plasticity*. In: Proceedings of the International Workshop in Memory of J.R.R. Klepaczko.
104. Voyiadjis, G.Z., Lodygowski, A., Deliktas, B., 2009b. *Non-Local Coupling of Friction and Damage in High Velocity Wear*. Technical Report, Air Force Institute of Technology, Wright–Patterson Air Force Base, Ohio.
105. Wei, R. P. "*Ultra High Strength Steel, Code 1225: Fe-18Ni-9Co-5Mo-Ti-Al.*" *Aerospace Structural Metals Handbook*, 1–39. CINDAS LLC, 1969.
106. Wikimedia Foundation, Inc. 2 September 2012. Retrieved March 10, 2013 from [https://en.wikipedia.org/wiki/Deformation\\_\(mechanics\)](https://en.wikipedia.org/wiki/Deformation_(mechanics)) and June 12, 2013 from [https://en.wikiversity.org/wiki/Nonlinear\\_finite\\_elements/Lagrangian\\_and\\_Eulerian\\_descriptions](https://en.wikiversity.org/wiki/Nonlinear_finite_elements/Lagrangian_and_Eulerian_descriptions)
107. Wolfson, M. R. *Wear, Solid Lubrication, and Bearing Material Investigation for High-Speed Track Applications*. Technical Report AFMDC-TR-60-7, Test Track Division, Air Force Missile Development Center, Holloman AFB, New Mexico, March 1960.
108. Zukas, J. A. *Introduction to Hydrocodes*. Elsevier, Amsterdam, 2004.

## Vita

Major Rodolfo G. Buentello Hernandez resided in Mexico until 1996, when he enlisted in the USAF. Rodolfo started his military career attending Technical School at Keesler AFB, GA where he was awarded as the Avionics Specialist Top Honor Graduate. Upon graduation, he was assigned to the 19<sup>th</sup> Maintenance Squadron at Robins AFB, GA.

During his tour at Robins AFB, he was granted permission to return to Mexico and finish his undergraduate studies. In 1997 he completed a B. S. in Mechanical and Electrical Engineering at the Instituto Tecnológico y de Estudios Superiores de Monterrey, Mexico. Shortly after graduation, he was accepted into the USAF Officer Training School and was commissioned on August 14, 1998.

Rodolfo's first assignment as an officer was in the Air Force Information and Warfare Center (AFIWC) at Kelly AFB, TX. At AFIWC, he designed and maintained Radar Warning Receiver and jammer models to identify and flag signals causing incorrect responses. During his station at Kelly AFB Rodolfo completed a M. S. in Engineering Systems Management at St. Mary's University.

In July 2001, Maj. Buentello was handpicked to serve in the 411<sup>th</sup> Flight Test Squadron located at Edwards AFB, CA. The 411<sup>th</sup> FTS was tasked with the USAF's #1-priority test program, the Raptor. For this elite unit Rodolfo tested the F-22's Electronic Warfare Systems and while doing so he earned a second master's degree, a M. A. S. in Aeronautical Engineering from Embry Riddle Aeronautical University in July 2003.

In June 2004, Rodolfo was hand-picked to follow-up the USAF's premier fighter to its Operational Test & Evaluation phase. He was assigned to the 59<sup>th</sup> Test & Evaluation Squadron at Nellis AFB, NV serving as the Lead F-22A Flight Test Engineer.

In 2006, Major Buentello was recommended to Det 1, 328<sup>th</sup> Armament Systems Group (ARSG) to fulfill the role of the Chief of Flight Testing. This detachment was part of a joint, Navy led Air-to-Air Missiles Systems Program Office (PMA-259) located at the Patuxent River Naval Air Station, MD. While leading PMA-259's Joint Test Team Maj. Buentello was selected to attend AFIT for a Doctor on Philosophy program. He began his doctoral studies on September 2010.

<b>REPORT DOCUMENTATION PAGE</b>			<i>Form Approved</i> <i>OMB No. 0704-0188</i>		
The public reporting burden for this collection of information is estimated to average 1 hour per response, including the time for reviewing instructions, searching existing data sources, gathering and maintaining the data needed, and completing and reviewing the collection of information. Send comments regarding this burden estimate or any other aspect of this collection of information, including suggestions for reducing this burden to Department of Defense, Washington Headquarters Services, Directorate for Information Operations and Reports (0704-0188), 1215 Jefferson Davis Highway, Suite 1204, Arlington, VA 22202-4302. Respondents should be aware that notwithstanding any other provision of law, no person shall be subject to any penalty for failing to comply with a collection of information if it does not display a currently valid OMB control number. PLEASE DO NOT RETURN YOUR FORM TO THE ABOVE ADDRESS.					
1. REPORT DATE (DD-MM-YYYY) 16-09-2013		2. REPORT TYPE Dissertation	3. DATES COVERED (From — To) Sep. 2010-Dec.2013		
4. TITLE AND SUBTITLE <b>3D Finite Element Modeling of Sliding Wear</b>			5a. CONTRACT NUMBER		
			5b. GRANT NUMBER		
			5c. PROGRAM ELEMENT NUMBER		
6. AUTHOR(S) Buentello Hernandez, Rodolfo G.			5d. PROJECT NUMBER		
			5e. TASK NUMBER		
			5f. WORK UNIT NUMBER		
7. PERFORMING ORGANIZATION NAME(S) AND ADDRESS(ES) Air Force Institute of Technology Graduate School of Engineering and Management (AFIT/ENY) 2950 Hobson Way WPAFB OH 45433-7765			8. PERFORMING ORGANIZATION REPORT NUMBER AFIT-ENY-DS-13-D-06		
9. SPONSORING / MONITORING AGENCY NAME(S) AND ADDRESS(ES) Air force Office of Scientific Research 875 Randolph St, Suite 325, room 3112 Arlington, VA 22203 PM Michael Kendra (703) 588-0671			10. SPONSOR/MONITOR'S ACRONYM(S) AFOSR/NA		
			11. SPONSOR/MONITOR'S REPORT NUMBER(S)		
12. DISTRIBUTION / AVAILABILITY STATEMENT DISTRIBUTION STATEMENT A. APPROVED FOR PUBLIC RELEASE; DISTRIBUTION UNLIMITED					
13. SUPPLEMENTARY NOTES This material is declared a work of the U.S. Government and is not subject to copyright protection in the United States.					
14. ABSTRACT This research focuses on the mechanical wear due to the sliding between two surfaces. Currently there is a need to identify and compare materials that would endure sliding wear under these severe conditions. The high costs of the high-speed sliding experiments has prevented the collection of the necessary data required to characterize wear. Simulating wear through Finite Elements (FE) would enable its prediction. This 3D wear model allows one to reasonably predict high-speed sliding mechanical wear. In the aerospace, automotive and weapon industries this model can aid in material selection, design and/or testing of systems subjected to high-speed sliding wear.					
15. SUBJECT TERMS High velocity, sliding, wear,Holloman High Speed Test Track (HHSTT), friction, finite element					
16. SECURITY CLASSIFICATION OF:			17. LIMITATION OF ABSTRACT	18. NUMBER OF PAGES	
a. REPORT	b. ABSTRACT	c. THIS PAGE	U	264	19a. NAME OF RESPONSIBLE PERSON Dr. Anthony. N. Palazotto
U	U	U			19b. TELEPHONE NUMBER (Include Area Code) (937)255-3636, ext 4599 (anthony.palazotto@afit.edu)